Caractérisation de la source sismique : depuis les études globales jusqu'aux analyses détaillées du processus de rupture

Martin Vallée

UNIVERSITÉ DE NICE - SOPHIA ANTIPOLIS - UFR SCIENCES

Ecole doctorale Sciences Fondamentales et appliquées

Habilitation à diriger des Recherches

Martin VALLÉE

Caractérisation de la source sismique : depuis les études globales jusqu'aux analyses détaillées du processus de rupture

« Séismes rapides, rapidement déterminés, ou lentement déclenchés »

Habilitation soutenue le 7 juin 2012 à 14h (Géoazur, Sophia Antipolis), devant le jury composé de:

Pascal BERNARD	Physicien IPGP, Paris	Rapporteur
Michel CAMPILLO	Professeur UJF, Isterre, Grenoble	Rapporteur
Françoise COURBOULEX	Chargée de Recherche CNRS, Geoazur, Nice	Examinatrice
Bertrand DELOUIS	Professeur UNS, Geoazur, Nice	Examinateur
Luis RIVERA	Professeur UDS, IPGS, Strasbourg	Rapporteur
Eléonore STUTZMANN	Physicienne IPGP, Paris	Examinatrice

Remerciements

Ce mémoire synthétise ma recherche effectuée en vue de mieux comprendre les séismes. Ce travail, initié à la fin du siècle dernier lors de ma thèse à Grenoble, s'est poursuivi lors de post-doctorats au CEA (Paris) puis à l'Observatoire du Vésuve à Naples. Depuis maintenant bientôt huit ans, j'ai pu développer ces recherches au sein du laboratoire Géoazur à Nice.

Cette habilitation a ainsi été permise par l'interaction avec de nombreuses personnes du monde scientifique, que je souhaite ici remercier. En commençant par la fin, je suis reconnaissant au jury d'avoir évalué ce mémoire et la soutenance associée : en premier lieu, je remercie les rapporteurs Pascal Bernard, Michel Campillo et Luis Rivera, mais aussi les examinateurs Françoise Courboulex, Bertrand Delouis et Eléonore Stutzmann.

Les travaux qui constituent ce mémoire doivent beaucoup au laboratoire Geoazur et à l'Institut de Recherche pour le Développement (IRD), qui m'ont tous deux permis, depuis 2004, de mener des recherches variées. L'interaction avec Bertrand Delouis et Françoise Courboulex a permis d'enrichir les recherches effectuées sur les séismes majeurs. Je remercie Jean-Mathieu Nocquet pour de nombreuses raisons ; pour n'en citer que deux, je pense à son son rôle moteur dans le projet en Equateur et aux collaborations fructueuses entre géodésie et sismologie qu'il a permises. Des discussions sur des sujets variés, entre autres avec Anne Deschamps, Mohamed Chlieh, Jean Virieux, Guust Nolet, Jean-Xavier Dessa, Stéphane Operto, Frédéric Cappa, Anthony Sladen, Isabelle Manighetti ou Mathilde Vergnolle m'ont conduit à mieux connaître des sujets qui m'était peu familiers. Je pense en particulier à la détermination de la structure terrestre, à l'apport de l'imagerie satellitaire et à l'instrumentation sismologique. Dans ce dernier domaine, je tiens aussi à remercier les ingénieurs et techniciens du laboratoire Didier Brunel, Christophe Maron, Fabrice Peix et Xavier Martin. Je remercie également les étudiants avec lesquels j'ai eu l'occasion de travailler ; le post-doctorat de Jean Charléty a été l'occasion d'échanges très utiles. Enfin, les recherches scientifiques dépendent de plus en plus d'une informatique performante : merci à Lionel Maurino, Caroline Ramel et plus récemment à David Chapeau pour leur aide ; et merci à Jenny Trévisan pour les cartes et la communication Web.

L'IRD a fortement soutenu le projet que nous avons monté en Equateur. Du côté Equatorien, l'Institut Géophysique (IG) à Quito a été un partenaire solide et efficace dans cette collaboration. Je tiens donc à la fois à remercier la représentation de l'IRD à Quito et de nombreux membres de l'IG : je pense en particulier à Hugo Yepes, Monica Segovia, Patricia Mothes, Sandro Vaca et Victor Alfonso, mais aussi à Cristina Ramos, Mayra Vaca et Paul Jarrin pour l'aspect technique.

A l'extérieur de Géoazur, des collaborations ont contribué à élargir le spectre de ma recherche. Les liens initiés durant mes post-doctorats avec le CEA et l'Université de Naples se sont poursuivis. En remontant encore un peu plus loin,

je remercie Michel Bouchon pour ses discussions et son intérêt à mes travaux, qui se sont poursuivis jusqu'à aujourd'hui. Enfin, la coopération initiée en 2009 avec Ana Ferreira à l'Université de Norwich a été, de mon point de vue, très fructueuse.

Pour terminer, je n'oublie pas le côté affectif et amical... Dans ces domaines, je pense d'abord à Marta, mais aussi à ma famille et à mes amis de Nice et d'ailleurs.

Nice, le 20 juin 2012

Table des matières

Remerciements **1**

Introduction **5**

I Observer les caractéristiques principales de la rupture sismique, à partir des données mondiales **7**

I.1 Les données sismologiques mondiales 8
I.1.1 Bref historique 8
I.1.2 Les réseaux à vocation mondiale 10
I.2 Les apports de la déconvolution par fonction de Green empirique 11
I.2.1 La fonction source apparente 11
I.2.2 Comment obtenir précisément les fonctions source apparentes 14
I.2.3 Limitations à haute fréquence 15
I.2.4 Extraction des informations sur la source sismique 17
I.2.5 Le séisme de Sumatra-Andaman du 26 décembre 2004 . . 19
I.3 La méthode SCARDEC 33
I.3.1 Idée générale 33
I.3.2 La méthode SCARDEC, et ses applications aux séismes de subductions majeurs 34
I.3.3 Validations de la méthode SCARDEC 56
I.3.4 Extension de la méthode aux magnitudes plus faibles et plus fortes 67
I.3.5 Application en temps quasi-réel 68
I.4 Perspectives : analyse systématique des caractéristiques de source 72

II Rentrer dans le détail du processus de rupture, à partir d'approches ou de données variées **74**

II.1 Diversification des distances d'observation de la source 75
II.1.1 Analyse conjointe des données locales, régionales, et télésismiques 75
II.1.2 Exemple d'application aux séismes de Molise (Italie, 2002) 77
II.2 Variabilité de la vitesse de rupture 82
II.2.1 Introduction 82

II.2.2 Observation du mode de rupture supershear 84
II.2.3 Les ondes de Mach générées par les séismes supershear . . 104
II.3 Les récents apports de la sismo-géodésie 110
II.3.1 Accroissement de la capacité d'observation des séismes . . 110
II.3.2 L'observation des mouvements forts 116
II.4 Perspectives : Intérêt des séismes particuliers 124

III Replacer la rupture dans le cycle sismique : Sismogénèse dans une zone de subduction active, Les Andes du Nord 126
III.1 Introduction : Objectifs généraux du projet « ADN » 127
III.2 Instrumentation 131
III.3 Caractéristiques de la sismicité modérée à forte 135
III.3.1 Sismicité passée de la marge Centre-Nord Equateur . . . 135
III.3.2 Déformations actuelles observées le long de la marge . . . 138
III.3.3 Mécanismes de la sismicité modérée récente 140
III.4 Un séisme lent, générateur d'une abondante sismicité 145
III.5 Perspectives : Mouvements asismiques et sismicité 166

Bibliographie 169

Annexes 182
A.1 Curriculum Vitae 183
A.2 Publications 184
A.3 Pilotage et participation à des projets de recherche 185
A.4 Encadrement de travaux de recherche 186
A.5 Enseignement 188
A.6 Animation scientifique 188

Introduction

Ce mémoire d'habilitation décrit ma recherche effectuée en vue de mieux comprendre le mécanisme des tremblements de terre. Les ondes sismiques sont les principales données qui donnent accès à cette information, et mes travaux sont donc en lien direct avec les observations des capteurs sismiques (ou géodésiques) capables de détecter ces ondes. Les qualité, quantité et type de données disponibles m'ont conduit à aborder cette thématique sous trois angles différents, qui recoupent les trois chapitres de ce mémoire.

A l'échelle mondiale, les capteurs large-bande du réseau global permettent une étude systématique et homogène de tous les séismes dont la magnitude est suffisante pour générer des ondes clairement analysables. Cette magnitude seuil est de l'ordre de 5.5-6 lorsque l'on analyse les ondes de volume se propageant dans la Terre. Par ailleurs, ces données sont accessibles en temps réel, ce qui permet d'obtenir des informations rapides sur les séismes, à condition que des techniques d'analyse automatisées soient mises en place. Ce double intérêt de l'approche globale -systématisme et rapidité- est développé dans le Chapitre I de ce mémoire.

L'échelle mondiale trouve ses limites lorsqu'on s'intéresse aux détails du processus de rupture. Alors que les données mondiales sont suffisantes pour imager les caractéristiques moyennes de source (mécanisme au foyer, profondeur, magnitude de moment, fonction source), elles ne permettent généralement pas d'extraire avec précision les informations internes à la rupture sismique (distribution de glissement, vitesse de rupture locale). Pour ce faire, il est nécessaire d'utiliser des données plus proches de l'événement sismique, et de développer des techniques d'analyse adaptées à chaque configuration (analyses en réseau, analyses comparées entre le séisme principal et l'un de ses précurseurs...). Par ailleurs, et contrairement à l'échelle globale - où les données large-bande sont les données « reines » de l'analyse de la source -, l'analyse à distance plus proche permet et/ou requiert de diversifier les données utilisées. Cela peut passer par l'utilisation des capteurs accélérometriques, ou par la nouvelle utilisation des capteurs GPS en tant que sismomètres. Le Chapitre II s'intéresse à cette thématique de résolution fine des propriétés de source, avec un intérêt particulier pour la détermination de la vitesse de rupture. La mise en évidence récente des vitesses de rupture supershear (plus rapides que les ondes de cisaillement) et de leurs conséquences constituent un point important de ce chapitre.

Enfin, il est intéressant de replacer la rupture sismique dans le cadre plus

large des conditions qui stimulent ou inhibent son déclenchement. Dans cet esprit, je présente dans le Chapitre III des éléments de réponse venant de l'observation continue de la zone de subduction Equatorienne. Cette observation - incluant capteurs large-bande, accéléromètres, et GPS - se déroule depuis 2008 dans le cadre du projet ANR ADN, soutenu par l'IRD et en collaboration avec l'Institut de Géophysique à Quito. Nous montrerons dans ce chapitre comment l'occurrence de séismes lents sur l'interface de subduction est un facteur déclenchant de la sismicité.

A la fin de chaque chapitre, je présenterai des éléments de perspectives dans les domaines concernés.

Enfin, les activités relatives à l'accompagnement de la recherche (implication dans les projets de recherche, encadrement d'étudiants, enseignement) sont présentées en fin de mémoire.

Chapitre I

Observer les caractéristiques principales de la rupture sismique, à partir des données mondiales

I.1 Les données sismologiques mondiales

I.1.1 Bref historique

Le réseau sismologique mondial a débuté dans les années 1960 au travers du projet WWSSN (World Wide Standardized Seismograph Network). Une centaine de stations (incluant des capteurs longue et courte-période, associés à une horloge précise) ont alors été déployées sur le globe (Figure I.1). Depuis cet effort pionnier d'accroissement et d'uniformisation de l'observation sismique, plusieurs améliorations décisives se sont produites. Au cours des années 1980, le développement de stations large-bande et digitales a grandement facilité l'analyse des signaux sismiques. D'une part, il est devenu inutile de chercher à « raccorder » les informations fournies par les capteurs courte et longue-période. D'autre part, les analyses informatiques ont pu être appliquées directement aux signaux enregistrés par les stations, sans les traitements préalables que nécessitent les données analogiques.

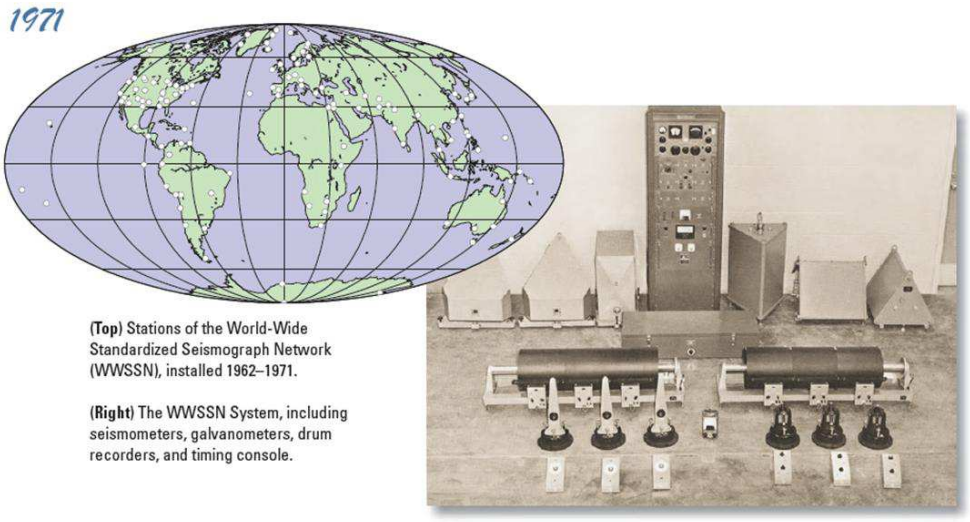

Fig. I.1 – Distribution géographique et instrumentation du réseau WWSSN en 1971 (Source : USGS, Alburquerque Seismological Laboratory)

Les années 1990 puis 2000 ont vu l'augmentation du nombre de stations large-bande mondiales. Des capteurs ont été installés dans des lieux difficiles d'accès et de maintenance (Antarctique, îles océaniques...), ce qui a amélioré la couverture mondiale. Aujourd'hui, même si la distribution reste hétérogène sur les continents, la limite principale reste la quasi-absence de capteurs sous-marins. A l'échelle nationale ou continentale, l'accroissement du nombre de stations a été encore plus spectaculaire, comme en témoignent le programme américain USArray (>400 stations) et les réseaux large-bande européen VEBSN (>300 stations) ou australien (>100 stations). Ces densifications locales sont

utiles à l'analyse de la sismicité mondiale, en particulier à travers les analyses de type « antenne » dont nous parlerons dans le chapitre II.

L'amélioration des télécommunications et de l'informatique (stockage, traitement) a aussi facilité l'analyse rapide et efficace de grands volumes de données sismiques. Les signaux continus de la plupart des stations mondiales sont aujourd'hui accessibles en temps réel. De plus, la récupération de dizaines de Giga-octets de données continues est devenue banale, avec des protocoles toujours plus simples d'utilisation. Les requêtes de données, concernant des séries temporelles haute-fréquence de longue durée ou des fenêtres de temps correspondants à des centaines de séismes, sont devenues classiques.

Enfin, durant ces phases de l'évolution du réseau mondial, le libre accès aux données a généralement été conservé. Ce point très positif (et d'ailleurs assez peu courant dans l'observation scientifique) permet à tous les chercheurs de travailler sur ces données mondiales, avec la seule contrainte d'avoir un ordinateur et un accès Internet. La Figure I.2 illustre, à travers les données large-bande aujourd'hui accessibles en temps réel sur le serveur d'IRIS (Incorporated Research Institutions for Seismology, `http://www.iris.edu`), l'évolution des données depuis 1971 et le WWSSN (Figure I.1).

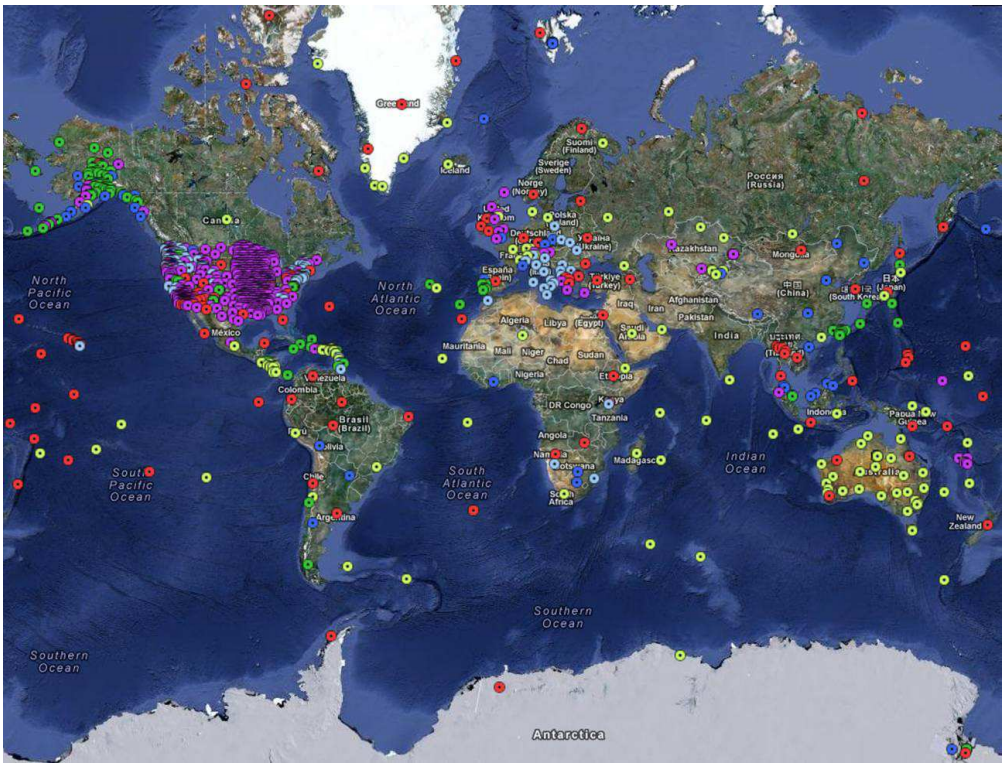

Fig. I.2 – Données large-bande accessibles en temps réel sur le serveur de données d'IRIS en 2012 (environ 1200 stations)

I.1.2 Les réseaux à vocation mondiale

Dans de nombreux types d'analyse de la sismicité mondiale, il n'est pas utile de multiplier les points d'observations proches les uns des autres. D'une part, le signal sismique varie généralement peu lorsque la source est lointaine, ce qui conduit à une redondance de l'information. D'autre part, cette densification de l'observation sera toujours locale, car la densité des stations dans d'autres azimuts restera plus faible. Une telle multiplication des données peut donc même être contre-productive, dans la mesure où certaines directions d'observations risquent de biaiser les analyses.

C'est pourquoi plusieurs réseaux ne sont constitués que de stations de très bonne qualité (très large-bande, si possible dans des sites très peu bruités tels que tunnels, puits, caves sismiques...), en privilégiant une couverture mondiale homogène. Cela a toujours été l'optique du réseau Géoscope (`http://geoscope.ipgp.fr`) depuis sa création au début des années 1980. Aujourd'hui, ce réseau dispose d'environ 30 stations, dont 25 sont accessibles en temps réel. Les réseaux IRIS (II, IU, IC), qui ont pris la suite du WWSSN, sont actuellement les contributeurs principaux de cette observation mondiale, avec près de 120 stations accessibles. Enfin, certains réseaux complémentent avantageusement la couverture terrestre, tels que le réseau GT (USGS) ou Geofon. Ces réseaux ont été fédérés depuis la fin des années 1980 au sein du FDSN (Federation of Digital broad band Seismic Network, `http://www.fdsn.org`), dont une carte récente est présentée dans la Figure I.3. L'avantage de ce super-réseau, qui ne donne accès qu'à un sous-ensemble des stations mondiales disponibles, est de fournir des stations de très bonne qualité avec une densité la plus homogène possible.

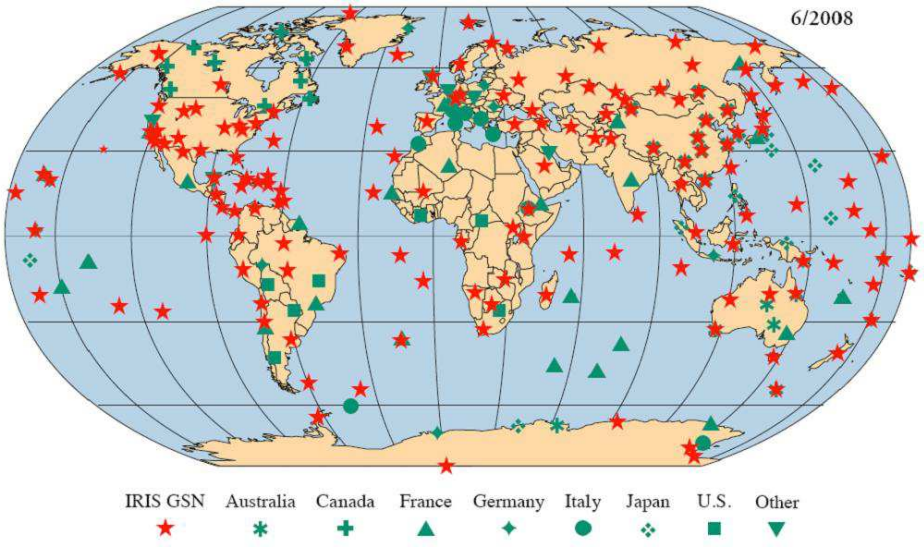

FIG. I.3 – Carte des stations affiliées au FDSN

I.2 Les apports de la déconvolution par fonction de Green empirique

I.2.1 La fonction source apparente

Nous considérons tout d'abord le cas général du déplacement généré par une source sismique placée dans un volume V. Nous notons G_{ij} le tenseur de Green, qui exprime le déplacement créé dans la direction i par une force unitaire appliquée dans la direction j. m_{ij} est la densité de moment sismique, qui décrit comment une facette d'un petit cube (situé dans le volume V), de normale i, est affectée dans la direction j par le séisme. Le récepteur est localisé en un point $\mathbf{x} = (x_1, x_2, x_3)$. Le théorème de représentation (voir par exemple *Aki and Richards*, 2002) nous apprend que le déplacement spectral U_i généré en $\mathbf{x}$ s'écrit :

$$U_i(\mathbf{x}, \omega) = \int_V m_{jl}(\mathbf{x}', \omega)\ G_{ij,l}(\mathbf{x}, \mathbf{x}', \omega) d\mathbf{x}' \tag{I.1}$$

Les notations usuelles suivantes sont utilisées :

- les indices spatiaux présents au second membre, mais absents du premier (ici j, l), impliquent la somme sur les valeurs possibles de ces indices (ici $j = 1, 2, 3$ et $l = 1, 2, 3$)
- la notation $_{,l}$ exprime la dérivée partielle $\frac{\partial}{\partial x_l}$
- les variables vectorielles sont notées en gras

Dans le cas particulier d'un petit séisme, la source sismique peut être considérée ponctuelle (localisée en $\mathbf{x^0}$). Sa fonction source est notée f et le tenseur des moments (unitaire) M_{jl}. Sa densité de moment s'écrit alors :

$$m_{jl}(\mathbf{x}', \omega) = f(\omega)\ M_{jl}\ \frac{\delta(\mathbf{x}' - \mathbf{x^0})}{i\omega} \tag{I.2}$$

L'utilisation de l'équation (I.1) permet de déterminer le déplacement généré par une telle source ponctuelle, que l'on note $u_i^0(\mathbf{x}, \mathbf{x^0}, \omega)$:

$$u_i^0(\mathbf{x}, \mathbf{x^0}, \omega) = f(\omega)\ M_{jl}\ \frac{G_{ij,l}(\mathbf{x}, \mathbf{x^0}, \omega)}{i\omega} \tag{I.3}$$

Nous considérons que le tenseur des moments M_{jl} décrit un glissement sur une faille plane (mouvement type « double-couple », en accord avec la grande majorité des séismes), et qu'un séisme plus fort s'est produit, dans le voisinage du point $\mathbf{x^0}$, avec le même mécanisme décrit par M_{jl}. L'hypocentre de ce séisme est localisé en $\mathbf{x^h}$. Nous choisissons l'orientation de la base de l'espace tel que le vecteur (0,0,1) soit orthogonal au plan de faille. La densité de moment du fort séisme s'exprime alors :

$$\begin{aligned} m_{jl}(\mathbf{x}', \omega) &= M_{jl}\ \mu\ \Delta u(x_1', x_2', \omega) e^{-i\omega t_r(x_1', x_2')}\ \delta(x_3' - x_3^h) \\ &= M_{jl}\ \mu\ \frac{\Delta \dot{u}(x_1', x_2', \omega)}{i\omega}\ e^{-i\omega t_r(x_1', x_2')}\ \delta(x_3' - x_3^h) \end{aligned} \tag{I.4}$$

μ est la rigidité du milieu, pouvant dépendre de la position du point sur la faille. Δu décrit le glissement d'un point (x'_1, x'_2) de la faille (et $\Delta \dot{u}$ la vitesse de glissement), à partir de l'instant où le front de rupture venant de l'hypocentre $\mathbf{x^h}$ a atteint ce point. Ce décalage du temps de rupture, par rapport au temps d'initiation à l'hypocentre, est donné par la fonction $t_r(x'_1, x'_2)$. Le déplacement généré s'écrit alors :

$$U_i(\mathbf{x}, \omega) = \frac{M_{jl}}{i\omega} \int_{L_1}^{L_2} \int_{W_1}^{W_2} G_{ij,l}(\mathbf{x}, (x'_1, x'_2, x^h_3), \omega)\ \mu\ \Delta\dot{u}(x'_1, x'_2, \omega) e^{-i\omega t_r(x'_1, x'_2)} dx'_1 dx'_2 \quad \text{(I.5)}$$

L_1, L_2, W_1, W_2 représentent les extrémités de la surface de glissement sur le plan de faille. Nous considérons maintenant que le tenseur de Green G_{ij} correspond à un train d'ondes de vecteur d'onde unique à la source $\mathbf{k} = (k_1, k_2, k_3) = \omega/c(\omega)\ (k^*_1, k^*_2, k^*_3) = \omega\ (s_1, s_2, s_3)$. $\mathbf{k}^*$, $\mathbf{s}$ et $c(\omega)$ sont respectivement le vecteur d'onde normalisé, le vecteur lenteur et la vitesse de phase du train d'ondes. Cette restriction à un unique vecteur d'onde $\mathbf{k}$ a d'importantes conséquences pour les données sismiques réelles. En effet, cela impose que les différents types d'ondes puissent être séparés temporellement, ou qu'un type d'ondes soit fortement dominant. Cela impose de plus que l'hypothèse de « source lointaine » (c'est-à-dire que $||\mathbf{x} - \mathbf{x^0}|| \gg (W_2 - W_1)$ et $||\mathbf{x} - \mathbf{x^0}|| \gg (L_2 - L_1)$) soit vérifiée. En effet, si ce n'est pas le cas, même si l'on considère un seul type d'onde, le vecteur $\mathbf{k}$ change. Dans la configuration des ondes télésismiques (distance à la source entre 3500 et 10000km), ces hypothèses sont généralement valides : il est possible de séparer temporellement les arrivées principales (onde P, onde S, ondes de surface) des arrivées suivantes, et l'hypothèse de source lointaine n'est remise en cause que pour des séismes exceptionnellement grands.

En théorie, même dans la configuration télésismique, le tenseur de Green varie de manière complexe suivant le point $\mathbf{x}'$ de la source. Néanmoins, deux caractéristiques de la Terre et de la sismicité permettent de simplifier cette relation. Tout d'abord, la Terre peut, dans une bonne approximation, être considérée comme un objet de structure sphérique, avec des variations qui ne dépendent que de la profondeur. Ensuite, la majorité des forts séismes ont une extension horizontale largement supérieure à leur extension verticale : c'est en particulier le cas des séismes compressifs sur l'interface de subduction, dont le pendage est peu raide (5°-30°) et des grands séismes crustaux de décrochement. En prenant en compte ces deux observations, l'effet de la localisation précise (x'_1, x'_2) sur G_{ij} s'exprime principalement par un déphasage du temps d'arrivée dépendant de $\mathbf{k}$:

$$G_{ij,l}(\mathbf{x}, (x'_1, x'_2, x^h_3), \omega) = G_{ij,l}(\mathbf{x}, \mathbf{x^h}, \omega)\ e^{i\Delta\phi(\mathbf{k}, \mathbf{x}', \mathbf{x^h})}, \quad \text{(I.6)}$$

avec

$$\Delta\phi(\mathbf{k}, \mathbf{x}', \mathbf{x^h}) = (k_1(x'_1 - x^h_1) + k_2(x'_2 - x^h_2)) \quad \text{(I.7)}$$

En faisant apparaître la position $\mathbf{x^0}$, l'équation précédente s'écrit :

$$G_{ij,l}(\mathbf{x}, (x'_1, x'_2, x^h_3), \omega) = G_{ij,l}(\mathbf{x}, \mathbf{x^0}, \omega) e^{i\mathbf{k}.(\mathbf{x^h} - \mathbf{x^0})}\ e^{i\Delta\phi(\mathbf{k}, \mathbf{x}', \mathbf{x^h})} \quad \text{(I.8)}$$

La combinaison des équations (I.5) et (I.8) conduit à :

$$\begin{aligned} U_i(\mathbf{x},\omega) =& M_{jl}\ \frac{G_{ij,l}(\mathbf{x},\mathbf{x^0},\omega)}{i\omega} e^{i\mathbf{k}.(\mathbf{x^h}-\mathbf{x^0})} \\ & \int_{L_1}^{L_2}\int_{W_1}^{W_2} \mu\ \Delta\dot{u}(x'_1,x'_2,\omega) e^{i(\Delta\phi(\mathbf{k},\mathbf{x'},\mathbf{x^h})-\omega t_r(x'_1,x'_2))} dx'_1 dx'_2\ , \end{aligned} \tag{I.9}$$

où l'on reconnaît la radiation générée par un point source en $\mathbf{x^0}$ (equation I.3). Le déplacement créé par le grand séisme en $\mathbf{x}$ peut donc s'exprimer :

$$U_i(\mathbf{x},\omega) = \frac{u_i^0(\mathbf{x},\mathbf{x^0},\omega)}{f(\omega)}\ e^{i\mathbf{k}.(\mathbf{x^h}-\mathbf{x^0})}\ F(\mathbf{k},\omega), \tag{I.10}$$

en ayant introduit la fonction suivante :

$$F(\mathbf{k},\omega) = \int_{L_1}^{L_2}\int_{W_1}^{W_2} \mu\ \Delta\dot{u}(x'_1,x'_2,\omega) e^{i(\Delta\phi(\mathbf{k},\mathbf{x'},\mathbf{x^h})-\omega t_r(x'_1,x'_2))} dx'_1 dx'_2 \tag{I.11}$$

F est essentiellement un terme de source, mais le terme de déphasage $\Delta\phi$, dépendant de $\mathbf{k}$, le rend également sensible à la configuration source-récepteur. C'est pourquoi F porte le nom de « fonction source apparente » ou « fonction source relative ». La dépendance de la configuration source-récepteur complique la comparaison systématique des séismes, pour laquelle il serait plus direct de travailler sur la fonction source absolue (correspondant a $\Delta\phi(\mathbf{k},\mathbf{x'},\mathbf{x^h}) = 0$ dans l'équation (I.11)). En revanche, si le nombre d'observations est important (variation de $\mathbf{k}$), cette dépendance permet d'obtenir des informations sur la fonction $\Delta\dot{u}$: des méthodes d'optimisation peuvent être utilisées pour déterminer les caractéristiques spatio-temporelles de $\Delta\dot{u}$ capables de reproduire la fonction F dans toutes les directions $\mathbf{k}$ observées. Un exemple d'application d'une telle analyse est donné dans l'article sur le séisme de Sumatra (2004) (*Vallée*, 2007) joint à ce mémoire.

La fonction source apparente est couramment utilisée car comme le montre l'équation (I.10), il est relativement facile de l'obtenir empiriquement. Il suffit théoriquement d'avoir enregistré à un récepteur, en plus du séisme d'intérêt, un autre petit séisme de mécanisme et localisation similaires, pour pouvoir estimer par division spectrale la fonction source apparente. La fonction source apparente ainsi obtenue doit seulement être corrigée du déphasage créé par les différences de localisation hypocentrale et de l'effet de la fonction source f du petit séisme. Dans le cas où l'on considère que f est instantanée et que les hypocentres des deux séismes sont colocalisés, il suffit de corriger du facteur d'échelle créé par le moment sismique du petit séisme.

C'est le principe des approches par « fonction de Green empirique », nom fréquemment donné au petit séisme (EGF en anglais). Ces méthodes ont été initiées par *Hartzell* (1978), puis fréquemment utilisées ou développées, par exemple par *Mueller* (1985), *Fukuyama and Irikura* (1986), *Mori and Frankel* (1990), *Ammon et al.* (1993), *Velasco et al.* (1994) ou *Courboulex et al.*

(1997). On peut d'ailleurs remarquer que le terme EGF est inexact car c'est « la fonction point-source empirique » qui est utilisée pour accéder à la fonction source apparente. L'avantage de cette approche est fort pour les ondes de propagation complexe dans la Terre, et en particulier pour les ondes de surface haute-fréquence. En effet, leur modélisation déterministe (à partir des modèles de Terre connus) est difficile, et c'est donc par l'approche empirique que l'on pourra extraire au mieux les fonctions source apparentes. Un autre avantage de cette méthode concerne les séismes anciens (année d'occurrence entre 1900-1910 et 1960-1970), pour lesquels la réponse instrumentale des récepteurs peut être difficile à obtenir. Dans l'approche par fonction de Green empirique, cette réponse instrumentale affecte de manière équivalente U_i et u_i^0, et n'a donc pas d'influence sur l'évaluation des fonctions source. Nous avons tiré profit de cet aspect pour analyser le fort séisme de Turquie de 1912 (*Aksoy et al.*, 2010).

I.2.2 Comment obtenir précisément les fonctions source apparentes

Même si les fonctions source apparentes peuvent être théoriquement directement extraites par division spectrale, ce processus est instable car des valeurs faibles de u_i^0 à certaines fréquences (causées par exemple par des différences de mécanisme ou de profondeur entre le choc principal et la fonction de Green empirique) peuvent conduire à des valeurs aberrantes de F. La technique la plus simple pour remédier à ce problème est celle du « water level » (voir *Clayton and Wiggins*, 1976). L'idée est d'imposer une valeur minimale à u_i^0, en vue d'éviter les effets importants d'un dénominateur anormalement faible.

D'autres techniques plus évoluées s'appuient sur les propriétés physiques de F pour stabiliser l'obtention de cette fonction. Il est utile pour cela d'exprimer la fonction F dans le domaine temporel. Dans le cas non dispersif où c est indépendant de la fréquence (valide pour les ondes de volume, et pour les ondes de surface si l'on se restreint à certaines bandes de fréquence), la transformée de Fourier inverse de F s'exprime :

$$F(\mathbf{s},t) = \int_{L_1}^{L_2}\int_{W_1}^{W_2} \mu\ \Delta\dot{u}(x_1',\ x_2',\ t + s_1.(x_1' - x_1^h) + s_2.(x_2' - x_2^h) - t_r(x_1',x_2'))\ dx_1'dx_2' \tag{I.12}$$

Par simplicité, nous conservons, pour les transformées de Fourier inverses des fonctions, les notations définies dans l'approche fréquentielle. L'équation (I.10) peut maintenant s'écrire sous la forme d'une convolution:

$$U_i(\mathbf{x},t)\ *\ f(t) = u_i^0(\mathbf{x},\mathbf{x^0},\ t + \ \mathbf{s}.(\mathbf{x^h} - \mathbf{x^0}))\ *\ F(\mathbf{s},t) \tag{I.13}$$

F peut donc être obtenue par *déconvolution*, désignée par l'opérateur $*^{-1}$:

$$F(\mathbf{s},t) = [U_i(\mathbf{x},t)\ *\ f(t)]\ *^{-1}\ u_i^0(\mathbf{x},\mathbf{x^0},\ t + \ \mathbf{s}.(\mathbf{x^h} - \mathbf{x^0})) \tag{I.14}$$

La fonction F possède quatre propriétés, qui découlent principalement des caractéristiques physiques de $\Delta\dot{u}$:

- (1) F est positive. Cela vient directement du fait que $\Delta\dot{u}$ est elle-même positive (une vitesse de glissement négative impliquerait que certains points de la faille bougent dans la direction opposée au mouvement défini par M_{jl}).
- (2) F est à support borné. Cela vient du fait que la durée du glissement local est finie.
- (3) Dans la grande majorité des cas, F est causale. Les exceptions à cette règle ne peuvent exister que dans le cas où le séisme a une vitesse de rupture supérieure à la vitesse de phase des ondes (cas des séismes « supershear » , où la vitesse de rupture est supérieure à la vitesse des ondes S ; voir chapitre II). Même dans ce cas, la non-causalité ne pourra se produire que dans des directions spécifiques où le déphasage lié à $\mathbf{s}$ dans l'expression (I.12) est maximal. Dans le cas d'une propagation de rupture à dominante horizontale observé à distance lointaine, seules les fonctions source apparentes déduites des ondes de surface peuvent être acausales. En effet, l'inclinaison proche de la verticale du vecteur $\mathbf{s}$ pour les ondes de volume conduit à une valeur modérée du déphasage $\mathbf{s}.(\mathbf{x}' - \mathbf{x}^{\mathbf{h}})$.
- (4) Par définition du moment sismique, l'intégrale temporelle de F est égale au moment sismique du séisme (noté M_0), et cela quelque soient les types d'ondes ou les directions considérées :

$$\int_{-\infty}^{+\infty} F(\mathbf{s}, t)dt = M_0, \ \forall \mathbf{s} \tag{I.15}$$

Ces propriétés peuvent être utilisées pour stabiliser l'obtention de la fonction source apparente. Par exemple, la condition de positivité est fréquemment prise en compte. J'ai proposé en 2004 (*Vallée et al.*, 2004) une approche permettant de prendre simultanément en compte ces quatre propriétés, en utilisant la méthode de Landweber introduite en sismologie par *Bertero et al.* (1997). J'ai pu montrer que l'insertion de ces conditions conduit à une meilleure évaluation des fonctions source, même en présence de données bruitées. En plus de cet intérêt de stabilisation, cette approche permet de rendre les fonctions source compatibles entre elles, ce qui est indispensable pour leur analyse ultérieure. Par exemple, si des fonctions source apparentes ne portent pas le même moment sismique, il est difficile de pouvoir extraire des caractéristiques fiables du processus de rupture.

I.2.3 Limitations à haute fréquence

Le paragraphe précédent décrit l'approche technique utilisée pour rendre les fonctions source apparentes aussi réalistes que possible. Mais la qualité de ces fonctions source dépend aussi logiquement du respect précis des hypothèses conduisant à l'équation (I.14).

Tout d'abord, l'EGF doit avoir un mécanisme et une profondeur similaire au choc principal, et posséder une source aussi impulsive que possible. En effet, dans ce cas, l'effet de sa fonction source f peut être négligé. Cette condition conduirait à choisir une EGF de très faible magnitude. Néanmoins, l'EGF doit aussi avoir un bon rapport signal/bruit pour des fréquences suffisamment basses - de telle manière que le moment sismique du fort séisme puisse être précisément extrait – ce qui interdit des magnitudes trop faibles. La prise en compte de ces deux limitations conduit en général à sélectionner des EGF ayant 1 à 2 degrés de magnitude de moins que le séisme principal. En contrepartie, la fonction f a elle-même une certaine complexité, qui a une influence dans l'équation (I.14). Si l'on prend en compte des lois d'échelle classiques où la durée d'un séisme croît comme la racine cubique de son moment sismique, la durée de la fonction f représentera typiquement 10% à 30% de la durée des fonctions source apparentes F. L'approche par EGF gagne donc à prendre en compte la fonction f, au moins de manière simplifiée (si cela n'est pas fait, on tend à obtenir par déconvolution des fonctions source apparentes plus courtes que la réalité); par exemple, on peut assimiler f à une fonction triangulaire, de durée reliée à sa magnitude par des lois d'échelle classiques. Cette durée peut aussi être estimée indépendamment, lorsque l'EGF est elle-même un séisme de magnitude modérée à forte. Dans tous les cas, il sera difficile d'estimer de manière indépendante les fréquences élevées de la fonction f, ce qui est une des causes limitant la qualité des fonctions apparentes à haute fréquence.

L'autre cause majeure est reliée aux caractéristiques spatiales du séisme principal. Lorsque l'étendue spatiale croît et devient significative par rapport à la distance source-station, la validité de l'équation (I.6) est remise en cause, particulièrement à haute fréquence. En effet, la dépendance spatiale de la fonction de Green ne peut plus simplement être modélisée par un déphasage dépendant du vecteur d'onde. L'ensemble du spectre de cette fonction de Green est affecté de manière complexe. Cette observation pourrait conduire à prendre en compte plusieurs EGFs selon la localisation de la rupture, approche qui peut être implémentée si l'on cherche à simuler la radiation d'un séisme à partir d'un modèle de source donné (voir par exemple une simulation de la radiation du séisme de Tohoku du 11 mars 2011, *Kurahashi and Irikura*, 2011). Néanmoins, dans l'approche déconvolutive, la position spatio-temporelle de la source est inconnue, ce qui ne permet pas facilement de prendre en compte plus d'une EGF.

L'extension spatiale du choc principal conduit donc à une perte d'information sur les hautes fréquences générées par la source. Cette limitation n'empêche cependant pas de travailler sur de très forts séismes, à condition de faire des analyses préalables de la variabilité des EGFs en fonction de la fréquence. Dans le cas du séisme de Sumatra (26/12/2004), où la source s'étend sur plus de 1200km de long, il apparaît difficile de ne considérer qu'une EGF, lorsqu'on utilise des stations situées à 7000-10000km de l'épicentre. Mais j'ai pu montrer (*Vallée*, 2007, présenté à la fin de cette section), à l'aide de données réelles de différentes EGFs possibles, que les fréquences inférieures à 0.01Hz respectaient

l'équation (I.6) sur l'ensemble de l'étendue du séisme. Sachant que ce séisme à une durée totale de plus de 500s, avec des fonctions sources apparentes atteignant une durée de plus de 800s, il reste une gamme de fréquences significative où l'approche par EGF nous apporte des informations sur la source sismique. D'une manière générale, on peut considérer que l'approche par EGF nous permet d'avoir accès à une bande de fréquence « utile » (notée $[F_{min}\ F_{max}]$) qui dépend de la taille du séisme, mais dont le rapport F_{max}/F_{min} reste relativement constant. La fréquence F_{min} est proche de l'inverse de la durée du séisme (les fréquences beaucoup plus basses n'étant plus considérées « utiles », car elles ne dépendent que du moment sismique) tandis que F_{max} est typiquement de l'ordre de $10.F_{min}$. L'information fournie par les fréquences plus élevées sera probablement perdue pour l'une et/ou l'autre des deux raisons précédentes (EGF non impulsive ou étendue spatiale du choc principal).

I.2.4 Extraction des informations sur la source sismique

Les fonctions source apparentes portent en elles – de manière intégrée – les caractéristiques locales du processus de rupture. Puisqu'on bénéficie de ces mesures intégrées pour différentes lenteurs $\mathbf{s}$, il est possible d'avoir des informations sur l'intégrant lui-même. Cependant, comme expliqué dans l'étude de *Menke* (1985), les lenteurs ne varient dans le cas réel que dans une faible gamme, ce qui ne permet pas d'avoir une détermination complète de la fonction $\Delta\dot{u}$.

Dans le cas où les fonctions source apparentes sont les seules données utilisées, cela nous amène à simplifier les modèles de source ; l'approximation la plus courante est de considérer que le séisme principal s'est propagé dans une direction préférentielle. Ce modèle est souvent une bonne modélisation de la réalité pour les grands séismes, en particulier dans les domaines intraplaques, où l'épaisseur crustale limite la propagation verticale de la rupture. Dans ce modèle en « ligne source », les fonctions source apparentes temporelles s'expriment

$$F(\mathbf{s},t) = \ W \ \int_{L_1}^{L_2} \mu \ \Delta\dot{u}(x_1',\ t + s_1.(x_1' - x_1^h) - t_r(x_1'))\ dx_1', \tag{I.16}$$

si l'on considère que la largeur W de la zone de rupture est constante. Si l'on conserve le cas général, on peut introduire la fonction m_L décrivant le moment sismique par unité de longueur de faille, et écrire les fonctions source apparentes :

$$F(\mathbf{s},t) = \ \int_{L_1}^{L_2} \dot{m_L}(x_1',\ t + s_1.(x_1' - x_1^h) - t_r(x_1'))\ dx_1', \tag{I.17}$$

C'est l'approche utilisée pour analyser le séisme de Sumatra (2004) dans l'article présenté dans la section suivante. Si m_L est supposée être une fonction rampe, la procédure d'optimisation visera à retrouver - à partir des fonctions apparentes observées - la valeur finale de la rampe, la durée d'activation, et le temps de rupture t_r en tout point de la faille.

Dans de nombreux cas d'analyse plus précise de la source sismique, les fonctions source apparentes sont utilisées en complément d'autres observations,

par exemple des données en champ proche (accéléromètres ou géodésie, voir chapitre II). Dans cette configuration, on peut conserver la représentation bi-dimensionnelle (équation I.12), et inverser ou valider le modèle de source pour le glissement en tout point de la faille.

Le caractère intégré des fonctions source apparentes donne naturellement accès au moment sismique du grand séisme (équation I.15). Dans le cas de séismes de magnitudes classiques (de 6 à 8–8.5), cette caractéristique du séisme principal peut être bien évaluée par ailleurs, par exemple par des méthodes en point-source ou en centroid (Global CMT). Il est alors plus efficace d'utiliser directement ce moment sismique pour stabiliser la déconvolution (voir section I.2.2). Paradoxalement, lorsque le séisme atteint des magnitudes très grandes (M>8.5–9), sa magnitude devient plus difficile à déterminer, en particulier car les effets liés à l'extension spatio-temporelle de la source ne peuvent être négligés, même à basse fréquence pour des stations très lointaines. L'avantage d'intégrer des fonctions source apparentes pour retrouver le moment sismique (et donc la magnitude) réside dans le fait que l'extension spatio-temporelle est prise en compte. Nous proposons donc une approche itérative, où la méthode de déconvolution stabilisée est appliquée, de manière successive, en utilisant des magnitudes de plus en plus grandes. Un critère de fit sur les reconstructions des formes d'onde à partir des fonctions source obtenues nous permet d'évaluer la magnitude optimale du séisme. Cette approche conduit à une magnitude proche de 9.1 pour le séisme de Sumatra 2004.

I.2.5 Le séisme de Sumatra-Andaman du 26 décembre 2004

L'article proposé dans cette section présente une application des approches et techniques décrites précédemment, dans le cas réel du séisme de Sumatra 2004. Cet article a été publié en janvier 2007 dans le journal *Bulletin of the Seismological Society of America*.

Bulletin of the Seismological Society of America, Vol. 97, No. 1A, pp. S103–S114, January 2007, doi: 10.1785/0120050616

Rupture Properties of the Giant Sumatra Earthquake Imaged by Empirical Green's Function Analysis

by Martin Vallée

Abstract Empirical green's function (EGF) analysis has remained little used to image the rupture properties of the giant 26 December 2004 Sumatra earthquake. The 2 November 2002 foreshock (M_w 7.2), close to the mainshock epicenter, gives us the opportunity to use its waveforms to empirically simulate the Rayleigh-wave propagation of the Sumatra earthquake. We first show that the exceptional size of the Sumatra earthquake does not prevent use of the EGF technique. Four aftershocks (M_w 5.9–6.1), distributed along the Sumatra–Andaman trench, are shown to have consistent Rayleigh waves for periods between 100 and 200 sec. At a lower frequency, we present two large earthquakes of the Mexican subduction zone (M_w 7.2–7.3, close to the selected EGF magnitude) for which long-period Green's functions (100–2000 sec) remain very similar, even if event epicenters are separated by about 650 km. This justifies the possibility of using the 2002 foreshock as an EGF for the whole rupture process of the Sumatra earthquake and shows more generally the very broad range of application of EGF technique. Then, a specific analysis reveals that seismic moment magnitude is close to 9.1 (seismic moment equal to 5.6×10^{22} N m). Moment release analysis along the Sumatra–Andaman trench shows two main slip episodes: one next to the northern extremity of Sumatra (~20-m slip) and the other one along the Nicobar Islands (~10-m slip), with a global extent of 1150–1200 km. Rupture velocity varies between values around 2.5 km/sec in the first half of the rupture and values closer to 2 km/sec in the second half. Total duration imaged by Rayleigh waves is 580 sec (± 20 sec) and no activity of the fault is found in the time scale between 600 and 2000 sec. In the hypothesis of even longer timescale slip, this phenomenon would be of the order of 10%–20% of the global moment and likely restricted to the Andaman Islands.

Introduction

On 26 December 2004, the giant Sumatra earthquake and especially its associated tsunami devastated a large part of Southeast Asia. This exceptional earthquake has stimulated active research in different areas of geophysics, which has lead to a better description of the phenomenon. Although early earthquake source analyses of teleseismic body waves (Yagi, 2004; Yamanaka, 2004; Ji, 2005) modeled a rupture length of a few hundred of kilometers, it soon appeared that this value had been strongly underevaluated. The first and simplest clue of a very long rupture came from aftershock locations that delineate a 1300-km-long zone (Fig. 1). First field observations (Department of Civil Engineering, 2005) and Global Positioning System (GPS) results (Centre for Earth Science Studies [CESS] Seismology Research Group, 2005; Survey of India, 2005) from the Andaman Islands also required that large fault slip took place close to these islands. Then, analyses of high-frequency body waves (Lomax, 2005; Ni *et al.*, 2005) or array analyses (de Groot-Hedlin, 2005; Guilbert *et al.*, 2005; Ishii *et al.*, 2005; Krüger and Ohrnberger, 2005) confirmed that rupture lasted at least 8 min and ruptured most parts of the subduction zone between Sumatra and Myanmar.

At the other extremity of the seismic frequency band, ultralong periods, normal modes recorded by worldwide seismometers have provided complementary information on the event. Analyses by Park *et al.* (2005), Stein and Okal (2005), and Lambotte *et al.* (2007) have shown that the M_w 9 value defined by the Harvard Centroid moment tensor (Harvard Seismology, 2004) has likely been underestimated. Magnitude as large as 9.3 has been proposed by Stein and Okal (2005). Using splitting of normal modes, Lambotte *et al.* (2007) have identified both a long duration (~500 sec) and extent (~1220 km) of the earthquake.

Finally, detailed seismological (Ammon *et al.*, 2005; Lay *et al.*, 2005) and geodetical analyses (Vigny *et al.*, 2005) have precisely determined the dimensions and properties of

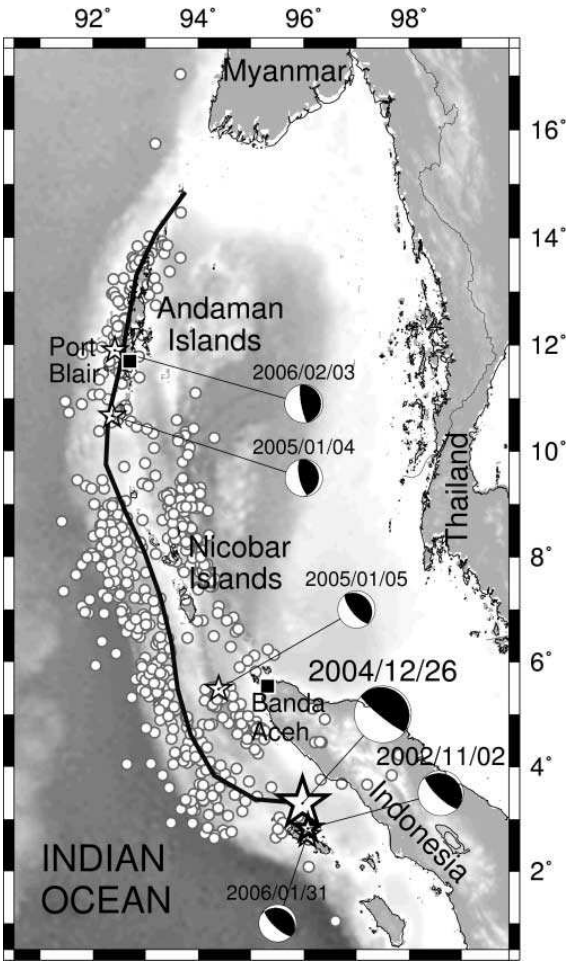

Figure 1. Location of earthquakes used to infer the rupture properties of the giant Sumatra event. Epicentral locations (NEIC) and Harvard CMT mechanisms (2004) of the mainshock (large thick star), of the 2 November 2002 selected EGF (small thick star), and of the four reference earthquakes used to examine Rayleigh waves consistency (small thin stars) are shown. These reference earthquakes sample most of the three-day aftershocks zone (white circles, NEIC, 2004).The thick line delineates the trench curvature of the Sumatra–Andaman subduction zone and defines the geometry of the line source model used in this study.

the rupture. In particular, very large GPS displacements all over the Southeast Asia peninsula obtained by Vigny *et al.* (2005) shows that fault slip occurred in a large part of the subduction zone, between 3° N and 12° N.

Thanks to this broad range of analyses there is today little doubt on the rupture extent of the Sumatra earthquake. Yet, some other characteristics are still debated, particularly the real duration and magnitude of the event. While much of the data can be explained by a ~550-sec-long source (Park *et al.*, 2005), the hypothesis of a much longer source is still considered. One of the main elements in favor of such an hypothesis comes from the location of the tsunamigenic source by backpropagating the arrival times of the waves in the Bengal Bay (Lay *et al.*, 2005). This delineates a 800-km-long zone and does not include the Andaman Islands, where large static displacements have been observed. The slow-slip hypothesis is still questioned because according to Vigny *et al.* (2005), no movement is seen at GPS stations in Southeast Asia for timescales longer than 15 min. On the other hand, Banerjee *et al.* (2005), by comparing seismological and geodetical slip models, have proposed that there is a 25%–35% moment deficit in the seismic models. The missing displacement would be due to slip occuring at periods longer than 1 hr, not able to efficiently generate neither seismic nor tsunami waves.

Magnitude is also discussed because very long period waves are required to adequately estimate the moment of such a large event. Thus, values estimated from body or short-period surface waves (<300 sec) likely underestimate the global moment. Normal modes, with periods of several thousands of seconds, have a higher potential to estimate moment magnitude (Park *et al.*, 2005; Stein and Okal, 2005; Lambotte *et al.*, 2007). Unfortunately, the measure is very sensitive on the earthquake dip, and dip values of 15° or 8° would respectively lead to moment magnitudes equal to 9.1 or 9.3. Finally, geodesy has measured displacements consistent with magnitudes bigger than 9, but the conversion to seismic moment is not direct because of trade-off with dip angle and rigidity structure (Banerjee *et al.*, 2005).

As another way to analyse this major event, I propose to use a smaller earthquake (M_w 7.2) to image the mainshock rupture, using the EGF approach. I will show that such an analysis can be adapted to this very long earthquake. First Rayleigh waves of four M_w ~6 aftershocks distributed along the Sumatra–Andaman trench will be shown to be consistent in the period band 100–200 sec. To examine the consistency at lower frequency, we will use two earthquakes of the Mexican subduction zone (M_w 7.2–7.3) and show waveforms similarity for periods between 100 and 2000 sec. Then a specific study on the optimal magnitude of the Sumatra earthquake is done before describing the rupture process of this unique event.

Empirical Green's Function (EGF) Approach

Generalities and Location Errors

The idea of the EGF method, already present in the late 1960s (Aki, 1967) and later applied to seismic source analysis (Hartzell, 1978), uses the fact that earthquake source process is similar regardless of the magnitude. Therefore a small earthquake (called EGF) can be used to model a big one, provided both events are similar in terms of mechanism and location. This approach has been subsequently used and

developed by Mueller (1985), Fukuyama and Irikura (1986), Mori and Frankel (1990), Ammon *et al.* (1993), Velasco *et al.* (1994), Ihmlé (1996), Courboulex *et al.* (1996), Bertero *et al.* (1997), and Vallée (2004). It has been shown that the EGF optimal magnitude is about 1–2 units smaller than the mainshock, in order to keep a good signal-to-noise ratio at low frequency. In the active Sumatra subduction zone, the best candidate is a M_w 7.2 earthquake that occurred in November 2002 (Fig. 1).

In a schematic way, seismic waves recorded at a distant seismic station contain two linear contributions: one coming from the earthquake's apparent moment rate and the other coming from Earth propagation. The Earth propagation complexity is present in a similar manner for both the EGF and the mainshock. Thus it is possible by a deconvolution to extract the apparent moment rate function (also called relative source time function [RSTF]) of the mainshock. Technically, the same wavetypes, at the same seismic stations, have to be studied for both earthquakes. In this case of a very large earthquake, surface waves constitute the best choice, because (1) they are sensitive to long periods and (2) they do not suffer from the wave mixing of body waves. In fact, for such a long-duration earthquake, individual body waves (*P, PP, S, SS*) are not separated and thus cannot be directly used (e.g., Ni *et al.*, 2005).

Of course, errors come from the fact that the propagation model given by the EGF is not perfect. For the Sumatra earthquake, with extent bigger than 1000 km, the most obvious error origin is the source location difference, in the later part of the rupture, between mainshock and EGF. Variations of trench azimuth and of age of the subducted lithosphere between north Sumatra and Andaman Islands may also lead to a significant modification of the Green's function. To examine quantitatively these potential problems, we can look at waveforms generated by similar but distant earthquakes. Unfortunately, it is not possible to directly compare our selected EGF (M_w 7.2) with other earthquakes in the Sumatra subduction zone. Indeed, except in the coda of the mainshock, no large thrust earthquake (M_w >6.4) occurred in the Nicobar–Andaman region. Thus we propose two analyses to provide insights on the waveforms similarity as a function of the interdistance between events. First we compare moderate magnitude (M_w 5.9–6.1) aftershocks of the Sumatra event. In this magnitude range, four thrust earthquakes, distributed from south to north along the Sumatra–Andaman trench have been selected: the M_w 5.9 31 January 2006 (2.70° N, 96.07° E, centroid depth 23 km); M_w 5.9 5 January 2005 (5.49° N, 94.39° E, centroid depth 33 km), M_w 5.9 4 January 2005 (10.67° N, 92.36° E, centroid depth 24 km), and M_w 6.1 3 February 2006 (11.90° N, 92.41° E, centroid depth 20 km) events. Their locations and mechanisms can be seen in Figure 1. The 31 January 2006 earthquake is very close, in terms of location and mechanism, to the 2 November 2002 EGF. Therefore, waveforms comparison between this event and the other ones will give meaningful elements on the validity of our EGF hypothesis.

We used data from worldwide FDSN broadband stations at epicentral distances between 55° and 125°. We have avoided closer stations, where the effect of earthquakes centroid difference is larger, as well as further stations, where R2 Rayleigh waves arrive soon after the end of R1 Rayleigh wave train. Figure 2 shows vertical seismograms for the four aftershocks, recorded at 12 stations with various azimuths. The thicker lines correspond to the earthquakes closer to the selected EGF. Six of the 10 stations later used in our study (namely FFC, PET, TAU, LSZ, PAB, ARU) are present in this analysis. The other ones, mainly located on oceanic islands (KIP, KWAJ, CRZF), cannot be compared because of low signal-to-noise ratio due to the relatively small aftershocks magnitude. Data has been windowed in the R1 Rayleigh-waves window, and seismograms initial time is based on the same phase velocity, corresponding to the arrival of Rayleigh waves at each station. Data has been bandpassed between 100 and 200 sec, because shorter periods are logically different due to the centroid difference and longer periods are not excited enough for these M_w 6.0 earthquakes.

Figure 2 shows that Rayleigh waves of the 5 January 2005 and of the 31 January 2006 earthquake (thickest lines) remain similar at most stations. This illustrates that in the analyzed frequency band (100–200 sec), the distance between events (360 km), the strike variation (~30°), the depth difference (~10 km), and the nature change of the subducted lithosphere only have a small influence on the shape of the Green's function. Even if it logically decreases, the Rayleigh waves consistency remains for the two other earthquakes (4 January 2005 and 3 February 2006), respectively located 970 km and 1100 km from the 31 January 2006 earthquake. Among the selected stations for the following analysis, correlation is good at FFC, PET, TAU, and LSZ and somewhat lower at ARU and PAB where amplitude of Rayleigh waves varies between earthquakes. This analysis shows that even in a very long and complex subduction zone, the EGF analysis is meaningful if we limit the study to long periods.

To examine more specifically the limitation at long periods, we need to refer to earthquakes of similar magnitude as our selected EGF (M_w 7.2). As explained before, a pair of such earthquakes does not exist in the Sumatra–Andaman subduction zone. Looking at other regions, we have found that Mexican subduction generated, in 1993 and 1995, two earthquakes suitable for this waveform comparison. On 10 September 1993, a M_w 7.2 earthquake occurred in the Chiapas region and on 14 September 1995, a M_w 7.3 earthquake occurred in the Guerrero region (Fig. 3). Both events have similar mechanisms and a centroid location difference of about 650 km (Harvard Seismology, 2004). Following the same analysis as for Sumatra aftershocks, we present in Figure 4 vertical Rayleigh waves generated by the two earthquakes at 16 stations of the global network. In this case, thanks to the better signal-to-noise ratio, waveforms remain nearly identical in the whole period band 100–2000 sec.

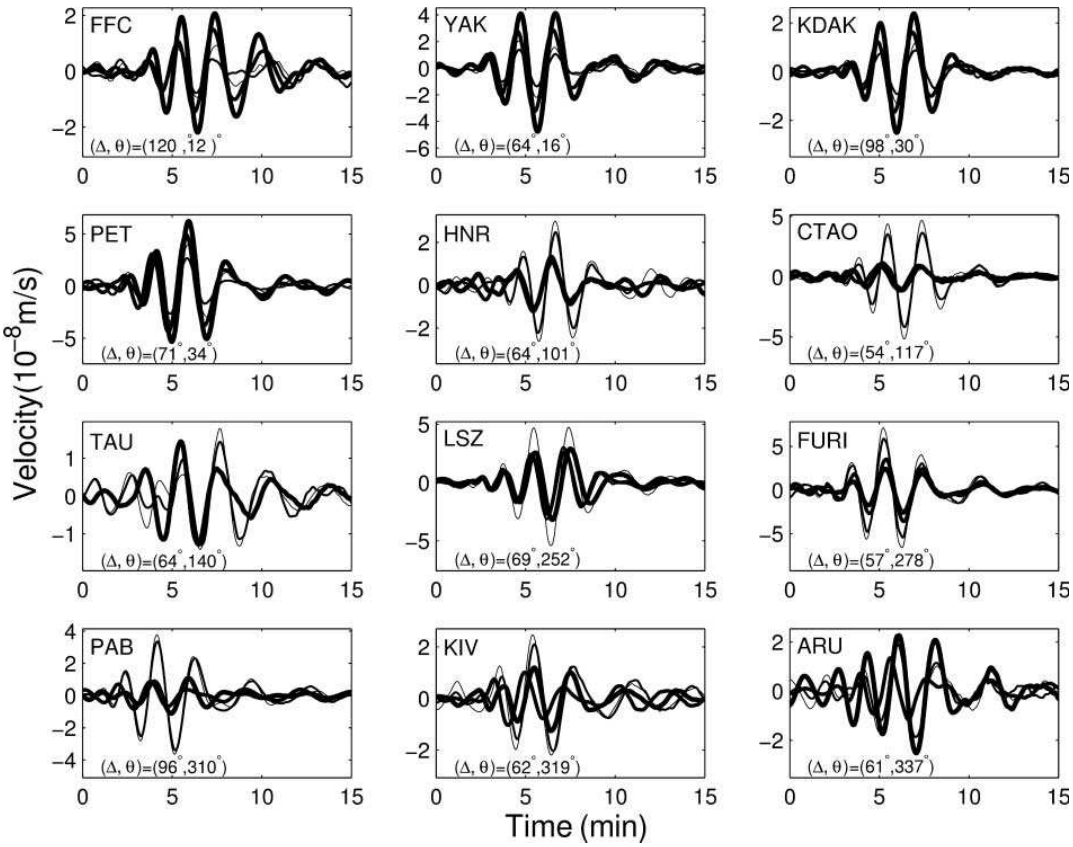

Figure 2. Comparison of Rayleigh waves recorded at the same stations for four earthquakes of the Sumatra–Andaman subduction zone. Thick lines refer to earthquakes close to the 2 November 2002 EGF. By order of decreasing thickness, lines refer to the 31 January 2006, 5 January 2005, 4 January 2005, and 3 February 2006 earthquakes (see their locations and mechanisms in Fig. 1). Rayleigh waves of the 5 January 2005 earthquake are noisy at TAU station and are not presented here. Name, epicentral distance (Δ), and azimuth (θ) are shown in the each subfigure. Vertical seismograms, aligned on the arrival of the Rayleigh waves, have been bandpass filtered between 100 and 200 sec.

These examples show, by a direct use of seismic data, that it is justified to use only one EGF to model Earth propagation, even for a very long and complex rupture zone. We have shown that periods longer that 100 sec remain reliable for most part of Sumatra earthquake rupture zone. At the other extremity of the frequency band, the analysis of M_w 7.2 earthquakes reveals that periods as long as 2000 sec are above the noise level. Subsequent analysis will therefore be done in the broad period range between 100 and 2000 sec.

Description of Deconvolution Method

Even if it has been illustrated that the entire rupture extent can be taken into account by only one EGF, it remains useful to use stabilization techniques to obtain the most reliable information about the source process. In particular, methods including corrections for mechanism difference and EGF duration (Ihmlé, 1996; Ihmlé and Ruegg, 1997) or positivity and temporal constraints on the RSTFs (Bertero *et al.*, 1997; Courboulex *et al.*, 1996) have been developed. I have shown for the very large 23 June 2001 Peru earthquake (M_w 8.4) that global rupture characteristics can be efficiently retrieved, provided some physical constraints on the RSTFs are respected (Vallée, 2004). Namely, positivity, causality, finite duration, and equal moment ratio constraints are shown to be very efficient to extract reliable moment rates. The equal moment ratio constraint simply states that the area of the RSTF has to be the same at all stations because it represents the moment ratio between the mainshock and the EGF. Details about the technique itself are not recalled here and can be found in Vallée (2004) and Vallée and Bouchon (2004).

As an illustration for the Sumatra earthquake case, Fig-

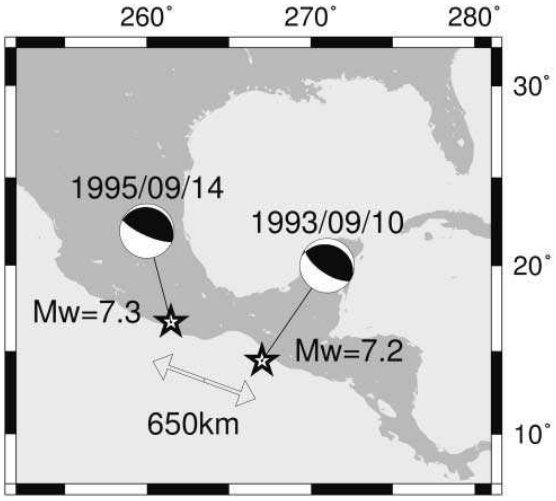

Figure 3. Map of Central America showing location of the Chiapas (10 September 1993) and Guerrero (14 September 1995) earthquakes used in this study. Values of moment magnitudes, focal mechanisms, and centroid locations (stars) are taken from Harvard CMT (Harvard Seismology, 2004).

ure 5 shows the analysis process for broadband station TAU (Tasmania) of the global network. Both EGF and mainshock Rayleigh waves have been prefiltered between 100 and 2000 sec to take into account the limitations underlined in the previous part. Magnitude of the Sumatra mainshock and EGF are respectively taken equal to 9.1 and 7.2 (Harvard CMT value), yielding a moment ratio of 620. Figure 5a first determines the optimal RSTF duration. To do so, we present the misfit between the real mainshocks and the reconstituted mainshock obtained by reconvolution of the RSTF with the EGF, as a function of the allowed duration of the RSTF. This misfit is a good indicator of the quality of the obtained deconvolution. The time at which the function becomes flat (ellipse) gives the simplest (i.e., shortest) RSTF able to well describe the seismic source. Figure 5b shows the RSTF corresponding to this optimal duration, and finally, Figure 5c presents a comparison between the real mainshock and the reconstituted mainshock for the preferred RSTF. At TAU station (azimuth 141°), the optimal RSTF duration is 840 sec long (Fig. 5a), which traduces the antidirective station position with respect to Sumatra earthquake propagation. The corresponding RSTF (Fig. 5b), which is able to reproduce very well the mainshock waveforms (Fig. 5c), gives interesting information on the temporal and spatial moment release of the event. This information is used later in the definition of the earthquake rupture process.

Application to the Determination of Sumatra Earthquake Seismic Moment

Before going into the details of the rupture process, we can use the deconvolution method in another way to refine the seismic moment of the mainshock. In fact, rather than considering the moment ratio as a constraint, we can do an optimization of this parameter by searching which moment ratio leads to the best RSTFs (by best RSTFs, we mean as before the shortest RSTFs for which the convolution with the EGF will be the closest from the mainshock waveforms). This offers a new way to define the seismic moment of this unique earthquake.

Therefore, we consider five values of the Sumatra earthquake moment magnitude (8.9, 9.0, 9.1, 9.2, 9.3), ranging over the possible magnitude values. The EGF magnitude is fixed to the 7.2 Harvard CMT value (moment of 9×10^{19} N m), because Harvard CMT technique based on long-period body and mantle waves is very reliable for this type of magnitude. For each of possible mainshock magnitude, we use the deconvolution technique described in the previous section. Figure 6 presents, at the two stations COR and KONO, the equivalent of Figure 5a for station TAU. But rather than representing only the misfit for a mainshock magnitude equal to 9.1, we show the five curves corresponding to the five hypotheses for Sumatra seismic moment. For station COR, all moment hypotheses lead to a similar quality RSTF if the allowed duration is very long. Yet the best misfit level is reached for duration of about 400 sec for magnitudes equal to 8.9, 9.0., and 9.1 whereas a duration longer than 600 sec is required to obtain a good RSTF for magnitudes 9.2 and 9.3. We thus consider that magnitudes equal to 9.2 or 9.3 are not optimal because they can give a good RSTF only if very long periods, little excited by surface waves, are added to the RSTF. For station KONO, the conclusion is even more direct: magnitudes equal to 8.9 or 9.0 are not able to yield a satisfactory RSTF whatever the duration. Figure 7 shows the results of a similar analysis for 18 stations of worldwide networks (IU, II, Geoscope, TGRS). Based on the criteria described for stations COR and KONO, the horizontal line represents, at each station, the possible values for earthquake magnitude. The observation of this figure reveals that a seismic moment magnitude equal to 9.1 (moment of 5.6×10^{22} N m) is the optimal value of the giant Sumatra earthquake, as seen by broadband Rayleigh waves (100–2000 sec).

Imaging of Rupture Properties

Using the M_w 9.1 value determined in the previous section, the stabilized deconvolution technique is used to retrieve RSTFs at stations of the global networks. Based on well-distributed azimuthal coverage, 10 RSTFs are selected and presented in Figure 8. Some striking features may immediately be commented on: the RSTFs durations vary from 300 sec in Europe (PAB and ARU) up to 900 sec in Antarctica (SBA). Such a behavior is expected because the earthquake propagation from southeast to northwest leads to an energy concentration in the northwest direction.

To estimate more quantatively the rupture process of Sumatra earthquake, a one-dimensional model of the earthquake is considered, in which seismic moment is released

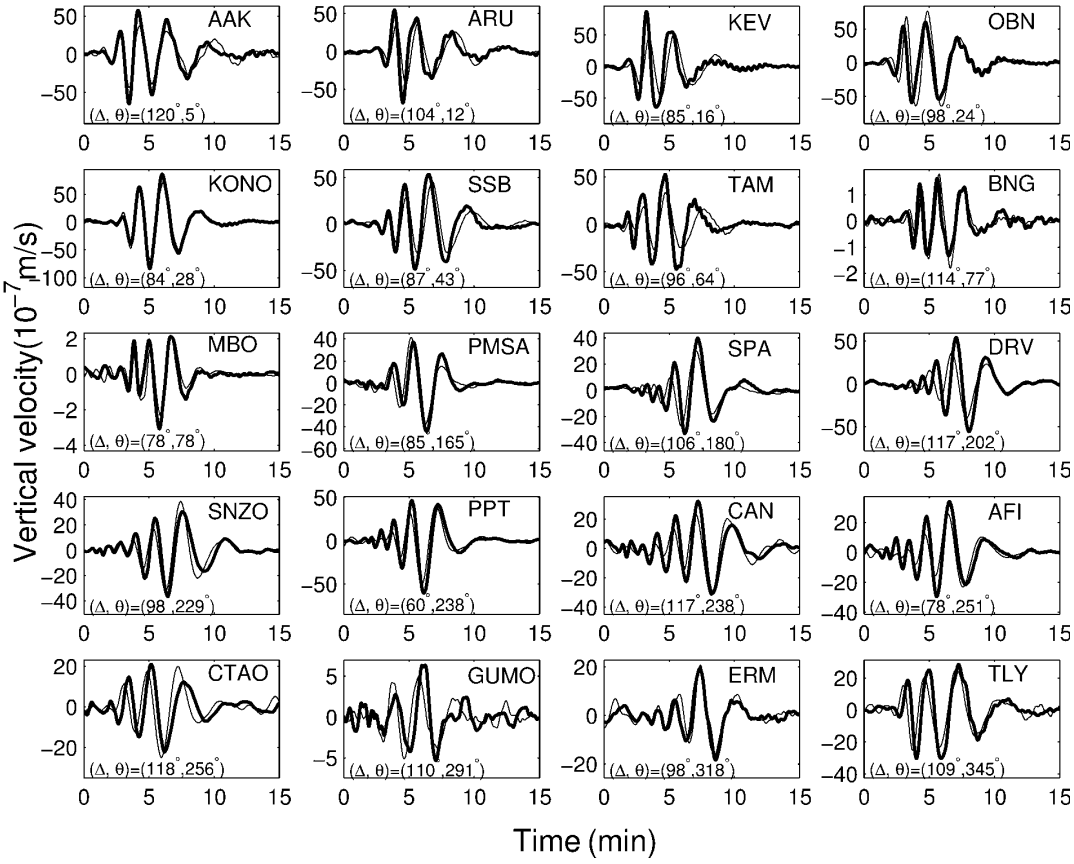

Figure 4. Comparison of Rayleigh waves recorded at the same stations for both Chiapas (thin lines) and Guerrero (thick lines) earthquakes. Station name, epicentral distance (Δ), and azimuth (θ) are shown in the each subfigure. Vertical seismograms, aligned on the arrival of the Rayleigh waves, have been bandpass filtered between 100 and 2000 sec.

along the trench. This line-source model, where trench curvature has been taken into account, is shown in Figure 1. Assuming such geometry, the RSTF F_θ observed in an azimuth θ can be written as the integral along the fault of length L:

$$F_\theta(t) = \int_0^L f_{\mathrm{m,d}}(x, t - T_\mathrm{r}(x,V_\mathrm{r}) + D(x,\theta,\theta_\mathrm{f},V_\phi))dx, \quad (1)$$

where f, the local source time function (i.e., defining the moment rate of a point located at distance x from hypocenter) is parametrized by moment per unit length m and moment per unit length duration d. Temporal contributions due to propagation time T_r (related to rupture velocity V_r) and spatial shift between source and station (D function) have to be taken into account. D is dependent on station azimuth θ, fault azimuth θ_f, and phase velocity V_φ; it can be simply evaluated knowing that D is simply equal to $(x \cos(\theta\text{-}\theta_\mathrm{f})/V_\varphi)$ for a constant azimuth segment fault. Rayleigh-wave phase velocity V_ϕ is averaged to 3.7 km/sec by observation of the arrival time of the EGF most energetic Rayleigh waves.

Equation (1) gives us a useful relation between the observation F_θ and source parameters m, V_r, and d; d takes into account time between slip initiation and slip termination at a point of the fault as well as time to propagate along the half-width of the fault. With slip in the range 5–20 m, slip velocity around 1 m/sec (Heaton, 1990), fault width of the order of 100–200 km, and rupture velocity of 2–3 km/sec, typical values for d are of the order of 25–60 sec.

Thus we keep as unknowns of equation (1) the moment per unit length m and the rupture velocity V_r on the fault. To retrieve these parameters, the 1500-km-long fault is discretized in 100-km-long segments. Slip is constrained to be zero at the last point of the fault, and local rupture velocity can vary between 1.4 and 3.3 km/sec. To define the 30 parameters of this optimization problem, residuals between observed RSTFs and RSTFs calculated with equation (1) have to be minimized. A small smoothing constraint is introduced

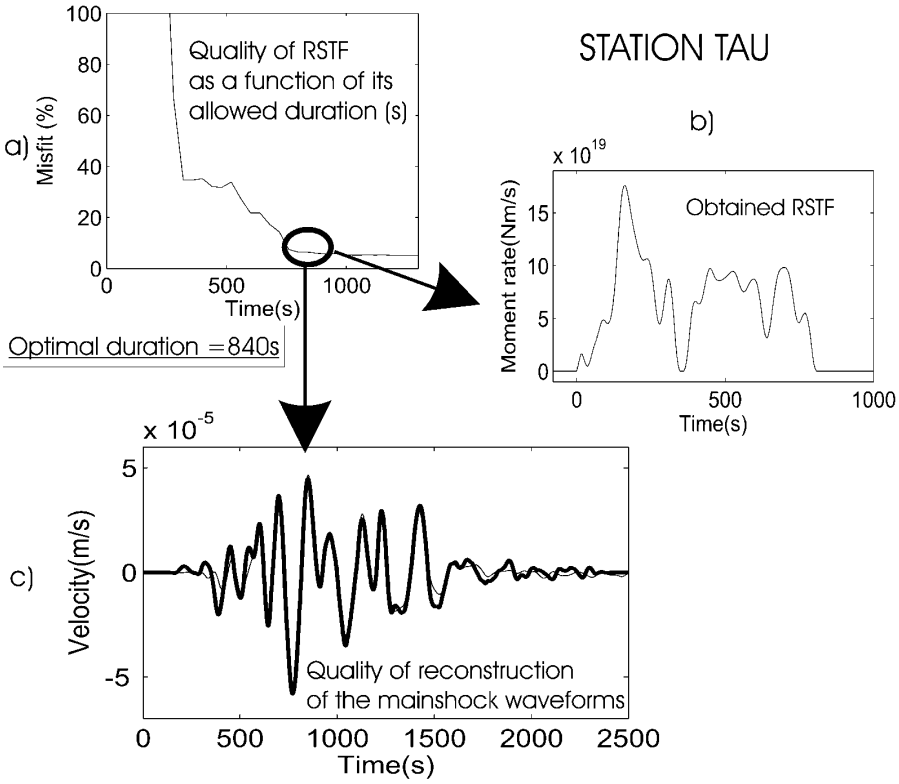

Figure 5. Illustration of the deconvolution technique for Rayleigh waves at station TAU (Tasmania). Deconvolution is done with four constraints (causality, positivity, finite duration, and moment ratio fixed to 620). First we impose a very short duration of the RSTF, which logically leads to a bad reconstruction of the mainshock waveforms by reconvolution with the EGF. The error associated with this reconstruction is our definition of the misfit used in (a). Then we allow a longer and longer duration that decreases the misfit in (a). When we reach an allowed duration of 840 sec the misfit is low (~6%) and cannot be improved further by a longer allowed duration. Therefore we select the 840-sec-long RSTF, presented in (b), as the most likely RSTF. The convolution of this RSTF with the EGF yields the thin line in (c), whereas the thick line is the real mainshock waveform.

for rupture velocity to reduce the instability of this parameter at fault points where seismic moment is low.

Before inversion, observed RSTFs have been smoothed to (1) reduce the effect of unreliable frequencies and (2) take into account the spatial sampling of the fault ($s_f = 100$ km), which prevents modeling high frequencies. Because of rupture propagation toward the north, smoothing has to be dependent on the azimuth, and its value is estimated by the following equation:

$$\text{Smooth} = 2s_f\left(\frac{1}{\bar{V}_r} - \frac{\cos(\theta - \bar{\theta}_f)}{V_\varphi}\right), \qquad (2)$$

where $\bar{V}_r$ and $\bar{\theta}_f$, average values of rupture velocity and fault azimuth, respectively, are here approximated to 2.25 km/sec and 342°. Using equation (2), smoothing values range from 26 sec for $\theta = 337°$ (ARU, directive station) to 134 sec for $\theta = 168°$ (SBA, antidirective station). The observed smoothed RSTFs are presented in Figure 9 (thick lines).

The inverse problem is then solved with the neighborhood algorithm (NA) (Sambridge, 1999). To estimate model uncertainties, we repeat the use of NA with different parameters, including variation of d in the range 25–60 sec and modification of rupture velocity smoothing constraint. Based on 12 NA runs, the averages and standard errors of moment per unit length and rupture velocity are presented in Figure 10. In Figure 9, synthetics corresponding to this average model are presented and compared with the observed RSTFs. It can be seen that the apparent duration and main features of each RSTF are well explained by the synthetic model. Moment per unit length and rupture velocity are not very well resolved close to hypocenter due to the line source approximation and the large influence of parameter d in the

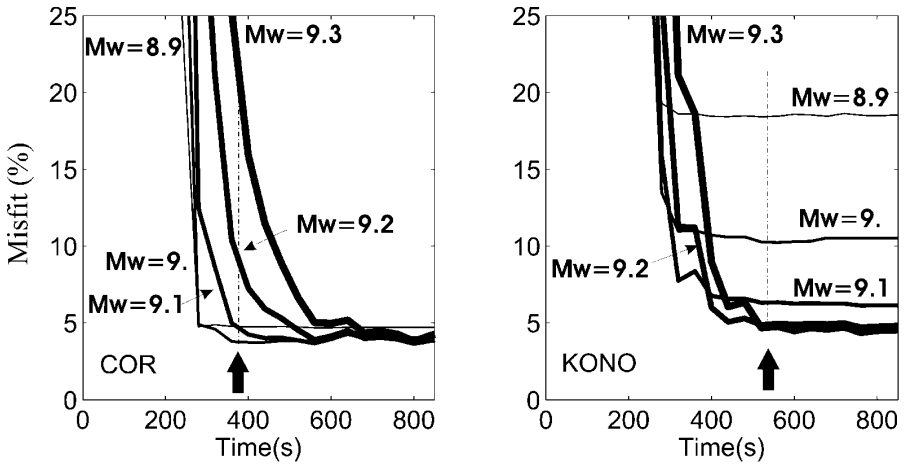

Figure 6. Illustration of the magnitude discrimination at stations COR and KONO. The line thicknesses refer to magnitude hypotheses, between 8.9 and 9.3. In both sub figures, the evolution of the misfit as a function of the RSTF allowed duration is presented (see Fig. 5a) for more details). At COR, the optimal RSTF duration is about 400 sec (arrow). Magnitudes 9.2 and 9.3 are able to produce a good RSTF, but only if a longer duration, including very low frequencies little excited by Rayleigh waves, is permitted. At KONO station, magnitudes 8.9 and 9.0 produce an agreement with data significantly less good than larger magnitudes. This illustrates that magnitude 9.1 is the most plausible magnitude of Sumatra earthquake. This is confirmed with a larger number of stations in Figure 7.

early part of the rupture. Elsewhere, models are very consistent from one inversion run to the other. Moment per unit length is found even more stable than rupture velocity. Standard errors of rupture velocity become logically large for distances longer 1200 km, where moment release is very low.

Moment per unit length can be converted to slip if rigidity and fault width are known. Taking a fault width equal to 150 km (Bilham *et al.*, 2005) and a classical rigidity equal to 3×10^{10} N m^{-2}, we present in Figure 11 the fault-slip distribution in the Sumatra–Andaman subduction zone. Slip reached values of the order of 20 m 200 km northwest of hypocenter. A secondary slip maximum of about 10 m occurred at Nicobar Islands, and slip remains large (>5 m) up to the South Andaman Islands. Rupture velocity is slow at the beginning (~1.8 km/sec) but this can also be due to our line source approximation that can be wrong in the early part (two-dimensional rupture propagation effects). Then, rupture accelerates to values of 2.4–2.5 km/sec for the next 500 km, before decelerating to 2 km/sec in the second half of the rupture process. Average rupture velocity is equal to 2.2 km/sec ($\pm$0.1) and global duration to 580s ($\pm$20 sec). The main characteristics of the Sumatra earthquake are shown in the map presented in Figure 11.

Conclusions and Discussion

From a methodological point of view, this study has confirmed the very broad range of application of the EGF technique. This method has been used until now on very different earthquake scales, from M_w ~2 earthquakes (e.g., Fischer, 2005) to M_w ~8 earthquakes (e.g., Courboulex *et al.*, 1997). It is shown here that this approach is also very helpful to deal with M_w >9 earthquakes. The limitations due to the extent of the rupture zone or to changes in fault orientation exist but can be taken into account by an appropriate filtering of the data. This assertion, which is intuitive in terms of seismic wavelengths, has been supported by the direct observation of seismic data in the Sumatra and Mexican subduction zones. An adaptation of the EGF technique is also proposed to search the optimal moment ratio between the mainshock and the EGF. In the Sumatra case, where the EGF moment is well known, such an approach has provided a simple and independent way to estimate the Sumatra mainshock moment. In other contexts, for example, if one wants to determine the magnitude of small events, the technique can also be used in the opposite direction: given the optimal moment ratio and the magnitude of the mainshock, the magnitude of a small EGF can be estimated.

The giant Sumatra earthquake, as imaged by very broadband Rayleigh waves (100–2000 sec), has a seismic moment equal to 5.6×10^{22} N m (M_w 9.1). The earthquake dynamically ruptured a 1100- to 1200-km long segment of the Sumatra–Andaman trench, and this process lasted about 580 sec ($\pm$20 s). This value is far beyond any earthquake rupture duration defined until now. For example, duration of the M_w 9.2 1964 Alaska earthquake has been estimated to 240 sec (Alaska Earthquake Information Center, 2005). Using

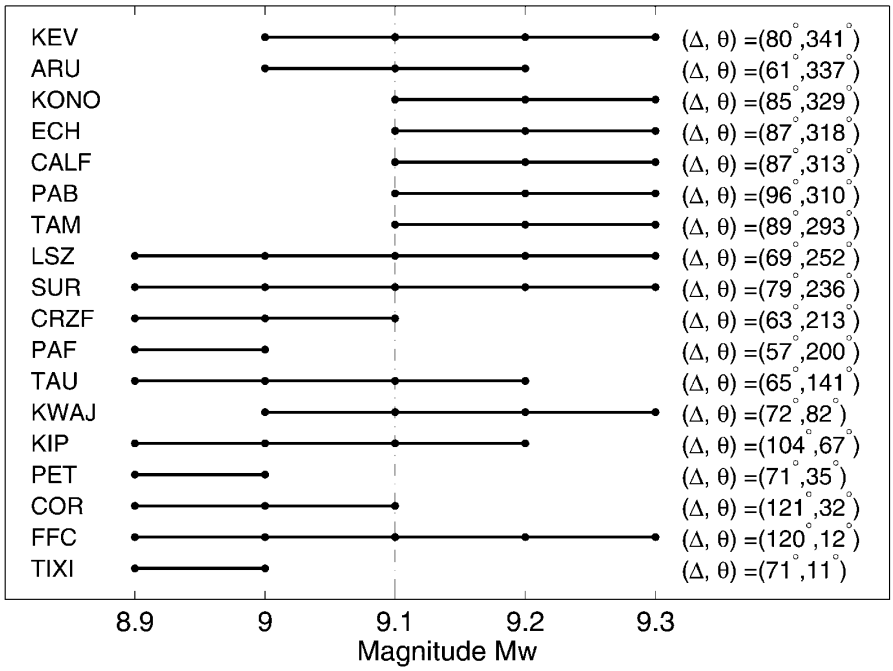

Figure 7. Optimal magnitude of the Sumatra earthquake given by 18 stations of the global network. Station names and their geographical position (epicentral distance Δ and azimuth θ) are specified. At each station, the horizontal line shows the possible magnitude values, according to the criteria described in Figure 6 for stations COR and KONO. The magnitude 9.1 hypothesis is in agreement with most stations (15 of 18) and is therefore the most likely one.

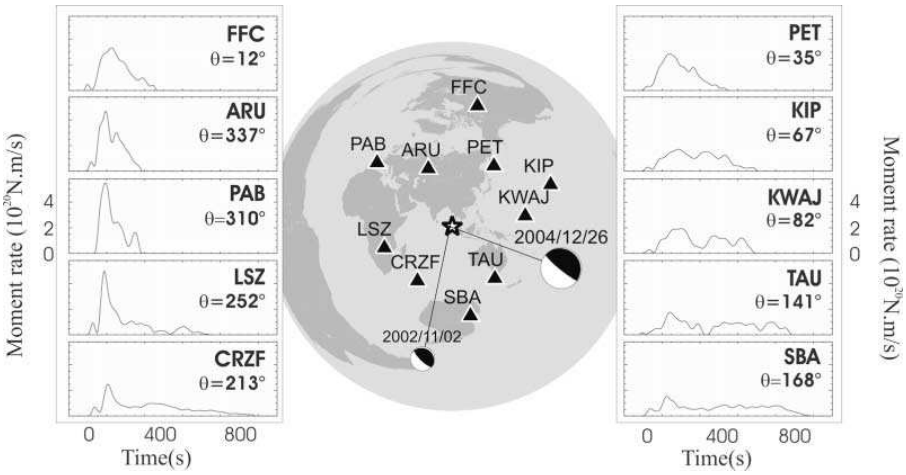

Figure 8. Map of selected seismic sensors (GSN and Geoscope networks) and moment rates (RSTFs) at each station. Harvard CMT (Harvard Seismology, 2004) mechanisms are specified for the mainshock and the EGF. Each RSTF has been obtained by deconvolution of surface waves (Rayleigh waves) between the mainshock of 26 December 2004 and the smaller earthquake (EGF) of 2 November 2002. Station names and azimuths to the north (θ) are specified. Note the much longer and less-impulsive RSTFs for stations to the south than for stations to the north.

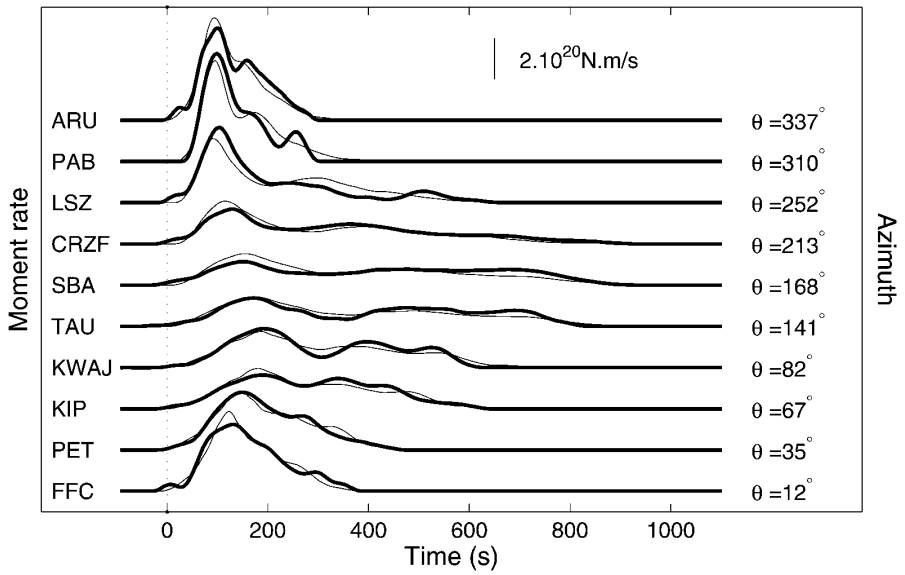

Figure 9. Agreement between observed (thick lines) and synthetic (thin lines) RSTFs as a function of the azimuth θ. Compared to Figure 8, observed RSTFs have been smoothed to reduce the effect of unreliable high frequencies and to take into account the spatial sampling (100 km) of the fault chosen in the simulation. Because of rupture propagation toward north, smoothing is dependent on the azimuth, ranging from 26 sec for $\theta = 337°$ (ARU, directive station) to 134 sec for $\theta = 168°$ (SBA, antidirective station). Synthetic RSTFs, corresponding to the average model (Fig. 10), are in good agreement with the observed ones.

the EGF analysis, the first 200 sec of the rupture are found to be very energetic, with a maximum slip of 20 m occurring 200 km away from the hypocenter, close to the bend of the trench (Ji, 2005). A secondary maximum is identified close to Nicobar Islands, with slip of about 10 m, and seismic rupture has kept propagating toward north up to the South Andaman Islands. This behavior is similar to the one derived from seismological data (Ammon *et al.*, 2005; Lay *et al.*, 2005), GPS data (Chlieh *et al.*, 2007), or tsumami data (Piatanesi and Lorito, 2007). Rupture velocity is everywhere—except at hypocenter—of the order of, or larger than, 2 km/sec, even if slower velocities have been allowed in the inversion. The average value is found equal to 2.2 km/sec, in agreement with most studies, which have defined this parameter between 2 and 2.5 km/sec (Ammon *et al.*, 2005; de Groot-Hedlin, 2005; Guilbert *et al.*, 2005; Lomax, 2005). More precisely, rupture velocity has reached a value of ~2.5 km/sec in the segment between Sumatra and Nicobar Islands, before slowing down to ~2 km/sec in the late part of the rupture.

The moment of 5.6×10^{22} N m defined by Rayleigh waves is close to the value found by much longer period data. For example, Park *et al.* (2005) by normal mode study, or Banerjee *et al.* (2005) with geodetical data and a realistic dip of the trench, have retrieved a value of $6–6.5 \times 10^{22}$ N m. This means that if slow slip exists, it is of the order of 10%–20% of the global moment released by the earthquake. This low value can also explain why Vigny *et al.* (2005) have not detected some slow process in their GPS data. Our study find large slip (10 m) in the Nicobar region, which is approximately the value required by subsidence observation (Bilham *et al.*, 2005). Thus, a longer timescale slip is not required in this part of the fault. Andaman Islands region is a different case. Except in the southern part, the modeled moment release is very low, whereas there has been some evidence of fault activity: aftershock sequence is dense up to 14° N, subsidence has been observed in the western shorelines of Andaman Islands (Bilham *et al.*, 2005), and GPS analysis seems to require significant slip in this zone. For compatibily of these observations we propose here that the slow-slip process, if present, has to be confined in the extreme north of the rupture zone, between 12° and 14° N.

Acknowledgments

I am grateful to the Federation of Digital Seismic Networks (FDSN) and to Geoscope and TGRS networks for free and easy access to broadband data. Revisions proposed by two anonymous reviewers and discussions inside Geosciences Azur laboratory have greatly contributed to improve the manuscript. Generic Mapping Tools (GMT) free software has been helpful to the preparation of the manuscript. This work has been funded by the Institut de la Recherche pour le Développement (IRD).

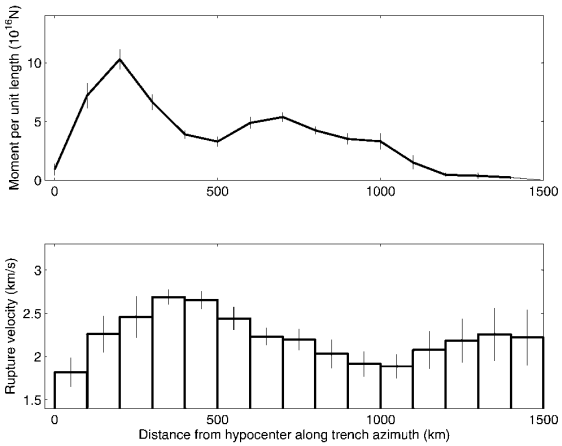

Figure 10. Moment distribution and rupture velocity models. Average models—based on 12 runs of NA with different tuning parameters—are presented in the upper part for moment per unit length and in the lower part for rupture velocity. Uncertainities corresponding to ($\pm\sigma$) are shown by vertical bars. The resolution for moment is good except for the region between Nicobar and Andaman islands (~1000 km from hypocenter) where model dispersion is larger. Rupture velocity is better resolved at the beginning of the rupture than in the later part, and the very small moment of the final part of the rupture process (>1200 km) logically results in a larger dispersion of the possible rupture velocities.

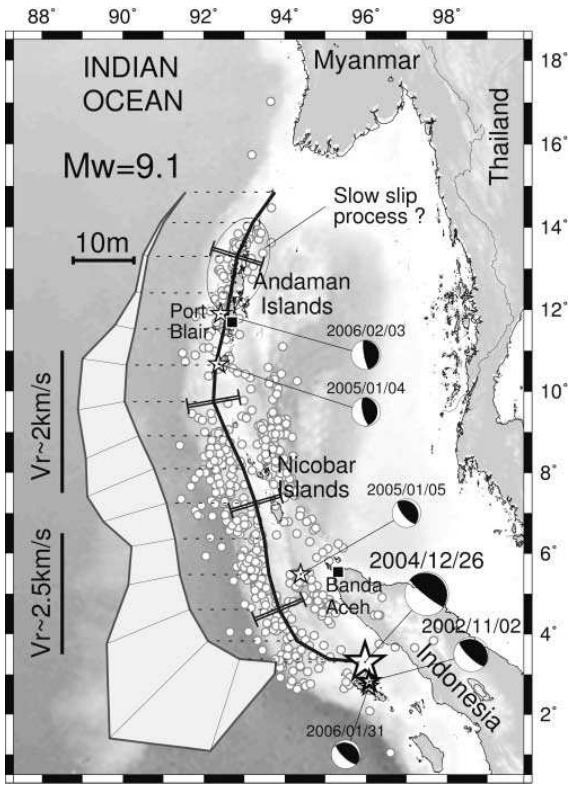

Figure 11. Rupture model of the giant Sumatra earthquake. The rupture extends from the north Sumatra to the south Andaman islands and can be compared with aftershocks occurring in the three days following the earthquake (white circles) (National Earthquake Information Center, 2004). Epicentral location (NEIC, 2004) and Harvard CMT mechanism (Harvard Seismology, 2004) of the mainshock (large thick star), of the EGF (small thick star), and of the four aftershocks used to examine Rayleigh waves consistency (small thin stars) are also shown. Selected fault geometry, represented by the thick black line, follows the trench curvature. Fault width, taken equal to 150 km (Bilham *et al.*, 2005), is shown with black lines perpendicular to the trench, assuming that fault dip is 15°. The average slip model along the trench (deduced from average model of Figure 10 and the 150-km-wide fault) is presented in the left part of the figure, shifted horizontally with respect to the fault position. Slip values have to be read along the thin line perpendicular to the local fault azimuth, according to the scale written above the slip model. Main features of the rupture velocity behavior are presented on the left of the slip model. Slow-slip process may have occurred in the central and north Andaman Islands, where seismic moment release is very low.

References

Aki, K. (1967). Scaling law of seismic spectrum, *J. Geophys. Res.* **72,** 1217–1231.

Alaska Earthquake Information Center (2005). The great Alaska earthquake of 1964, www.aeic.alaska.edu/quakes/Alaska_1964_earthquake.html (last accessed November 2006).

Ammon, C. J., C. Ji, H.-K. Thio, D. Robinson, S. Ni, V. Hjorleifsdottir, H. Kanamori, T. Lay, S. Das, D. Helmberger, G. Ichinose, J. Polet, and D. Wald (2005). Rupture process of the 2004 Sumatra–Andaman earthquake, *Science* **308,** 1133–1139.

Ammon, C. J., A. A. Velasco, and T. Lay (1993). Rapid estimation of rupture directivity: application to the 1992 Landers (Ms = 7.4) and Cape Mendocino (Ms = 7.2), California earthquakes, *Geophys. Res. Lett.* **20,** 97–100.

Banerjee, P., F. F. Pollitz, and R. Burgmann (2005). The size and duration of the Sumatra–Andaman earthquake from far-field static offsets, *Science* **308,** 1769–1772.

Bertero, M., D. Bindi, P. Boccacci, M. Cattaneo, C. Eva, and V. Lanza (1997). Application of the projected Landweber method to the estimation of the source time function in seismology, *Inverse Problems* **13,** 465–486.

Bilham, R., E. R. Engdahl, N. Feldl, and S. P. Satyabala (2005). Partial and complete rupture of the Indo-Andaman plate boundary 1847–2004, *Seism. Res. Lett.* **76,** 299–311.

Centre for Earth Science Studies (CESS) Seismology Research Group (2005). Preliminary estimates of the geodetic GPS survey in the Andaman & Nicobar Islands conducted by CESS, http://www.seires.net/content/view/122/52/ (last accessed July 2006).

Chlieh, M., J. P. Avouac, V. Hjorleifsdottir, T. R. A. Song, C. Ji, K. Sieh, A. Sladen, H. Hebert, L. Prawirodirdjo, Y. Bock, and J. Galetzka

(2007). Coseismic slip and afterslip of the great (M_w 9.15) Sumatra–Andaman Earthquake of 2004, *Bull. Seism. Soc. Am.* **97,** no. 1A, S152–S173.

Courboulex, F., S. K. Singh, J. Pacheco, and C. Ammon (1997). The October 9, 1995 Colima-Jalisco, Mexico, earthquake (Mw 8): a study of the rupture process, *Geophys. Res. Lett.* **24,** 1019–1022.

Courboulex, F., J. Virieux, A. Deschamps, D. Gibert, and A. Zollo (1996). Source investigation of a small event using empirical Green's functions and simulated annealing, *Geophys. J. Int.* **125,** 768–780.

de Groot-Hedlin, C. D. (2005). Estimation of the rupture length and velocity of the Great Sumatra earthquake of Dec 26, 2004 using hydroacoustic signals, *Geophys. Res. Lett.* **32,** L11303, doi 10.1029/2005GL022695.

Department of Civil Engineering (2005). Indian Institute of Technology Kanpur, Quick Report on the Study of the 2004 Sumatra Earthquake and Tsunami Effects, http://cires.colorado.edu/~bilham/IndonesiAndaman2004_files/KanpurMalek.pdf. (last accessed November 2006).

Fischer, T. (2005). Modelling of multiple events using empirical Green's functions: method, application to swarm earthquakes, and implications for their rupture propagation, *Geophys. J. Int.* **163,** 991–1005.

Fukuyama, E., and K. Irikura (1986). Rupture process of the 1983 Japan Sea (Akita-Oki) earthquake using a waveform inversion method, *Bull. Seism. Soc. Am.* **76,** 1623–1640.

Global Centroid Moment Tensor (CMT) Project catalog search, www.globalcmt.org/CMTsearch.html (last accessed November 2006).

Guilbert, J., J. Vergoz, E. Schisselé, A. Roueff, and Y. Cansi (2005). Use of hydroacoustic and seismic arrays to observe rupture propagation and source extent of the M_w 9.0 Sumatra earthquake, *Geophys. Res. Lett.* **32,** L15310, doi 10.1029/2005GL022966.

Hartzell, S. H. (1978). Earthquake aftershocks as Green's functions, *Geophys. Res. Lett.* **5,** 1–4.

Heaton, T. (1990). Evidence for and implications of self-healing pulses of slip in earthquake rupture, *Phys. Earth. Planet. Interiors* **64,** 1–10.

Ihmlé, P. F (1996). Frequency dependent relocation of the 1992 Nicaragua slow earthquake: an empirical Green's function approach, *Geophys. J. Int.* **127,** 75–85.

Ihmlé, P. F., and J. C. Ruegg (1997). Source tomography by simulated annealing using broad-band surface waves and geodetic data: application to the Mw = 8.1 Chile 1995 event, *Geophys. J. Int.* **131,** 146–158.

Ishii, M., P. Shearer, H. Houston, and J. E. Vidale (2005). Extent, duration and speed of the 2004 Sumatra–Andaman earthquake imaged by the Hi-Net array, *Nature* **435,** 933–936.

Ji, C. (2005). Magnitude 9.0 off the west coast of northern Sumatra Sunday, December 26, 2004 at 00:58:53 UTC, Preliminary rupture model, http://neic.usgs.gov/neis/eq_depot/2004/eq_041226/neic_slav_ff.html (last accessed November 2006).

Krüger, F., and M. Ohrnberger (2005). Tracking the rupture of the M_w = 9.3 Sumatra earthquake over 1,150 km at teleseismic distance, *Nature* **435,** 937–939.

Lambotte, S., L. Rivera, and J. Hinderer (2007). Constraining the overall kinematics of the 2004 Sumatra and the 2005 Nias earthquakes using the Earth's gravest free oscillations, *Bull. Seism. Soc. Am.* **97,** no. 1A, S128–S138.

Lay, T., H. Kanamori, C. J. Ammon, M. Nettles, S. N. Ward, R. C. Aster, S. L. Beck, S. L. Bilek, M. R. Brudzinski, R. Butler, H. R. DeShon, G. Ekstrom, K. Satake, and S. Sipkin (2005). The great Sumatra–Andaman earthquake of 26 December 2004, *Science* **308,** 1127–1133.

Lomax, A. (2005). Rapid estimation of rupture extent for large earthquakes: application to the 2004, M9 Sumatra–Andaman mega-thrust, *Geophys. Res. Lett*. **32,** L10314, doi 10.1029/2005GL022437.

Mori, J., and A. Frankel (1990). Source parameters for small events associated with the 1986 North Palm Springs, California, earthquake determined using empirical Green functions, *Bull. Seism. Soc. Am*. **80,** 278–295.

Mueller, C. S. (1985). Source pulse enhancement by deconvolution of an empirical Green's function, *Geophys. Res. Lett.* **12,** 33–36.

National Earthquake Information Center (2004). http://neic.usgs.gov/neis/epic/epic.html (last accessed November 2006).

Ni, S., H. Kanamori, and D. Helmberger (2005). High frequency radiation from the 2004 Great Sumatra–Andaman earthquake, *Nature* **434,** 582.

Park, J., T.-R. A. Song, J. Tromp, E. Okal, S. Stein, G. Roult, E. Clevede, G. Laske, H. Kanamori, P. Davis, J. Berger, C. Braitenberg, M. Van Camp, X. Lei, H. Sun, H. Xu, and S. Rosat (2005). Earth's free oscillations excited by the 26 December 2004 Sumatra–Andaman earthquake, *Science* **308,** 1139–1144.

Piatanesi, A., and S. Lorito (2007). Rupture process of the 2004 Sumatra–Andaman earthquake from tsunami waveforms inversion, *Bull. Seism. Soc. Am.* **97,** no. lA, S223–S231.

Sambridge, M. (1999). Geophysical inversion with a neighborhood algorithm. I. Searching a parameter space, *Geophys J. Int.* **138,** 479–494.

Stein, S., and E. Okal (2005). Ultra-long period seismic moment of the great December 26, 2004 Sumatra earthquake and implications for the slip process, *Nature* **434,** 581.

Survey of India (2005). http://news.indiainfo.com/2005/01/15/1501survey.html (last accessed November 2006).

Vallée, M. (2004). Stabilizing the empirical Green function analysis: development of the projected Landweber method, *Bull. Seism. Soc. Am.* **94,** 394–409.

Vallée, M., and M. Bouchon (2004). Imaging coseismic rupture in far field by slip patches, *Geophys. J. Int.* **156,** 615–630.

Velasco, A. A., C. J. Ammon, and T. Lay (1994). Empirical Green function deconvolution of broadband surface waves: rupture directivity of the 1992 Landers, California (M_w = 7.3), *Bull. Seism. Soc. Am.* **84,** 735–750.

Vigny, C., W. Simons, S. Abu, R. Bamphenyu, C. Satirapod, N. Choosakul, C. Subarya, A. Socquet, K. Omar, H. Abidin, and B. A. C. Ambrosius (2005). Insight into the 2004 Sumatra–Andaman earthquake from GPS measurements in southeast Asia, *Nature* **436,** 201–206.

Yagi, Y. (2004). Preliminary results of rupture process for 2004 off coast of northern Sumatra giant earthquake, http://iisee.kenken.go.jp/staff/yagi/eq/Sumatra2004/Sumatra2004.html (last accessed November 2006).

Yamanaka, Y. (2004). 04/12/26 off West coast of northern Sumatra, EIC Seismological Note No. 161, www.eri.u-tokyo.ac.jp/sanchu/Seismo Note/2004/EIC161e.html (last accessed November 2006).

Géosciences Azur, IRD
250 avenue Albert Einstein
06560 Valbonne, France

Manuscript received 16 January 2006.

Annexe à l'étude du séisme de Sumatra

L'article précédent ne présente pas explicitement les formes d'ondes du choc principal et de la fonction de Green empirique choisie. La figure ci-dessous I.A.1 donne une illustration de ces signaux, observés sur la composante verticale de la station Géoscope CAN (Australie). La fenêtre utilisée pour la déconvolution, comprise entre les temps $T0$ et $T1$, inclut l'ensemble des ondes de Rayleigh du choc principal. La fonction source apparente obtenue par déconvolution, non reproduite ici, est très similaire à celle obtenue pour la station TAU (Figure 5 de l'article). La très longue durée apparente, supérieure à 800s, se traduit par l'émission prolongée des ondes de Rayleigh durant le choc principal.

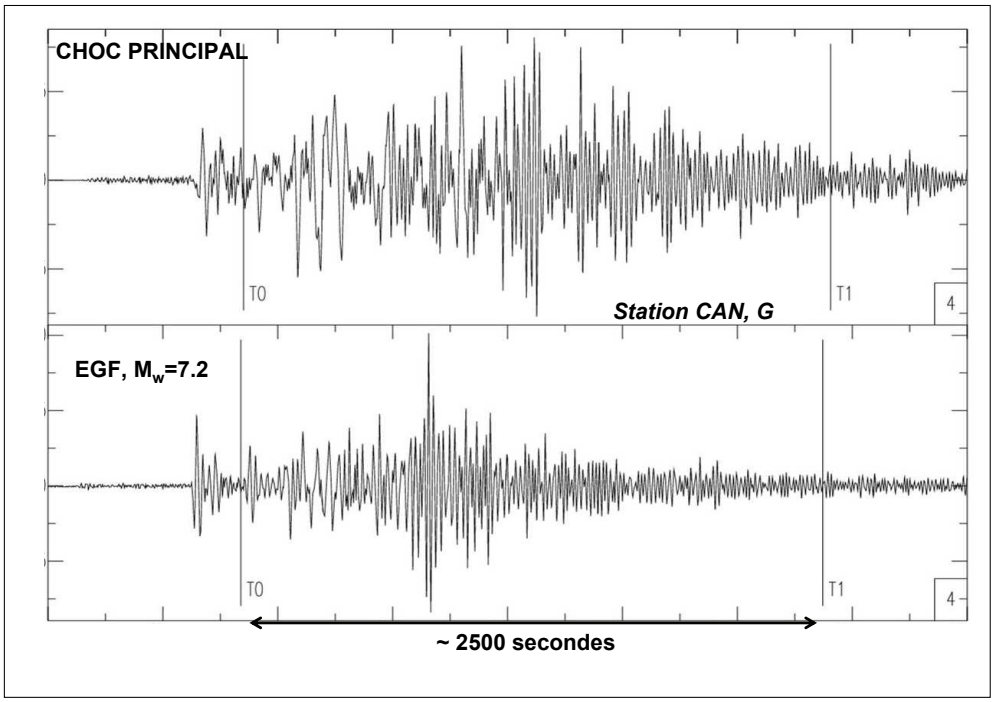

FIG. I.A.1 - Illustration des signaux du choc principal et de la fonction de Green empirique.

I.3 La méthode SCARDEC

I.3.1 Idée générale

Les approches décrites dans la section I.1, fondées sur l'approche par déconvolution de fonction de Green empirique, présentent l'inconvénient qu'un petit séisme « pilote » doit exister et que l'on doit pouvoir préalablement connaître ses caractéristiques (profondeur, mécanisme, moment sismique). Cela empêche les analyses systématiques des séismes ainsi que la détermination rapide de leurs caractéristiques de source. Pour remédier à cette limitation, nous pouvons estimer de manière déterministe la radiation générée par un séisme ponctuel. L'intérêt supplémentaire est de pouvoir simuler la radiation d'un séisme dont la fonction source est très proche d'une impulsion, ce qui n'est pas le cas pour les EGFs, et perturbe l'analyse haute-fréquence des fonctions source apparentes (voir section précédente). Cet avantage est théoriquement réduit par notre connaissance imparfaite du détail de la structure terrestre, qui limite la qualité à haute fréquence des fonctions de Green déterministes. Néanmoins, en se réduisant aux ondes de volumes dont la modélisation peut être obtenue simplement par la théorie des rais (ondes P et SH, et à un degré moindre PP, PcP et ScS), les formes d'onde peuvent être précises jusqu'à des fréquences proches du Hertz, ce qui permet d'analyser les fonctions source de nombreux séismes.

La section (1.2.2) nous a montré que les fonctions source apparentes sont des fonctions certes inconnues, mais sur lesquelles on connaît plusieurs propriétés *a priori* (positivité, causalité, support borné, intégrale temporelle égale au moment sismique). Cette observation nous permet de concevoir un nouveau schéma d'inversion, dans lequel le mécanisme, la profondeur ET les fonctions source apparentes peuvent être déterminés simultanément : considérant un mécanisme et une profondeur « tests » $\mathbf{M_t}$ et z_t, la radiation point-source à une station i (notée $G^0_{t,i}$) pour ces paramètres peut être calculée. Ensuite, la déconvolution des formes d'ondes U_i du choc principal par $G^0_{t,i}$ (pour un type d'onde donné), en utilisant la méthode de *Vallée* (2004), nous permet d'obtenir des fonctions source $F_{t,i}$ respectant toutes les propriétés physiques *a priori*. En revanche, l'accord entre les reconvolutions $R_{t,i}(= G^0_{t,i} * F_{t,i})$ et les formes d'ondes U_i du choc principal sera probablement mauvais pour ce jeu de paramètres initial $(\mathbf{M_t}, z_t)$. La méthode d'optimisation a donc pour but de définir le jeu de paramètres $(\mathbf{M_0}, z_0)$, qui permet de maximiser l'accord entre toutes les reconvolutions $R_{0,i}$ et les formes d'ondes du choc principal. Cette approche fournit, de manière intrinsèque, les fonctions source apparentes optimales $F_{0,i}$. C'est le principe général de la méthode SCARDEC (*Vallée et al.*, 2011), dont le détail, les avantages et des applications sont fournis dans les pages suivantes.

I.3.2 La méthode SCARDEC, et ses applications aux séismes de subductions majeurs

Cet article a été publié en janvier 2011 dans le journal *Geophysical Journal International*.

Geophysical Journal International

Geophys. J. Int. (2011) **184,** 338–358 doi: 10.1111/j.1365-246X.2010.04836.x

SCARDEC: a new technique for the rapid determination of seismic moment magnitude, focal mechanism and source time functions for large earthquakes using body-wave deconvolution

M. Vallée,[1] J. Charléty,[1] A. M. G. Ferreira,[2,3] B. Delouis[1] and J. Vergoz[4]

[1] *Geoazur, Observatoire de la Côte d'Azur, IRD, CNRS, Université de Nice–Sophia Antipolis, Valbonne, France. E-mail: vallee@geoazur.unice.fr*
[2] *School of Environmental Sciences, University of East Anglia, Norwich, UK*
[3] *ICIST, Instituto Superior Técnico, Lisboa, Portugal*
[4] *Laboratoire de Détection Géophysique, CEA, Bruyères le Chatel, France*

Accepted 2010 October 4. Received 2010 September 15; in original form 2010 January 29

SUMMARY

Accurate and fast magnitude determination for large, shallow earthquakes is of key importance for post-seismic response and tsumami alert purposes. When no local real-time data are available, which is today the case for most subduction earthquakes, the first information comes from teleseismic body waves. Standard body-wave methods give accurate magnitudes for earthquakes up to $M_w = 7$–7.5. For larger earthquakes, the analysis is more complex, because of the non-validity of the point-source approximation and of the interaction between direct and surface-reflected phases. The latter effect acts as a strong high-pass filter, which complicates the magnitude determination. We here propose an automated deconvolutive approach, which does not impose any simplifying assumptions about the rupture process, thus being well adapted to large earthquakes. We first determine the source duration based on the length of the high frequency (1–3 Hz) signal content. The deconvolution of synthetic double-couple point source signals—depending on the four earthquake parameters strike, dip, rake and depth—from the windowed real data body-wave signals (including *P, PcP, PP*, *SH* and *ScS* waves) gives the apparent source time function (STF). We search the optimal combination of these four parameters that respects the physical features of any STF: causality, positivity and stability of the seismic moment at all stations. Once this combination is retrieved, the integration of the STFs gives directly the moment magnitude. We apply this new approach, referred as the SCARDEC method, to most of the major subduction earthquakes in the period 1990–2010. Magnitude differences between the Global Centroid Moment Tensor (CMT) and the SCARDEC method may reach 0.2, but values are found consistent if we take into account that the Global CMT solutions for large, shallow earthquakes suffer from a known trade-off between dip and seismic moment. We show by modelling long-period surface waves of these events that the source parameters retrieved using the SCARDEC method explain the observed surface waves as well as the Global CMT parameters, thus confirming the existing trade-off. For some well-instrumented earthquakes, our results are also supported by independent studies based on local geodetic or strong motion data. This study is mainly focused on moment determination. However, the SCARDEC method also informs us about the focal mechanism and source depth, and can be a starting point to study systematically the complexity of the STF.

Key words: Inverse theory; Earthquake source observations; Body waves; Surface waves and free oscillations; Wave propagation; Subduction zone processes.

GJI Seismology

1 INTRODUCTION

Most major earthquakes ($M > 7.5$) occur in subduction zones, often in places where there is sparse local seismological or geodetical instrumentation. In these cases, the knowledge that we can obtain about these events depends mainly on our ability to analyse the teleseismic wavefield. Efficient methods are important both to give accurate information in the near-real time (tsunami alert, post-seismic reaction) and to provide later precise and systematic information on the seismicity (tectonics, seismic source understanding and seismic

hazard...). Current methods to analyse teleseismic waves usually involve two main steps. First, simplified source models are used to determine the earthquake's focal mechanism, magnitude and depth. Then, detailed analyses can be done to retrieve further information about the seismic source process (location of major slip zones, average rupture velocity...). A refinement of moment magnitude can also be done in this second step.

However, for major earthquakes, the possibility to decouple fault geometry and source processes has to be questioned. When using classical body-wave (*P* and/or *SH*) point-source approaches (e.g. Nabelek 1984; Ruff & Miller 1994; Goldstein & Dodge 1999), we intrinsically impose that the source time function (STF) is the same at all stations. This assumption is reasonable for moderate earthquakes, at least if high frequency waves are discarded, but becomes increasingly invalid as the magnitude and source dimension increase; extended source effects cause the STFs to be dependent on the recording station. Methods incorporating source complexity in the definition of the focal mechanism exist, but generally require some tuning, as for example, the iterative approach of Kikuchi & Kanamori (1991) or the slip patch method of Vallée & Bouchon (2004). For large shallow earthquakes, another complication arises because the low-frequency part of the signal, which controls the seismic moment determination, is strongly attenuated by destructive interferences between direct wave (*P*) and surface reflected phases (*pP, sP*).

Apart from simple body-wave point-source methods, the other main class of semi-automatic methods used to determine focal mechanism, depth and magnitude is the centroid approach. This technique, based on the work of Dziewonski *et al.* (1981), is today routinely implemented in the Global Centroid Moment Tensor (GCMT) catalogue, which is extensively used in tectonic studies. Based on low-frequency body and/or surface waves, the method simultaneously optimizes the location and timing of the centroid of the source (which can be seen as the spatial and temporal barycentre of the earthquake) and the seismic moment tensor. The method is very attractive because it incorporates in the centroid location the major complexities of the source. The high-frequency STF variability is also a minor problem, because low-frequency surface waves (generally periods of about 150 s) strongly control the solution. However the method presents a few drawbacks. First, its interest for tsunami alert is limited because it requires the recording of slow surface waves at teleseismic distances. Second, when the earthquake is large ($M_w \geq 7.8$) and shallow, the GCMT solution is obtained using mostly low-frequency surface waves. As a consequence, it suffers from a well-known trade-off between the fault's dip δ and the seismic moment M_0 (e.g. Kanamori & Given 1981). For dip-slip earthquakes, the method precisely retrieves the quantity ($M_0 \sin 2\delta$), but cannot accurately resolve the two parameters separately. Because large subduction earthquakes often occur on shallow-dipping planes (where $\sin 2\delta \sim 2\delta$), the effect of the trade-off is large for this type of earthquakes. For example, values of dip of 6° or 12° would lead to an uncertainty of a factor of 2 for M_0, or an uncertainty of 0.2 in moment magnitude M_w. The latter problem also occurs for the recently developed *W*-phase approach (Kanamori 1993; Kanamori & Rivera 2008), which uses the low-frequency information of the beginning of the seismic signals (between *P* and *S* waves). A last minor problem with GCMT is the empirical determination of the source half-duration. Low values of this parameter make the wave amplitudes larger, which implies that lower values of the earthquake moment are required to explain the data. In the Global CMT (GCMT) routine, the half-duration is not inverted but is fixed as a function of the magnitude. However there is a large duration diversity, even for earthquakes of the same magnitude. As an example for earthquakes given with $M_w = 7.7$ in the GCMT catalogue, we can take the 2001/01/13 El Salvador earthquake and the 2006/07/17 Java earthquake. The first one is a short and impulsive earthquake (duration of about 15 s; Vallée *et al.* 2003), while the second one is a slow tsunami earthquake with duration around 150 s (Ammon *et al.* 2006). Consistently, the latter study determines a moment magnitude 0.1 larger than that reported in the GCMT catalogue for the 2006 Java earthquake.

Because magnitude is a decisive information for alert purposes, some studies aim at determining the moment magnitude without resolving the focal mechanism or the depth. One of these methods is known as the M_{wP} method (Tsuboi *et al.* 1995). It directly integrates the *P*-wave displacement to estimate the associated moment magnitude. The method first requires an azimuthal average of the displacements to take into account the radiation pattern. Another greater problem arises if reflected phases *pP* or *sP* arrive before the end of the direct *P* radiation (which is always the case for large shallow earthquakes); arrival of these waves strongly pollute the measured amplitude displacements. Other methods, based on semi-empirical considerations, analyse the high-frequency part of the *P* radiation to determine the source duration (Ni *et al.* 2005; Lomax 2005), and then use a refined M_{wP} approach (Lomax & Michelini 2009), energy considerations (Lomax *et al.* 2007) or amplitude measurements (Hara 2007) to retrieve the moment magnitude. These approaches can be very useful to get a first idea of the size of a major earthquakes, but lack a physical basis to better understand the characteristics of these events.

The goal of this study is to provide a fast and reliable determination of the main characteristics of major earthquakes, without using empirical relationships or oversimplifications of the source process. The objective is to provide both rapid information and reliable source characteristics, useful for further analyses of the earthquakes. We present here a way to do so, based on a deconvolutive approach of a broad range of body waves (*P, PcP, PP*, *S, ScS*, along with all the associated surface reflected phases). The STF can have an arbitrary complexity and the apparent STFs may differ from station to station, as expected for large earthquakes. This approach, that we will name the SCARDEC method, is applied to most subduction earthquakes with $M_w \geq 7.8$ in the period 1990–2010. Results are generally found close to GCMT parameters. However, for half of the earthquakes, the fault's dip angle is found steeper and the seismic moment is smaller (by up to a factor of 2) than in the GCMT catalogue. In these cases, we check by forward modelling that our proposed model explains surface wave data as well as the GCMT model. We show in the following sections that the SCARDEC method reliably determines the first-order characteristics of large earthquakes, using seismic data arriving in the 30 min following the earthquake origin time. Moreover, the method provides as a by-product the apparent STFs, which are valuable for further analyses of the source process.

2 SCARDEC METHOD

2.1 Wave modelling and data selection

In the teleseismic range ($30° < \Delta < 90 - 95°$), the modelling of direct *P* and *SH* Green's functions along with the associated local surface reflections (*pP, sP, sS*) can be carried out accurately using standard ray techniques. We use here the method of Bouchon (1976), which includes the reflectivity method (Fuchs & Müller

Table 1. Teleseismic data used for each subduction earthquake in this study. Index, name, date and GCMT moment magnitude of each event are first given. *P* stations and *SH* stations indicate the number of stations used in the analysis of compressive and transverse body waves, respectively. *P* gap and *SH* gap are the maximum azimuthal gaps (°) between stations for compressive and transverse body waves, respectively.

n^0	Name	Date	*M*w GCMT	*P* stations	*P* gap	*SH* stations	*SH* gap
1	Java	02/06/1994	7.76	14	72.8	13	91.7
2	Chile	30/07/1995	8.00	11	84.2	14	62.3
3	Jalisco	09/10/1995	7.98	10	98.2	11	88.4
4	Kuril	03/12/1995	7.88	18	74.0	18	74.0
5	Minahassa	01/01/1996	7.87	18	42.3	18	41.7
6	IrianJaya	17/02/1996	8.19	13	65.7	13	65.7
7	Andreanof	10/06/1996	7.88	19	65.6	20	65.6
8	Kamtchatka	05/12/1997	7.76	20	62.0	18	62.3
9	Peru	23/06/2001	8.39	15	59.8	15	70.6
10	Hokkaido	25/09/2003	8.26	20	59.9	22	59.9
11	Sumatra	28/03/2005	8.62	23	39.4	26	33.7
12	Kuril	15/11/2006	8.30	21	47.9	17	77.7
13	Solomon	01/04/2007	8.07	16	72.5	17	74.6
14	Peru	15/08/2007	7.97	15	75.9	19	42.6
15	Sumatra	12/09/2007	8.49	18	62.2	21	40.2
16	NewZealand	15/07/2009	7.78	18	71.8	18	71.8
17	Chile	27/02/2010	8.79	18	49.4	18	57.6

1971; Müller 1985) for both source and receiver crusts. The mantle propagation is simply taken into account by geometrical spreading and attenuation (t*) factors. Take-off angles below the crust and the geometrical spreading factor are deduced from the global traveltime model IASP91 (Kennett & Engdahl 1991). Simple modifications of the same technique allow us to model the core-reflected (*PcP* and *ScS*) and surface-reflected (*PP* and *SS*) phases. In both cases, take-off angles and geometrical spreading have to be computed from the traveltime derivatives of the corresponding phases. For the core-reflected phases, the computed Green's function has to be multiplied by the reflection coefficient at the core surface (1 for *ScS*, because we use only the transverse component). For the surface-reflected phases, we multiply the Green's function by the reflection coefficient at the Earth's surface and Hilbert-transform the resulting wavefield. Modelling of surface-reflected phases is imprecise for distances shorter than 60°, because these waves remain in the heterogeneous upper mantle. Thus the Green's function including direct, core and surface-reflected phases can be computed in the range from 60° to 90–95°. Currently, even in this restrained distance range, the station distribution of the seismic global network (FDSN) insures a suitable azimuthal coverage (see e.g. Table 1).

For the scope of our method, the *PcP, PP* and *ScS* phases have to be used because for large earthquakes with long source durations, one of these phases interferes with the direct *P* or *SH* wave. For a 100 -s-long superficial source, this occurs with the *PcP* phase for distances larger than 40° and with *ScS* for distances larger than 60°. For a 150 -s-long superficial source, this occurs with the *PcP* phase for distances larger than 35°, with the *PP* phase for distances shorter than 70° and with *ScS* for distances larger than 50°. The integration of the *SS* phase in our method is less useful, because in the 60–95° distance range, it arrives at least 240 s after the *S* wave. Moreover, its arrival time can be close (150 s) to the Love waves arrival at distances around 60°, causing significant wave interference. Using the combination of *P, PcP* and *PP* in the 60–90° distance range and of *SH* and *ScS* in the 60–95° distance range, we can analyse earthquakes with a source duration up to 250 s ($M_w = 8.7$–9). For longer—but very rare—earthquakes, some mixing between phases would still occur, which impedes the precise analysis of giant earthquakes. We call hereafter 'compressive waves' the three phases *P, PcP* and *PP*, and 'transverse waves' the two phases *S* and *ScS*.

We propose here to check our method for the major interplate subduction earthquakes of the last 20 yr. Specifically, we select earthquakes occurring between 1990 and 2010, with moment magnitude larger than 7.8, with a thrust mechanism and with depth smaller than 50 km. Such a request from the GCMT catalogue (http://www.globalcmt.org/CMTsearch.html) gives a list of 23 earthquakes. In this list, we do not consider the Sichuan earthquake (continental intraplate). In addition, we do not include the 2000 November 16 New Ireland, 2000 November 17 New Britain, 2007 September 12 (23h49) Sumatra and 2009 October 7 (22h18) Santa Cruz earthquakes, because they were preceded within a day by a similar or larger earthquake, which makes the waveforms noisy. We finally discard the 2004 Sumatra earthquake because the source duration is much longer than 250 s. For such an earthquake, we believe that its giant character is most efficiently identified by its very long high-frequency duration (Lomax 2005; Ni *et al.* 2005). The remaining 17 earthquakes are presented in Table 1 and on the map of Fig. 1. For each of these earthquakes, we automatically retrieve FDSN broad-band data using the IRIS Wilber interface (http://www.iris.edu/wilber). When several stations are present in a 10° azimuthal range, we only select the one with the best signal-to-noise ratio. The number of stations selected for compressive and transverse waves, along with the largest azimuthal gap, are shown in Table 1.

2.2 Source duration determination

The first step in our method is to estimate the earthquake source duration. This can be sometimes directly read on the *P*-wave seismograms, but some subjective interpretation is necessary, in particular when the earthquake is long and little impulsive, or when the *pP* and *sP* phases lengthen the signal. For an automated approach, we follow the methods based on the high-frequency *P*-wave duration (e.g. Lomax 2005; Ni *et al.* 2005). These methods use the simple observation that at high frequency (around 2 Hz), the vertical component teleseismic waveform is mostly dominated by the

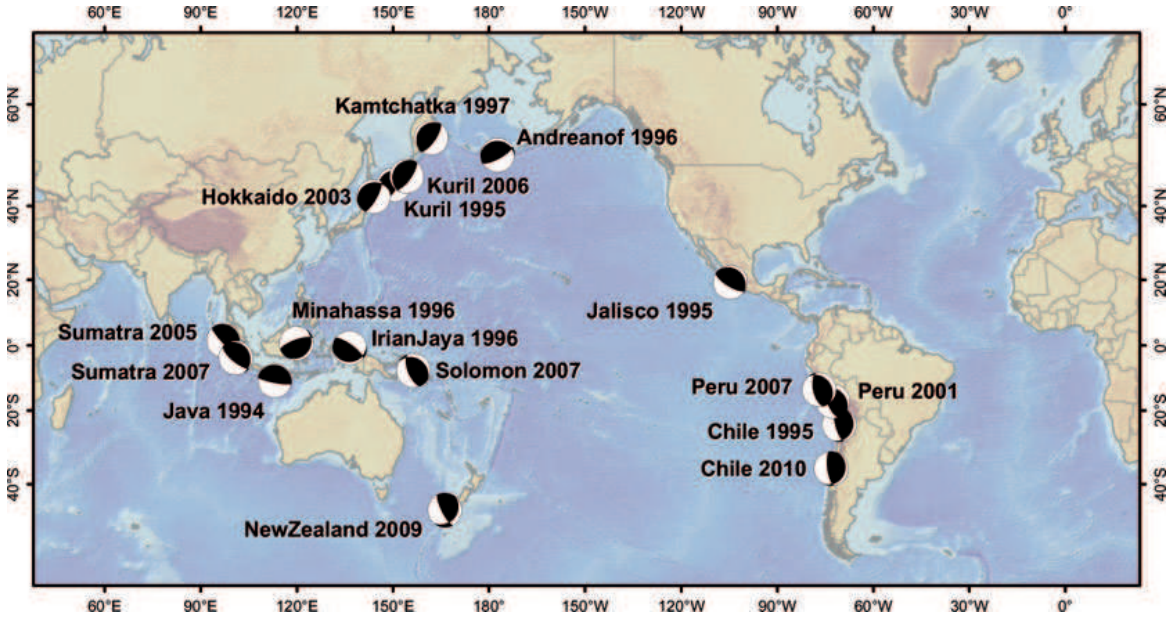

Figure 1. Location of the studied subduction earthquakes. The focal mechanisms determined in this study are presented at the epicentral location of each earthquake.

direct *P* wave. Therefore a measurement of the duration of the signal in this frequency range gives a good estimation of the source duration.

In practice, some care has to be taken to automatically determine the end of the high-frequency signal. In particular, some noisy stations can lead to a large overestimation of the *P*-wave duration. Moreover, even for stations with good signal-to-noise ratio, a complex *P*-wave coda lengthens the high-frequency signal (Fig. 2). As in previous studies (Lomax 2005; Ni *et al.* 2005), we thus have to tune the duration measurement's criteria. We use the following procedure, based on systematic tests with a large earthquake catalogue (about 50 earthquakes with magnitude larger than 7): for each of the n vertical component signals, we select the time of the first *P*-wave arrival (T_0) as the origin time. After bandpass filtering between 1

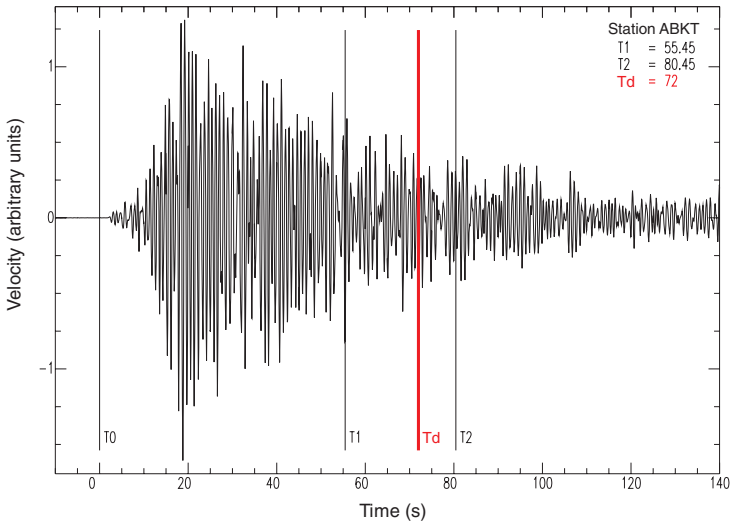

Figure 2. Source duration determination by high-frequency analysis of vertical teleseismic waveforms. The origin time T_0 is the time of the first *P*-wave arrival. After defining the times T_1 for the n vertical teleseismic waveforms and classing them by ascending order, we extract the station corresponding to the index $n/4$ (see main text). We show an illustrative example for the 2003 Hokkaido earthquake, for which ABKT is the selected station. The vertical waveforms bandpass filtered between 1 Hz and 3 Hz, along with the times T_1, T_2 and T_d—estimate of the rupture duration—are shown in this figure.

and 3 Hz, we locate the time of the last signal point which is above 50 per cent of the maximum of the signal (T_1). We class the times T_1 by ascending order, and select the time T_1 with index $n/4$ in the ordered list. This reduces the chance of using stations which underestimate (rare) or overestimate (more common) the signal duration. The choice of using the time with index $n/4$ comes from extensive tests with our large earthquake catalogue, after having tried a variety of different criteria. As an estimation of the robustness of the measurement, we have also checked that stations corresponding to indices neighbours of $n/4$ give a very similar estimation. The signal corresponding to this index, in the case of the 2003 Hokkaido earthquake, is presented in Fig. 2.

We now consider the time T_2 equal to $(T_1 + 25)$ s. The time T_1 is lengthened for three reasons. First, given the criterion used to define T_1 (last point above 50 per cent of the signal maximum), it is very likely that we miss the final part of the source emission. Second, we aim at defining a source duration which does not underestimate the source duration seen at any station. In fact, directivity effects may cause the source duration to be apparently longer in some azimuths. Third, it is better to slightly overestimate the source duration than to underestimate it. Overestimation of the source duration results in the introduction of some low-amplitude noise signal while underestimation implies that a part of the real source emission is not considered. The choice of the 25 s value mainly comes from this third criterion: we have checked with our test catalogue that this additional time prevents us from underestimating the source duration. Finally, we subtract to T_2 the $(pP - P)$ time to take into account that for shallow and intermediate-depth earthquakes, the *pP* phase also contributes to the high-frequency, vertical component seismogram, lengthening the signal. This final time, noted T_d, is presented in Table 2 for all the earthquakes of this study.

For compressive waves (*P, PcP, PP*), this time T_d is directly used as an estimate of the source duration. For transverse waves (*SH, ScS*), directivity effects are expected to be larger. Simple calculations for a unilateral rupture with a fast 3.5 km s^{-1} rupture velocity show us that these directivity effects may lead to an apparent duration 15 per cent longer for transverse waves than for compressive waves. We thus take the value $1.15.T_d$ as an estimate of the transverse waves source duration.

Table 2. Source duration T_d determined by high-frequency analysis (1-3 Hz) of vertical teleseismic waveforms.

n^0	Name	Date	T_d (s)
1	Java	02/06/1994	110.3
2	Chile	30/07/1995	96.3
3	Jalisco	09/10/1995	71.9
4	Kuril	03/12/1995	63.8
5	Minahassa	01/01/1996	66.3
6	IrianJaya	17/02/1996	105.4
7	Andreanof	10/06/1996	64.5
8	Kamtchatka	05/12/1997	55.8
9	Peru	23/06/2001	121.0
10	Hokkaido	25/09/2003	72.0
11	Sumatra	28/03/2005	105.8
12	Kuril	15/11/2006	117.7
13	Solomon	01/04/2007	91.6
14	Peru	15/08/2007	121.4
15	Sumatra	12/09/2007	105.2
16	NewZealand	15/07/2009	66.2
17	Chile	27/02/2010	127.4

2.3 Deconvolutive approach

Most body-wave methods use strong *a priori* constraints on the source process for the fast determination of the earthquake's magnitude and focal mechanism. Generally, the absolute STF is represented by discrete points and the methods optimize the value of these points together with the depth and the focal mechanism parameters to determine the focal mechanism and magnitude (Nabelek 1984; Ruff & Miller 1994; Goldstein & Dodge 1999). Such approaches do not give a complete freedom to the STF, and, most importantly, impose that the STF is the same for all stations. This is not a serious concern for moderate-to-large earthquakes (up to $M_w = 7{-}7.5$) because directivity effects, which cause changes in the STF at each station, are generally weak. However, for larger earthquakes, these effects increase and using a unique STF for all stations becomes a poor approximation. Modifications of the method of Nabelek (1984) and Ruff & Miller (1994) have been introduced to take into account a very simple directivity (i.e. unilateral propagation with a constant rupture velocity), but they cannot fully represent the diversity of directivity effects (due e.g. to bi-dimensional propagation or changes in rupture velocity). An alternative could be to low-pass filter the body waves, for example below 0.01 Hz, to reduce the high-frequency directivity effects. However this is not a solution either because the body waves would interfere with other low-frequency waves, such as the *W* phase (Kanamori 1993).

Another difficulty arises for large and shallow earthquakes. It is well known that the direct *P*-wave displacement is directly the STF, if we correct for focal mechanism and propagation constants (e.g. Lay & Wallace 1995, p. 337). Therefore, for deep earthquakes (or, more precisely, for depths such that the end of the earthquake occurs before the arrival of *pP* wave), resolving the seismic moment is relatively straightforward because it only requires an integration of the direct *P* wave, after correcting for the required constants. For shallower earthquakes, the direct *P* wave interferes with *pP* and *sP* waves. It creates a more complex *P* wave train and causes a reduction of its low-frequency content because one of the *pP* or *sP* waves generally have an opposite polarity (high-pass filter effect). When optimizing the agreement between synthetics and such complex *P* wave train, the fit will thus be much more influenced by some high-frequency features (little affected by the destructive interferences between *P*, *pP* and *sP* wave) than by the reduced-amplitude low-frequency features. The obtained STF is likely peaky, reproducing the impulsive parts of the *P* wave train, and lacks some long-period trend. This last effect explains why there is a tendency of underestimating the seismic moment of large earthquakes when using classical *P*-wave methods.

The basic idea of this study is to propose a method able to retrieve the first-order characteristics of earthquakes (seismic moment, depth and focal mechanism) without imposing constraints on the source process. We begin with the classic representation theorem (e.g. Aki & Richards 2002, p. 51) of the teleseismic displacement U, which depends on the source term f and the propagation term $G_{\phi,\delta,\lambda}$ (where ϕ, δ, λ are respectively the strike, dip and rake of the earthquake). Neglecting the along-dip extension of the source (line-source approximation), we have

$$U(\omega) = \int_{L_1}^{L_2} f(x,\omega)\, G_{\phi,\delta,\lambda}(x, z_c, \omega)\, \mathrm{d}x, \quad (1)$$

where L_1 and L_2 are the lateral edges of the fault, and z_c is an average depth of the earthquake. For an individual body wave in a spherical Earth, $G_{\phi,\delta,\lambda}$ can be easily modelled

as

$$G_{\phi,\delta,\lambda}(x, z_c, \omega) = G^0_{\phi,\delta,\lambda}(z_c, \omega)\, \mathrm{e}^{\mathrm{i}\vec{k}.\vec{x}} \quad \forall x \in [L_1 L_2], \tag{2}$$

where $\vec{k}$ is the wave vector of the considered body wave. G^0 represents the teleseismic wavefield generated by a double-couple point source located at the earthquake hypocentre. This term can be numerically evaluated using the techniques explained in Section 2.1. For a propagating rupture along the fault, the source term f may be written as

$$f(x, \omega) = s(x, \omega)\mathrm{e}^{-\mathrm{i}\omega T_r(x)}, \tag{3}$$

where s is the local STF describing the shape of the movement of each point x of the fault and T_r is the rupture propagation time. We can now rewrite (1) as

$$U(\omega) = G^0_{\phi,\delta,\lambda}(z_c, \omega) \int_{L_1}^{L_2} s(x, \omega)\mathrm{e}^{\mathrm{i}(\vec{k}.\vec{x} - \omega T_r(x))}\, \mathrm{d}x. \tag{4}$$

In the time domain, (4) may be written as

$$U(t) = G^0_{\phi,\delta,\lambda}(z_c, t) * F(t) \tag{5}$$

where F, often called the apparent or relative source time function (RSTF), is

$$F(t) = \int_{L_1}^{L_2} s\left(x, t + \frac{x\, \sin\theta\, \cos(\phi - \alpha)}{v_\phi} - T_r(x)\right) \mathrm{d}x. \tag{6}$$

In this last equation, θ, v_ϕ are respectively the take-off angle and phase velocity of the considered body wave, and α is the azimuth of the recording station. These last three parameters, which depend on the body wave type and/or the location of the station, explain why F is called an apparent or relative STF. However, F has an important integral property, independent of the wave type or station location

$$\int_0^\infty F(t)\, \mathrm{d}t = M_0 \quad \forall \alpha, \theta, v_\phi, \tag{7}$$

where M_0 is the seismic moment of the earthquake. F has also three other important properties, which directly come from the properties of the local STF s: F is a positive, causal and bounded function. As we have an estimate of the global source duration T_d, we can be more precise on this last property and assert that F has to be bounded at T_d. The causality property comes from the fact that for body waves the directivity term $\Gamma = \frac{x \sin\theta \cos(\phi - \alpha)}{v_\phi}$ is shorter than $T_r(x)$, even in the intrasonic rupture propagation regime. Finally, because θ is small and v_ϕ is high (particularly for the faster P wave), the directivity term Γ remains moderate for body waves. This implies that the function F cannot differ a lot from station to station. Therefore, when deconvolving $G^0_{\phi,\delta,\lambda}(z_c, t)$—for a given set of parameters (ϕ, δ, λ, z_c)—from $U(t)$ at all recording stations, the tested set of parameters is realistic only if the deconvolution result F^1 verifies the five following conditions:

(i) F^1 is positive;
(ii) F^1 is causal;
(iii) F^1 is bounded to T_d;
(iv) the time integral of F^1 is constant for all stations and
(v) F^1 varies moderately from station to station, particularly for P waves.

Respecting all these conditions at all stations and for all body wave types puts strong constraints on the set of four parameters on which depend the deconvolution. The idea of this study is therefore that even if we do not know what really happens inside the source (function s, rupture propagation T_r), we have enough information on F to constrain the focal mechanism and depth of the earthquake. Clearly, these constraints are stronger when a maximum of stations and wave types are taken into account, because it better samples the focal sphere. Here, we compute $G^0_{\phi,\delta,\lambda}(z_c, t)$ separately for compressive body waves and for transverse body waves, using the epicentral location given in the NEIC catalogue (http://neic.usgs.gov/neis/epic/). For compressive body waves, we include the direct P wave, the *PcP* and *PP* waves. For transverse body waves, we include the direct *SH* wave and the *ScS* (transverse) wave. In both cases, all the refracted and reflected waves in the source and receiver crust are considered. Because we use a Moho depth of 35 km with a simple linear wave velocity increase (between 6 km s^{-1} and 8 km s^{-1} for P waves), the only energetic waves generated in the crust are the local surface reflected waves (i.e. *pP, sP, sS*, and similarly *pPcP, sPcP, sScS, pPP, sPP*). We show in Fig. 3(b) an example of the term $G^0_{\phi,\delta,\lambda}(z_c, t)$ for the compressive waves. There is an approximation in deconvolving in this way the compressive and transverse wavefield. In fact, the take-off angles—between *P, PcP* and *PP* waves on one hand and between *SH* and *ScS* waves on the other hand—vary while the derivation between eqs (1) and (6) is theoretically exact only if all the waves share the same wave vector. However, the changes remain moderate (no more than 20° variation) and the gain obtained in integrating the *PcP, ScS* and *PP* waves, both for the better sampling of the focal sphere and for the analysis of long earthquakes, justifies this approximation.

It would however be difficult to follow exactly the methodology explained above to determine the optimal set of parameters (ϕ, δ, λ, z_c). First, an unconstrained deconvolution is well known to be unstable and second it would be very difficult to build a misfit function that simultaneously takes into account the five conditions. A more efficient way to do is to constrain the deconvolution result F^1 to respect the conditions, and then to estimate the misfit by reconvolving F^1 with $G^0_{\phi,\delta,\lambda}(z_c, t)$ and comparing with U. Conditions (i), (ii) and (iii) can be integrated in the deconvolution process with the method of Bertero *et al.* (1997). Condition (iv) can be taken into account with the method of Vallée (2004). We present in Fig. 3(c) the result of the constrained deconvolution, for the compressive body waves recorded at station NOUC during the 2003 Hokkaido earthquake. In this example, (ϕ, δ, λ, z_c) = (251°, 22°, 129°, 35 km), T_d = 72s, and M_w = 8.15. Such parameters are shown here to be realistic because when reconvolving the stabilized deconvolution result with $G^0_{\phi,\delta,\lambda}(z_c, t)$ the agreement with the observed waveforms is good (Fig. 3d).

2.4 Optimization strategy

2.4.1 Optimal source model

Before analysing seismic body waves to determine the earthquake focal mechanism and depth, we first have to define the suitable body-wave frequency band. In fact, both very low and very high frequencies have to be discarded. The lower limit is constrained by the existence of the low-frequency W phase (Kanamori 1993), which becomes predominant for frequencies lower than 0.005 Hz (Kanamori & Rivera 2008). The upper limit is governed by several factors. First, we model the earthquake depth extension by its average depth. This is clearly not exact at high frequency, and imposes us to reject the high-frequency signal content to keep the deconvolutive approach robust. Such filtering also allows us to reduce the influence of local variations of focal mechanism. Second, while the direct P and *SH* waves can be precisely modelled for short periods (down to a few seconds), this is not the case for the *PcP, ScS* and *PP* waves included in this study. The first two waves interact with the

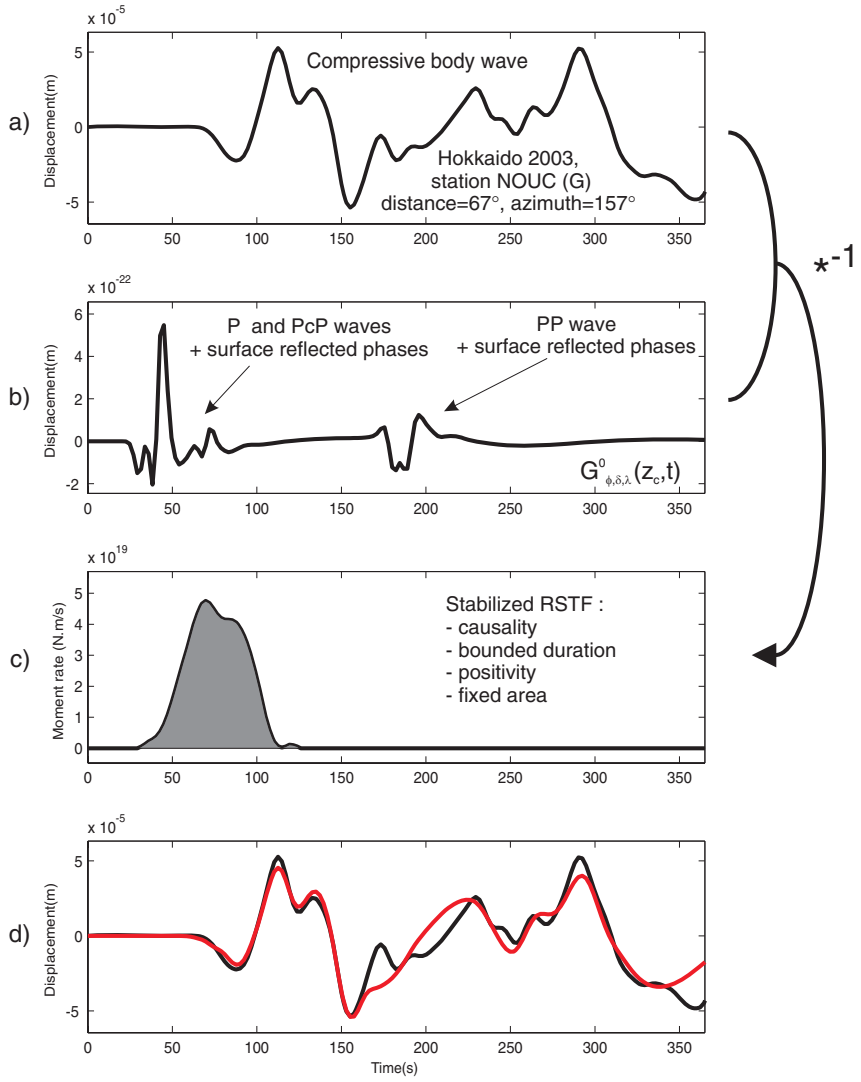

Figure 3. Principle of the deconvolutive approach. (a) Example of teleseismic compressive waveform. The waveform shows the vertical displacement recorded at station NOUC (Geoscope) after the 2003 Hokkaido earthquake. We show the first 300 s after the *P*-wave arrival, bandpass filtered between 0.005 Hz and 0.03 Hz (see filter types in the main text). (b) Theoretical propagation function ($G^0_{\phi,\delta,\lambda}(z_c, t)$) for compressive waves, including *P, PcP* and *PP* waves. The seismic source is represented by a double-couple point-source of moment 1 N m s^{-1}. $G^0_{\phi,\delta,\lambda}(z_c, t)$ is computed for $(\phi, \delta, \lambda, z_c) = (251°, 22°, 129°, 35$ km), and high-pass filtered at 0.005 Hz. (c) Stabilized deconvolution of (b) from (a), using conditions (i)–(iv) (see main text). Moment magnitude used to constrain the seismic moment (condition iv), is $M_w = 8.15$. The obtained function is the RSTF smoothed at 0.03 Hz. Note that an advance shift has been introduced in $G^0_{\phi,\delta,\lambda}(z_c, t)$ (b), so that the beginning of the RSTF is not too close from the origin time. (d) Comparison between observed waveforms [black; same signal as in (a)], and reconstructed waveforms [red; by convolution between (b) and (c) signals].

complex D'' region, and the latter one crosses two additional times the heterogeneous lithosphere and crust. As a result, these waves have a high-frequency content both less energetic and more difficult to model than the direct waves. Finally we also have a practical constraint, because the computing time for the stabilized deconvolutions depends directly on the number of samples. Considering only low frequencies allows us to reduce the number of samples and to accelerate the deconvolution process.

We take into account the high-frequency limitation by filtering the frequencies higher than 0.03 Hz. To do so, we convolve the data with f_g, defined as a time-shifted Gaussian function of standard error 4.4 s (which leads to a corner frequency at −3 dB of 0.03 Hz) and time integral equal to 1. The time-shift is selected so that only negligible energy arrives before origin time, making f_g very close to a causal function. Eq. (5) can be written as

$$U(t) \times f_g(t) = G^0_{\phi,\delta,\lambda}(z_c, t) * F(t) * f_g(t). \quad (8)$$

Deconvolving $G^0_{\phi,\delta,\lambda}(z_c, t)$ from $(U(t) * f_g(t))$ therefore gives a more reliable smoothed RSTF. The conditions for the RSTFs defined in Section 2.3 remain valid, as f_g is a causal positive function with

time integral equal to 1. Only the condition (iii) has to be slightly modified, because the obtained RSTF is now bounded at a time larger than T_d, due to the duration of f_g. For the low-frequency limit, a six-pole Butterworth high-pass filter at 0.005 Hz is applied both to the data and to the computed $G^0_{\phi,\delta,\lambda}(z_c, t)$, so that the conditions derived in Section 2.3 remain unchanged.

To optimize the set of parameters $(\phi, \delta, \lambda, z_c)$, we first deconvolve the computed function $G^0_{\phi,\delta,\lambda}(z_c, t)$ for transverse body waves, using stabilizing conditions (i), (ii) and (iii). By integration of the obtained RSTFs at each station, we have independent estimates of the seismic moment. There are several advantages in estimating the seismic moment from transverse body waves rather than from compressive body waves. First, *S* waves have a lower frequency content than *P* waves, which make them more sensitive to the zero-frequency seismic moment. Then, transverse *S* waves have only one local surface reflected phase (*sS*), which can be of the same polarity as the direct *SH* wave. Therefore, compared to the compressive waves, they suffer less from the high-pass filtering effect described before. Finally, when looking at the propagation coefficients which relate the focal mechanism to the radiated wavefield, there is no apparent trade-off between focal parameters and seismic moment (see e.g. coefficients $b1$ and $b2$ in Bouchon 1976, p. 523). For compressive body waves, there is a factor (called $a2$ in Bouchon 1976) which depends only on $\sin\lambda \sin 2\delta$. This term becomes predominant when take-off angles approach the vertical direction. In this case, compressive waves suffer from a similar trade-off as low-frequency surface waves, the seismic moment becoming strongly dependent on the focal mechanism parameters.

Once estimated the seismic moment at all stations for transverse body waves, we select its median value (called M_{0m}) and now deconvolve both transverse and compressive waves, using stabilizing conditions (i), (ii), (iii) and (iv). For this last condition, the moment at all stations is constrained to be equal at M_{0m}. The obtained RSTFs are then reconvolved with $G^0_{\phi,\delta,\lambda}(z_c, t)$, and we call the result of this operation U^1. The misfit ϵ_1 between data U and synthetics U^1 is evaluated using the classical variance reduction

$$\epsilon_1 = 1/N \sum_{i=1}^{N} C(i) \frac{\int_{t_0}^{t_0+t_f} \left(U_i^1(t) - U_i(t)\right)^2 \, \mathrm{d}t}{\int_{t_0}^{t_0+t_f} (U_i(t))^2 \, \mathrm{d}t}, \quad (9)$$

where N is the number of stations, C is a weighting factor accounting for the non-homogeneity of the station azimuth distribution, t_f is the fitting duration and t_0 refers to the arrival time of the direct *P* or *SH* wave. We evaluate ϵ_1 separately for compressive and transverse waves. In the case of compressive waves, t_f is fixed to the differential time between direct *P* arrival and *PPP* arrival, because this latter wave is not taken into account in the analysis. For transverse waves, it is fixed to the differential time between direct *S* and *SS* wave. This insures that a duration of at least 210 s is used to determine the fit for each station and each wave type. To take into account condition (v), we first estimate the average F_m of the obtained RSTFs noted F_i^1 for each station *i*.

$$F_m(t) = 1/N \sum_{i=1}^{N} F_i^1(t). \quad (10)$$

Then we define ϵ_2, measuring the non-similarity of the RSTFs.

$$\epsilon_2 = 1/N \sum_{i=1}^{N} \frac{\int_0^{T_d} \left(F_i^1(t) - F_m(t)\right)^2 \, \mathrm{d}t}{\int_0^{T_d} (F_m(t))^2 \, \mathrm{d}t}. \quad (11)$$

The computation of ϵ_2 is also done separately for compressive and transverse waves. Calling ϵ_1^P and ϵ_1^S, the misfit ϵ_1 computed for compressive and transverse waves, respectively, and ϵ_2^P and ϵ_2^S, the misfit ϵ_2 computed for compressive and transverse waves, respectively, we define the global misfit ϵ as

$$\epsilon = \left[\epsilon_1^P \left(1. + a^P \epsilon_2^P\right) + W_{PS} \left(\epsilon_1^S \left(1. + a^S \epsilon_2^S\right)\right)\right] / [1 + W_{PS}]. \quad (12)$$

a^P and a^S are chosen, respectively, equal to 2. and 1., to take into account that transverse RSTFs are expected to vary more than compressive RSTFs. Using larger values for a^P and a^S (up to 10 and 5, respectively) has a negligible effect on the results. W_{PS} is taken equal to 0.5, because a precise analysis of transverse waves is more difficult (in particular because the beginning of the signal may be noisy and because a part of the strong *SV* component may contaminate the signal). The chosen misfit function logically gives more weight to the ϵ_1 terms. The ϵ_2 terms, quantifying the similarity of the RSTFs, are only used as second-order stabilizing constraints. This makes the misfit function very different from most classical source inversions, where the RSTFs are intrinsically the same at each station. Because ϵ_2 terms have a small weight in the computation of ϵ, ϵ can be seen as the weighted average of ϵ_1^P and ϵ_1^S. This makes the values of ϵ directly interpretable as classical variance reduction values (i.e. $\epsilon = 0$ corresponds to a perfect reconstruction of the waveforms and $\epsilon = 1$ to the null hypothesis). Using the misfit function ϵ, and (ϕ, δ, λ, z_c) as inversion parameters, the optimal set of parameters is determined by the Neighbourhood Algorithm (NA, Sambridge 1999). ϕ, δ and λ are, respectively, allowed to vary in the [0°–360°], [0°–90°] and [−180°–180°] ranges. z_c can freely vary between $(z_n - 50)$ km and $(z_n + 50)$ km, where z_n is the event depth (in kilometres) retrieved in the NEIC catalogue. If $z_n - 50$ is smaller than 12, the minimal depth considered in NA is fixed at 12 km, as in the GCMT method. The main steps of the optimization procedure are summarized in Fig. 4. We hereafter refer to this approach as the SCARDEC method (from 'Seismic source ChAracteristics Retrieved from DEConvolvolvin g teleseismic body waves').

2.4.2 Dip, depth and moment uncertainties

Body wave analysis is expected to have a good dip and depth resolution because the take-off angles sample well the central part of the focal sphere and because the time arrival of surface-reflected phases are directly related to depth. We can verify this by computing the misfit variation when dip and depth vary around their optimal values. Fixing the strike and rake to their optimal values, we compute the misfit corresponding to depths at ±30 km around the optimal value and dips at ± 15° around the optimal value. Examination of this bi-dimensional misfit function for a broad range of earthquakes has shown us that in general the misfit varies little close to the optimal parameter set. However, when parameter values significantly differ from the optimal combination, the misfit value begins to increase sharply. We have observed that the change between these two behaviours occurs when the misfit function is about 10 per cent larger than its optimal value (see also the next section for actual examples). We thus consider that the acceptable parameters are those leading to misfit values not exceeding the optimal value by more than 10 per cent. The parameter range defined by this uncertainty analysis gives us information on the resolution of the SCARDEC method. Additionally, this analysis allows us to assess the sensitivity of the seismic moment to these acceptable variations of dip and depth.

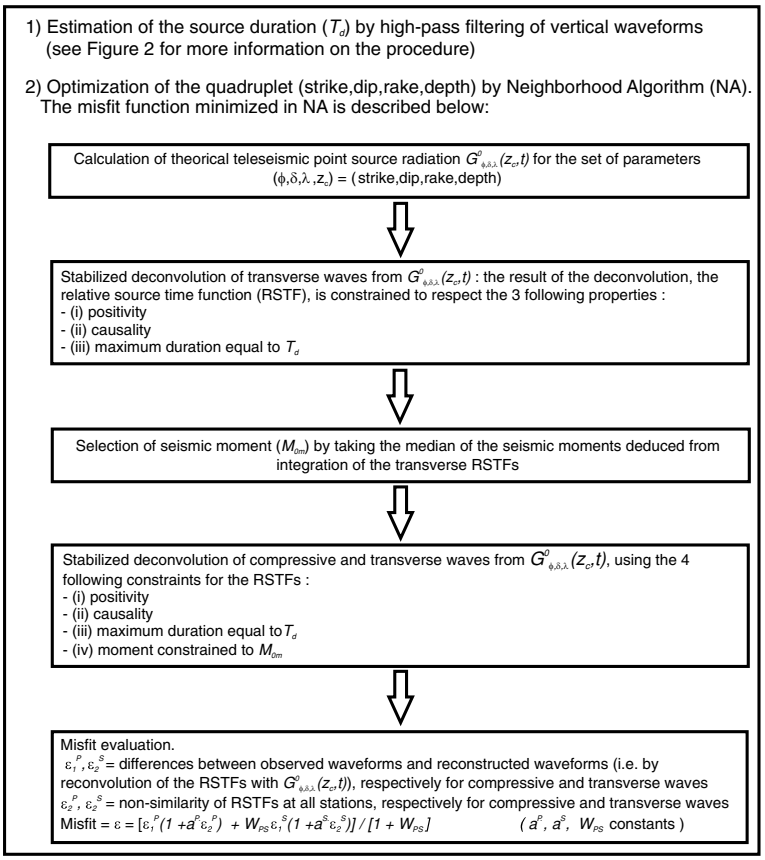

Figure 4. Flowchart explaining the principles of the SCARDEC method: diagram of moment magnitude, focal mechanism and depth optimization.

3 APPLICATION TO MAJOR SUBDUCTION EARTHQUAKES IN THE PERIOD 1990–2010

3.1 Detailed results for one event: the 2003 Hokkaido earthquake

We first detail the results for the 2003 September 25 Hokkaido earthquake. This earthquake is particularly interesting, because it is one of the very few major subduction earthquakes which was recorded and analysed with a large amount of seismological and geodetical data (see following sections).

The results obtained for this earthquake are presented in Fig. 5 for the source model and its uncertainties, and in Fig. 6 for the agreement between data and synthetics. The optimization process of minimizing ϵ has lead to determine $\phi = 251^\circ$, $\delta = 22^\circ$, $\lambda = 129^\circ$ and $z_c = 35$ km. The magnitude associated with this mechanism and depth is $M_w = 8.15$. The figures show that, with this optimal focal mechanism and depth, the RSTFs respecting the physical conditions (i), (ii), (iii) and (iv) are able to explain well the teleseismic displacement data ($\epsilon = 0.104$). The RSTFs for the various stations are similar, but clearly not identical. For example, a clear feature is that RSTFs in southeastern azimuths (i.e. stations PPT, RAR, NOUC and CTAO) are less impulsive than in northwestern azimuths (i.e. ABKT, GNI and MLR). This characteristic agrees well with detailed studies of this earthquake (Koketsu *et al.* 2004; Yagi 2004), which have shown that the rupture propagation of the Hokkaido earthquake was mainly in the downdip direction. This observed variability also gives an insight of the interest of the SCARDEC method compared to classical point source techniques. The use of these latter methods, which intrinsically impose the equality of the RSTFs, are expected to introduce biases in the determination of focal mechanism and magnitude. In fact, the use of a unique RSTF would reduce the agreement between data and synthetics. Because of this reduced fit, the reliability of the solution should decrease.

The estimation of dip and depth uncertainties can be seen in the bottom-left-hand side of Fig. 5. Considering that the acceptable solutions are inside the area where misfit is smaller than 1.1 times its optimal value (see Section 2.4.2), we determine that dip and depth are respectively equal to $22 \pm 3^\circ$ and 33 ± 8 km. The extreme values of magnitude associated with the acceptable dip and depth variability are 8.12 and 8.16.

Strike and rake are found very close to GCMT values ($\phi = 250^\circ$, $\lambda = 132^\circ$). Depth for the optimal model is deeper than GCMT (35 km versus 28 km), but if we take into account the uncertainties, we see that the depth of 28 km is acceptable. However, even with the uncertainties, we find that dip and magnitude differs from

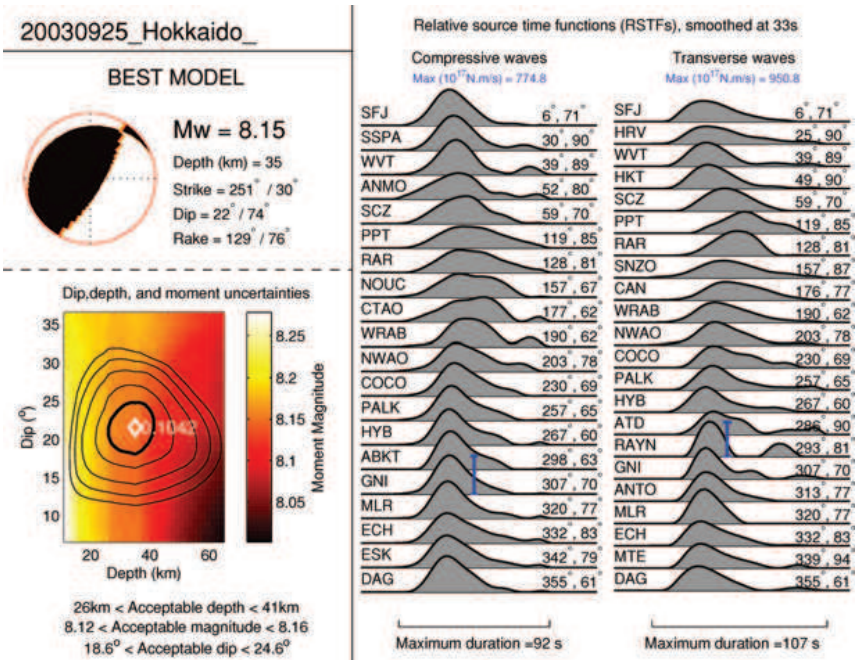

Figure 5. Source parameters, uncertainties and RSTFs. (Top left-hand side) Optimal values of moment magnitude, depth and focal mechanism. (Bottom left-hand side) Uncertainty analysis: misfit and moment magnitude changes as a function of dip and depth variations around their optimal values. Optimal dip and depth are indicated by the white diamond (the best misfit value is also shown). The thick line is the iso-misfit contour (noted C1) joining points with misfit 10 per cent larger than the best value. The four thin lines are the iso-misfit contours joining points with misfit 25 per cent, 50 per cent, 75 per cent and 100 per cent larger than the best value. Note that the observation of these misfit contours shows well the bell-shaped form of the misfit function, with a flat minimum surrounded by a sharp increase of the misfit. Moment magnitude associated with each (dip-depth) couple is shown with the colour scale. Acceptable values of dip, depth and magnitude are those which are inside the C1 contour. (Right) Relative source time functions (RSTFs) for compressive and transverse waves. These RSTFs are smoothed at 33 s (see main text) so that their durations are longer than the actual ones. The indicated maximum values correspond to the absolute maximum of all the moment rates, respectively, for compressive and transverse RSTFs. The corresponding scale is indicated by the blue bars, which are plotted next to the location of the maximal RSTF. For each RSTF, the name of the station, its azimuth and epicentral distance are shown.

GCMT. Dip is found 8–14° steeper than CMT and moment magnitude 0.11–0.15 smaller than GCMT. We show in the following paragraphs that other earthquakes share this property of a steeper dip associated with a smaller magnitude.

3.2 Global results

Results for the 17 studied earthquakes are presented in Table 3. Individual results—presented in a similar way as in Figs 5 and 6 for the 2003 Hokkaido earthquake—can be found in the Supplementary Figs 1 to 16. Considering the uncertainties, we observe a good depth agreement with GCMT. On the other hand, there are differences in strike and rake, up to 30° (event 7, Andreanof 1996 and event 13, Solomon 2007), for some earthquakes. The variations of these two parameters are not uncorrelated because the value $(\phi - \lambda)$ is much more consistent between GCMT and SCARDEC method. This is expected as body waves, having their take-off angle close to the vertical, cannot detect very accurately if there is a small strike-slip component in these shallow-dip thrust earthquakes. Sensitivity tests show however that the uncertainty should not be larger than ±15° for a 20° dipping fault. Differences larger than this uncertainty are thus thought to be meaningful, which is consistent with detailed studies of the 1996 Andreanof and 2007 Solomon earthquakes. In the first case, both the trench geometry and the study of Kisslinger & Kikuchi (1997) indicate that the fault strike is between the GCMT strike and the strike retrieved here. In the second case, the studies of Furlong *et al.* (2009) and Chen *et al.* (2009), as well as the trench geometry, show a fault strike very close to our determination.

The other clear difference with GCMT concerns the moment magnitude and dip. This latter parameter is reliably retrieved by body wave analysis because it is very sensitive to waves with take-off angles close to vertical. For about half of the studied earthquakes (Jalisco 1995, Kuril 1995, Minahassa 1996, Andreanof 1996, Peru 2001, Hokkaido 2003, Sumatra 2005 and Sumatra 2007), we clearly determine a steeper dip, associated with a smaller magnitude, than GCMT. Other earthquakes also indicate a similar behaviour, but given the uncertainties, the solutions remain consistent with GCMT. Dip angle comparisons, including uncertainties, are presented in Fig. 7. The observed differences may be due to the well-known trade-off between magnitude and dip affecting the GCMT results. We recall that the product $M_0 \sin 2\delta$ can be accurately resolved but that the relative weight of the two factors remains much less known. This means that a larger M_0 (and thus a larger M_w) with a smaller δ, or reciprocally a smaller M_w with a larger δ are plausible solutions.

To quantitatively evaluate if SCARDEC solutions are consistent with the expected trade-off, we can compare the obtained magnitude with a corrected GCMT magnitude, called $M_w^{'c}$ and expressed as

$$M_w^{'c} = 2/3 \log\left(\frac{M_0^c \sin 2\delta^c}{\sin 2\delta^d}\right) - 6.06\,, \qquad (13)$$

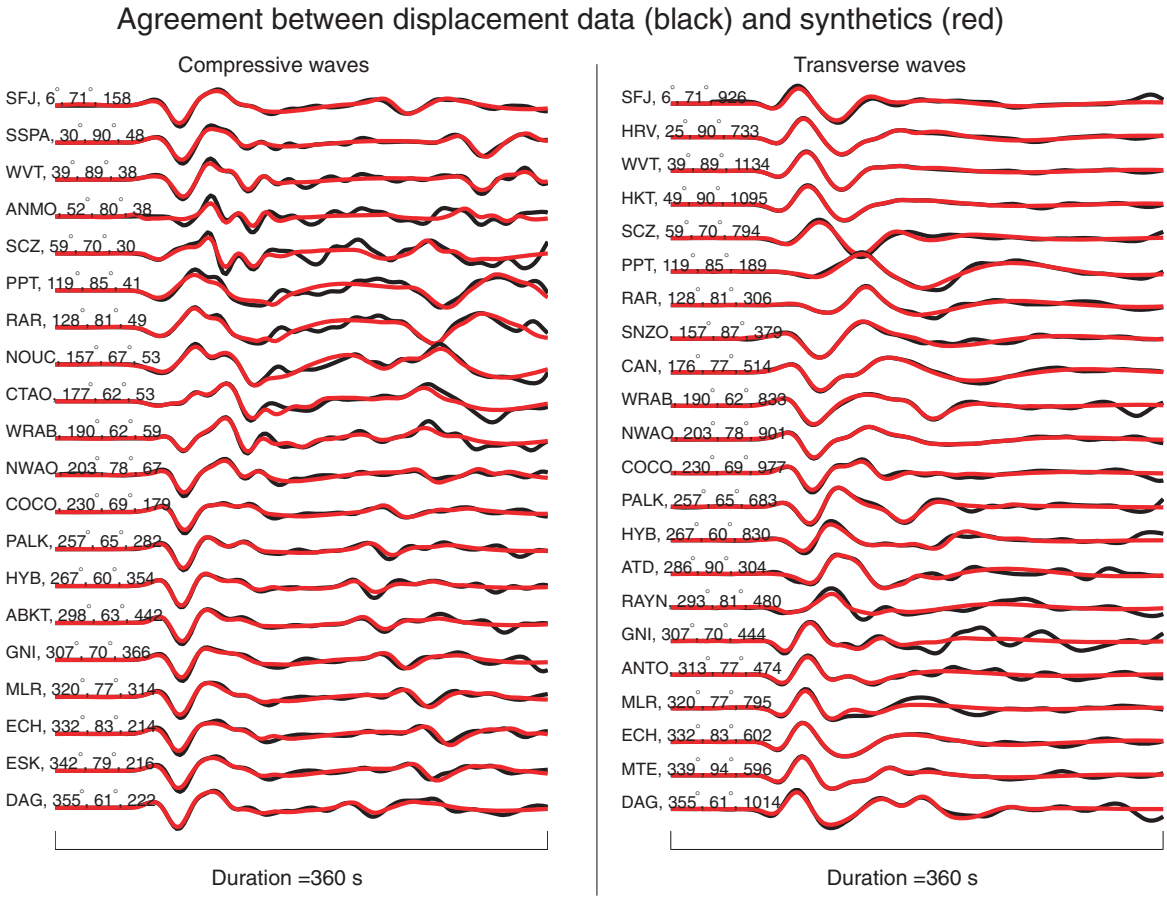

Figure 6. Agreement between data (black) and synthetics (red) for compressive waves (left-hand side) and transverse waves (right-hand side). For each station and wave type, synthetics are obtained from the convolution between $G^0_{\phi,\delta,\lambda}(z_c, t)$ and the obtained RSTF. The name of the station, its azimuth and distance, and the displacement maximum absolute value (in micrometres) of each signal are also shown.

where M_0^c is the GCMT seismic moment in N.m and δ^c and δ^d are the dips retrieved by GCMT and SCARDEC method, respectively. To be consistent with the $M_0 \sin 2\delta$ dependency, we should have $M_w^d = M_w'^c$, where M_w^d is the magnitude found in the present analysis. As there is a clear magnitude dependency on the earthquake's depth (see Fig. 5 and Supplementary Figures), it is more consistent to compare M_w^c, M_w^d and $M_w'^c$ for the same depth. Because the GCMT depths are inside or very close to the error bars of the depths determined in this study, we select M_w^d as the moment magnitude calculated at the GCMT depth (keeping the other three optimal parameters of the deconvolution, namely ϕ, δ, λ). Fig. 8(a) first shows the direct magnitude comparison between M_w^d and M_w^c. We see that there is some dispersion around the $x = y$ line, particularly for high magnitudes (>8.1), where $M_w^c > M_w^d$. In Fig. 8(b), where M_w^d is now plotted against $M_w'^c$, the dispersion is much smaller, and earthquakes are well aligned along the $x = y$ line. While the average difference between M_w^d and M_w^c is 0.095, the average difference between M_w^d and $M_w'^c$ is only 0.044. This indicates that a large part of the differences between the GCMT and the SCARDEC method can be explained by the trade-off affecting the low-frequency surface wave analysis. We note that M_w^d tends to slightly overestimate $M_w'^c$ (average overestimation equal to 0.03) and attribute this effect to the slight overestimation of the source duration (see Section 2.2), which may cause some late signals in the RSTFs.

After correction of the $M_w - \delta$ trade-off, the main remaining differences may also be explained. Only two earthquakes show a difference between M_w^d and $M_w'^c$ larger than 0.09: the 1996 Minahassa earthquake (event 5) and the 2007 Peru earthquake event 14. For the first one, the dip determined by GCMT is very small (6°) so that $M_w'^c$ is very sensitive to δ^d. Taking δ^d equal to 10°, which is a value inside the uncertainties we estimated, would make M_w^d and $M_w'^c$ consistent. The 2007 Peru earthquake is a long-duration earthquake with respect to its magnitude (see Table 2). This suggests that the choice of a magnitude-dependent half-duration causes the GCMT solution to underestimate the moment magnitude.

The usual explanation of the underestimation of seismic moment by body-wave analysis invokes low-frequency source processes, which would be better resolved by the lower frequency surface waves. However, there is no real theoretical reason for this assertion, at least when source duration is significantly shorter than the longest

Table 3. Comparison between SCARDEC results and GCMT source parameters. The first column shows the index of each earthquake (see Table 1). Strike (°), dip (°), rake (°), depth (km) and moment magnitude (ϕ, δ, λ, z_c, M_w) are given for both approaches, respectively. We also provide the acceptable ranges for dip, depth and moment magnitude (respectively $\Delta\delta$, Δz_c, ΔM_w) determined by our uncertainty analysis.

	Global CMT					SCARDEC							
n^0	ϕ	δ	λ	z	M_w	ϕ	δ	λ	z	M_w	$\Delta\delta$	Δz	ΔM_w
1	278	7	89	15	7.76	291	10	105	30	7.63	8-12	13-42	7.57–7.70
2	354	22	87	29	8.00	17	24	115	30	8.07	22-25	24-36	8.07–8.07
3	302	9	92	15	7.98	312	20	99	13	7.80	18-23	0-17	7.77–7.82
4	225	12	95	26	7.88	240	21	115	19	7.82	17-25	13-28	7.79–7.86
5	36	6	54	15	7.87	38	15	59	27	7.67	9-19	18-36	7.66–7.71
6	103	11	69	15	8.19	84	15	53	12	8.10	11-18	0-18	8.06–8.14
7	248	17	84	29	7.88	273	25	116	18	7.82	22-31	13-27	7.80–7.85
8	202	23	74	34	7.76	215	20	88	32	7.81	17-23	21-41	7.79–7.83
9	310	18	63	30	8.39	307	29	59	35	8.36	26-33	26-43	8.34–8.37
10	250	11	132	28	8.26	251	22	129	35	8.15	19-25	26-41	8.12–8.16
11	333	8	118	26	8.62	327	14	105	30	8.46	12-17	21-39	8.44–8.47
12	215	15	92	14	8.30	205	17	83	12	8.25	13-19	0-12	8.25–8.28
13	333	37	121	14	8.07	304	33	65	19	8.06	29-35	15-28	8.04–8.09
14	321	28	63	34	7.97	324	28	69	33	8.12	22-33	21-44	8.10–8.14
15	328	9	114	24	8.49	331	16	112	19	8.35	12-20	13-31	8.33–8.39
16	25	26	138	23	7.78	37	29	147	35	7.72	24-34	22-41	7.67–7.74
17	19	18	116	23	8.79	24	21	119	35	8.74	18-25	25-40	8.72–8.74

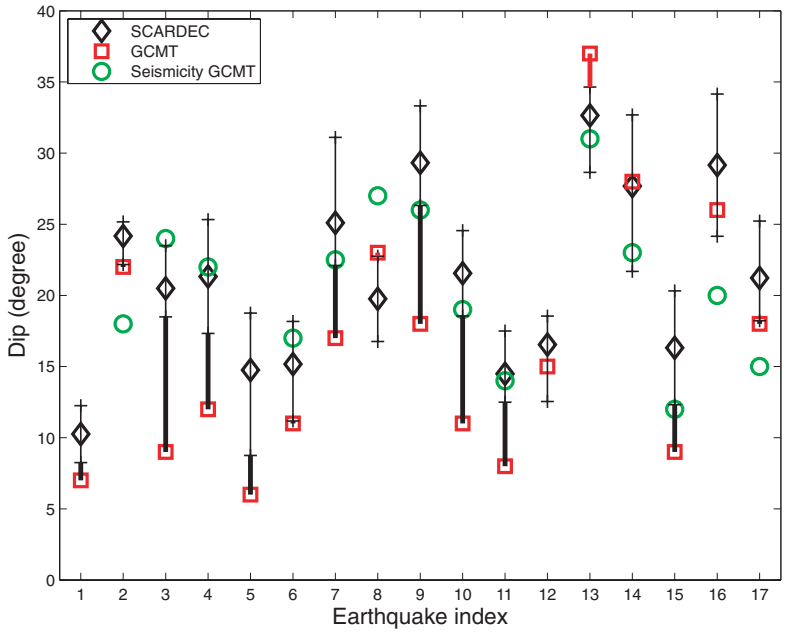

Figure 7. Earthquake fault dip comparisons. For each earthquake (see correspondence between indices and earthquakes in Tables 1 or 2), we show the best dip found by SCARDEC method (black diamond) and by GCMT (red square). Extreme values determined by our uncertainty analysis are shown by the '+' signs, so that the possible dips are along the thin black line joining these '+' signs. When existing, the thick lines indicate the discrepancy between GCMT and SCARDEC dip values; black lines indicate that we retrieve a dip steeper than GCMT, whereas red lines indicate the opposite. Green circles show the median dip values inferred by GCMT for moderate-to-large seismicity in the same region and period of occurrence as the main shock (see Section 5). Three earthquakes do not have enough foreshocks or aftershocks to define this independent information.

period present in the seismograms. If $G_{\phi,\delta,\lambda}(x, z_c, \omega)$ is correctly estimated, the deconvolution of this term from U gives the broad-band RSTF, from which the moment can be directly calculated. Moreover, if this intrinsic underestimation of seismic moment by body waves was true, it would subsist even after the sin 2δ factor correction.

4 AGREEMENT BETWEEN SCARDEC BODY-WAVE SOLUTIONS AND LONG-PERIOD SURFACE WAVE DATA

To further validate the moment magnitudes and focal mechanisms determined in this study it is important to test if they can explain data

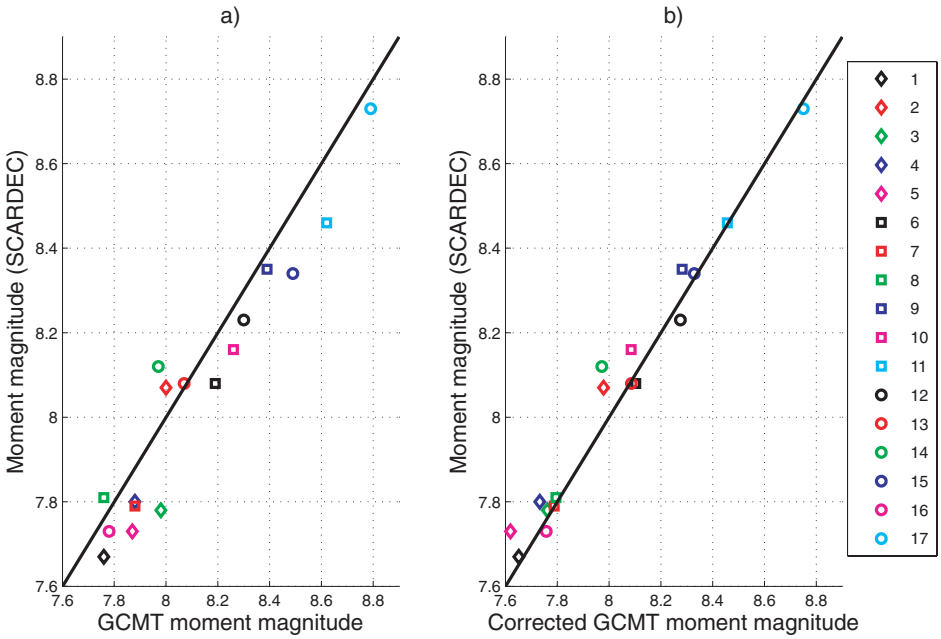

Figure 8. Effect of the $M_w - \delta$ trade-off on the differences in moment magnitude between the GCMT and SCARDEC methods. (a) Direct comparison between the SCARDEC and GCMT moment magnitudes. (b) Comparison between the SCARDEC moment magnitude and the corrected GCMT magnitude, taking into account the $M_w - \delta$ trade-off (see the expression of the corrected magnitude in the main text). The SCARDEC moment magnitude is the magnitude computed for the same depth as GCMT, as explained in the text. In both cases, the black line shows the $x = y$ line, where there is a perfect agreement between both magnitude estimates. The agreement clearly improves when we take into account the trade-off. Each earthquake is represented by a symbol referring to the indices shown in the right part of the figure (see correspondence between earthquakes and indices in Tables 1 or 2).

that were not used to constrain them, notably long-period surface wave data. In this section we compare real long-period surface wave seismograms with theoretical seismograms calculated using our new seismic source parameters.

We calculate synthetic seismograms for long-period ($T \geq 40$ s), three-component fundamental mode, minor-arc, surface waves using a full ray theory approach (e.g. Ferreira & Woodhouse 2007). We use the 3-D mantle model S20RTS (Ritsema *et al.* 1999) combined with the global crust model CRUST2.0 (Bassin *et al.* 2000). We calculate seismograms using different point source models: (i) GCMT source parameters and (ii) the centroid latitude, longitude and origin time reported by the GCMT, the depth as determined in this study and a moment tensor calculated from the seismic moment and fault geometry determined in this study, assuming a pure double-couple mechanism; we consider a variety of possible source models by taking into account the determined uncertainties in depth, dip and moment magnitude (see Section 2.4.2) and refer to them as SCARDEC models. In both cases, a triangular STF is used with a half-duration as reported in the GCMT catalogue.

To test how well these different seismic source models explain long-period surface waves, we compare the synthetic seismograms with real broad-band data from the FDSN. Instrument response deconvolution is conducted on the seismograms and the horizontal components are rotated into longitudinal and transverse directions for each earthquake. The data are convolved with the response of an SRO instrument and low-pass cosine tapered to capture the low-frequency characteristics of the signal (typically between $T =$ 150–200 s, depending on the particular earthquake).

Figs 9 and 10 compare synthetic seismograms (red, green) with real data (black) recorded at various stations from the FDSN, following the 2003 September 25 Hokkaido earthquake (see earthquake number 10 in Table 3 of this paper). For this earthquake, SCARDEC predicts a steeper fault than in the GCMT model by $8^\circ - 14^\circ$ and a moment magnitude of $M_w = 8.12 - 8.16$ rather than the magnitude $M_w = 8.26$ reported in the GCMT catalogue. The synthetics in red are calculated for the GCMT source model, whereas the synthetics in green correspond to a SCARDEC model with the optimal strike, dip and rake, with a depth of 41 km and a magnitude of 8.12. The synthetic seismograms calculated using the SCARDEC source model explain the phase of the long-period Rayleigh waves as well as the GCMT model. Moreover, for Rayleigh waves, the SCARDEC model explains the amplitude data slightly better than the GCMT model, notably for stations WVT, KIP, PPT, COCO and PALK (Fig. 9). For Love waves, the GCMT model explains the data slightly better than the SCARDEC model, particularly for stations RAR, ARU, MLR and MORC (Fig. 10).

We quantify the fit between synthetics and data by measuring both phase shifts and amplitude ratios between synthetic and real surface wave data in the time domain. A time window is selected centred on the maximum amplitude of the desired wave train, with its edges at zero-crossings of the seismograms, to minimise errors in the measurements. A non-linear least-squares algorithm calculates the phase shift and amplitude factor that best fits the synthetic waveform to the real seismogram. Moreover, we calculate the waveform misfit $m^2 = \frac{(\mathbf{s}-\mathbf{d})^2}{\mathbf{d}^T\mathbf{d}}$ also in the time domain, where $\mathbf{s}$ are the theoretical seismograms and $\mathbf{d}$ are the data. Table 4 shows the average phase,

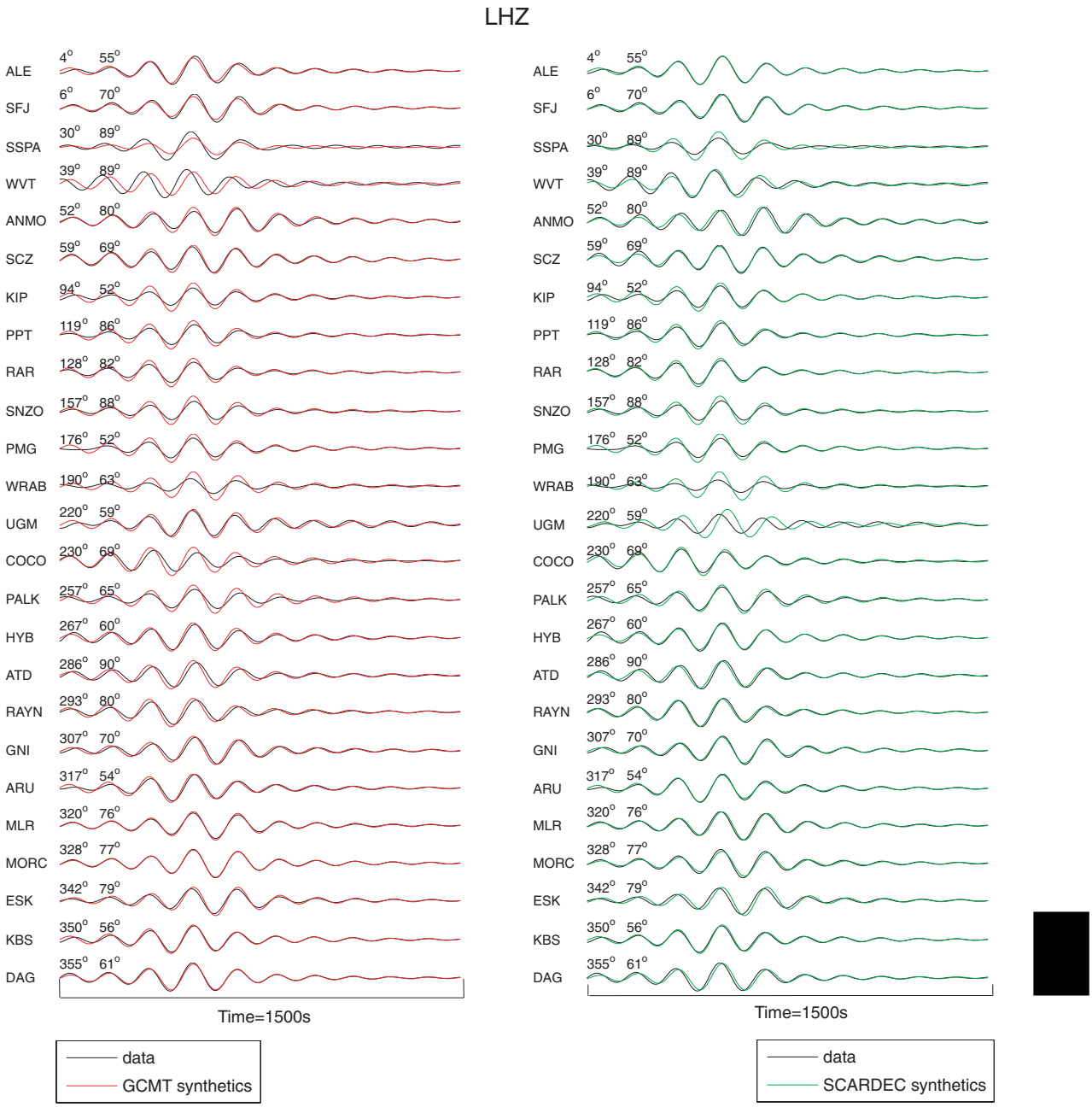

Figure 9. Comparison of vertical component observed Rayleigh waves (black) with theoretical seismograms (red, green) at various stations of the FDSN, following the 2003 Hokkaido earthquake. The name of each station is shown in the left of the waveforms and the corresponding source–receiver azimuth and epicentral distance are shown in the top, respectively. The synthetic seismograms are calculated for the earthquake source parameters in the GCMT catalogue (red) and for the parameters in the SCARDEC model (green; see main text for details). All traces have been deconvolved from instrumental response followed by convolution with the response of an SRO instrument and low-pass cosine tapered around T = 150 s.

amplitude and waveform misfits between data and synthetics over all the stations, for the GCMT and SCARDEC source models for the 2003 Hokkaido earthquake. It is clear that the differences in misfits are small, so that overall the GCMT and SCARDEC source models explain the long-period surface wave data equally well. Thus, for the Hokkaido earthquake, a source model with a fault dip angle of 11° and moment magnitude $M_w = 8.26$ (as in the GCMT catalogue) is as compatible with long-period surface waves as a fault

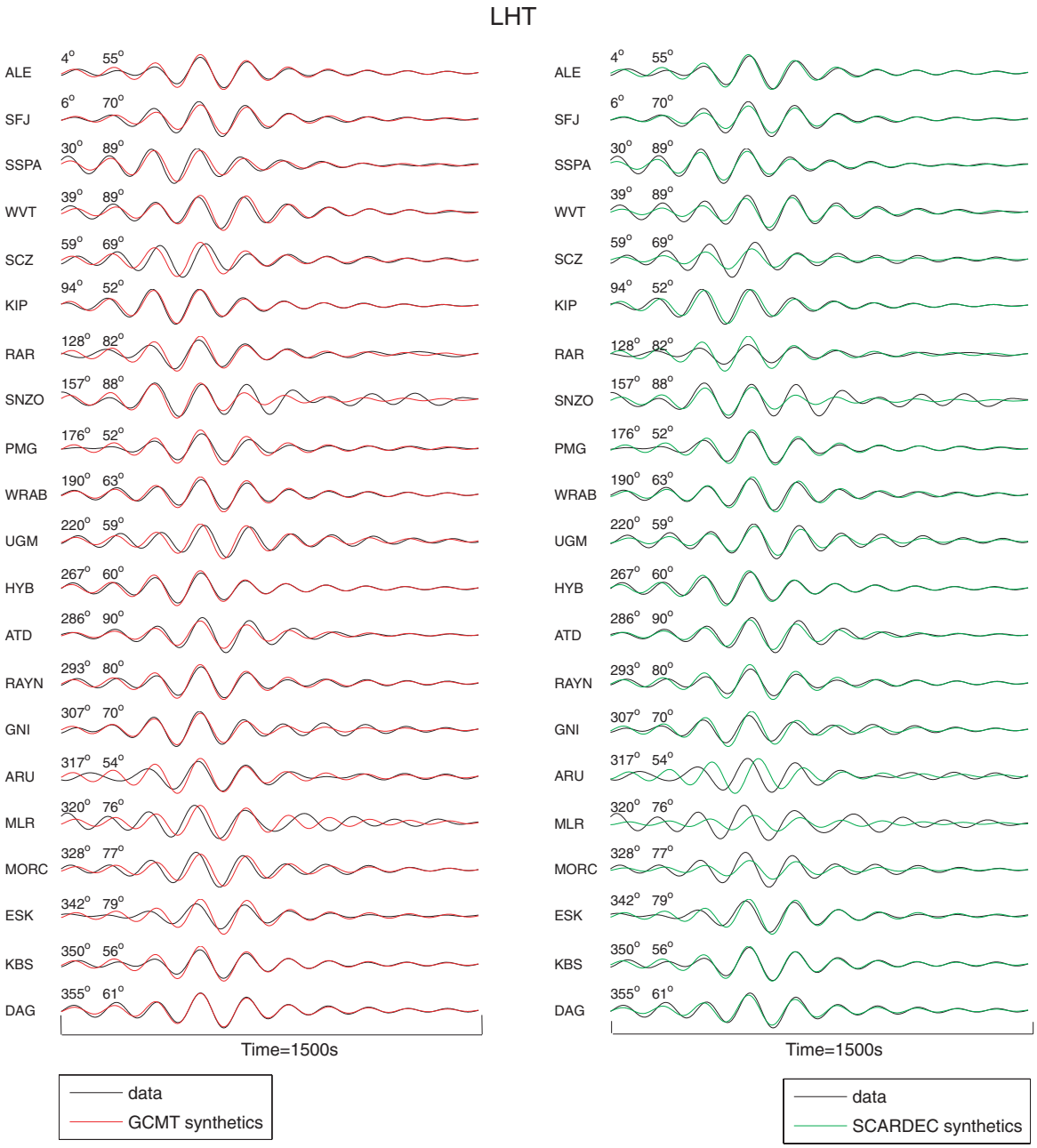

Figure 10. Same as in Fig. 9, but for transverse component Love waves.

dip angle of 22° together with a moment magnitude of $M_w = 8.12$. This clearly illustrates the trade-off between the fault's dip angle and the seismic moment for shallow earthquakes when determining these parameters using long-period surface waves, as explained in previous sections. To further verify our comparisons, we also calculated theoretical seismograms using the spectral element method (Komatitsch & Tromp 2002) for the GCMT and SCARDEC source models and compared them with real data, obtaining very similar results to those for full ray theory synthetics.

We carried out these comparisons between real data and synthetics for all the studied earthquakes for which the GCMT parameters are not within the range of acceptable moment magnitude and/or fault dip determined in this study. We found that in all cases the conclusions were similar to those for the 2003 Hokkaido earthquake,

Table 4. Average of phase ($\delta\psi$), amplitude (δA) and waveform (m^2) misfits between three-component long-period surface wave synthetic seismograms and data for the stations in Figs 9–10, for the source models GCMT and SCARDEC for the 2003 September 25 Hokkaido earthquake (see text for details). Perfect fit corresponds to $\delta\psi = 0\ \ s$, $\delta A = 1$ and $m^2 = \frac{(\mathbf{s}-\mathbf{d})^2}{\mathbf{d}^T\mathbf{d}} = 0$, where **s** are the theoretical seismograms and **d** are the data.

	$\delta\psi$ (s)		δA		m^2	
	GCMT	SCARDEC	GCMT	SCARDEC	GCMT	SCARDEC
Z	6.7	6.3	0.89	0.90	0.15	0.16
L	6.8	5.9	0.91	0.97	0.10	0.08
T	8.1	8.6	0.98	1.18	0.12	0.13

Table 5. Same as in Table 4, but for the 2005 March 28 Sumatra earthquake (see text for details).

	$\delta\psi$ (s)		δA		m^2	
	GCMT	SCARDEC	GCMT	SCARDEC	GCMT	SCARDEC
Z	11.4	10.8	0.79	0.98	0.23	0.20
L	12.0	10.4	0.81	0.89	0.35	0.25
T	7.7	8.2	0.81	0.99	0.30	0.32

that is, overall the earthquake source parameters determined in this study explain long-period surface waves as well as the parameters reported in the GCMT catalogue. We show a second example of long-period surface wave comparisons for the 2005 March 28 Sumatra earthquake (see earthquake number 11 in Table 3 of this paper). Supplementary Figs 17 and 18 show waveform comparisons between GCMT synthetics and those calculated using the best-fitting SCARDEC model, and the corresponding misfits are presented in Table 5. The SCARDEC model explains the phase data as well as the GCMT model, with a slight overall improvement in the amplitude fit as shown in Table 5. This better agreement can be seen, for example, for Rayleigh waves recorded at stations ANTO, ECH and ESK and for Love waves recorded at stations ESK, OBN and KBS (Supplementary Figs 17 and 18). This shows that the optimal moment magnitude $M_w = 8.46$ for the 2005 March 28 Sumatra earthquake determined in this study is as compatible with long-period surface wave data as the larger moment magnitude $M_w = 8.62$ reported in the GCMT catalogue, despite of the fact that long-period surface waves are not used in this study to retrieve earthquake moment magnitude and focal mechanism.

5 DIP AND MAGNITUDE OF MAJOR SUBDUCTION EARTHQUAKES

We have shown in the two previous sections that the source parameters deduced from a broad range of body waves (including *P, PcP, PP*, *SH* and *ScS* waves) explain long-period surface waves as well as the GCMT source parameters. In this section, we compare our results with other sources of information available for these major earthquakes.

In the list of the studied earthquakes, the 2003 Hokkaido earthquake is by far the best instrumented event. A dense array of accelerometers and GPS, located along the Japan coast, recorded well the local ground motion. Several studies used these data to provide independent estimates of magnitude and focal mechanism. Yagi (2004) used both teleseismic and strong motion data to determine a moment magnitude $M_w = 8.0$ associated with a dip of 20°. Using only strong motion data, Honda *et al.* (2004) have found a similar mechanism, with a dip of 18°. Koketsu *et al.* (2004) have successfully modelled both strong motion and GPS data using the 20° dip retrieved by Yamanaka & Kikuchi (2003). Miyazaki *et al.* (2004) analysed only high rate GPS data and have also found a dip equal to 20° and a moment magnitude of 8.1. In all these studies, only Honda *et al.* (2004) found a moment magnitude close to GCMT ($M_w = 8.25$). All the other analyses have determined a moment magnitude between 8 and 8.15. We also have information on the interplate geometry based on aftershock relocation. Using OBS data, Machida *et al.* (2009) have simultaneously estimated the aftershock hypocentres and the local 3-D velocity model. This analysis reveals that the angle of the dipping plate is equal or steeper than 16° in the source area of the 2003 earthquake. Gathering the available information, we find a magnitude-dip couple closer to the SCARDEC results ($M_w = 8.14 \pm 0.02$; $\delta = 22 \pm 3°$) than to the GCMT parameters ($M_w = 8.26$; $\delta = 11°$).

To a lesser extent, there is also interesting independent information for the 2005 Sumatra (Nias) earthquake. This earthquake was recorded by continuous GPS located in Sumatra and in islands (Simeulue, Nias) above the rupture plane. There are also data coming from coral uplifts. Konca *et al.* (2007) used GPS and coral data together with teleseismic waves (body waves and normal modes) to determine the rupture process of the 2005 Sumatra earthquake. These authors suggest that the combination of normal mode and geodetic data gives a good resolution on the magnitude-dip couple. Once possible ranges of magnitude and dip angle are estimated by normal-mode data analysis, geodetic data are used to determine the most appropriate magnitude value, which suppresses the $M_w - \delta$ trade-off. A drawback of this approach is that the rigidity structure around the earthquake fault must be well known, which is generally difficult in remote subduction zones. Konca *et al.* (2007) report that a fault plane with dip equal or steeper than 12° would lead to a too small magnitude to explain the geodetic data. However when looking at their selected rigidity structure, we observe that most part of the coseismic slip is located below 22 km depth, in a region where the rigidity is high (68.5 GPa, typical of upper-mantle values). However, it is very likely that for a major interplate earthquake, the rigidity is actually between crustal (∼30 GPa) and upper-mantle values. Thus, the rigidity selected by Konca *et al.* (2007) is probably an upper bound of the realistic rigidity. Choosing smaller rigidity values would make steeper dips acceptable. Interestingly, Kreemer *et al.* (2006) have also analysed the coseismic GPS displacements to retrieve the coseismic slip on the fault. In their fault geometry model, they allow the dip to vary from 8° at the surface to 23° at 50 km depth. They can explain well the GPS vectors with a moment magnitude of 8.37, calculated in a medium with a crustal rigidity of 30GPa. This moment magnitude would be equal to 8.61 in a 68.5 GPa rigidity structure, which agrees with the results of Konca *et al.* (2007). These two studies show that SCARDEC results for the 2005 Sumatra earthquake ($M_w = 8.45 \pm 0.02$; $\delta = 15 \pm 3°$) are realistic.

For the other earthquakes (Jalisco 1995, Kuril 1995, Minahassa 1996, Andreanof 1996, Peru 2001 and Sumatra 2007) where we obtain clear differences with GCMT, there are fewer independent estimates of the moment magnitude. For the first five ones, we can mainly compare our results with other studies analysing teleseismic body waves. Interestingly, most studies that refine the GCMT mechanism using their own modelling generally obtain steeper dips than GCMT. This is the case of the study of Mendoza & Hartzell (1999) for the 1995 Jalisco earthquake in which they found that a dip of 14° explains data better that the 9° GCMT value. Similarly, Shao

& Ji (2007) have modelled the 1995 Kuril earthquake with a dip of 18° (to be compared to the 12° GCMT value). The optimal focal mechanism of Kisslinger & Kikuchi (1997) for the 1996 Andreanof earthquake also shows a steeper dip than GCMT (21° versus 17°). For the 1996 Minahassa earthquake, the difference between the dip determined by Gomez *et al.* (2000), equal to $7 \pm 3°$, and GCMT (6°) is small. The 2001 Peru earthquake dip was found steeper than GCMT by Kikuchi & Yamanaka (2001) and Bilek & Ruff (2002) (respectively, by 3° and 5°). A counterexample exists for this 2001 Peru earthquake, where Giovanni *et al.* (2002) have assumed a dip of 14° (compared to the GCMT value of 18°), but without detailing the reason of this choice. The 2007 Sumatra earthquake has been analysed both with geodetic and teleseismic data. Yagi (2007) used teleseismic data, obtaining a dip of 18°, which is twice the GCMT dip value. Konca *et al.* (2008) have successfully modelled teleseismic and geodetic data with a 15° dip plane. The same dip value has been retrieved by Yamanaka (2007). Among the studies of these six earthquakes, the study of Bilek & Ruff (2002) for the 2001 Peru earthquake is the only one to find a moment magnitude very close to GCMT. All other analyses have determined a moment magnitude 0.05–0.28 smaller than GCMT.

A last external information comes from the focal mechanisms of moderate-to-large earthquakes ($5.5 < M_w < 7.2$) occurring in the vicinity of the main shocks. In this magnitude range, GCMT makes also use of body waves so that the $M_w - \delta$ trade-off reduces. Hjörleifsdóttir & Ekström (2010) have recently confirmed, using synthetic data computed in a realistic Earth, that GCMT results are close to the real source parameters when both body and surface waves are used. Assuming that thrusting foreshocks and aftershocks occur on the same interplate plane as the main shock, we get another independent information on the fault geometry. For each of the large subduction earthquakes studied, we retrieve in the GCMT catalogue the earthquakes satisfying the following criteria (z_m is the centroid depth of the main shock):

(1) thrust mechanism,
(2) moment magnitude between 5.5 and 7.2,
(3) origin time between 1 month before the main shock and 3 months after the main shock,
(4) epicentral location within two degrees in latitude and longitude compared to the main shock's centroid and
(5) depth larger than $(z_m - 20)$ km and smaller than $(z_m + 5)$ km.

This last criterion has been selected to exclude earthquakes considerably deeper than the main shocks, for which it can be argued that their steeper dips are simply due to the bending at depth of the subducting plate. Considering this same bending plate hypothesis, we would expect that this dissymmetric depth criterion would lead to some underestimation of the main shock dip. If, for a given earthquake, the selection includes at least two earthquakes, we take the median dip value (noted δ_a) as an estimate of the local fault geometry. Three earthquakes (Java 1994, Minahassa 1996 and Kuril 2006) have at most one suitable foreshock or aftershock and thus cannot be considered here. The median values δ_a for all other studied earthquakes have been represented in Fig. 7 (green circles), along with the GCMT main shock dip (red squares). For nine over 14 earthquakes, δ_a is found steeper than the GCMT main shock dip, in spite of the dissymmetric depth criterion. The average difference between δ_a and GCMT dip is 6.4°, while the difference between δ_a and the SCARDEC dip is only 3.9°. These independent sources of information support the idea that the fault's dip angle determination in this study is more precise than the one of GCMT.

6 DISCUSSION AND PERSPECTIVES

6.1 Advantages of the SCARDEC method

Our body-wave deconvolutive approach allows us to determine both quickly and reliably the moment magnitude of major earthquakes. The method is automated, with two main steps. First the source duration is estimated based on the high-frequency content of teleseismic body waves, and then the optimization process of stabilized RSTFs gives us access to the moment magnitude, as well as to the focal mechanism and depth of the earthquake. The resolution of these earthquake parameters is enhanced by using a broad range of teleseismic waves (*P, PcP, PP, S, ScS*). These waves also have the advantage of arriving within a 30-min interval following the event origin. The entire inversion process requires less than 30 min on a simple computer with a 2.33 GHz processor. The parallelized version of the SCARDEC method, done on a 16-core machine, reduces this time to less than 5 min. Using the real-time transmission available for most of the FDSN data, a SCARDEC solution can therefore be obtained 35 min after the earthquake's occurrence.

As the SCARDEC method does not make the assumption that the STF is the same at each teleseismic station, it is better adapted to large earthquakes than most of the automated techniques used to analyse source parameters of distant events. Compared to extended source methods (Olson & Apsel 1982; Hartzell & Heaton 1983), it presents the advantage that no constraints are imposed on the spatio-temporal complexity of the rupture process. For example, the rupture velocity regimes, the shape of the local STF or the slip roughness do not enter in the parametrization of the inversion. This last point can also explain why the method should not be subject to underestimation of the moment magnitude. Because the shape of the STF is free for each station, the deconvolution transfers the whole waveform energy to the STF. The method does not suffer from inappropriate parametrization of the source process which could impede the modelling of some features of the waveforms and could result in a smaller moment magnitude.

In addition to arriving faster than surface waves, body waves are not sensitive to the magnitude-dip trade-off that affects shallow earthquake determinations using surface waves. This explains why we have found for some earthquakes values of magnitude and dip different from GCMT. Though different, we show that the values agree well after correcting the GCMT parameters for the existing trade-off. We have confirmed by forward modelling that SCARDEC parameters explain long-period surface waves as well as GCMT parameters. Other independent information, including studies analysing geodetic data or focal mechanisms of moderate seismicity, also support our findings. For about half of the large subduction earthquakes studied here, the magnitude-dip trade-off seems to cause the GCMT method to preferentially underestimate the dip and overestimate the seismic moment than the opposite. The two earthquakes for which we obtain the most convincing evidence of this behaviour are the 2003 Hokkaido and the 2005 Sumatra earthquakes. In both cases our estimate of the seismic moment is smaller (M_w reduced by 0.1–0.18) than the GCMT value.

The accurate determination of seismic moment of major earthquakes provides valuable information both for a better anticipation of the consequences of these events (e.g. for tsunami alert) and as a first-order parameter for more detailed earthquake source process studies. It also has an important role in assessing the balance between seismic and aseismic deformation in the Earth, because this balance is strongly influenced by the largest earthquakes. Considering all the earthquakes analysed here, we find that their cumulative

seismic moment deduced from SCARDEC solutions is about 25 per cent smaller than the one inferred from GCMT catalogue. As a result, the part of the aseismic processes (creep, silent earthquakes) in the global deformation processes is expected to be larger.

In this study, we have applied the SCARDEC method to the major subduction earthquakes. However the use of the method is not limited to this tectonic setting or to very large earthquakes. Without any modification, we apply the SCARDEC method to the recent earthquakes with magnitudes larger than $M_w = 6.8$. Results for the most significant events can be seen in the webpage http://geoazur.oca.eu/spip.php?rubrique57. For smaller earthquakes (down to magnitude 6), the method can also be used but requires two modifications. First, data filtering has to be changed because low frequencies are little excited by moderate earthquakes. As an example, we have analysed the $M_w = 6.3$ Aquila earthquake (Italy, 2009 April 06) in the 0.0125–0.1 Hz frequency band. Second, the automatic determination of the source duration T_d (see Section 2.2) gives values longer than the actual duration. This is due to the larger number of noisy stations and also to the fact that *P*-coda affects proportionally more the short duration source signals than the longer ones. This duration has thus to be determined either by signal inspection or as a function of the earthquake magnitude.

6.2 Source time function properties

In the SCARDEC method, we use primarily the physical constraints of the RSTFs as efficient criteria to optimize the focal mechanism and depth. However once the optimal parameter set is retrieved, the obtained RSTFs themselves provide valuable information on the earthquake rupture process. At the first order, we can observe for each earthquake the common features of all the RSTFs. In the analysed frequency band (0.005–0.03 Hz), some of the earthquakes have a simple moment release distribution (e.g. the Hokkaido earthquake; see Fig. 5), while other earthquakes are shown to be more complex, such as, for example, the Peru 2001 and 2007 earthquakes (Supplementary Figs 9 and 13). Both these earthquakes show two main episodes of moment release, which is confirmed by other analyses. More precisely, it is well known that the RSTFs give robust information on the preferential direction of the rupture propagation (e.g. Velasco *et al.* 1994); RSTFs tend to have shorter durations and higher amplitudes in the rupture propagation direction. This shows us, for example, that the 1995 Jalisco earthquake propagated in the northwest direction (Supplementary Fig. 3), while the 2001 Peru earthquake propagated in the southeast direction (Supplementary Fig. 9).

These source characteristics can be analysed more quantitatively when looking at higher frequency RSTFs. This can be done by a simple extension of the SCARDEC method. Once the optimal parameter set is determined, we can deconvolve both compressive and transverse body waves in a broader frequency range. To do so, we reduce the standard error of the Gaussian function f_g (eq. 8) and keep the same high-pass filtering corner (0.005 Hz). Using a standard error of 0.27 s, we can now retrieve RSTFs in a broad frequency range (0.005–0.5 Hz). Fig. 11 shows these broad-band RSTFs obtained for the 2003 Hokkaido earthquake. These RSTFs can be seen

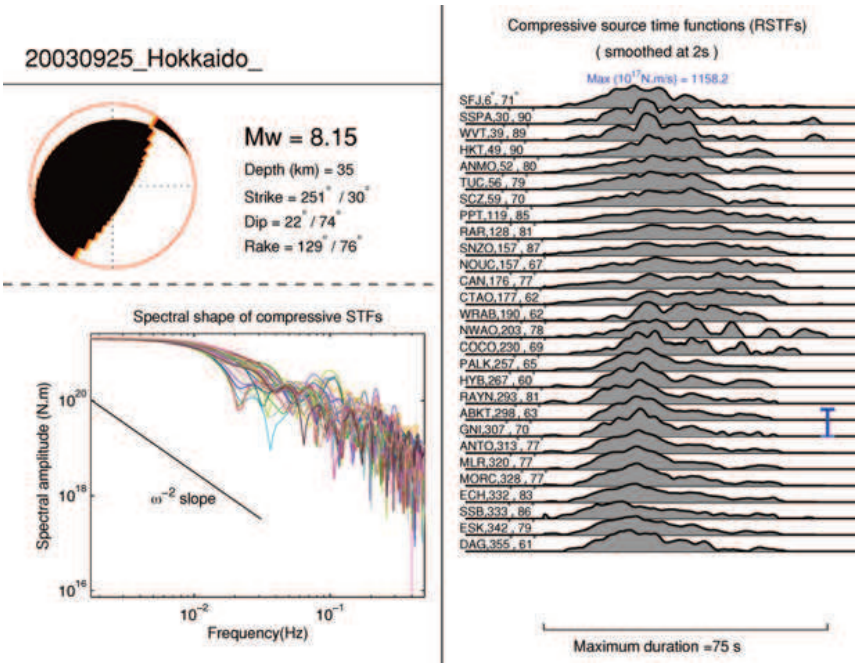

Figure 11. Broad-band RSTFs for the 2003 Hokkaido earthquake, in the time and frequency domains. (Top left-hand side) Optimal values of moment magnitude, depth and focal mechanism. (Bottom left-hand side) Spectrum of the broad-band compressive waves RSTFs (0.005–0.5 Hz). The classical ω^{-2} slope is shown in the left part of the figure. (Right-hand side) Broad-band RSTFs, in the time domain, for compressive waves. Compared to the RSTFs obtained in Fig. 5, the time properties can now be directly interpreted, because the smoothing time (2 s) is much smaller than the source duration (about 60 s). The indicated maximum value corresponds to the absolute maximum of all the moment rates. The corresponding scale is indicated by the blue bar, which is plotted next to the location of the maximal RSTF. For each RSTF, the name of the station, its azimuth and epicentral distance are presented.

as 'simplified' seismograms, because the source term is still present while most of the propagation term has been removed. These indirect data are thus well adapted for the application of extended source methods (Olson & Apsel 1982; Hartzell & Heaton 1983), to retrieve the rupture process on the earthquake fault. Because the method is automated, another perspective is to systematically analyse the rupture complexity on a large earthquake catalogue. This complexity can be estimated from the shape of the temporal RSTFs (right-hand part of Fig. 11), or from their spectral characteristics (left-hand part of Fig. 11). In the frequency domain, we can compare in particular the frequency decay with the classical ω^{-2} law (Brune 1970). Future applications of the SCARDEC model include the analysis of the diversity of earthquake complexity as a function of the earthquake location, the tectonics environment or the nature of the faults.

ACKNOWLEDGMENTS

We are grateful to the FDSN global network for free access to teleseismic data and to the Wilber II Interface (IRIS) for easy download of these data. We thank the two anonymous reviewers for their interesting comments, and Romain Brossier for helping us with the parallelization of the SCARDEC method. We also thank Jenny Trévisan for helping us with some figures of this manuscript, and Jocelyn Guilbert for making possible an internal contract between CNRS (Centre National de la Recherche Scientifique) and CEA (Commissariat à l′ Energie Atomique). This work has also been supported by the IRD (Institut de la Recherche pour le Développement), the CNRS and the European project SAFER. AMGF and MV thank support from the Alliance: Franco-British Partnership Programme 2010 (Project 10.007). AMGF is grateful to support from the European Commission's Initial Training Network project QUEST (contract FP7-PEOPLE-ITN-2008-238007) and to the High Performance Computing Cluster supported by the Research Computing Service at the University of East Anglia.

REFERENCES

Aki, K. & Richards, P.G., 2002. *Quantitative Seismology,* 2nd Edn, University Science Books, Sausalito, CA.

Ammon, C.J., Kanamori, H., Lay, T. & Velasco, A.A., 2006. The 17 July 2006 Java tsunami earthquake, *Geophys. Res. Lett.,* **33,** L24308, doi:10.1029/2006GL028005.

Bassin, C., Laske, G. & Masters, G., 2000. The current limits of resolution for surface wave tomography in North America, *EOS, Trans. Am. geophys. Un.,* **F897,** 81.

Bertero, M., Bindi, D., Boccacci, P., Cattaneo, M., Eva, C. & Lanza, V., 1997. Application of the projected Landweber method to the estimation of the source time function in seismology, *Inverse Probl.,* **13,** 465–486.

Bilek, S.L. & Ruff, L.J., 2002. Analysis of the June 23, 2001 Mw=8.4 Peru underthrusting earthquake and its aftershocks, *Geophys. Res. Lett.,* **29**(20), 1960, doi:10.1029/2002GL015543.

Bouchon, M., 1976. Teleseismic body wave radiation from a seismic source in a layered medium, *Geophys. J. R. astr. Soc.,* **47,** 515–530.

Brune, J.N., 1970. Tectonic stress and the spectra of seismic shear waves from earthquakes, *J. geophys. Res.,* **75,** 4997–5009.

Chen, T., Newman, A.V., Feng, L. & Fritz, H.M., 2009. Slip distribution from the 1 April 2007 Solomon Islands earthquake: a unique image of near-trench rupture, *Geophys. Res. Lett.,* **36,** L16307, doi:10.1029/2009GL039496.

Dziewonski, A.M., Chou, T.A. & Woodhouse, J.H., 1981. Determination of earthquake source parameters from waveform data for studies of global and regional seismicity, *J. geophys. Res.,* **86,** 2825–2852.

Ferreira, A.M.G. & Woodhouse, J., 2007. Source, path and receiver effects on seismic surface waves, *Geophys. J. Int.,* **168,** 109–232.

Fuchs, K. & Müller, G., 1971. Computation of synthetic seismograms with the reflectivity method and comparison with observations, *Geophys. J. R. astr. Soc.,* **23,** 417–433.

Furlong, K., Lay, T. & Ammon, C., 2009. A great earthquake rupture across a rapidly evolving three-plate boundary, *Science,* **324**(5924), 226–229.

Giovanni, M.K., Beck, S.L. & Wagner, L., 2002. The June 23, 2001 Peru earthquake and the southern Peru subduction zone, *Geophys. Res. Lett.,* **29**(21), 2018, doi:10.1029/2002GL015774.

Goldstein, P. & Dodge, D., 1999. Fast and accurate depth and source mechanism estimation using P-waveform modelling: a tool for special event analysis, event screening, and regional calibration, *Geophys. Res. Lett.,* **26,** 2569–2572.

Gomez, J.M., Madariaga, R., Walpersdorf, A. & Chalard, E., 2000. The 1996 earthquakes in Sulawesi, Indonesia, *Bull. seism. Soc. Am.,* **90,** 739–751.

Hara, T., 2007. Measurement of duration of high-frequency energy radiation and its application to determination of magnitudes of large shallow earthquakes, *Earth Planets Space*, **59,** 227–231.

Hartzell, S.H. & Heaton, T.H., 1983. Inversion of strong ground motion and teleseismic waveform data for the fault rupture history of the 1979 Imperial Valley, California, earthquake, *Bull. seism. Soc. Am.,* **73,** 1553–1583.

Hjörleifsdóttir, V. & Ekström, G., 2010. Effects of three-dimensional Earth structure on CMT earthquake parameters, *Phys. Earth planet. Int.,* **179,** 178–190, doi:10.1016/j.pepi.2009.11.003.

Honda, R., Aoi, S., Morikawa, N., Sekiguchi, H., Kunugi, T. & Fujiwara, H., 2004. Ground motion and rupture process of the 2003 Tokachi-oki earthquake obtained from strong motion data of K-NET and KiK-net, *Earth Planets Space,* **56,** 317–332.

Kanamori, H., 1993. W phase, *Geophys. Res. Lett.,* **20**(16), 1691–1694.

Kanamori, H. & Given, J., 1981. Use of long-period surface waves for rapid determination of earthquake-source parameters, *Phys. Earth planet. Int.,* **27,** 8–31.

Kanamori, H. & Rivera, L., 2008. Source inversion of W phase: speeding up seismic tsunami warning, *Geophys. J. Int.,* **175,** 222–238.

Kennett, B.L.N. & Engdahl, E.R., 1991. Travel times for global earthquake location and phase association, *Geophys. J. Int.,* **105,** 429–465.

Kikuchi, M. & Kanamori, H., 1991. Inversion of complex body waves III, *Bull. seism. Soc. Am.,* **81,** 2335–2350.

Kikuchi, M. & Yamanaka, Y., 2001. EIC Seismological Note N105, Earthquake Information Center, University of Tokyo, http://wwweic.eri.u-tokyo.ac.jp/EIC/EIC_News/105E.html (last accessed 2010 October 29).

Kisslinger, C. & Kikuchi, M., 1997. Aftershocks of the Andreanof Islands Earthquake of June 10, 1996, and local seismotectonics, *Geophys. Res. Lett.,* **24**(15), 1883–1886.

Koketsu, K., Hikima, K., Miyazaki, S. & Ide, S., 2004. Joint inversion of strong motion and geodetic data for the source process of the 2003 Tokachi-oki, Hokkaido, earthquake *Earth Planets Space,* **56**(3), 329–334.

Komatitsch, D. & Tromp, J., 2002. Spectral-element simulations of global seismic wave propagation II. Three-dimensional models, oceans, rotation and self-gravitation, *Geophys. J. Int.,* **150,** 308–318.

Konca, A.O. *et al.*, 2007. Rupture kinematics of the 2005 Mw 8.6 Nias-Simeulue Earthquake from the joint inversion of seismic and geodetic data, *Bull. seism. Soc. Am.,* **97**(1A), S307–S322.

Konca, A.O. *et al.*, 2008. Partial rupture of a locked patch of the Sumatra megathrust during the 2007 earthquake sequence, *Nature,* **456,** 631–635.

Kreemer, C., Blewitt, G. & Maerten, F., 2006. Co- and postseismic deformation of the 28 March 2005 Nias Mw 8.7 earthquake from continuous GPS data, *Geophys. Res. Lett.,* **33,** L07307, doi:10.1029/2005GL025566.

Lay, T. & Wallace, T.C., 1995. *Modern Global Seismology,* Academic Press, San Diego, California.

Lomax, A., 2005. Rapid estimation of rupture extent for large earthquakes: application to the 2004, M9 Sumatra-Andaman mega-thrust, *Geophys. Res. Lett.,* **32,** L10314, doi:10.1029/2005GL022437.

Lomax, A. & Michelini, A., 2009. Mwpd: A duration-amplitude procedure for rapid determination of earthquake magnitude and tsunamigenic potential from *P* waveforms, *Geophys. J. Int.,* **176,** 200–214.

Lomax, A., Michelini, A. & Piatanesi, A., 2007. An energy-duration procedure for rapid determination of earthquake magnitude and tsunamigenic potential, *Geophys. J. Int.,* **170,** 1195–1209, doi:10.1111/j.1365-246X.2007.03469.x

Machida, Y. *et al.*, 2009. Heterogeneous structure around the rupture area of the 2003 Tokachi-oki earthquake (Mw = 8.0), Japan, as revealed by aftershock observations using Ocean Bottom Seismometers, *Tectonophysics,* **465**(1-4), 164–176, ISSN 0040-1951, doi:10.1016/j.tecto.2008.11.009.

Mendoza, C. & Hartzell, S., 1999. Fault-slip distribution of the 1995 Colima-Jalisco, Mexico, earthquake, *Bull. seism. Soc. Am.,* **89,** 1338–1344.

Miyazaki, S. *et al.*, 2004. Modeling the rupture process of the 2003 September 25 Tokachi-Oki (Hokkaido) earthquake using 1-Hz GPS data, *Geophys. Res. Lett.,* **31,** L21603, doi:10.1029/2004GL021457.

Müller, G., 1985. The reflectivity method: a tutorial, *J. Geophys.,* **58,** 153–174.

Nabelek, J.L., 1984. Determination of earthquake source parameters from inversion of body waves, *Ph.D. Dissertation*, 361 pp., Mass. Inst. of. Technol., Cambridge

Ni, S., Kanamori, H. & Helmberger, D., 2005. Energy radiation from the Sumatra earthquake, *Nature*, **434**(7033), 582–582.

Olson, A.H. & Apsel, R.J., 1982. Finite fault and inverse theory with applications to the 1979 Imperial Valley earthquake, *Bull. seism. Soc. Am.,* **72,** 1969–2001.

Ritsema, J., van Heijst, H. & Woodhouse, J., 1999. Complex shear wave velocity structure imaged beneath Africa and Iceland, *Science*, **286,** 1925–1928.

Ruff, L.J. & Miller, A.D., 1994. Rupture process of large earthquakes in the northern Mexico subduction zone, *Pure appl. Geophys.,* **142,** 101–172.

Sambridge, M., 1999. Geophysical inversion with a neighbourhood algorithm. I. Searching a parameter space, *Geophys. J. Int.,* **138,** 479–494.

Shao, G. & Ji, C., 2007. Preliminary result of the Dec 3, 1995 Mw 7.81 Kuril Earthquake, http://www.geol.ucsb.edu/faculty/ji/big_earthquakes/1995/12/smooth/1995kuril.html (last accessed 2010 October 29).

Tsuboi, S., Abe, K., Takano, K. & Yamanaka, Y., 1995. Rapid determination of Mw from broadband P waveforms, *Bull. seism. Soc. Am.,* **83,** 606–613.

Vallée, M., 2004. Stabilizing the empirical Green function analysis: development of the projected Landweber method, *Bull. seism. Soc. Am.,* **94,** 394–409.

Vallée, M. & Bouchon, M., 2004. Imaging coseismic rupture in far field by slip patches, *Geophys. J. Int.,* **156,** 615–630.

Vallée, M., Bouchon, M. & Schwartz, S.Y., 2003. The 13 January 2001 El Salvador earthquake: a multidata analysis, *J. geophys. Res.,* **108**(B4), 2203, doi:10.1029/2002JB001922.

Velasco, A.A., Ammon, C.J. & Lay, T., 1994. Empirical Green function deconvolution of broadband surface waves: rupture directivity of the 1992 Landers, California (Mw = 7.3) earthquake, *Bull. seism. Soc. Am.,* **84,** 735–750.

Yagi, Y., 2004. Source rupture process of the 2003 Tokachi-oki earthquake determined by joint inversion of teleseismic body wave and strong ground motion data, *Earth Planets Space,* **56** (3), 311–316.

Yagi, Y., 2007. The 2007/09/12 Sumatra earthquake, http://www.geo.tsukuba.ac.jp/press_HP/yagi/EQ/20070912 (last accessed 2010 October 29).

Yamanaka, Y., 2007. The South Sumatra (07/09/12) earthquake, http://www.seis.nagoya-u.ac.jp/sanchu/Seismo_Note/2007/070912.jpg (last accessed 2010 October 29).

Yamanaka, Y. & Kikuchi, M., 2003. Source process of the recurrent Tokachi-oki earthquake on September 26, 2003, inferred from teleseismic body waves, *Earth Planets Space,* **55,** e21–e24.

SUPPORTING INFORMATION

Additional Supporting Information may be found in the online version of this article:

Figure S1. Results for the 1994 Java earthquake. (Top panel) Focal mechanism, depth, magnitude, uncertainties and RSTFs. See Fig. 5 for more details. (Bottom panel) Agreement between data and synthetics, see Fig. 6 for more details.

Figure S2. Results for the 1995 Chile earthquake. (Top panel) Focal mechanism, depth, magnitude, uncertainties and RSTFs. See Fig. 5 for more details. (Bottom panel) Agreement between data and synthetics, see Fig. 6 for more details.

Figure S3. Results for the 1995 Jalisco earthquake. (Top panel) Focal mechanism, depth, magnitude, uncertainties and RSTFs. See Fig. 5 for more details. (Bottom panel) Agreement between data and synthetics, see Fig. 6 for more details

Figure S4. Results for the 1995 Kuril earthquake. (Top panel) Focal mechanism, depth, magnitude, uncertainties and RSTFs. See Fig. 5 for more details. (Bottom panel) Agreement between data and synthetics, see Fig. 6 for more details.

Figure S5. Results for the 1996 Minahassa earthquake. (Top panel) Focal mechanism, depth, magnitude, uncertainties and RSTFs. See Fig. 5 for more details. (Bottom panel) Agreement between data and synthetics, see Fig. 6 for more details.

Figure S6. Results for the 1996 Irian-Jaya earthquake. (Top panel) Focal mechanism, depth, magnitude, uncertainties and RSTFs. See Fig. 5 for more details. (Bottom panel) Agreement between data and synthetics, see Fig. 6 for more details.

Figure S7. Results for the 1996 Andreanof earthquake. (Top panel) Focal mechanism, depth, magnitude, uncertainties and RSTFs. See Fig. 5 for more details. (Bottom panel) Agreement between data and synthetics, see Fig. 6 for more details.

Figure S8. Results for the 1997 Kamtchatka earthquake. (Top panel) Focal mechanism, depth, magnitude, uncertainties and RSTFs. See Fig. 5 for more details. (Bottom panel) Agreement between data and synthetics, see Fig. 6 for more details.

Figure S9. Results for the 2001 Peru earthquake. (Top panel) Focal mechanism, depth, magnitude, uncertainties and RSTFs. See Fig. 5 for more details. (Bottom panel) Agreement between data and synthetics, see Fig. 6 for more details.

Figure S10. Results for the 2005 Sumatra earthquake. (Top panel) Focal mechanism, depth, magnitude, uncertainties and RSTFs. See Fig. 5 for more details. (Bottom panel) Agreement between data and synthetics, see Fig. 6 for more details.

Figure S11. Results for the 2006 Kuril earthquake. (Top panel) Focal mechanism, depth, magnitude, uncertainties and RSTFs. See Fig. 5 for more details. (Bottom panel) Agreement between data and synthetics, see Fig. 6 for more details.

Figure S12. Results for the 2007 Solomon earthquake. (Top panel) Focal mechanism, depth, magnitude, uncertainties and RSTFs. See Fig. 5 for more details. (Bottom panel) Agreement between data and synthetics, see Fig. 6 for more details.

Figure S13. Results for the 2007 Peru earthquake. (Top panel) Focal mechanism, depth, magnitude, uncertainties and RSTFs. See Fig. 5 for more details. (Bottom panel) Agreement between data and synthetics, see Fig. 6 for more details.

Figure S14. Results for the 2007 Sumatra earthquake. (Top panel) Focal mechanism, depth, magnitude, uncertainties and RSTFs. See Fig. 5 for more details. (Bottom panel) Agreement between data and synthetics, see Fig. 6 for more details.

Figure S15. Results for the 2009 New-Zealand earthquake. (Top panel) Focal mechanism, depth, magnitude, uncertainties and RSTFs. See Fig. 5 for more details. (Bottom panel) Agreement between data and synthetics, see Fig. 6 for more details.

Figure S16. Results for the 2010 Chile earthquake. (Top panel) Focal mechanism, depth, magnitude, uncertainties and RSTFs. See Fig. 5 for more details. (Bottom panel) Agreement between data and synthetics, see Fig. 6 for more details.

Figure S17. Comparison of vertical component observed Rayleigh waves (black) with theoretical seismograms (red, green) at various stations of the FDSN, following the 2005 March 28 Sumatra earthquake. The name of each station is shown in the left of the waveforms and the corresponding source–receiver azimuth and epicentral distance are shown in the top, respectively. The synthetic seismograms are calculated for the earthquake source parameters in the GCMT catalogue (red) and for the parameters in the SCARDEC model (green; see main text for details). All traces have been low-pass cosine tapered around $T = 200$ s.

Figure S18. Same as in Supplementary Fig. 17, but for transverse component Love waves.

Please note: Wiley-Blackwell are not responsible for the content or functionality of any supporting materials supplied by the authors. Any queries (other than missing material) should be directed to the corresponding author for the article.

I.3.3 Validations de la méthode SCARDEC

Dans l'article précédent, plusieurs validations partielles de la méthode SCARDEC ont été effectuées. En particulier, nous avons pu montrer que les différences observées avec Global CMT ne contredisent pas les ondes de surface, qui ne sont pourtant pas utilisées dans la méthode SCARDEC. Par ailleurs, des informations externes sur les séismes analysés (études spécifiques de chacun des séismes, compatibilité avec la sismicité proche de plus faible magnitude) tendent à supporter les valeurs de dip, magnitude et profondeurs déterminés par la méthode SCARDEC.

Une validation plus poussée peut être faite à partir de l'application de la méthode SCARDEC à des séismes synthétiques, dont les ondes sont simulées dans des modèles de Terre réalistes. La solution étant connue, cette approche nous permet d'estimer la précision de la méthode. Cette validation a été faite en collaboration avec Ana Ferreira (UEA, Norwich, Angleterre) qui a choisi ou construit les modèles de source, puis simulé les ondes dans une Terre tri-dimensionnelle par la méthode SPECFEM (*Komatitsch et al.*, 2002). Le modèle de Terre utilisé dans les tests suivant est S20RTS (*Ritsema et al.*, 1999), couplé avec le modèle de croute CRUST2.0 (*Bassin et al.*, 2000). La méthode SCARDEC a été appliquée en « aveugle », avec des informations similaires à celles que l'on possède 30 minutes après un séisme : les formes d'ondes à toutes les stations télésismiques jusqu'à l'arrivée de l'onde SS, la localisation épicentrale, et la profondeur du séisme avec une incertitude de 20km. La différence principale avec le cas réel est la détermination de la durée de la source. Dans le cas de données réelles, la méthode utilise le contenu haute-fréquence (autour de 1–3Hz) de l'onde P pour estimer la durée de source. Ici, les hautes fréquences ne sont pas simulées de manière réaliste par la méthode SPECFEM, ce qui conduit à imposer cette durée selon le modèle de source testé. Je présente maintenant deux cas de complexité croissante. Pour des raisons de clarté, je commence par décrire les modèles de source, même si, chronologiquement, ils n'ont été confrontés aux résultats de SCARDEC que dans un second temps.

Dans le premier cas, le séisme est simulé par 6 points source le long de la côte Equateur-Colombie. Le mécanisme de chacun de ces points est fixe mais la profondeur et le moment sismique varient (voir Figure I.4a)). Le déclenchement temporel de chacun de ces points reproduit une rupture unilatérale vers le Nord sur environ 200km (Figure 1.4). La solution SCARDEC est présentée dans les figures I.5, I.6, et I.7. La figure I.5 montre le mécanisme et la profondeur optimaux, ainsi que l'incertitude sur la profondeur et le dip. L'accord aux « données » est également visible. En considérant les barres d'erreur, le dip, la magnitude et la profondeur sont très proches du modèle d'entrée. Le strike et le rake présentent un certain écart (1^o à comparer à 10^o, et 69^o à comparer à 75^o, respectivement). Cette difficulté à résoudre très précisément le strike et le rake, pour des séismes de subduction analysés par des ondes de volume, est attendue. Cela est décrit dans la section 3.2 de l'article sur la méthode SCARDEC, où nous évaluons que des écarts jusqu'à 15^o sont prévisibles. Comme attendu,

la différence ($strike - rake$) est, elle, beaucoup plus stable entre résultats et modèle d'entrée.

La figure I.6 correspond à une extension de la méthode SCARDEC elle-même, déjà évoqué dans la section 6.2 de l'article : une fois les meilleurs paramètres de source déterminés, par analyse basse-fréquence, on peut les fixer afin d'obtenir les fonctions source réalistes, par une déconvolution à plus haute fréquence. Les fonctions source obtenues montrent une grande similarité entre elles, mais indiquent aussi la propagation vers le nord de la rupture. Les fonctions source sont en effet plus longues et de moindre amplitude dans les azimuts proches de 180^o. La figure I.7 propose un résumé de l'analyse SCARDEC pour ce premier test (voir la légende correspondante pour plus de détails). Le mécanisme, la profondeur, et la magnitude, mais aussi la fonction source « typique » sont très similaires au modèle d'entrée. Ce premier test révèle ainsi les aspects positifs suivants :

- les perturbations liées à une Terre tridimensionnelle, en tout cas celles liées aux modèles S20RTS, affectent peu les résultats
- L'extension spatiale de 200km est bien prise en compte par les fonctions source apparentes, les effets liés à la dépendance spatiale de la fonction de Green pouvant être négligés
- La variation de profondeur durant le séisme (ici entre 20km et 40km) biaise peu les résultats

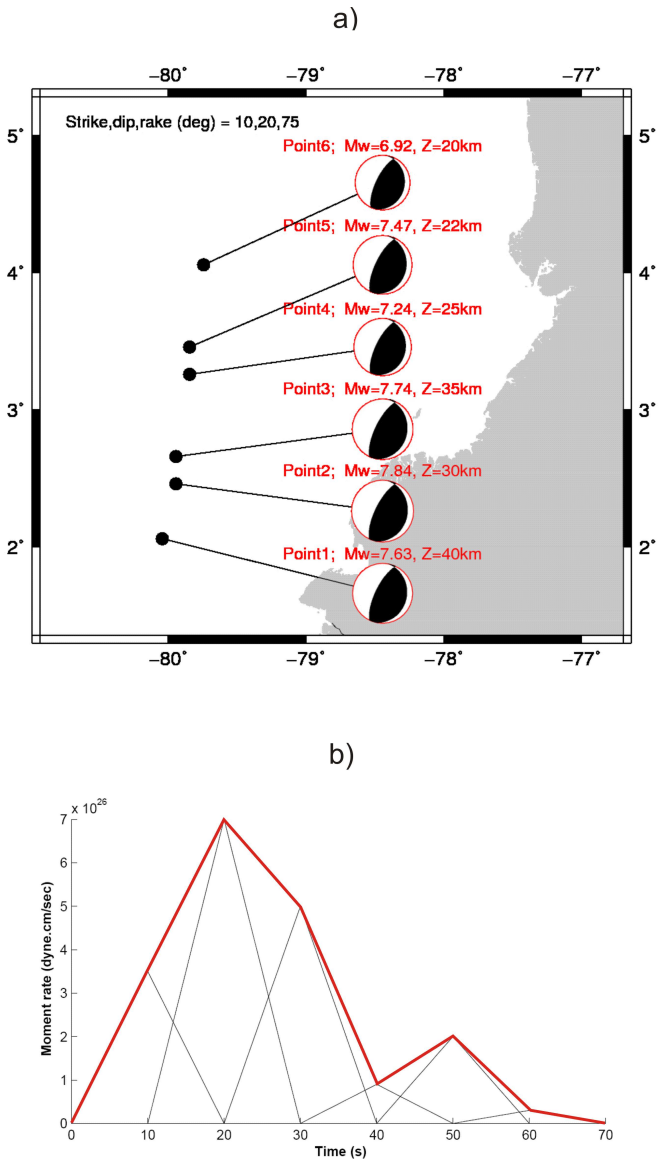

FIG. I.4 – Modèle de source à 6 points, utilisé pour la première validation en « test aveugle ». La localisation spatiale est présentée en a), et l'aspect temporel en b). En b) est indiquée l'évolution temporelle du taux de moment de chaque point individuel (lignes fines), ainsi que le taux de moment cumulé (fonction source absolue, en rouge). La rupture se propage donc du Sud vers le Nord, avec un mécanisme double-couple constant (strike,dip,rake = $10^o, 20^o, 75^o$), mais des profondeurs et moments sismiques variables. La profondeur moyenne (centroid) est de 32km et la magnitude globale M_w est 8.12.

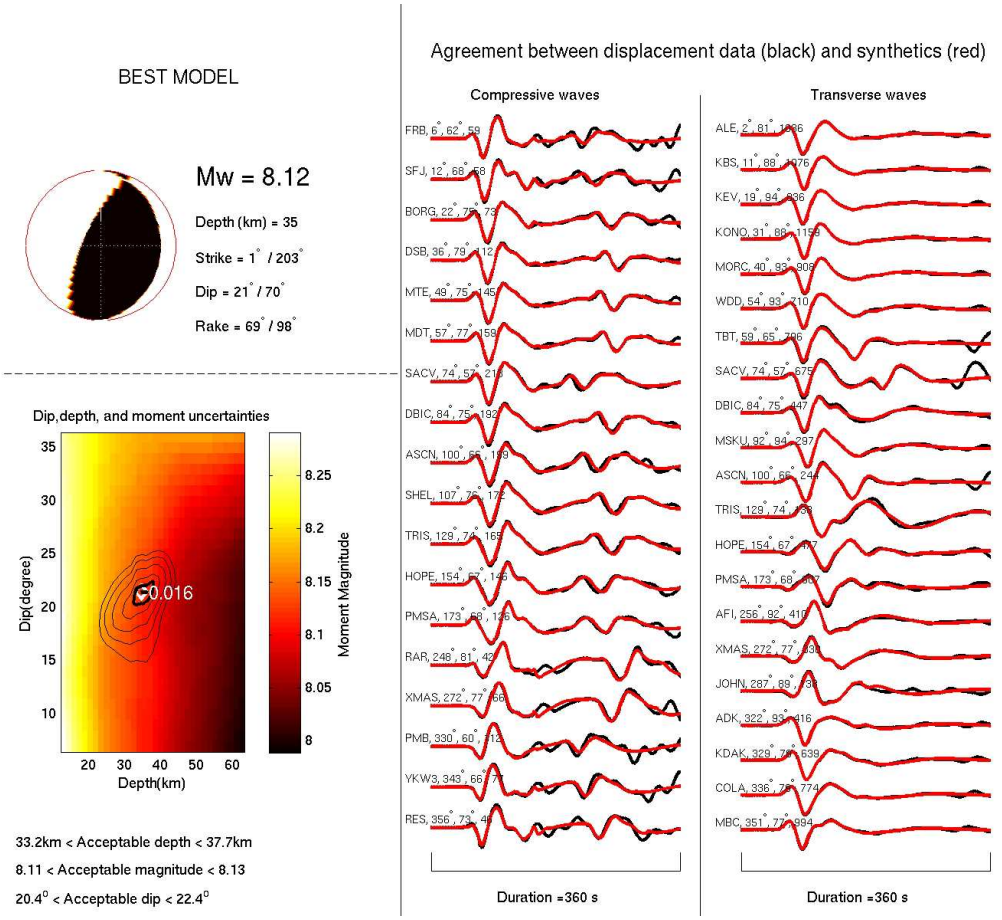

FIG. I.5 – En haut à gauche : meilleur modèle de source obtenu par la méthode SCARDEC. En bas à gauche : Incertitude sur le dip et la profondeur, évaluée par une recherche en grille autour de la solution optimale. L'évolution de la magnitude associée à chaque couple (profondeur-dip) testé est indiquée par l'échelle de couleur. La courbe en gras délimite les solutions considérées acceptables, qui n'accroissent pas le misfit de plus de 10%. Les autres courbes fines délimitent les domaines qui accroissent le misfit de 25%, 50%, 75% et 100%. Au centre : Accord entre données (noir) et synthétiques (rouge), pour les ondes compressives, qui correspondent aux phases P, PcP et PP enregistrées sur la composante verticale. A droite : Accord entre « données » (noir) et synthétiques (rouge), pour les ondes transverses, qui correspondent aux phases S, et ScS enregistrées sur la composante transverse. Les synthétiques sont la reconvolution de la radiation point-source optimale avec les fonctions source optimales (voir Figure 4 de l'article sur la méthode SCARDEC). Dans ces deux dernières sous-figures, données et synthétiques sont filtrés dans la gamme de fréquences [0.005Hz-0.03Hz]. Le nom de la station, son azimut, sa distance épicentrale, et les valeurs maximales d'amplitude (en μm) sont précisés pour chaque sismogramme.

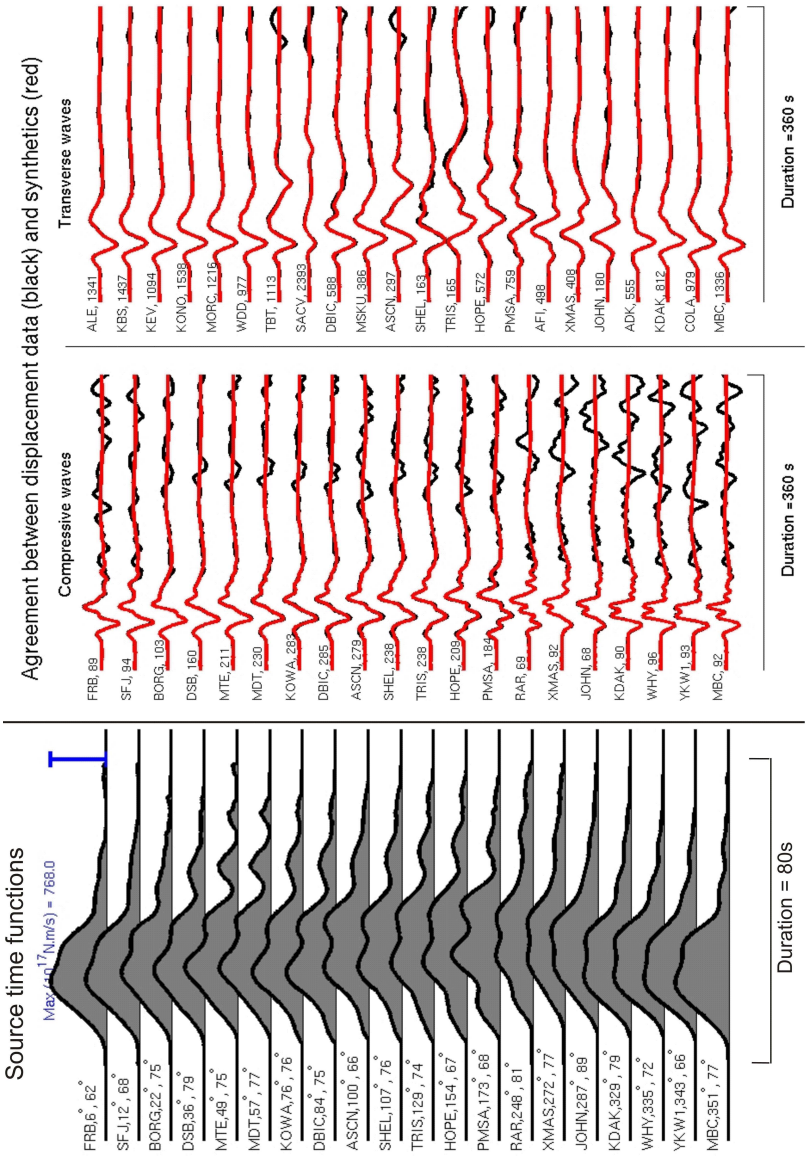

FIG. I.6 – En bas : fonctions source apparentes réalistes, obtenues par déconvolution de la radiation point-source optimale dans la gamme [0.005Hz- 1Hz]. Le nom de la station, son azimut et sa distance épicentrale sont précisés pour chaque fonction source. L'échelle d'amplitude est la même pour toutes les fonctions source : l'amplitude maximale est indiquée par la barre bleue dont l'échelle correspond à la valeur indiquée en haut de la figure (ici 768 $10^{17} N.m/s$). Noter que la propagation de la rupture vers le Nord est visible, avec des fonctions source apparentes plus compactes dans les directions proches de l'azimut 0^o. En haut et au centre : Accord entre « données » (noir) et synthétiques (rouge), présentés de la même manière que dans la figure I.5. Dans cette étude plus haute fréquence les ondes PP ne sont volontairement pas incluses dans l'analyse. Données et synthétiques sont filtrés dans la gamme de fréquences [0.005Hz-1Hz]. Le nom de la station et les valeurs maximales d'amplitude (en μm) sont précisés pour chaque sismogramme.

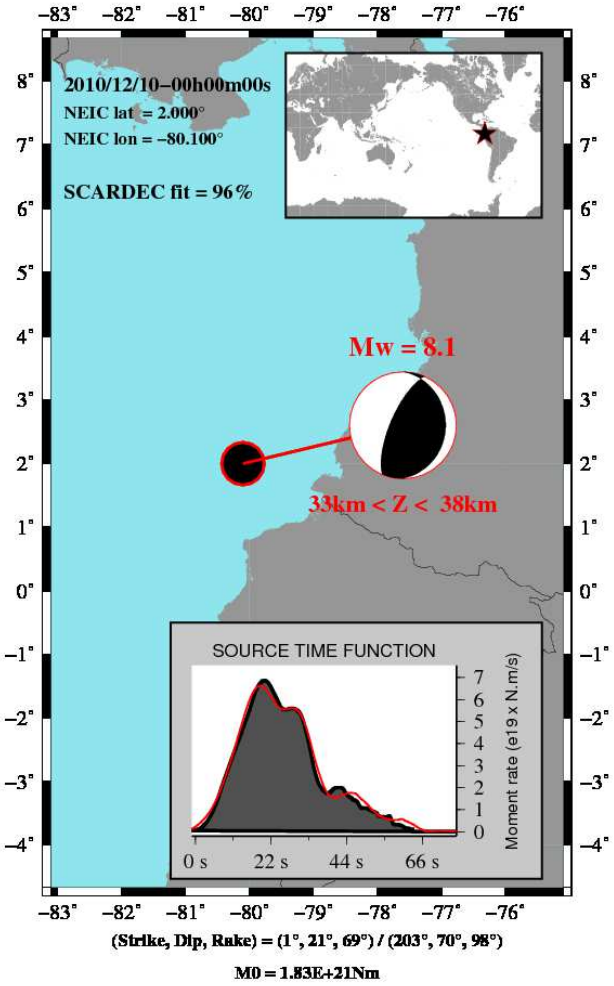

FIG. I.7 – Carte résumant les résultats du premier test. La fonction source présentée en gris (appelée fonction source « typique » dans le texte) correspond à la déconvolution d'une station individuelle, pour les ondes compressives. Elle a été choisie en fonction de l'accord reconvolution–données (fit visible sur la figure I.6), et de sa ressemblance avec une moyenne des fonctions source. Cette moyenne est représentée par la courbe rouge. Cette représentation permet, dans les cas réels, d'avoir une évaluation de la qualité des déconvolutions : lorsque la fonction source choisie est proche de la moyenne, cela montre la robustesse de la solution obtenue. Lorsqu'il y a de petites différences, cela peut indiquer la présence d'effets de directivité. Enfin, de grandes différences témoignent de difficultés à obtenir les fonctions source. En effet, les effets dus à l'extension spatio-temporelle restent modérés pour l'onde P télésismique, et ne peuvent donc pas être invoqués pour expliquer des changements majeurs de la forme des fonctions source. Noter la grande similarité entre les résultats présentés dans cette figure (mécanisme, profondeur et fonction source) et le modèle d'entrée présenté dans la figure I.4

Le deuxième test correspond à un scénario plus réaliste, puisque le modèle de source est directement calqué sur un résultat d'inversion. Dans la figure I.8 est en effet présenté le modèle cinématique de l'USGS décrivant le scénario spatio-temporel de la rupture du séisme de Maule (Chili, 27 février 2010, `http://earthquake.usgs.gov/earthquakes/eqinthenews/2010/us2010tfan/finite_fault.php`). La faille est plus longue que dans le cas précédent (400km), et s'étend sur une gamme de profondeurs plus large. Enfin, le rake est variable sur la faille. Les solutions SCARDEC sont présentées de la même manière que dans le cas précédent, dans les figures I.9, I.10 et I.11. Nous retrouvons un bon accord avec le modèle initial, en termes de paramètres de source comme de fonction source temporelle. Comme précédemment, nous observons une déviation concernant le strike et le rake d'environ 10^o, qui est très fortement réduite si l'on considère la différence $(strike - rake)$. Par rapport au cas précédent, le dip est moins précisément déterminé (3 degrés d'écart), ce qui est probablement dû à la complexité plus grande du processus de rupture.

En dehors des deux exemples présentés ici, nous avons effectué d'autres tests, en variant les localisations épicentrales, les profondeurs, les modèles de source, et en utilisant également un autre modèle de Terre 3D (S40RTS, *Ritsema et al.*, 2011.). Il apparaît que les différences entre résultats et modèles ne montrent pas de biais systématiques et restent faibles. Les différences typiques obtenues, pour des modèles de séismes de subduction interplaques sur des failles planaires, sont les suivantes :

- dip déterminé avec une erreur de moins de 4 degrés
- erreur maximale sur la profondeur moyenne de l'ordre de 8km
- erreur sur la magnitude inférieure à 0.05
- erreur sur le strike et le rake pouvant atteindre 20^o, en particulier dans des modèles avec un rake non constant sur des failles très plates. Mais l'erreur sur la différence de ces deux paramètres est réduite à quelques degrés.

Ces erreurs typiques peuvent être accrues dans le cas où le séisme présente un mécanisme composite, ou des différences de profondeur significatives (supérieures à 30-40km) entre plusieurs zones de glissement importantes. Dans ces cas où l'hypothèse de fonction de Green unique est violée, le mécanisme retrouvé peut avoir des différences plus fortes avec le modèle moyen réel. Nous avons en particulier observé que le mécanisme et la profondeur au voisinage de l'hypocentre influencent la solution obtenue. Néanmoins, ces cas peuvent souvent être décelés par une diminution de l'accord entre données et synthétiques dans les figures du type I.5 ou I.9, ou par une trop grande variabilité des fonctions source obtenues.

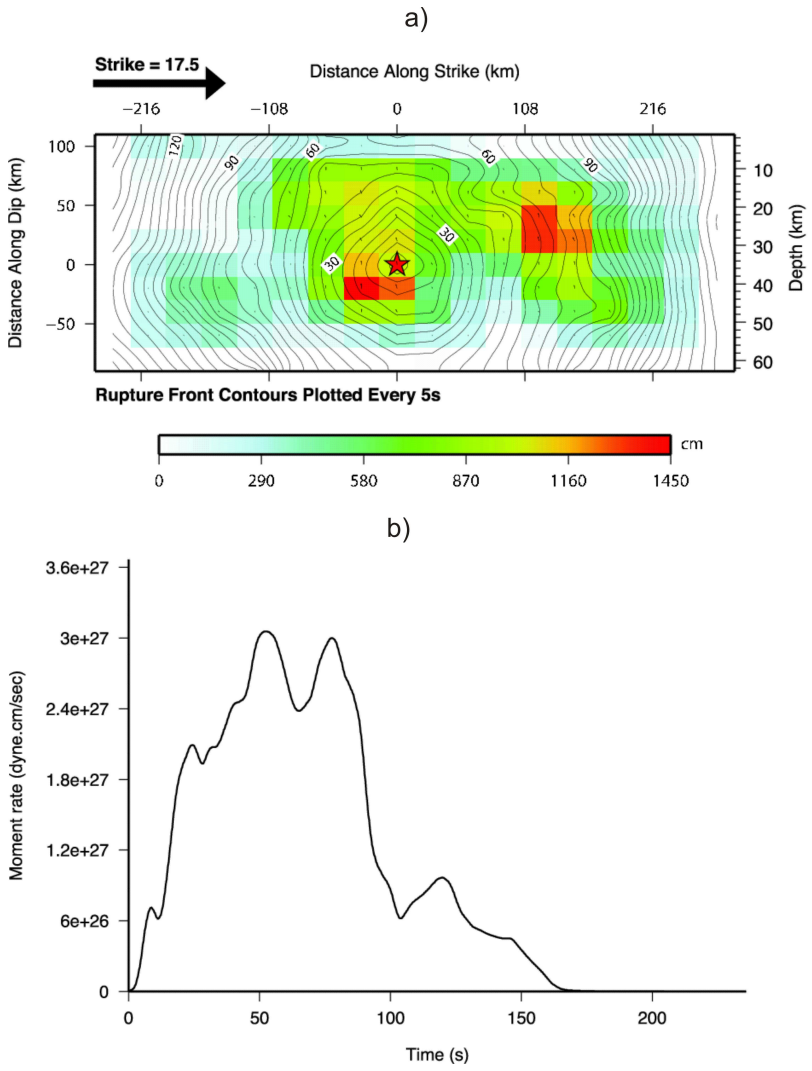

FIG. I.8 – Modèle de source pour le deuxième test. Ce modèle correspond à celui publié par l'USGS pour le séisme de Maule (Chili) du 27 février 2010. a) Distribution spatio-temporelle du glissement. La direction du strike est indiquée par la flèche noire et l'hypocentre par l'étoile rouge. L'amplitude du glissement se lit sur l'échelle de couleur, et le rake local est indiqué par les petites flèches. Les contours montrent le temps d'initiation du glissement. Le dip de ce modèle est de 18^o, le rake moyen de 107^o et la profondeur moyenne (centroid) de 28km. b) Fonction source absolue. Le moment du séisme est 2.4 10^{22}N.m ce qui équivaut à $M_w = 8.85$. Pour ce deuxième test, ce modèle a simplement été translaté sur la marge Equateur-Colombie.

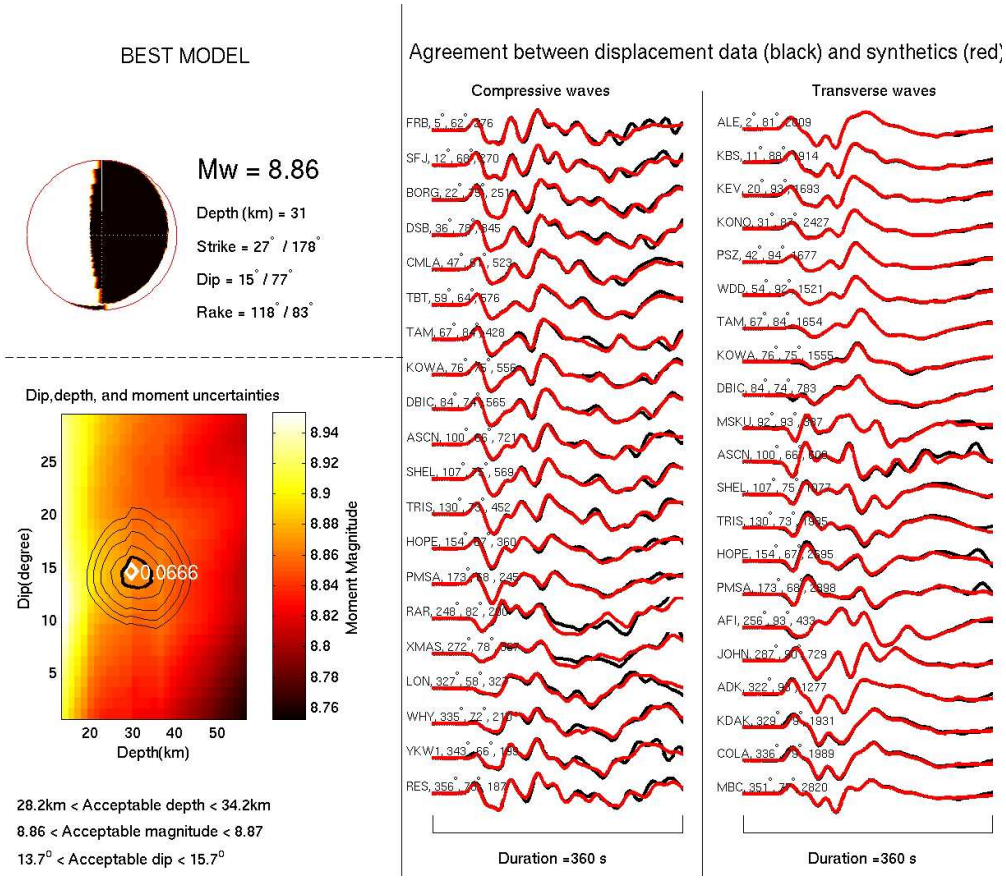

FIG. I.9 – Similaire à la figure I.5, pour le deuxième test.

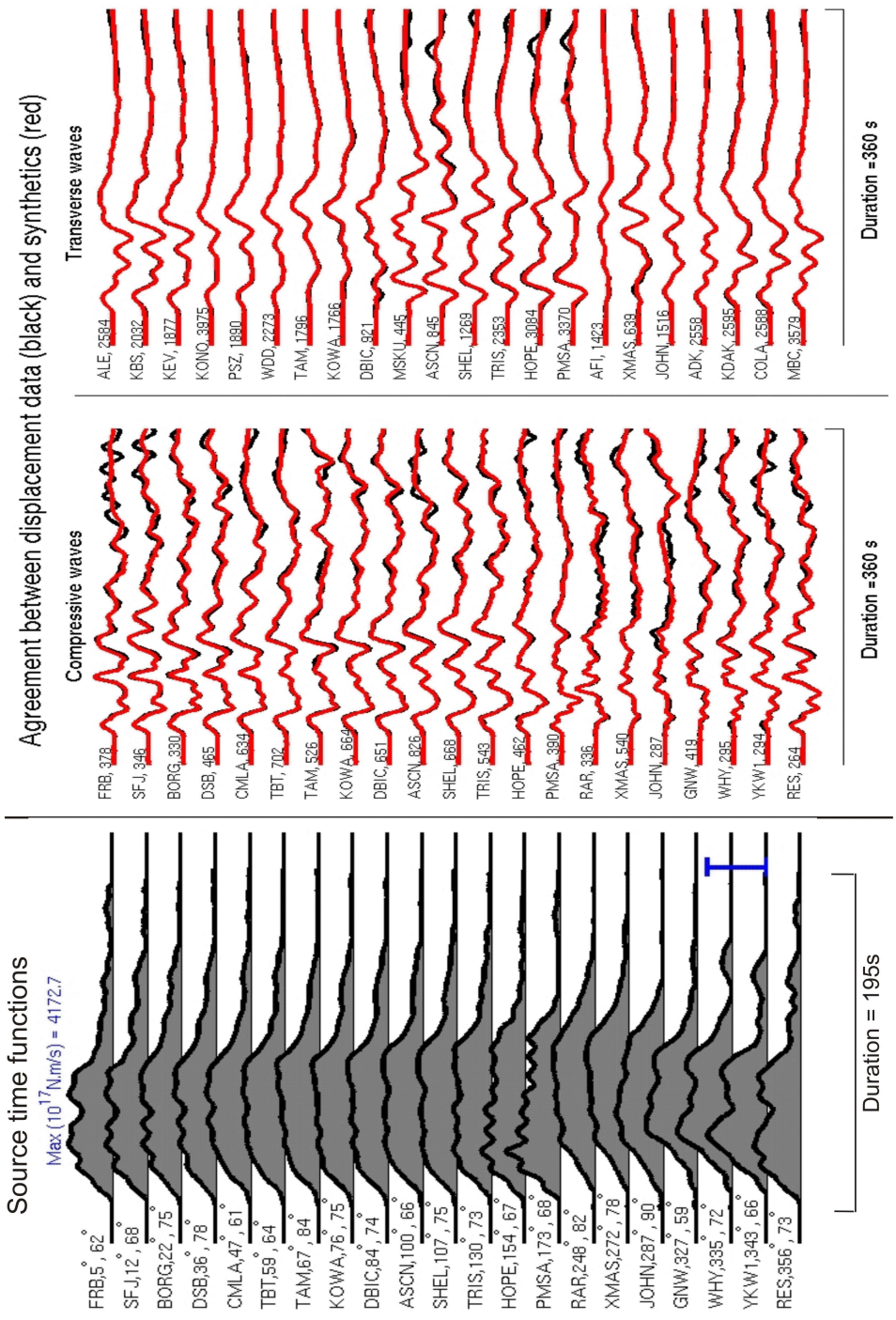

FIG. I.10 – Similaire à la figure I.6, pour le deuxième test

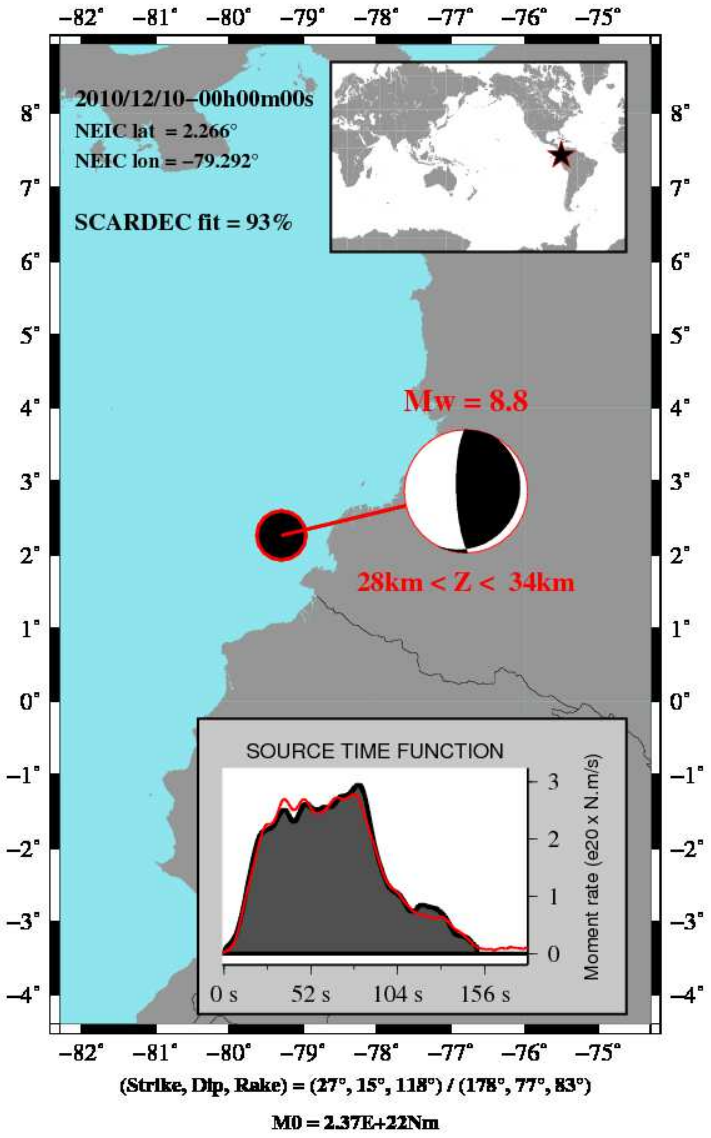

FIG. I.11 – Carte résumant les résultats du deuxième test. Voir figure I.7. Noter la grande similarité entre les résultats présentés dans cette figure (mécanisme, profondeur et fonction source) et le modèle d'entrée présenté dans la figure I.8

I.3.4 Extension de la méthode aux magnitudes plus faibles et plus fortes

La méthode SCARDEC a initialement été développée pour l'analyse des séismes de subduction majeurs, avec l'objectif spécifique de mieux découpler les valeurs de dip et de moment sismique. Néanmoins, comme la plupart des approches utilisant les ondes de volume télésismiques, son cadre d'application est beaucoup plus large : tous les types de séismes dont la magnitude est supérieure à 5.5–6 (magnitude qui correspond à un rapport signal/bruit satisfaisant pour des données lointaines) sont potentiellement analysables.

Quelques adaptations de la méthode sont cependant nécessaires. Tout d'abord, la gamme de fréquence doit être modifiée. La fréquence de coupure passe-haut utilisée pour les séismes de magnitude supérieure à 7 (0.005Hz) doit en particulier être augmentée, pour conserver un bon rapport signal sur bruit. Nous travaillons ainsi dans une gamme (0.0125Hz–0.04Hz) pour les séismes de magnitude égale ou inférieure à 6. De plus, dans le cas des petits séismes, la durée de source ne peut pas être précisément estimée par l'analyse haute-fréquence des ondes P. Nous remplaçons donc cette première étape en imposant une durée maximale en fonction de la magnitude. Cette durée reste volontairement plus longue qu'une durée classique pour un séisme d'une magnitude donnée, cela afin de permettre l'identification de séismes longs et peu impulsifs. Nous autorisons ainsi une durée maximale d'une dizaine de secondes pour un séisme de magnitude 6. Cette durée croît avec la magnitude, jusqu'à permettre une durée de 50s pour un séisme de magnitude 7. Ces deux modifications nécessitent de connaître la magnitude du séisme afin de déterminer la bande de fréquence et la durée de source maximale. Nous effectuons donc une première application de la méthode SCARDEC à partir d'une magnitude initiale, fournie par exemple par des analyses simples de l'amplitude des ondes du séisme. La magnitude résultante de cette première application nous permet ensuite de répéter la méthode SCARDEC avec plus de précision.

Pour les séismes de très forte magnitude associée à une longue durée de source, nous avons récemment également modifié la gamme de fréquence d'étude. La fréquence de coupure de 0.005Hz peut être en effet un peu trop haute pour permettre la détermination précise du moment sismique de séismes dont la durée est largement supérieure à 100s. Ces séismes étaient en petit nombre dans l'échantillon utilisé dans l'article sur la méthode SCARDEC ; cependant, notre analyse récente des séismes de Java du 17/07/2006 ou du Japon du 11/03/2011, qui ont une durée de l'ordre de 150s (*Ammon et al.*, 2006 ; *Ammon et al.*, 2011), nous a orienté vers un abaissement de cette fréquence jusqu'à 0.003Hz. Ce choix peut être discuté car il conduit à une interaction plus forte des ondes P analysées avec la phase W (*Kanamori*, 1993 ; *Kanamori and Rivera*, 2008) - qui n'est pas prise en compte dans notre méthode. Cependant, le fait que la grande majorité de la bande de fréquence reste dans une gamme où la phase W est de faible amplitude, ainsi que le fait de se restreindre au début du sismogramme (et non pas à l'ensemble des ondes arrivant entre l'onde P et S) devraient limiter

cet effet indésirable.

Ces deux modifications permettent d'analyser l'ensemble de la sismicité mondiale de magnitude modérée à forte. Par rapport à une méthode en patchs de glissement (*Vallée and Bouchon*, 2004) que nous avions développée précédemment, la méthode SCARDEC est ainsi beaucoup plus générale ; en effet, tous les effets de complexité spatio-temporelle de la source, tant qu'ils n'affectent pas son mécanisme, sont naturellement pris en compte. La méthode des patchs permettait en revanche d'avoir des informations sur la distribution spatiale du glissement. Cette information n'est pas directement fournie par SCARDEC, mais peut être déduite a posteriori par l'analyse des fonctions source apparentes.

I.3.5 Application en temps quasi-réel

La méthode SCARDEC est naturellement adaptable en temps quasi-réel. Aujourd'hui, des protocoles efficaces d'interrogation des serveurs de données permettent de stocker en temps très peu différé les données du réseau mondial. Le protocole seedlink et des outils associés (« slarchive » en particulier, voir `http://www.seiscomp3.org/wiki/doc/applications/slarchive`) rendent négligeables le délai entre l'acquisition de la donnée et sa présence sur un ordinateur personnel. Ainsi, tous les sismogrammes nécessaires à SCARDEC peuvent être disponibles dès que les ondes télésismiques sont arrivées aux stations les plus lointaines, soit environ 32 minutes après le temps origine du séisme. Dans ce même laps de temps, les informations de premier ordre nécessaires à SCARDEC (localisation, temps origine et première estimation de la magnitude) sont fournies, avec une précision suffisante, par plusieurs organismes (USGS et EMSC en particulier).

Nous avons donc adopté la stratégie suivante. Nous effectuons une veille informatique régulière sur le site d'alerte de l'USGS (`http://earthquake.usgs.gov/earthquakes/recenteqsww/Quakes/quakes_big.php`), afin de détecter tout nouveau séisme de magnitude supérieure à 5.5. Si tel est le cas, nous déclenchons la récupération des données par l'outil « slarchive », à partir du temps origine du séisme. Ce déclenchement est typiquement initié 10-15 minutes après le temps origine (temps nécessaire à la localisation du séisme par les ondes P). Durant les 15-20 minutes suivantes, les données s'accumulent et nous prenons en compte les éventuelles mises à jour de la localisation et de la magnitude par l'USGS. Après 32 minutes, la méthode SCARDEC est appliquée.

La méthode nécessite elle-même entre 5 et 12 minutes, selon le nombre de données utilisables. Par rapport à l'article initial sur la méthode SCARDEC, ce temps a en effet pu être considérablement réduit grâce à la parallélisation du code. Ainsi, la solution définitive est fournie entre 37 et 45 minutes après le temps origine du séisme. Si l'on compare avec les analyses de la phase W, ce temps est plus lent que la première détermination réalisée avec les ondes télésismiques proches, mais comparable avec la solution finale (*Duputel et al.*, 2012).

Dès l'obtention des résultats (mécanisme, profondeur et M_w), la solution est publiée sur le site : `http://geoazur.oca.eu/SCARDEC`, ainsi que sur le site de l'EMSC (`http://www.emsc-csem.org/Earthquake/tensors.php`). Ces solutions en temps quasi-réel fournissent les paramètres de source pour la plupart des séismes de magnitude supérieure à 6, et incluent les séismes de magnitude [5.4–6] quand la configuration est favorable. La raison principale de l'absence de certains séismes forts est l'occurrence de crises sismiques, où plusieurs séismes importants se produisent successivement. Puisqu'un séisme important crée des oscillations de la surface terrestre pendant plusieurs heures, il devient difficile d'analyser la sismicité suivante. La fonction source typique est également fournie sur le premier des deux sites Web, à condition qu'elle puisse être déterminée précisément : les cas typiques d'absence de la fonction source sont les « petits » séismes (magnitude proche ou inférieure à 6) pour lesquels les données peuvent être trop bruitées à haute fréquence, les séismes avec un changement de mécanisme durant leur rupture, et comme précédemment les séquences de séismes importants. La page `https://geoazur.oca.eu/spip.php?article1072` résume les informations principales sur l'adaptation de SCARDEC au temps quasi-réel.

Afin d'illustrer les résultats sur des exemples récents, je présente dans la figure I.12 la solution obtenue pour le séisme de Oaxaca (Mexique, $M_w = 7.4$, 20 mars 2012). Cette solution a été disponible 43 minutes après le temps origine. En plus de l'amélioration de la magnitude (les premières informations donnaient $M_w = 7.6$), de la confirmation de la nature interplaque du séisme, cette figure montre que la source est simple et impulsive, avec une durée de seulement 12s.

En comparaison, je présente dans la figure I.13 la solution obtenue pour un plus petit séisme, qui s'est produit quelques jours auparavant en Papouasie ($M_w = 6.2$, 14 mars 2012). La solution a également été obtenue une quarantaine de minutes après le temps origine. Bien que les différences de magnitude impliquent que le séisme du Mexique ait un moment sismique 60 fois plus grand, les durées de source des deux séismes sont très proches. Ces deux exemples illustrent l'aspect opérationnel de la méthode SCARDEC ; ils montrent également que des informations de variabilité de la source sismique, dont nous parlerons dans la section suivante, sont clairement mises en évidence.

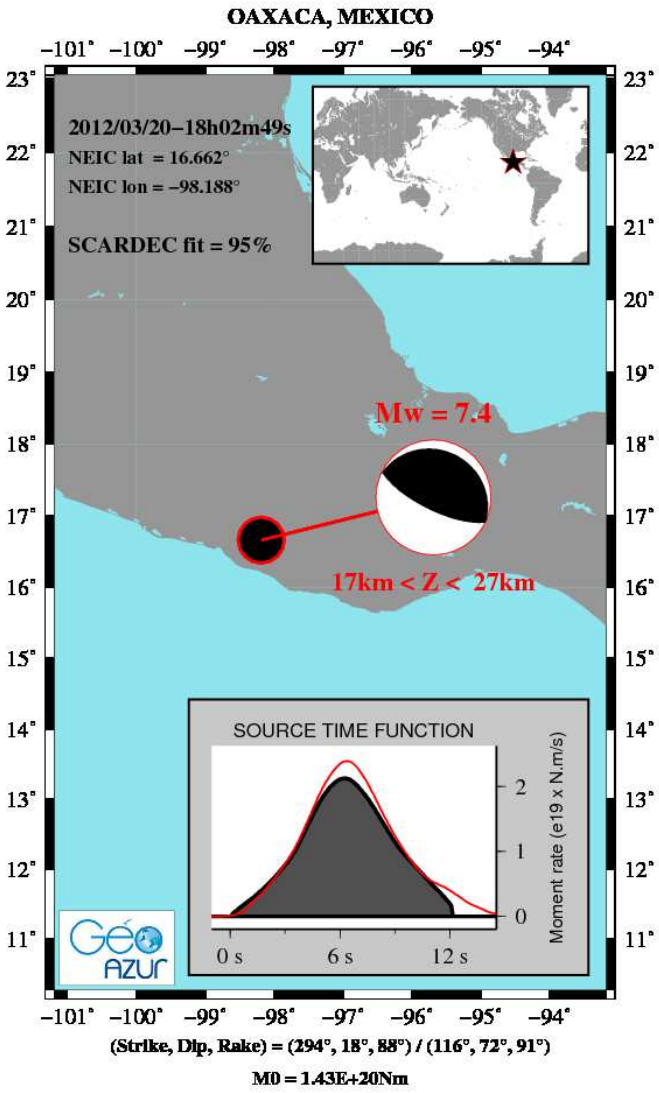

FIG. I.12 – Carte résumant les résultats pour l'analyse en temps quasi-réel du séisme du Mexique (20/03/2012). Voir figure I.7

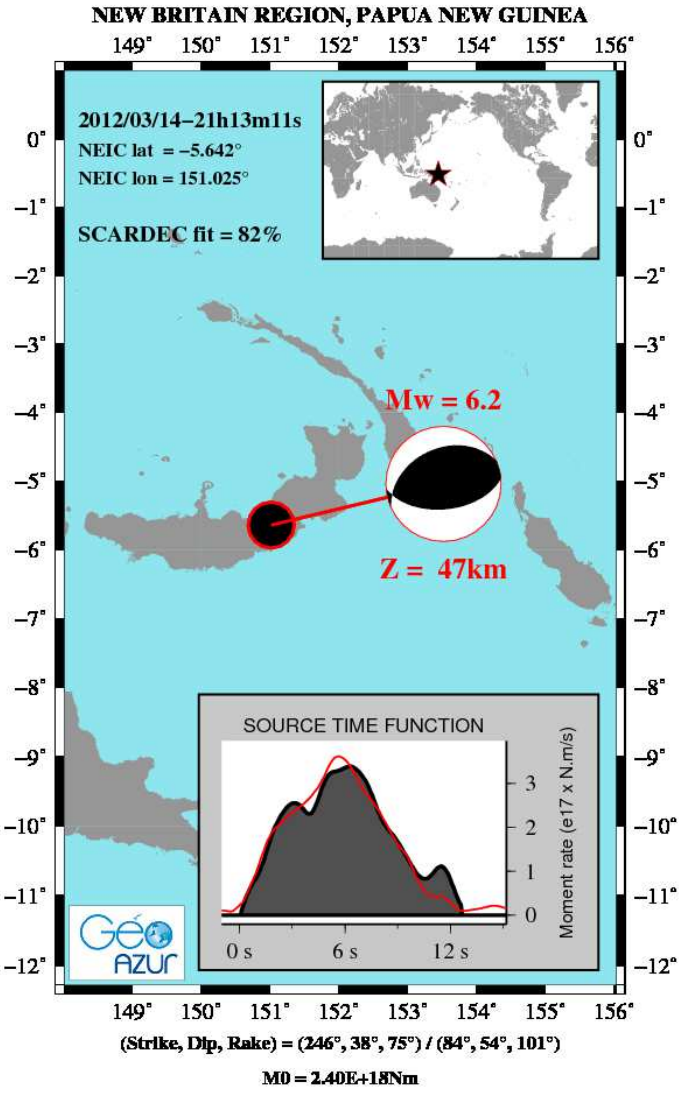

FIG. I.13 – Carte résumant les résultats pour l'analyse en temps quasi-réel du séisme de Papouasie (14/03/2012). Voir figure I.7

I.4 Perspectives : analyse systématique des caractéristiques de source

La méthode SCARDEC fonctionne donc sans intervention extérieure, sur une large gamme de magnitudes, et en un temps relativement court. Les fonctions source peuvent être obtenues pour toutes les profondeurs et les types de mécanisme, dès que la magnitude est suffisamment élevée (typiquement supérieure à 6). Cela permet d'envisager une vaste analyse des caractéristiques de source, sachant que plus de 2400 séismes de magnitude supérieure à 6.1 se sont produits dans les 20 dernières années, et que les données correspondantes sont toutes facilement accessibles.

Ce type d'approche de la sismicité à partir des fonctions source a déjà été abordé dans les années passées. Les analyses se sont d'abord concentrées sur les séismes intermédiaires et profonds (>100km), l'objectif étant d'estimer si les séismes profonds présentaient une nature différente de leurs homologues superficiels (*Chung and Kanamori*, 1980, *Fukao and Kikuchi*, 1987). Ce type d'étude est facilité par l'absence d'interaction entre l'onde P directe et les phases de profondeurs (pP, sP) : cela permet l'utilisation de méthodes beaucoup plus simples pour estimer la fonction source, comme un simple stack (*Vidale and Houston*, 1993) ou un réalignement des sismogrammes pour extraire une forme d'ondes commune (*Tocheport et al.*, 2007). Ces études se basent principalement sur la durée des fonctions source (normalisée par le moment sismique) et ont pu montrer que cette dernière a tendance à se réduire avec la profondeur. Dans une certaine proportion, cette réduction est attendue, car la rigidité Terrestre augmente avec la profondeur ; et puisque la vitesse de rupture est liée à la rigidité au travers de la vitesse de phase des ondes, une réduction de la durée est attendue pour les séismes profonds. La difficulté est de savoir si cet effet explique entièrement la variation observée (*Bos et al.*, 1998), ou seulement très partiellement (*Vidale and Houston*, 1993 ; *Tocheport et al.*, 2007).

De même, l'analyse de la durée a été faite sur les séismes de subduction interplaques, dans un cadre global (*Bilek and Lay*, 1999, *Bilek et al.*, 2004), ou ciblée sur une zone précise comme celle d'Alaska (*Ekström and Engdahl*, 1989) ou de Sumatra-Andaman (*Bilek*, 2007). Des conclusions similaires ont pu être tirées, avec une tendance à des durées plus longues pour les séismes très superficiels (profondeur inférieure à 20km). L'explication la plus naturelle est aussi l'augmentation de la rigidité avec la profondeur mais d'autres hypothèses, comme un changement de la chute de contrainte le long de l'interface, peuvent aussi être invoquées.

D'une manière générale, ces études sont rarement basées sur l'ensemble des propriétés de la fonction source, mais seulement sur sa durée. Ce paramètre est de plus sujet à caution, car la terminaison de la rupture peut être peu claire. Seules quelques études comme celle de *Singh and Mortera* (1991) tentent d'interpréter les caractéristiques de la fonction source et de sa complexité pour les relier au contexte tectonique. Il est pourtant suggéré que la forme de la

fonction source apporte de riches informations, par exemple sur la chute de contrainte statique et dynamique (*Ruff*, 1999). Les études précédentes ont aussi souvent utilisé des catalogues non exhaustifs, en se réduisant à des contextes tectoniques ou des gammes de magnitudes donnés. Un catalogue proposant les fonctions source de nombreux séismes avait été initié par Larry Ruff (Université du Michigan) dans les années 1990, mais ce catalogue ne semble pas avoir été tenu à jour depuis.

Les objectifs d'analyse avec la méthode SCARDEC sont donc de s'intéresser au comportement d'un nombre d'événements le plus large possible, en extrayant des nouvelles caractéristiques de la fonction source. La plus évidente, sur laquelle nous avons commencé à travailler, est sa valeur maximale. L'application des lois d'échelle simples (chute de contrainte et vitesse de rupture constante) prévoit que ce pic de relâchement de moment noté $\dot{M}_{max}$ devrait évoluer avec le moment sismique M_0 comme :

$$\dot{M}_{max} \propto M_0^{2/3} \tag{I.18}$$

Les écarts à cette loi impliquent, comme la variation de la durée, des changements dans la vitesse de rupture (pouvant être dus à la rigidité) ou dans la chute de contrainte. La mesure de $\dot{M}_{max}$ présente cependant l'avantage d'être beaucoup moins subjective que celle de la durée. D'autres caractéristiques des fonctions source ont été peu analysées de manière exhaustive, comme ses propriétés spectrales à haute fréquence par rapport à la loi ω^{-2} (*Aki*, 1967). Le but sera ensuite de relier les éventuels écarts systématiques aux lois d'échelle simples à des propriétés autres que la profondeur. On peut en particulier espérer mettre en évidence des comportements sismiques différents pour des failles jeunes par rapport à des failles délimitant les plaques majeures terrestres, actives depuis des millions d'années.

Enfin, l'analyse systématique des caractéristiques de source peut aussi conduire à la mise en évidence de séismes individuels qui s'éloignent grandement des comportements classiques. On peut penser à des événements anormalement impulsifs, ou au contraire particulièrement peu énergétiques. Aujourd'hui, de tels séismes peuvent être méconnus, s'ils n'appartiennent pas à la catégorie des séismes « notables » (forte magnitude et/ou importants dégâts). En effet, ce ne sont généralement que ces derniers qui font l'objet d'études spécifiques. La grande majorité des autres séismes ne reste donc connue que par des caractéristiques de premier ordre, comme leur localisation, leur magnitude et leur mécanisme. De par leur nombre, seule l'utilisation de méthodes systématiques permet d'espérer déceler des propriétés anormales chez quelques–uns d'entre eux. Cette piste de recherche est intéressante en elle-même, mais permet surtout de cibler des séismes qui mériteraient une analyse plus poussée, en utilisant par exemple les méthodes décrites dans le chapitre suivant.

Chapitre II

Rentrer dans le détail du processus de rupture, à partir d'approches ou de données variées

II.1 Diversification des distances d'observation de la source

II.1.1 Analyse conjointe des données locales, régionales, et télésismiques

L'étude télésismique du processus de rupture est limitée par la difficulté à séparer les effets spatiaux des effets temporels (*Menke*, 1985). L'ajout des données proches permet de réduire significativement cette incertitude (*Hartzell and Heaton*, 1983). En effet, si l'on reprend l'équation générale (I.5) de la radiation sismique, le terme de propagation $G_{ij,l}$ (fonction de Green) inclut alors trois termes (champs proche, intermédiaire et lointain) qui ont chacun une dépendance spécifique à la distance source–station (*Aki and Richards*, 2002). Cette dépendance à la distance r de la source (respectivement en $1/r^4$, $1/r^2$ et $1/r$ pour les trois termes précités) rend dominantes les radiations venant des points de la faille les plus proches de la station. Le processus sismique pourra donc localement être bien imagé, car les effets d'intégration sur la faille de l'équation (I.5) seront réduits. Il faut cependant remarquer que, sauf dans le cas où les enregistrements proches sont très nombreux et régulièrement repartis autour du séisme, les données télésismiques resteront utiles pour conserver une vision globale du séisme, non biaisée par quelques enregistrements locaux.

Un autre avantage des données proches réside dans le fait que $G_{ij,l}$ devient aussi sensible à l'azimut d'un point de la faille, car le mécanisme « vu » par la station change. Puisque cette dépendance en fonction du mécanisme est également spécifique à chacun des termes de la fonction de Green, elle aidera à une meilleure détermination du processus de rupture. Cet effet est particulièrement utile pour des stations localisées dans un azimut orthogonal à celui de la faille, et à une distance comparable à la longueur de la faille. Dans ce cas, la distance à la faille varie relativement peu (ce qui limite l'effet décrit précédemment) mais le changement de géométrie entre un point de la source et la station permettra une bonne détermination du processus de rupture.

Les données situées dans différentes gammes de distances du séisme apportent donc des informations complémentaires sur la rupture sismique. Sauf dans les rares contextes où la zone de rupture est couverte d'accéléromètres (exemple du séisme de Tottori (Japon) du 6 Octobre 2000 ($M_w = 6.7$)), il est ainsi utile de les associer afin de mieux imager la rupture sismique. Les données très proches de la source - tout comme les données télésismiques d'onde de volume – ont l'intérêt que la fonction de Green peut être simplement évaluée numériquement jusqu'à des périodes assez courtes (typiquement quelques secondes). En effet, pour une source proche, un modèle unidimensionnel de la structure terrestre est généralement suffisant ; dans ce cas, le champ complet peut être par exemple simulé par la méthode des nombres d'ondes discrets (*Bouchon*, 1981). Ce n'est pas le cas des données régionales, où la dépendance à la structure tridimensionnelle de la Terre devient très forte. Cela impose de ne considérer que des périodes plus longues, d'avoir une approche par fonction de

Green empirique, ou d'utiliser des méthodes de simulation d'ondes performantes associées à un modèle de Terre détaillé.

L'analyse du processus de rupture consiste donc à résoudre des équations du type (I.5), où la fonction $G_{ij,l}$ est considérée connue, et les inconnues sont les fonctions glissement Δu et temps de rupture t_r. Nous ajoutons généralement des contraintes supplémentaires sur ces fonctions : La dépendance temporelle de Δu est représentée par un nombre discret de fonctions rampes décalées en temps (*Olson and Apsel*, 1982, *Hartzell and Heaton*, 1983), et t_r est contraint à respecter une hypothèse de causalité par rapport à l'hypocentre. L'optimisation de ces fonctions afin d'ajuster au mieux les données est un problème non linéaire, qui peut se résoudre par des méthodes d'exploration globale de l'espace des paramètres : les algorithmes de recuit simulé (*Kirkpatrick et al.*, 1983 ; *Cerný*, 1985) ou de voisinage (Neighborhood Algorithm, *Sambridge*, 1999) permettent par exemple de réaliser cette optimisation. Lorsqu'on utilise plusieurs types d'onde, le poids accordé à l'accord de chaque donnée peut avoir une influence sur le résultat obtenu. Il est alors utile d'évaluer a priori (par des modèles synthétiques) et a posteriori (sur l'analyse du séisme lui-même) la résolution intrinsèque de chaque type d'ondes (*Delouis et al.*, 2002 ; *Delouis et al.*, 2004).

Je présente dans ce chapitre deux exemples où nous avons analysé conjointement les ondes sismiques radiées dans différentes gammes de distance : L'étude des séismes « jumeaux » de Molise (Italie, 2002 ; *Vallée and Di Luccio*, 2005) est décrite à la suite de cette introduction. L'analyse du séisme de Maule (Chili, 27 février 2010 ; *Delouis et al.*, 2010) - où nous avons aussi intégré l'analyse de la géodésie statique et cinématique - est reportée à la fin de ce chapitre. Dans les deux cas, nous discuterons comment l'imagerie plus fine de la rupture a apporté des informations sur le fonctionnement de ces séismes.

II.1.2 Exemple d'application aux séismes de Molise (Italie, 2002)

Lors de mon post-doctorat à l'Observatoire du Vésuve et à l'Université de Naples, nous nous sommes intéressés à l'occurrence d'une crise sismique de la province de Molise (Italie centrale). Le 31 Octobre 2002 s'est produit un séisme de magnitude 5.8, suivi le lendemain par un séisme très similaire en termes de mécanisme et magnitude. L'analyse conjointe de données locales, régionales et télésismiques révèle que les zones de rupture de ces deux séismes sont de plus contigües et de taille comparable. Cette observation amène naturellement le questionnement suivant : pourquoi y a-t-il eu un écart de 29 heures entre ces deux séismes, quel mécanisme a pu empêcher qu'un seul séisme de magnitude 6 se produise, en englobant dynamiquement les deux zones de rupture ? Ces phénomènes de « chocs principaux multiples », fréquents en Italie (voir également la séquence de Colfiorito du 26 septembre 1997), sont encore mal compris aujourd'hui.

GEOPHYSICAL RESEARCH LETTERS, VOL. 32, L12309, doi:10.1029/2005GL022687, 2005

Source analysis of the 2002 Molise, southern Italy, twin earthquakes (10/31 and 11/01)

Martin Vallée[1,2] and Francesca Di Luccio[3]

Received 10 February 2005; revised 4 May 2005; accepted 18 May 2005; published 24 June 2005.

[1] On October 31, 2002, a moderate size earthquake (Mw = 5.8) occurred in Molise region, southern Italy, causing loss of young human lives in a school collapse and destructions in several villages. The day after, a slightly smaller earthquake happened a few kilometers westward from the first one, without making strong damage. We use a complete set of seismological data (global, regional and local, including both body and surface waves) to better understand the source process of these two events. We show that the two earthquakes are similar, in terms of hypocentral depth, focal mechanism, and source kinematics. Moreover, the imaged slip zones are almost contiguous which makes the time delay between the two shocks (29 hours) an open question. The identified updip rupture propagation has amplified the radiation usually created by such Mw = 5.8 earthquakes at 15–20 km depth. We model a maximum acceleration zone in agreement with location of damaged villages. **Citation:** Vallée, M., and F. Di Luccio (2005), Source analysis of the 2002 Molise, southern Italy, twin earthquakes (10/31 and 11/01), *Geophys. Res. Lett.*, *32*, L12309, doi:10.1029/2005GL022687.

1. Introduction

[2] The Appenninic seismicity, central and southern Italy, is often constituted of multishock sequences, with at least two main earthquakes of similar magnitude. With a time interval between events varying between a few tenths of seconds to several months, such a behaviour was observed for Irpinia (11/23/1980), Abruzzo (1984), Potenza (Basilicata, 1990–1991) and Umbria-Marche (1997) earthquakes. In a similar way, the 2002 Molise sequence was characterized by compound earthquakes (10/31/2002 and 01/11/2002).

[3] The first shock (thereafter called MS1) occurred in the vicinity of the village of San Giuliano di Puglia (Figure 1c), where it caused the death of 29 people, most of them in the collapse of a primary school. The earthquake hypocenter was located at mid-crust depth and its mechanism was almost pure strike slip (Figure 1). The analysis of aftershock activity [*De Gori and Molise Working Group*, 2004] shows that the causal fault was the East-West striking one. The second shock (thereafter called MS2) occurred 8 km west of the first one, with very similar properties. This earthquake was strongly felt but did not cause any additional casualties. Details on the tectonic setting of this sequence are given by *Valensise et al.* [2004] and *Di Bucci and Mazzoli* [2003]. We show here how the conjoint use of various seismic data gives us information on the earthquakes source processes and how these processes are related to the damages in the epicentral area.

2. Coseismic Data

[4] We make use of a broad range of seismic data, taking into account simultaneously teleseimic, regional and local seismic signals (Figure 1). Teleseismic data come from the Global Seismic Network (GSN) and Geoscope broad-band sensors. We have selected 10 recordings for P waves and 8 for SH waves, at epicentral distances ranging between 35° and 80° (Figure 1a). The P-wave and SH-wave data of both shocks, for representative stations, can be seen in Figures 2a and 2b, respectively. The azimuthal coverage is good in the whole eastern direction, but because of the relatively small magnitudes of the events (Mw 5.7–5.8) and the large distances from North America, no good data was available at west of the earthquakes.

[5] Teleseismic data offer a good resolution about global rupture process and source depth (due to reflected phases) but they do not provide a good estimate of the earthquake lateral extension, as waves do. So we add regional data in Europe provided by Geofon and GSN networks. To avoid the difficult high frequency modelling at these distances, we use the Empirical Green Function (EGF) approach. This technique, widely used since the first studies of *Hartzell* [1978], uses the signal of a smaller event to model the Green function of the main earthquake. The usual requests for the smaller event is to be at least one degree in magnitude smaller than the mainshock and to have a similar location and focal mechanism. The study of *Di Luccio et al.* [2005], which has defined the centroid moment tensors for the main events of the Molise sequence [see *Di Luccio et al.*, 2005, Table 1] informs us of the potential candidates for an EGF. Among them, we select the 2002/11/01 17:21 earthquake (Mw = 4.5), which meets the best the EGF requirements. We have checked that results are similar with the 2002/11/12 aftershock (Mw = 4.6).

[6] We use the technique described by *Vallée* [2004], which stabilizes the classical deconvolution between the mainshock and the EGF in order to obtain more reliable Relative Source Time Functions (RSTFs). These RSTFs, obtained at various azimuths, give information on the source process itself. We apply this technique to surface waves to better detect lateral rupture directivity effects. Selected stations (see *Vallée* [2004] for the criteria of selection) are presented in Figure 1b and obtained RSTFs, for both events, can be seen in Figure 2c.

[1]Osservatorio Vesuviano, Istituto Nazionale di Geofisica e Vulcanologia, Naples, Italy.
[2]Now at Géosciences Azur, Institut de Recherche pour le Développement, Nice, France.
[3]Istituto Nazionale di Geofisica e Vulcanologia, Rome, Italy.

0094-8276/05/2005GL022687$05.00

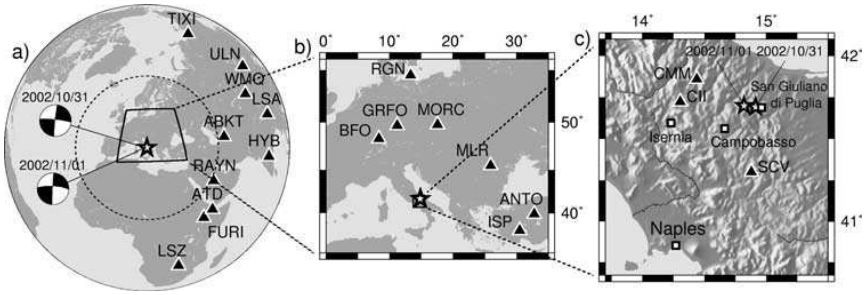

Figure 1. Receivers and earthquakes location. (a) Teleseismic stations providing P and SH recordings. All 10 stations are used for P waves whereas we have not used the SH signals of ULN and FURI, too close from the nodal planes. (b) Location of regional stations used in the EGF analysis. (c) Location of the local stations and of San Giuliano di Puglia, the most damaged village.

[7] Finally, we use local data which are even more sensitive to source size because Green functions spatially vary along the fault. No digital recordings closer than 36 km from the sources were available. Three stations, CII (MedNet broadband station), CMM and SCV (RAN, Rete Accelerometrica Nazionale, accelerometers), are at distances between 36 km and 50 km (Figure 1c). We select only the transverse component (Figure 2d) because its modelling is less dependent on accurate 3D velocity structure.

3. Source Identification Procedure

[8] The analysis of teleseismic and especially local seismic waves requires the knowledge of the source structure. To define the crustal velocity model, we use the work of *Mostardini and Merlini* [1986] to define the first kilometers, and the wide angle seismic profiles analysed by *Scarascia et al.* [1994] to define the lower crust structure. The model, presented in Table 1, remains too simple to fully explain the complexity of local data and we include in the inversion only the larger amplitude CII and SCV stations.

[9] The seismic wave field at teleseismic distances (P and SH waves) is computed using a source embedded in a layered medium [*Bouchon*, 1976; *Müller*, 1985] convolved with the mantle propagation effects (attenuation and geometrical spreading). To correct for errors in theoretical arrival times, we have manually picked the first P wave arrival. Moreover, we allow a time shift up to ±3 s for P waves and ±5 s for SH waves and select the shift corresponding to the best correlation. The local seismic wave field is calculated with the discrete wave number method [*Bouchon*, 1981] associated to the reflectivity method.

[10] The parametrisation of the source itself is done with the slip patch approach [*Vallée and Bouchon*, 2004], which describes the main earthquake characteristics in a synthetic manner: namely, we look directly for the location and size of the main slip patches on the fault. This presents the main advantage - with respect to a more classical gridded fault parameterization - to considerably reduce the number of parameters describing the faulting process. In the one-patch model case, this technique needs the definition of 10 parameters: focal mechanism (3), hypocentral depth, position of the patch with respect to the hypocenter (2), size of the elliptical patch (2), slip and rupture velocity inside the patch. Local slip duration is generally poorly resolved and we have fixed it to 0.5 s. With slip values of a few tenths of cm, it yields a slip velocity of the order of 1 m/s, in agreement with earthquake dynamics. Equations relating the body wave displacements and RSTFs to the patch(es) parameters are described by *Vallée and Bouchon* [2004]. In

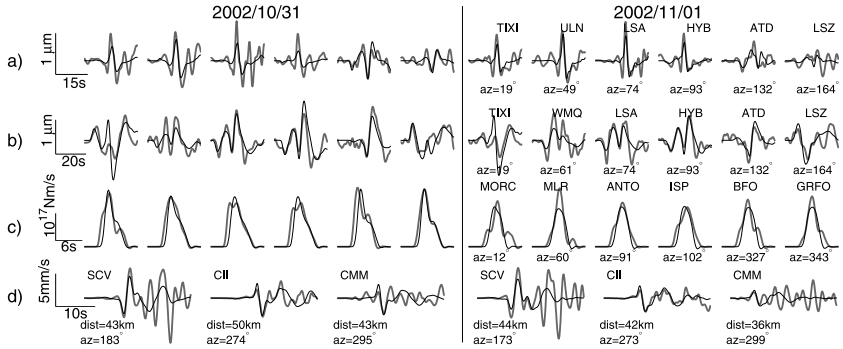

Figure 2. Agreement between data and synthetics (both lowpass filtered at 0.5 Hz) for representative stations. Waveforms relative to the MS1 are on the left and these of MS2 on the right. (a) P waves. (b) SH waves. (c) RSTFs deduced from the EGF analysis. (d) Local data; CMM station is presented but was not used to define the inverse model. Data are represented by thick gray lines whereas synthetics corresponding to the source models of Figure 3 are thin black lines. Selected stations and scales are the same for both shocks. Names and azimuths of stations are written on the right for the MS2 but, for clarity, have not been repeated for MS1. Agreement between data and synthetics at all stations can be seen in Figure A1.

Table 1. Crustal Model Used in the Source Analysis[a]

Th, km	V_P, km/s	V_S, km/s	ρ, kg/m^3	Q_P	Q_S
3.	4.	2.3	2400	300	150
28.	6.3	3.64	2750	600	300
0	8.	4.62	3250	1000	500

[a]*Th*, V_P, V_S, ρ, Q_P, Q_S are respectively the layer thickness, P-wave velocity, S-wave velocity, density and quality factor for P and S waves.

a similar manner as for body waves, we can relate the local wave field (computed in terms of discrete wave number method) to the patch parameters.

4. Source Inversion of MS1 and MS2

[11] The precise fault mechanism and hypocentral depth are crucial parameters for the source analysis and we choose to evaluate them separately. Using slip patch method only with teleseismic body waves, we determine that an hypocentral depth of 16 km for MS1 and 18 km for MS2, and a focal mechanism of (strike = 276°, dip = 84°, rake = 183°) for MS1 and (strike = 273°, dip = 76°, rake = 182°) for MS2 give the best agreement between synthetics and data. The necessity of a slightly different mechanism for both shocks can be seen for example with the noticeably different SH signals at station ATD (Figure 2b). The North-dipping plane defined for MS2 is also consistent with aftershock activity [*De Gori and Molise Working Group*, 2004].

[12] Knowing the focal depth and mechanism, we then investigate the other source characteristics by inverting simultaneously the three types of data. Given the simplicity of P, SH, and RSTFs waveforms, the introduction of a multi-patch model is not required. Thus, we aim at retrieving for both shocks the remaining 6 parameters of the one-patch model: position of the patch with respect to the hypocenter, size of the patch, slip and rupture velocity inside the patch. To do so, we minimize, in terms of L1 norm, the difference between data and synthetics (both low-pass filtered at 0.5 Hz), using the Neighborhood Algorithm (NA) [*Sambridge*, 1999]. The weight to different data is assigned in a way that one P waveform, one SH waveform, one RSTF and one local waveform have a similar importance in the inversion process. Tests done with a stronger weight for body waves logically result in a less well defined rupture lateral extension. In the misfit function, we also add the minimization of maximum slip as a slight constraint, to prevent from unphysical high stress drop models. By a repeated use of NA with different starting points, we define the mean values and standard errors of the main source parameters (Table 2). Agreement to seismic data is presented in Figure 2 and Figure A1[1]. Visualization of the best slip models is shown in Figure 3.

[13] The inversion results clearly show (Table 2 and Figure 3) that the two earthquakes are similar, not only in terms of depth, magnitude and focal mechanism, but also in terms of source kinematics. In particular both earthquakes exhibit a clear updip rupture propagation, with the rupture reaching about 6 km deep for MS1 and 9 km for MS2. MS1 is found only a bit larger (Mw = 5.8 versus Mw = 5.7), with a longer duration (5.4 s versus 4.1 s). The resolution on lateral extent is lower for MS1 because of a stronger trade-off with average slip in the patch (thus giving similar global moment). Rupture velocity as low as 1.1 km/s for MS1 was already identified in the preliminary source model of *Di Luccio et al.* [2005]. Using a larger number of seismic stations and different types of data, we confirm here a rather low rupture velocity (2 km/s, representing 55% of the shear velocity), but closer to classical models of earthquake rupture.

Table 2. Source Parameters Defined by the One-Patch Model Inversion for the 10/31/2002 (MS1, Hypocentral Depth = 16 km) and 01/11/2002 (MS2, Hypocentral Depth = 18 km) Shocks[a]

	MS1	MS2
Moment (10^{17} N.m)	5.46 (±0.16)	3.58 (±0.1)
Duration, s	5.39 (±0.13)	4.1 (±0.11)
Average slip, m	0.25 (±0.14)	0.15 (±0.02)
Rupture velocity, km/s	2.01 (±0.23)	2.56 (±0.19)
Top depth, km	6.03 (±1.08)	9.02 (±0.59)
Bottom depth, km	20.15 (±0.67)	18.43 (±0.12)
Eastward extension, km	2.46 (±0.57)	3.82 (±0.3)
Westward extension, km	2.74 (±1.28)	4.75 (±0.49)

[a]We present mean values and standard errors (between brackets) deduced from the 10 best models coming from 10 independent runs of NA.

[14] Our inversion for MS1 can also be compared with the work of *Gorini et al.* [2004]. Modelling peak ground accelerations, this study has identified both an updip and eastern rupture propagation. This latter property is not retrieved with our data, because the small variation of the RSTFs with azimuth constitutes a strong evidence for a bilateral rupture propagation. We also note that the eastern directivity is not obvious in the distribution of seismic intensities (http://www.ingv.it/roma/reti/rms/terremoti/italia/molise/molise.html).

5. Discussion

[15] We have shown that the two main earthquakes of the Molise sequence are kinematically similar, and that their

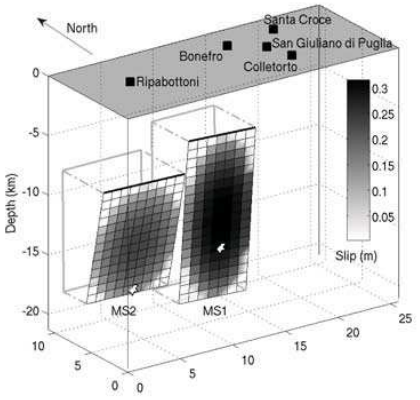

Figure 3. 3D visualization of the earthquakes slip showing that the two imaged slip patterns are almost contiguous. We present here typical slip models, which are the best models given by NA the closest from the mean values of Table 2. Hypocenters are indicated by white stars and map scales (East, North, vertical) are in km.

[1]Auxiliary material is available at ftp://ftp.agu.org/apend/gl/2005GL022687.

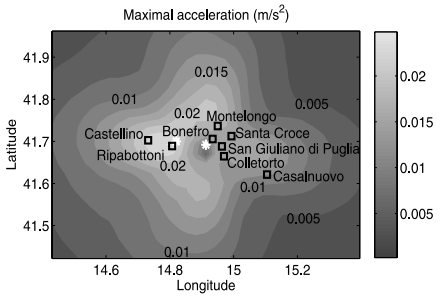

Figure 4. Location of maximum acceleration areas compared to the location of villages having experienced a seismic intensity superior or equal to VII.

slip patterns are almost contiguous. Postseismic activity [*Castello et al.*, 2005] is interestingly related with slip distribution. Few aftershocks occurred at depths between 10 and 20 km - where coseismic slip was large - whereas deeper and especially shallower events were much more common. In terms of earthquake mechanics, the main question that rises from this study is the 29 hour delay between the two events. Considering the spatial vicinity between the two shocks, it is interesting that the second event has not been dynamically triggered by the first one, resulting in a Mw = 6.0 earthquake. It shows that the distances between the two faults (of the order of 1 km) and/or their dip difference (8°) were enough to play the role of a barrier. As discussed by *Di Luccio et al.* [2005], low seismic energy, consistent with slow rupture velocity, could explain why the first shock was unable to dynamically trigger the second one. This example is as puzzling as the 1997 Umbria-Marche sequence, where two closely related earthquakes were separated by a 9 hour-delay [*Hernandez et al.*, 2004].

[16] Concerning seismic damage, the updip rupture propagation has had two important consequences. The more obvious one is the presence of slip close to the Earth surface (up to 6 km deep for MS1). The other one is the occurrence of the well-known directivity effect, which amplifies the radiation in the direction of the rupture propagation. The stronger damages due to MS1 in comparison to MS2 can be attributed to the combination of the following factors: (1) slightly larger seismic moment, (2) shallower top depth of the rupture and (3) epicenter closer to San Giuliano di Puglia in which site effects are particularly strong [*Azzara et al.*, 2003]. In terms of seismic risk assessment, this mid-crustal seismicity should be carefully considered in particular if the updip propagation generally characterizes the rupture process. Analysis of 2002 Molise aftershocks (Mw = 4–4.5), for which a denser accelerometric array was present, should be able to answer this question.

[17] In conclusion, we model in Figure 4 the location of maximum accelerations generated by the destructive first shock (MS1). To do so, we use our kinematical model (Figure 3) and calculate the seismic radiation on each point of a 2.5 × 2.5 km^2 grid (global size equal to 80 × 60 km^2) with the discrete wave number method [*Bouchon*, 1981]. This approach, purely deterministic, is not a strong motion simulation in which contributions from 3D structure, high frequency radiation and site effects should be included. In this sense we do not aim at retrieving realistic values of seismic accelerations. But finite-extent source effects (source extension, directivity) are present in the calculation and so, this method is able to provide an estimate, quickly and simply after an earthquake, of the potentially damaged zone. Figure 4 represents the maximum acceleration values (below 0.5 Hz) in the epicentral area. The East-West elongation of the maximum radiation area is in agreement with the villages having experienced a seismic intensity equal or superior to VII.

[18] **Acknowledgments.** We thank P. De Gori, A. Herrero, L. Improta, A. Zollo, G. Iannaccone, and N.A. Pino for fruitful discussions. This study has also been improved by the careful reviews of J. Zahradnik and Y. Yagi. We are grateful to GSN, GEOFON, Geoscope, and MedNet networks for access to broadband data and to the RAN (Rete Accelerometrica Nazionale, managed by the Servizio Sismico Nazionale) for access to accelerometric data. GMT and Latex free softwares were helpful to the preparation of the manuscript. This work was funded by the European "Marie Curie" fellowship MEIF-CT-2003-500901.

References

Azzara, R. M., T. Braun, F. Cara, G. Cultrera, G. Di Giulio, F. Marra, and A. Rovelli (2003), The ML 5.4 Molise earthquake (central Italy) of October 31, 2002: Why so destructive effects in San Giuliano di Puglia, *Geophys. Res. Abstr.*, *5*, 09611.

Bouchon, M. (1976), Teleseismic body wave radiation from a seismic source in a layered medium, *Geophys. J. R. Astron. Soc.*, *47*, 515–530.

Bouchon, M. (1981), A simple method to calculate Green's functions for elastic layered media, *Bull. Seismol. Soc. Am.*, *71*, 959–971.

Castello, B., G. Selvaggi, C. Chiarabba, and A. Amato (2005), *CSI Catalogo Della Sismicita Italiana 1981–2002, Versione 1.0*, Ist. Naz. di Geofis. e Vulcanol., Rome. (Available at http://www.ingv.it/CSI.)

De Gori, P., and Molise Working Group (2004), A first analysis of the 2002 Molise earthquake seismic sequence, *Geophys. Res. Abstr.*, *6*, 04040.

Di Bucci, D., and S. Mazzoli (2003), The October–November 2002 Molise seismic sequence (southern Italy): An expression of Adria intraplate deformation, *J. Geol. Soc. London*, *160*, 503–506.

Di Luccio, F., E. Fukuyama, and N. A. Pino (2005), The 2002 Molise earthquake sequence: What can we learn about the tectonics of southern Italy?, *Tectonophysics*, in press.

Gorini, A., S. Marcucci, P. Marsan, and G. Milana (2004), Strong motion records of the 2002 Molise, Italy, earthquake sequence and stochastic simulation of the main shock, *Earthquake Spectra*, *20*, S65.

Hartzell, S. H. (1978), Earthquake aftershocks as Green's functions, *Geophys. Res. Lett.*, *5*, 1–4.

Hernandez, B., M. Cocco, F. Cotton, S. Stramondo, O. Scotti, F. Courboulex, and M. Campillo (2004), Rupture history of the 1997 Umbria-Marche (central Italy) main shocks from the inversion of GPS, DInSAR and near field strong motion data, *Ann. Geophys.*, *47*, 1355–1376.

Mostardini, F., and S. Merlini (1986), Appennino centro-meridionale: Sezioni geologiche e proposta di modello strutturale, *Mem. Soc. Geol. It.*, *35*, 177–202.

Müller, G. (1985), The reflectivity method: A tutorial, *J. Geophys.*, *58*, 153–174.

Sambridge, M. (1999), Geophysical inversion with a neighbourhood algorithm. I. Searching a parameter space, *Geophys. J. Int.*, *138*, 479–494.

Scarascia, S., A. Lozej, and R. Cassinis (1994), Crustal structures of the Ligurian, Tyrrhenian and Ionian seas and adjacent onshore areas interpreted form wide angle seismic profiles, *Boll. Geofis. Teor. Appl.*, *36*, 5–19.

Valensise, G., D. Pantosti, and R. Basili (2004), Seismology and tectonic setting of the Molise, Italy, earthquake, *Earthquake Spectra*, *20*, S23.

Vallée, M. (2004), Stabilizing the empirical Green function analysis: Development of the projected Landweber method, *Bull. Seismol. Soc. Am.*, *94*, 394–409.

Vallée, M., and M. Bouchon (2004), Imaging coseismic rupture in far field by slip patches, *Geophys. J. Int.*, *156*, 615–630.

F. Di Luccio, Istituto Nazionale di Geofisica e Vulcanologia, I-00143 Rome, Italy.

M. Vallée, Géosciences Azur, IRD, F-06560 Valbonne, France. (vallee@geoazur.unice.fr)

II.2 Variabilité de la vitesse de rupture

II.2.1 Introduction

La vitesse de rupture est une caractéristique qui a une influence forte sur notre compréhension du processus sismique et sur les radiations engendrées. Schématiquement, la rupture sismique se propage d'un point A à un point B voisin de la faille car le glissement du point A radie une augmentation de la contrainte cisaillante sur le point B. Si cette contrainte est suffisamment forte, elle dépasse le seuil de résistance à la friction en B, ce qui cause le glissement du point B. Ce glissement crée lui-même une augmentation de la contrainte sur le point suivant, ce qui peut permettre au processus de se poursuivre.

La propagation d'une rupture dépend donc des valeurs d'augmentation de la contrainte radiée en B. La rupture est favorisée dans la configuration suivante :

- le point A a subi une chute de contrainte importante
- cette chute de contrainte en A a été efficacement convertie en énergie sismique radiée, sans être utilisée par d'autres processus (énergie de « fracturation », nécessaire à vaincre la résistance de la faille)
- le point B était déjà proche du seuil de résistance

En d'autres termes, cela signifie que la rupture se produit plus facilement quand l'énergie de déformation élastique relâchée (venant de la tectonique, au premier ordre) est à la fois élevée et efficacement convertie en énergie radiée. Par ailleurs, une faille dont tous les points sont proches du seuil rompt plus facilement.

Lorsque la rupture peut se propager, sa vitesse est également dépendante des paramètres précédents, comme cela a été montré dans les années 1970 (*Burridge*, 1973 ; *Andrews*, 1976). Dans le cas d'une rupture en mode II (ou mode plan, c'est-à-dire que la direction de propagation est colinéraire avec le glissement), cette vitesse peut soit être inférieure à la vitesse des ondes de Rayleigh (« subRayleigh »), soit comprise entre la vitesse des ondes S et P (« supershear » ou « intersonique »). Le régime supershear est de plus en plus probable lorsque les trois conditions précédentes sont vérifiées (*Andrews*, 1976 ; voir le paramètre k introduit par *Madariaga and Olsen*, 2000). En effet, un mécanisme simple de transition au régime supershear vient du fait que la résistance de la faille est vaincue par les contraintes radiées à des vitesses intersoniques (*Dunham*, 2007). Puisque ces contraintes sont plus faibles que celles radiées à la vitesse subRayleigh, cela implique une configuration encore plus favorable à la rupture sismique.

Dans la réalité, les vitesses de rupture sismiques ont été longtemps supposées appartenir seulement au premier régime, c'est-à-dire plus lentes que la vitesse de Rayleigh. Cela semblait donc indiquer des propriétés communes de la loi de friction et de la chute de contrainte, quels que soient les contextes sismiques. Cependant, dans la dernière décennie, la rupture supershear a pu été observée ou fortement suggérée pour plusieurs séismes (Izmit, Turquie, 1999 ; Duzce, Turquie, 1999 ; Kokoxili, Tibet, 2001 ; Denali, Alaska, 2002 ; voir références dans les articles de ce chapitre). Plus récemment, la rupture supershear a également

été fortement suggérée pour le séisme de Yushu (*Wang and Mori*, 2012). Nous avons montré, à partir de deux études complémentaires (voir section suivante), que le regime supershear peut être particulièrement bien mis en évidence pour le séisme de Kokoxili.

Ce comportement est donc bien réel dans la nature, ce qui implique que certaines failles (peut-être seulement les longues failles décrochantes) ont des propriétés de chutes de contrainte élevées ou d'énergies de fracture réduites. Une autre hypothèse viendrait de leur géométrie, qui est souvent rectiligne sur de longs segments (au moins plusieurs dizaines de kilomètres). Cette simplicité géométrique - surtout si on l'extrapole à une simplicité des paramètres mécaniques comme l'état de contrainte et la loi de friction - peut favoriser la poursuite du régime supershear une fois qu'il a été initié. L'absence de répliques sur la faille elle-même durant les séismes supershear (*Bouchon and Karabulut*, 2008), ainsi que les modèles dynamiques sur des failles simples, dans lesquelles le régime supershear est facilement atteint et maintenu, sont des arguments en faveur de cette hypothèse.

Par ailleurs, la radiation sismique créée par une rupture supershear est profondément différente de celle d'une rupture subRayleigh. La modification principale est la présence d'ondes de Mach. Ce phénomène est propre à toute émission d'ondes qui se fait à une vitesse plus rapide que la vitesse de propagation des ondes du milieu. Il est simplement dû au fait que dans certaines directions d'observation, les radiations générées par tous les points de la faille interfèrent constructivement. Je présente plus loin la première observation de ces ondes à distance régionale, ici aussi dans le cas du séisme de Kokoxili. La présence de ces ondes est une confirmation supplémentaire de l'existence du régime supershear, mais pose aussi de nouvelles questions sur leur rôle dans les mouvements forts générés au voisinage des séismes. Il est clair que leur amplitude attendue, dans des cas où la rupture est cohérente et se produit dans un milieu homogène, sera très forte (*Bernard and Baumont*, 2005). Cependant, les observations très parcellaires des pics d'accélération au voisinage de séismes supershear ne montrent pas des valeurs élevées (*Ellsworth et al.*, 2004). Plusieurs hypothèses sont donc aujourd'hui envisagées :

- ces rares points d'observation n'étaient pas placés dans des directions favorables par rapport au cône de Mach, sur lequel l'amplitude maximale se produit
- le processus de rupture et/ou le milieu de propagation est suffisamment incohérent pour détruire les effets constructifs à haute fréquence (*Andrews*, 2010 ; *Bizzarri et al.*, 2010)
- les ruptures supershear ne se produisent que sur des failles simples, ce qui limite le contenu haute-fréquence des ondes dès leur émission à la source (*Bizzarri et al.*, 2010).

II.2.2 Observation du mode de rupture supershear

Dans cette section sont reproduits deux articles (*Bouchon and Vallée*, 2003 ; *Vallée et al.*, 2008), qui documentent l'existence de la rupture supershear lors du séisme de Kokoxili (Tibet, 14/11/2001). Le premier article se base sur l'analyse et l'inversion des données régionales, pour montrer qu'une vitesse de rupture moyenne rapide (3.9km/s, à comparer à la vitesse de cisaillement de l'ordre de 3.5km/) est nécessaire pour expliquer les données. Une accélération de la vitesse en cours de rupture est également mise en évidence.

Le deuxième article est une analyse encore plus observationnelle, fondée sur les techniques d'analyse en réseau. Le réseau étudié est situé au Népal, à environ 1000km de la source du séisme de Kokoxili. L'avantage de cette approche est de d'imager directement la progression de la rupture, sans avoir recours à des approches d'inversion. Nous présentons d'abord une description de la méthode, avant de montrer comment les ondes observées au travers du réseau détectent une vitesse de rupture supershear sur un segment d'environ 170km de long. En parallèle, cette étude montre que les zones de transition entre régime subRayleigh et supershear émettent la majorité des radiations haute-fréquence. Le document présenté à la suite de l'article est un compte-rendu de ses résultats principaux, présenté dans la section « News and Views » du journal *Science*.

(~3000 m depth), below which abyssal waters are devoid of detectable reflections (Fig. 4). Because this feature is consistent in the sections, we speculate that the transition from reflective to transparent waters at ~3000 m depth may represent the boundary between Labrador Sea Water and Norwegian-Greenland Overflow Water of the Deep Western Boundary Current (*22, 23*).

The ability to create detailed images of thermohaline structure in the ocean with low-frequency marine seismic reflection techniques adds a promising new tool for studies of oceanographic processes. The structures imaged in our North Atlantic transects have important implications for oceanic mixing and exchange processes and raise the possibility that the boundaries of deep water masses such as North Atlantic Bottom Water can be mapped seismically. Low-frequency seismic reflection techniques appear well-tuned to image thermohaline fine structure, provided that layers are at least 5 m thick and laterally continuous over hundreds of meters. Reflection techniques offer several advantages—including enhanced lateral resolution (trace spacing of ~6 m), the ability to simultaneously image large sections of the ocean, and opportunities for three-dimensional and time-lapse imaging—that make them an ideal complement to more traditional methods of probing the ocean, which are more limited in their space-time resolution. Finally, our results imply that the extensive global archive of marine seismic reflection data constitutes a large, untapped resource for probing ocean structure.

References and Notes

1. H. Stommel, K. N. Federov, *Tellus* **19**, 306 (1967).
2. R. D. Pingree, *Deep Sea Res.* **16**, 275 (1969).
3. R. W. Schmitt, H. Perkins, J. D. Boyd, M. C. Stalcup, *Deep Sea Res.* **34**, 1655 (1987).
4. T. M. Joyce, *Deep Sea Res.* **23**, 1175 (1976).
5. T. M. Joyce, *J. Phys. Oceanogr.* **7**, 626 (1977).
6. T. M. Joyce, W. Zenk, J. M. Toole, *J. Geophys. Res.* **83**, 6093 (1978).
7. D. Rudnick, R. Ferrari, *Science* **283**, 526 (1999).
8. J. Gonella, D. Michon, *C. R. Acad. Sci. Paris Ser. II* **306**, 781 (1988).
9. J. D. Phillips, D. F. Dean, in *Ocean Variability and Acoustic Propagation*, J. Potter, A. Warn-Varnas, Eds. (Kluwer Academic, Dordrecht, Netherlands, 1991), pp. 199–214.
10. L. R. Haury, M. G. Briscoe, M. H. Orr, *Nature* **278**, 312 (1979).
11. P. H. Wiebe, T. K. Stanton, M. C. Benfield, D. G. Mountain, C. H. Greene, *IEEE J. Ocean. Eng.* **22**, 445 (1997).
12. The observed reflections are coherent in both the shot and CMP domains, and thus cannot be seafloor multiples from previous shots, which are coherent only in the shot domain.
13. We have not applied migration (a process that places dipping events in their proper spatial position) to the images shown. However, because of the small dips of reflectors, migration does not change the images appreciably. We show unmigrated sections because migration artifacts from the seafloor reflection, which has a much higher amplitude than the water column reflections, degrades the deeper portions of migrated sections.
14. The sound source was a 140-liter, 20-element airgun array, and reflections were recorded on a 480-channel, 6-km-long hydrophone streamer. Data were digitized at a sample interval of 4 ms and have a frequency content of 10 to 100 Hz, with a peak frequency near 40 Hz.
15. R. W. Schmitt, D. T. Georgi, *J. Mar. Res.* **40** (suppl.), 659 (1982).
16. D. T. Georgi, R. W. Schmitt, *J. Phys. Oceanogr.* **13**, 632 (1983).
17. Using data corrected for spherical divergence, we calculated the reflection coefficient of the seafloor as $-A_{mult}/A_{sf}$, where A_{mult} is the amplitude of the first seafloor multiple and A_{sf} is the amplitude of the seafloor reflection (*18*). We then calculated reflection coefficients in the water column from the ratio of the amplitudes of water column reflections and the seafloor reflection.
18. M. Warner, *Tectonophysics* **173**, 15 (1990).
19. C. Garrett, W. Munk, *Annu. Rev. Fluid Mech.* **11**, 339 (1979).
20. Because the profiles are collected by a ship traveling at a rate of about 8 km/hour, the images can only be regarded as instantaneous "snapshots" at local scales of about 2 km.
21. B. Ruddick, K. Richards, *Prog. Oceanogr.* **56**, 499 (2003).
22. R. S. Pickart, W. M. Smethie, J. R. N. Lazier, E. P. Jones, W. J. Jenkins, *J. Geophys. Res.* **101**, 20711 (1996).
23. R. S. Pickart, *Deep Sea Res.* **29**, 1553 (1992).
24. P. Wessel, W. H. F. Smith, *Eos* **72**, 441 (1991).

25. We thank the captain and crew of the R/V *Maurice Ewing* for a successful cruise, and A. Gorman, D. Lizarralde, J. Stennett, K. Polzin, T. Joyce, E. Montgomery, and D. Shillington for helpful conversations. B. Tucholke, K. Louden, J. Hopper, H. C. Larsen, and H. van Avendonk contributed to data acquisition. Data were processed using Sioseis, Paradigm's Focus software, and Generic Mapping Tools (*24*). Supported by NSF grants OCE-9819599 (W.S.H.) and OCE-0081502 (R.W.S.).

31 March 2003; accepted 29 May 2003

Observation of Long Supershear Rupture During the Magnitude 8.1 Kunlunshan Earthquake

Michel Bouchon* and Martin Vallée

The 2001 Kunlunshan earthquake was an extraordinary event that produced a 400-km-long surface rupture. Regional broadband recordings of this event provide an opportunity to accurately observe the speed at which a fault ruptures during an earthquake, which has important implications for seismic risk and for understanding earthquake physics. We determined that rupture propagated on the 400-km-long fault at an average speed of 3.7 to 3.9 km/s, which exceeds the shear velocity of the brittle part of the crust. Rupture started at sub–Rayleigh wave velocity and became supershear, probably approaching 5 km/s, after about 100 km of propagation.

The Kunlunshan earthquake that hit Tibet on 14 November 2001 produced the longest rupture yet observed for an earthquake on land. The mapped surface break of the earthquake extends for ~400 km (*1*, *2*). The exceptional length of this event and the presence of several regional broadband stations of the China Digital Seismic and Incorporated Research Institutions for Seismology (IRIS) networks provide a unique opportunity to determine the speed at which rupture propagates on a fault during an earthquake. In the past, it has been thought that earthquake rupture can only propagate at speeds below the Rayleigh-wave velocity of crustal rocks, which, at about 0.92 times the shear (*S*)–wave velocity, lies in the range of 3.0 to 3.2 km/s for the brittle part of the crust. This belief was backed by fracture dynamics theory, which shows that a rupture cannot propagate at a speed between the Rayleigh-wave and *S*-wave velocities. However, more recent works (*3*–*5*) show that, although the range of velocity between the Rayleigh and *S* waves is not allowed, shear cracks can theoretically propagate at intersonic speeds; that is, at speeds between the *S*-wave and the pressure (*P*)–wave velocities. Subsequent theoretical (*6*–*8*) and experimental (*9*, *10*) studies in fracture dynamics confirm these findings.

Values of rupture velocity inferred from studies of earthquakes support the Rayleigh velocity limit to earthquake rupture with a few exceptions of reported observations of supershear rupture (*11*–*15*). Although these observations have not been fully accepted, they have nevertheless generated strong interest in understanding conditions that can lead to supershear rupture (*16*, *17*) and in assessing its seismic risk consequences (*18*).

The Kunlunshan earthquake was recorded in Tibet and surrounding regions by broadband seismic stations (fig. S1). These stations lie at distances between 600 and 1900 km from the fault, a distance range at which the records are dominated by surface (Rayleigh and Love) waves and, especially, because of the strike-slip mechanism of the

Université Joseph Fourier and Centre National de la Recherche Scientifique, Laboratoire de Géophysique Interne et Tectonophysique, Boîte postale 53, 38041 Grenoble, France.

*To whom correspondence should be addressed. E-mail: Michel.Bouchon@ujf-grenoble.fr

earthquake, by Love waves. We used these surface waves to infer the rupture velocity of the earthquake. To do this, we needed to determine the travel-time velocity of Love waves along the various source-station paths.

A year before the Kunlunshan earthquake, an earthquake of magnitude 5.4 occurred in the epicentral area of the Kunlunshan earthquake. We used records from this 5.4 earthquake (fig. S1) to determine the one-dimensional lithospheric velocity structure beneath the fault and receivers. We divided the lithosphere into 5-km-thick layers and inverted the *S*-wave velocity in each layer. This inversion was carried out independently for each station and was based on matching the observed records of the earthquake with the ones calculated by the discrete wave number method (*19*). Because Love waves are polarized transverse to their direction of propagation, we used the record component at each station that is transverse to the epicenter-station path. As the main shock records contain mostly energy at periods longer than 20 s, we low-pass filtered the records above 20 s. We obtained good fits to the waveforms and *S*-wave velocity models (fig. S1 and table S1) that represent the crustal or lithospheric structure averaged over the paths from the source to each station. The crustal thickness of the models ranges from 50 km for paths to northeastern China (the BJT station) and Mongolia (the ULN station) to 65 km for paths almost entirely across the Tibetan Plateau (the LSA and KMI stations).

Knowing the velocity structure, we then simulated the earthquake rupture and calculated the resulting ground motion at each station. We modeled the Kunlunshan earthquake as a rupture that started at the hypocenter and propagated radially on the fault. The N99°E fault plane is vertical and follows the mapped surface breaks (*1*, *2*). The fault slip (fig. S2) is the one measured in the field (*2*) and is assumed to be uniform with depth. To the east, the fault model extends to the end of the mapped surface rupture (94°47.706′E, 35°33.387′N) (*2*). To the west, it ends 15 km west of the U.S. Geological Survey epicentral location (90°32.4′E, 35°57.0′N), giving the fault rupture a total length of 400 km. The precise western termination of the fault, which is not well recognized in the field, is not critical, because slip west of the epicenter is small and did not radiate much seismic energy. The hypocentral depth was set at 15 km, but the synthetic records are unsensitive to it. The calculated waveforms are also unsensitive to the bottom depth of the fault. For the ground-motion calculation, which we performed with the discrete wave number method (*19*), the fault plane was discretized into point sources located at 2-km intervals along the strike and along the depth. At each point, slip began at the arrival of the rupture front and was assumed to grow at a constant rate for 5 s, after which time it reached the value measured in the field. This choice of rise time corresponds to an average slip velocity of about 1 m/s over the fault and is based on previous studies of large earthquakes (*15*, *20*).

We first determined how well a near-Rayleigh rupture velocity could explain the observed Love-wave records. This comparison between synthetics and data is shown (Fig. 1A) for the stations that lay in the forward direction relative to the propagating rupture and that, for this reason, were highly sensitive to the rupture velocity. The velocity considered was 3 km/s, which is close to the Rayleigh velocity of the upper crust. For this value, the timing of the synthetics did not match the timing of the observed waveforms. When we lowered the rupture velocity below 3 km/s, the fit to the data deteriorated further.

To infer the rupture velocity, we divided the 400-km-long fault into four 100-km-long segments and performed a grid search to determine the values that best fit the observations. The best fit obtained (Fig. 1B) corresponds to an average rupture velocity of 3.9 km/s, with a sub-Rayleigh velocity of 2.4 km/s on the first segment and supershear velocities close to 5 km/s on the other three segments. An independent inversion of each record separately yielded results consistent with a rupture that is sub-Rayleigh on the first segment and supershear on the other three. Calculations done with a single 400-km-long segment (i.e., not allowing for spatial variations in rupture velocity) yielded a rupture velocity of 3.7 to 3.8 km/s, regardless of the stations considered.

One of the recording stations, WMQ, lies in the back azimuth relative to the propagating rupture. As a result, the various arrivals there were more spread out in time (Fig. 2A) and two of them can be identified: The first pulse of the Love-wave train originated from the epicentral area, whereas the largest pulse of the wave train was radiated from the fault area that slipped the most during the earthquake. The time difference between these two phases provides a constraint on the rupture velocity. To determine it, we again divided the fault into four 100-km-long segments and performed a grid search that allowed the rupture to vary between 2 and 6 km/s on each segment. The best fit to the record (Fig. 2A) is obtained for a sub-Rayleigh velocity of 2.8 km/s on the first segment and a supershear velocity of 5 km/s on the second and third segments. Rupture velocity on the last segment is poorly resolved, because the records at WMQ are not sensitive to rupture on this part of the fault, where slip is smaller and which lies further from the station. Rupture velocity values on the first three segments yielded an average rupture speed of 3.9 km/s for the first 300 km of rupture. A grid search performed for a single 400-km-long segment with uniform rupture velocity yielded the same value.

The remaining station, LSA, is the one closest to the source and is located in a direction almost perpendicular to the fault. This location provides a wide-angle view of the fault. The horizontal motion displayed at the station in different time windows (Fig. 2, B to E) shows how the direction of incoming seismic energy changes with time. The first window corresponds to the first seconds of energy arrival from the earthquake. This energy travels as *P* waves, which are polarized in the direction of

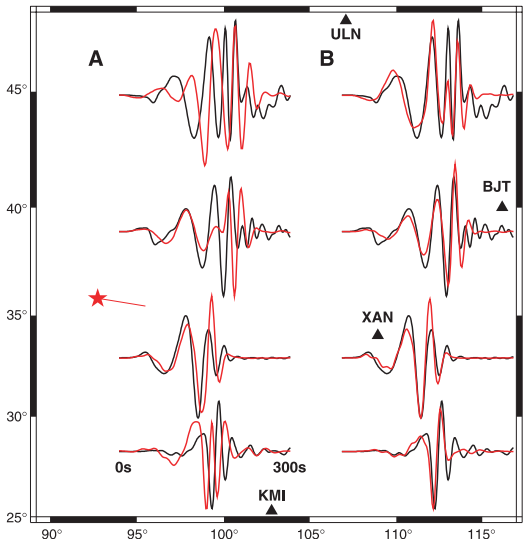

Fig. 1. Comparison between the recorded ground motion (in black) for the Kunlunshan earthquake and the one calculated (in red) for (**A**) a rupture velocity of 3 km/s and (**B**) the best-fitting rupture velocity, which averages 3.9 km/s. The component shown is the horizontal displacement in the direction transverse to the epicenter-station path; it starts with a reduced time equal to the epicentral distance divided by 4.5 km/s. The epicenter (star), the fault geometry (red line), and the station locations (triangles) are displayed.

REPORTS

propagation so that the horizontal motion displays their incoming direction, which corresponds to the epicentral location (Fig. 2B). The second time window (Fig. 2C) includes the beginning of the Love-wave arrivals, which, being polarized transverse to their travel direction, also point to the epicentral location. The third time window (Fig. 2D) corresponds to the first Love-wave cycle. The horizontal motion is an elongated distorted ellipse, described clockwise as a function of time. This elliptical motion results from a combination of large displacements (Love waves) transverse and small displacements (Rayleigh waves) radial to the travel direction. The axis of the first half of the ellipse runs nearly east-west, whereas the axis of the second half is tilted to the south. This indicates that the direction of the incoming waves rotated clockwise, which in turn shows the eastward propagation along the fault of the source of energy released during the first ~30 s of rupture. The fourth time window (Fig. 2E) displays the horizontal motion between 63 s and 79 s after the beginning of the Love-wave arrivals. The motion is still approximately elliptical, but the ellipse axis has now rotated to a direction that indicates that the corresponding source of energy radiation was approaching the eastern end of the fault. Although a precise estimate of rupture velocity is not possible from the diagrams because of the presence of Rayleigh waves and the long duration of a Love-wave cycle, they indicate that between 60 s and 80 s after the start of rupture, the source of energy was well past the middle of the fault and approaching the easternmost part of the rupture. This requires a fast propagation of the rupture and supports the observations at the other stations.

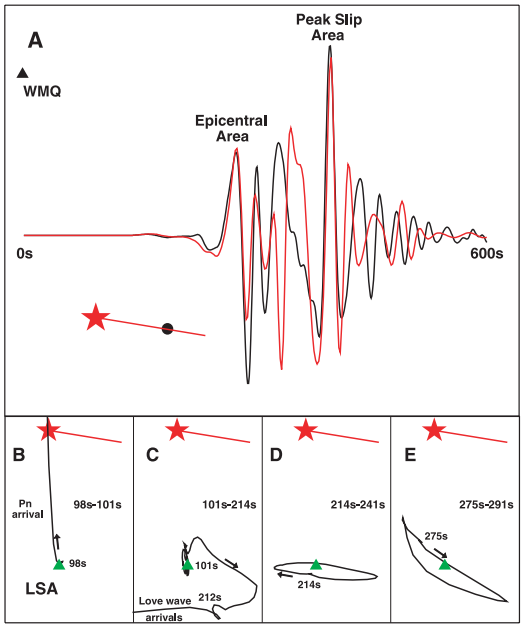

Fig. 2. (**A**) Comparison between the ground motion recorded at WMQ in the direction transverse to the epicenter-station path (in black) with the one calculated (in red) for the best-fitting rupture velocity. The epicenter (star), fault geometry (red line), area of peak slip (black circle), and station location (triangle) are displayed. (**B** to **E**). Time evolution of the horizontal displacement recorded at LSA. The time starts at the origin time of the earthquake. The arrow indicates the evolution of particle motion with increasing time. The polarity of motion in frame (B) is reversed to show the direction of incoming waves. Pn is the first wave arrival.

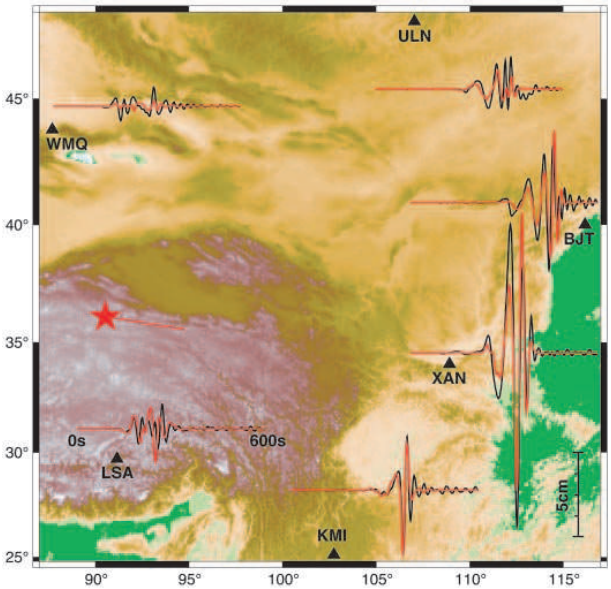

Fig. 3. Comparison of the recorded (black) and computed (red) ground motion in the direction transverse to the epicenter-station paths. A station amplitude correction determined from the amplitude matching of the precursory shock relative to the IRIS station ULN has been applied to the data. Each signal begins 50 s before the *P*-wave arrival and is 600 s long. The depth of faulting is 17 km and the average rupture velocity of the model is 3.9 km/s, with specific values of 2.4, 5.0, 4.8, and 5.0 km/s on the four 100-km-long segments; these individual values are not resolved precisely, but they indicate that rupture started at sub-Rayleigh velocity and became supershear, probably approaching 5 km/s, after some 100 km of propagation.

The elastic energy radiated by the earthquake is closely linked to the rupture velocity. The recorded ground motion displays a strong directivity effect (Fig. 3), because most of the radiated energy is focused along azimuths close to the direction of rupture propagation. This observed azimuthal pattern is explained by the rupture velocity values that we have previously inferred. The amplitude matching between data and synthetics indicates that the seismogenic depth is close to 17 km, which yields a seismic moment of about 6.2×10^{20} N·m.

References and Notes

1. A. Lin *et al.*, *Science* **296**, 2015 (2002).
2. X. Xu, W. Chen, W. Ma, G. Yu, G. Chen, *Seism. Res. Lett.* **73**, 884 (2002).
3. R. Burridge, *Geophys. J.* **35**, 439 (1973).
4. D. J. Andrews, *J. Geophys. Res.* **81**, 5679 (1976).
5. S. Das, K. Aki, *Geophys. J. Roy. Astr. Soc.* **50**, 643 (1977).
6. L. B. Freund, *J. Geophys. Res.* **84**, 2199 (1979).
7. S. M. Day, *Bull. Seism. Soc. Am.* **72**, 1881 (1982).
8. P. G. Okubo, *J. Geophys. Res.* **94**, 12321 (1989).
9. A. J. Rosakis, O. Samudrala, D. Coker, *Science* **284**, 1337 (1999).
10. A. J. Rosakis, O. Samudrala, D. Coker, *Mat. Res. Innovat.* **3**, 236 (2000).
11. R. J. Archuleta, *J. Geophys. Res.* **89**, 4559 (1984).
12. P. Spudich, E. Cranswick, *Bull. Seism. Soc. Am.* **74**, 2083 (1984).
13. K. B. Olsen, R. Madariaga, R. J. Archuleta, *Science* **278**, 834 (1997).
14. W. L. Ellsworth, M. Çelebi, *Am. Geophys. Union, Fall Meeting Suppl.* **80**, F648 (1999).
15. M. Bouchon *et al.*, *Geophys. Res. Lett.* **27**, 3013 (2000).
16. J. Weertman, *Geophys. Res. Lett.* **29**, 109 (2002).
17. E. M. Dunham, P. Favreau, J. M. Carlson, *Science* **299**, 1557 (2003).
18. P. Bernard, *Europ. Seism. Comm. XXVIII Meeting* (2002).
19. M. Bouchon, *Bull. Seism. Soc. Am.* **71**, 959 (1981).
20. R. Madariaga, K. B. Olsen, in *International Handbook of Earthquakes and Engineering Seismology*, W. Lee, H. Kanamori, P. Jennings, C. Kisslinger, Eds. (Academic Press, London, 2002), p. 175.
21. We thank the three anonymous referees for their constructive reviews.

Supporting Online Material
www.sciencemag.org/cgi/content/full/301/5634/824/DC1
Figs. S1 and S2
Table S1

14 May 2003; accepted 3 July 2003

JOURNAL OF GEOPHYSICAL RESEARCH, VOL. 113, B07305, doi:10.1029/2007JB005520, 2008

The 14 November 2001 Kokoxili (Tibet) earthquake: High-frequency seismic radiation originating from the transitions between sub-Rayleigh and supershear rupture velocity regimes

M. Vallée,[1] M. Landès,[2] N. M. Shapiro,[2] and Y. Klinger[2]

Received 23 November 2007; revised 31 March 2008; accepted 5 May 2008; published 24 July 2008.

[1] Seismic array based analysis of the major Kokoxili earthquake (Tibet, 14 November 2001) yields an unambiguous reconstruction of the seismic rupture history and relates it to the generated seismic radiation. We demonstrate that after a classical sub-Rayleigh velocity stage, the rupture speed has jumped to supershear values close to compressional wave velocity over a 175-km-long fault segment, before abruptly slowing down in the late part of the earthquake. The transition locations between these three phases are correlated with the fault geometry and are associated with the most energetic radiation. This observation proves that the rupture velocity changes, as theoretically predicted, are a primary source of high-frequency seismic radiation. This result requires reconsidering the origins of seismic damage, generally attributed to slip variations.

Citation: Vallée, M., M. Landès, N. M. Shapiro, and Y. Klinger (2008), The 14 November 2001 Kokoxili (Tibet) earthquake: High-frequency seismic radiation originating from the transitions between sub-Rayleigh and supershear rupture velocity regimes, *J. Geophys. Res.*, *113*, B07305, doi:10.1029/2007JB005520.

1. Introduction

[2] Seismic rupture mechanics aims at better understanding of how stresses stored in the Earth are released by earthquakes. When stresses overcome the fault friction, rupture initiates and then propagates with different velocities, depending on the rupture potential energy and fault properties [*Andrews*, 1976; *Day*, 1982; *Festa and Vilotte*, 2006; *Dunham*, 2007]. It has been theoretically demonstrated in the 1970s [*Andrews*, 1976] that two rupture velocity modes are possible: either the rupture propagates slower than the Rayleigh velocity (about 0.92 times the shear (*S*) wave velocity), or between the shear and the compressional (*P*) velocity. This last regime, called supershear, can exist only if the fault prestress level is high, compared to the failure stress and the residual stress. Moreover fracture energy has to be sufficiently low to permit the development of the supershear phase within the finite length of a real fault [*Andrews*, 1976; *Dunham*, 2007].

[3] Rupture supershear propagation does not only provide information about the physical processes leading to earthquakes, but it also strongly modifies the nature of seismic radiation and thus the origins of the damaging waves generated by earthquakes. The most striking difference between supershear and sub-Rayleigh rupture is the presence of an energetic and potentially destructive Mach *S* wave [*Bernard and Baumont*, 2005]. Determining if a supershear rupture necessarily implies more devastating effects than a sub-Rayleigh rupture is today an active research area. As a matter of fact, the Mach cone effect could be reduced by a smoother source time function, intrinsically related to the supershear propagation dynamics [*Ellsworth et al.*, 2004; *Bizzarri and Spudich*, 2008]. Moreover, if the rupture continuously propagates close to an upper limit (*P* wave velocity), high-frequency radiation related to rupture accelerations and decelerations is reduced. These velocity variations of the rupture front are theoretically known to be a primary source of high-frequency seismic radiation [*Madariaga*, 1977; *Campillo*, 1983; *Sato*, 1994].

[4] Today, it has been shown that both regimes cohabit in laboratory experiments that mimic earthquake rupture [*Rosakis et al.*, 1999]. There is also growing evidence that this may be the case for the real-world events. The first earthquake for which supershear mode has been proposed is the 1979 Imperial Valley earthquake (M_w = 6.5) [*Archuleta*, 1984; *Spudich and Cranswick*, 1984]. More recent works have shown that this behavior could be more frequent than previously expected: the 1999 Izmit earthquake (M_w = 7.4) [*Bouchon et al.*, 2000, 2001], the 1999 Duzce earthquake (M_w = 7.1) [*Bouchon et al.*, 2001], the 2001 Kokoxili earthquake (M_w = 7.8) [*Bouchon and Vallée*, 2003; *Robinson et al.*, 2006] and the 2002 Denali earthquake (M_w = 7.9) [*Ellsworth et al.*, 2004; *Dunham and Archuleta*, 2004; *Aagaard and Heaton*, 2004] all present some indications for supershear rupture. The main weakness of most of these studies, which also explains why the existence of supershear rupture has not been fully accepted, is that rapid rupture velocities are derived from earthquake source inversions,

[1] Géosciences Azur, University of Nice Sophia Antipolis, IRD, CNRS, UPMC, Valbonne, France.
[2] Institut de Physique du Globe de Paris and CNRS, Paris, France.

0148-0227/08/2007JB005520$09.00

affected by some trade-offs between parameters (slip, rupture velocity, risetime) [*Beresnev*, 2003]. An exception is the early work of *Spudich and Cranswick* [1984], which provides a more direct observation of the moderate Imperial Valley earthquake by an array technique. Because of the limited information on the supershear regime, and its strong implications in terms of earthquake physics and seismic radiation, scientists have underlined the need of new analyses and observations of rapid rupture velocities [*Das*, 2007].

[5] In this study, our first goal is to provide a clear observation of the supershear regime. We focus on the 14 November 2001 Kokoxili earthquake, where an array of broad band stations deployed in Nepal allows us to track the rupture propagation, with a similar approach as that of *Spudich and Cranswick* [1984]. We show that the array configuration, associated with the exceptional length of the event, allows us to well identify a long fault segment where supershear rupture has occurred. We demonstrate that earthquake rupture velocity may even approach the compressional (P) wave velocity. Going further, we put in light the first-order importance that the rupture transition points have on seismic radiation. These points, where rupture accelerates to supershear velocity and then decelerates to the sub-Rayleigh regime, are shown to be localized zones of the fault which emit most of the high-frequency content of the seismic radiation. These localized zones are well correlated with geometrical fault complexities, illustrating the interactions between rupture regimes, seismic radiation and fault geometry.

2. Array Analysis of the Kokoxili Earthquake

2.1. The 14 November 2001 Kokoxili Earthquake

[6] On 14 November 2001, the major Kokoxili earthquake (M_w = 7.8) struck an arid region in the northern Tibet (Figure 1). This exceptional event ruptured the Kunlun fault, one of the major left-lateral strike-slip faults accommodating the eastward extrusion of Tibet in response to Indian collision [*Van der Woerd et al.*, 2002]. Its rupture length, about 400 km, has made this earthquake the longest inland event ever recorded by digital seismology. Most of the rupture has propagated unilaterally eastward, from the epicenter located at 90.5°E, 35.9°N to the beginning of the Kunlun Pass fault at 94.5°E, 35.6°N [*Klinger et al.*, 2005; *Lasserre et al.*, 2005; *Xu et al.*, 2006; *Klinger et al.*, 2006]. Classical methods of source process inversion have revealed that the rupture propagation was faster than usually observed, with average velocities ranging between 3.4 and 4.5 km/s [*Bouchon and Vallée*, 2003; *Antolik et al.*, 2004; *Ozacar and Beck*, 2004; *Robinson et al.*, 2006; *Tocheport et al.*, 2006]. Although these results indicate a likely existence of the supershear regime, some uncertainties have impeded further investigations of the earthquake source process. In particular, the conjoint inversion of slip and rupture velocity does not allow to precisely separate which of the two effects is dominant in terms of seismic radiation.

2.2. Data and Array Method

[7] During the Himalayan Nepal Tibet Seismic Experiment (HIMNT), a temporary network of broadband seismometers (Streckeisen STS2) was deployed in Nepal and Tibet in 2001–2003 to study the Himalaya structure [*Schulte-Pelkum et al.*, 2005; *Monsalve et al.*, 2006]. The Kokoxili earthquake, as well as its numerous aftershocks, has been well recorded by a large part of this network. This data set offers a very favorable configuration to track the rupture propagation using array techniques [*Krüger and Ohrnberger*, 2005; *Ishii et al.*, 2005]. Depending on the location of the radiating points along the Kunlun fault, the time shifts of the radiation arrivals change at the HIMNT stations. The basic idea is to define, at each time of the seismograms, the location of the radiating points that agree the best with the observed time shifts. The formulation of this optimization problem is described as follows. Assuming that the instantaneous source is located at a fault location x_i, with Rayleigh waves phase velocity through the array V_j, the family of stacked velocity signals U_{ij} windowed in the interval $[t_0 - T_w/2,\ t_0 + T_w/2]$ is written as

$$U_{ij}(t) = \sum_{k=1}^{N} \frac{W_{t_0,T_w}\left[u_k\left(t - \Delta t_{ijk}\right)\right]}{A_{k,t_0,T_w}} \tag{1}$$

where the time shift Δt_{ijk} is defined as

$$\Delta t_{ijk} = (r_{i1} - r_{ik})/V_j \tag{2}$$

W_{t_0,T_w} is the rectangular window function with center t_0 and width T_w, N is the number of stations, u_k is the velocity seismogram of station k, and r_{ik} is the distance between point located at x_i and station k. A_{k,t_0,T_w} normalizes the amplitude for each seismogram inside each window, with respect to a given reference station. This normalization factor is used to take into account amplitude changes between stations due to different geometrical spreading effects and different radiation amplitudes. The family of stacked energy signals E_{ij}, windowed in the interval $[t_0 - T_w/2,\ t_0 + T_w/2]$ is defined as

$$E_{ij}(t) = \sum_{k=1}^{N} \frac{W_{t_0,T_w}\left[u_k^2\left(t - \Delta t_{ijk}\right)\right]}{A_{k,t_0,T_w}^2} \tag{3}$$

and the semblance [*Neidell and Taner*, 1971] in the interval $[t_0 - T_w/2,\ t_0 + T_w/2]$ is expressed as

$$S_{ij} = \frac{\int_{t0-T_w/2}^{t0+T_w/2} U_{ij}^2(t)dt}{N\int_{t0-T_w/2}^{t0+T_w/2} E_{ij}(t)dt} \tag{4}$$

Since the time series U and E are discrete, discrete sums are used to evaluate S_{ij}.

[8] The HIMNT stations are located about 1000 km from the Kokoxili earthquake. At such distances, Rayleigh surface waves are by far the most energetic signal in the vertical seismograms for a superficial earthquake (see aftershock seismograms in Figure 1). Moreover, aftershock signals show that body waves are complex and not enough separated in time to analyze the 100-s-long duration of the main shock. We therefore apply the array technique to Rayleigh waves recorded at seven stations (Figure 1, see their locations in Table 1) and filtered between 0.04 Hz and 0.1 Hz using a two-pass, two-pole, Butterworth filter. Lower

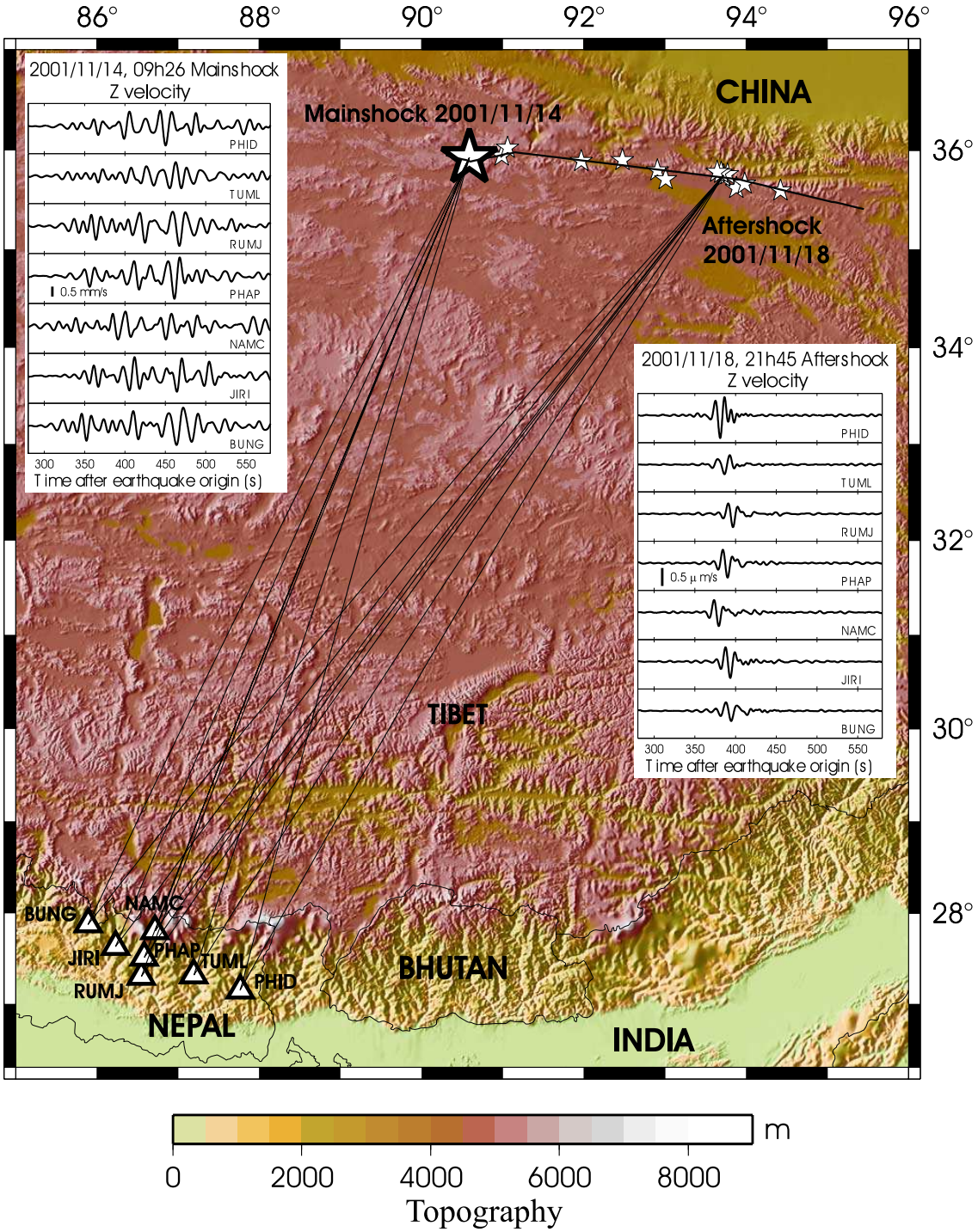

Figure 1. Location of the earthquakes (stars) and the HIMNT seismic stations selected in this study (triangles). The large star shows the main shock epicenter, and the smaller stars indicate the locations of the aftershocks used to estimate array accuracy (Figure 2). Vertical ground motion velocities at the seven stations (filtered between 0.04 and 0.1 Hz) are shown both for the main shock (left inset) and for an aftershock (right inset).

Table 1. Location of the Seven HIMNT Stations Selected in This Study

Station	Latitude	Longitude	Elevation (m)
PHID	27.1501	87.7645	1176
TUML	27.3208	87.1950	360
RUMJ	27.3038	86.5482	1319
PHAP	27.5150	86.5842	2488
NAMC	27.8027	86.7146	3523
JIRI	27.6342	86.2303	1866
BUNG	27.8771	85.8909	1191

frequencies reduce the array resolving power, while higher frequencies have little coherency because of the station separation. T_w is taken equal to 25 s, which is longer than the dominant period of the filtered seismograms (10–15 s). Longer windows would reduce the spatial resolving power. We successively shift t_0 in steps of 5 s, and calculate for each window the semblance associated with the possible values of x_i (along the Kunlun fault trace) and V_j. The optimal semblance values define the actual fault emission location and phase velocity.

[9] The array analyses are possibly biased by regional crustal heterogeneity which deflects the seismic wavefield (off-great circle propagation). This may cause a discrepancy between the observed arrival direction and the actual station-source azimuth. In order to correct this bias, 14 aftershocks with known locations were analyzed. In this case, the source location does not change when the window moves. Figure 2a shows an example of coherency optimization (in terms of semblance) for one of these aftershocks, which leads to the determination of the source location. Phase velocity and longitude are the only unknowns of this analysis because latitude is constrained by the knowledge of the fault trace [*Klinger et al.*, 2005; *Lasserre et al.*, 2005; *Xu et al.*, 2006; *Klinger et al.*, 2006]. Figure 2b shows the bias between the results of the array analysis and the aftershock locations given by earthquake catalogs based on global wave arrival times. The systematic trend can be corrected by a simple parabolic optimization which is then taken into account when analyzing the main shock rupture propagation.

3. Origins of the High-Frequency Seismic Radiation

3.1. Correlation Between Seismic Radiation and Geometrical Complexities of the Kunlun Fault

[10] Considering that a curvilinear source along the Kunlun fault is an excellent approximation for the very long shallow Kokoxili earthquake, the array analysis resolves the instantaneous location of the radiating point on the fault. Repeating the analysis over progressive seismogram time windows, we can precisely illuminate the parts of the faults that generated most of the seismic radiation in the investigated frequency band (0.04–0.1 Hz). Given the global duration of the earthquake (100 s), this frequency range is well beyond the corner frequency and is therefore related to the high-frequency behavior of the earthquake.

[11] Analysis of the time semblance diagram (Figure 3a) reveals four local maxima corresponding to four different emission locations. All array detections over the progressive time windows are reported in Table S1 in the auxiliary material.[1] The source locations relative to local semblance maxima do not move when the time of the window center varies around the optimal value. This is simply explained considering that semblance analysis identifies an individualized waveform complexity, which is also retrieved for nearby windows integrating this complexity. Locations corresponding to these local maxima represent the four independent location emissions that our analysis is able to accurately resolve. Figures 3b, 3c, 3d, and 3e illustrate the array analysis of these well-resolved high-frequency source emitting points, taking into account the correction deduced from aftershocks.

[12] In order to estimate the uncertainties associated with these determinations, we follow the statistical approach of *Fletcher et al.* [2006]. We first check that our procedure does not depend on the choice of a reference station. Then we simulate noise-contaminated signals, where the noise is the difference, randomized in phase, between the stacked signal and the real signals at each station. Repeating the semblance analysis over 2000 realizations of the noise-contaminated signals, we define the 95% location confidence level, which we add in Figure 3. The first emission location (P0) is found close to the rupture epicenter (90.85°E). Semblance and confidence level are not excellent (0.65 and ±0.32, respectively) for P0, which is likely due to the low radiation of the Rayleigh waves in this direction, close to the nodal plane. Subsequent analysis of Love waves shows that clear energy originates from the epicenter region. The second and third points (P1 and P2) are very clearly defined (semblance is 0.94 and 0.93, respectively). P1 is located at 92.02°E (±0.1) and P2 at 93.96°E (±0.2). The very high semblance at P1 and P2 shows that some localized wave emissions occur at these points of the fault. As a matter of fact, extended emissions, on distances longer than the studied wavelengths (30 km), would reduce the semblance. The last point (P3) is found at the rupture termination (94.5°E), with a confidence level of ±0.27. Finally, five other points with lower energy and coherency are defined along the Kunlun fault and are represented together with P0, P1, P2, and P3 in Figure 4.

[13] The location of P1 and P2 strongly suggests that the seismic radiation is closely correlated with the rupture geometry. Precise analysis of the surface rupture produced by the Kokoxili earthquake reveals azimuth changes and jogs [*Klinger et al.*, 2005; *Xu et al.*, 2006; *Klinger et al.*, 2006], indicating limits of segments for the coseismic rupture. One of the clearest complexities is the azimuth change of 5.7° located at 92.05°E, associated with a large push-up (Figure 5). When the earthquake reaches this geometrical complexity, the rupture transfers from the main localized fault to a myriad of small faults before resuming on the next localized segment [*Klinger et al.*, 2006; *King and Nabelek*, 1985; *King*, 1986]. P1 location (92.02°E ± 0.1) matches very well this fault feature. Our analysis, based on periods longer than 10 s (wavelengths larger than about 30 km), does not directly prove that this 2-km-long feature is responsible for the emitted radiation. However, if this complexity is the origin of a major rupture propagation

[1] Auxiliary materials are available in the HTML. doi:10.1029/2007JB005520.

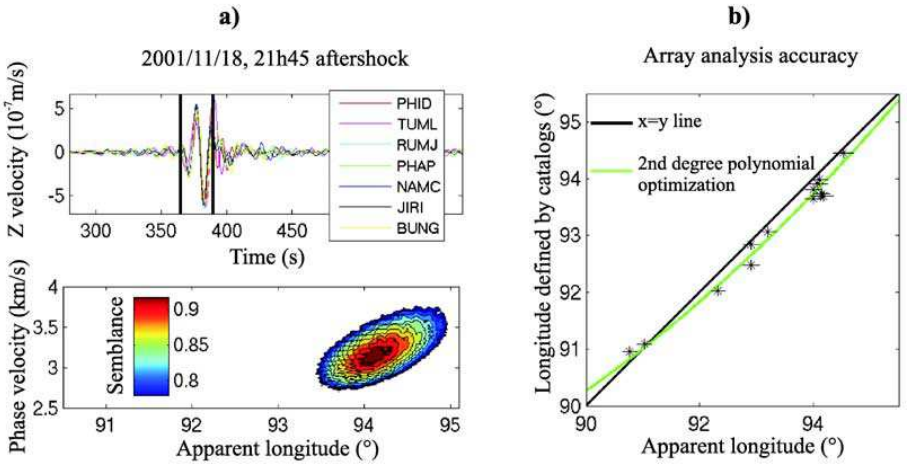

Figure 2. Array analysis of Kokoxili earthquake aftershocks. (a) Example of the 18 November 2001 aftershock. (top) Optimal signal coherency of the seven seismograms. Black thick lines show the 25-s window over which semblance has been computed. (bottom) Semblance sensitivity to fault location (longitude) and to phase velocity. (b) Comparison between longitude defined by array analysis and by earthquake catalogues (National Earthquake Information Center (NEIC), International Seismological Centre, EHB catalog [*Engdahl et al.*, 1998]. Error bars for both location types are shown. A simple second degree polynomial optimization (green curve) corrects for the bias generated by structure complexities deflecting the wavefield.

change, it influences seismic radiation on a large frequency range. Successive analysis shows, for example, that a localized rupture velocity step strongly modifies the seismic radiation for periods between 10 and 25 s. The location of P2 also correlates very well with the largest azimuth change of the fault (7.8°) and, interestingly, with the highest density of aftershocks (Figure 4).

[14] The spatial collocations between the strongest fault complexities and the most energetic radiations indicate that the geometry of the Kunlun fault played an important role in the rupture propagation. However, at this stage, it is not clear if the radiation directly originates from the complexities (for example, change in focal mechanism) or if the complexities were the starting point of different rupture behaviors, which in turn modified the seismic radiation. The subsequent analysis, where a detailed temporal study is added to the spatial radiation distribution, helps us to answer this question.

3.2. Subshear and Supershear Rupture Velocity Regimes

[15] Onset times (*Ti*) associated with fault emission locations (*Pi*) cannot be determined with enough precision from the stacked signals because of the uncertainties related to the width of time window (25 s). To accurately obtain *Ti*, we conjointly use the period-time amplitude diagrams [*Levshin et al.*, 1989] generated by *Pi* and by a nearby aftershock noted *A*. Period-time diagram computed from an aftershock *A* is used to define, as a function of period τ, group time dispersion curves $D_A(\tau)$ for the paths connecting this aftershock and the considered stations [*Shapiro et al.*, 1997]. The next step is to evaluate the group time dispersion curve associated with a subevent *Pi* assuming that there is no significant structural differences between two closely located paths. In this case, we only have to correct for the distance and the dispersion curve $D_{Pi}(\tau)$ associated with *Pi*, is related to $D_A(\tau)$ by

$$D_{Pi}(\tau) = \frac{R_{Pi}}{R_A} D_A(\tau) \tag{5}$$

where R_{Pi} and R_A are the distances between the array and *Pi* and the array and *A*, respectively.

[16] We denote by $Ei(\tau,t)$ the period-time amplitude diagram associated with *Pi*. *Ti* is obtained by maximizing the integral:

$$L(T) = \int_{D_{Pi}(\tau)+T} Ei(\tau, t)\, dl \tag{6}$$

$L(T)$ simply expresses the amplitude integrated along the dispersion curve shifted by a time delay *T*. Amplitude period-time diagrams associated with *Pi* and aftershocks are computed from corresponding weighted semblance stacks [*Kennett*, 1987]. This weighted semblance stack is a simple modification of the stack U_{ij} (equation (1)), in which we multiply the stack value at time *t* by its associated semblance S_{ij}, computed over a window centered on *t*. This helps us to isolate energy coming from desired locations. Figure 6 illustrates how this method is able to measure onset time *T*1 for the subevent P1 using the 21 November 2001 aftershock as reference. To define the uncertainty associated with the measured onset time (44.7 s), we used again noise-contaminated signals (see above for more information about the procedure), both for *Pi* and the aftershock. This shows us that the 95% time confidence level is ±0.7 s.

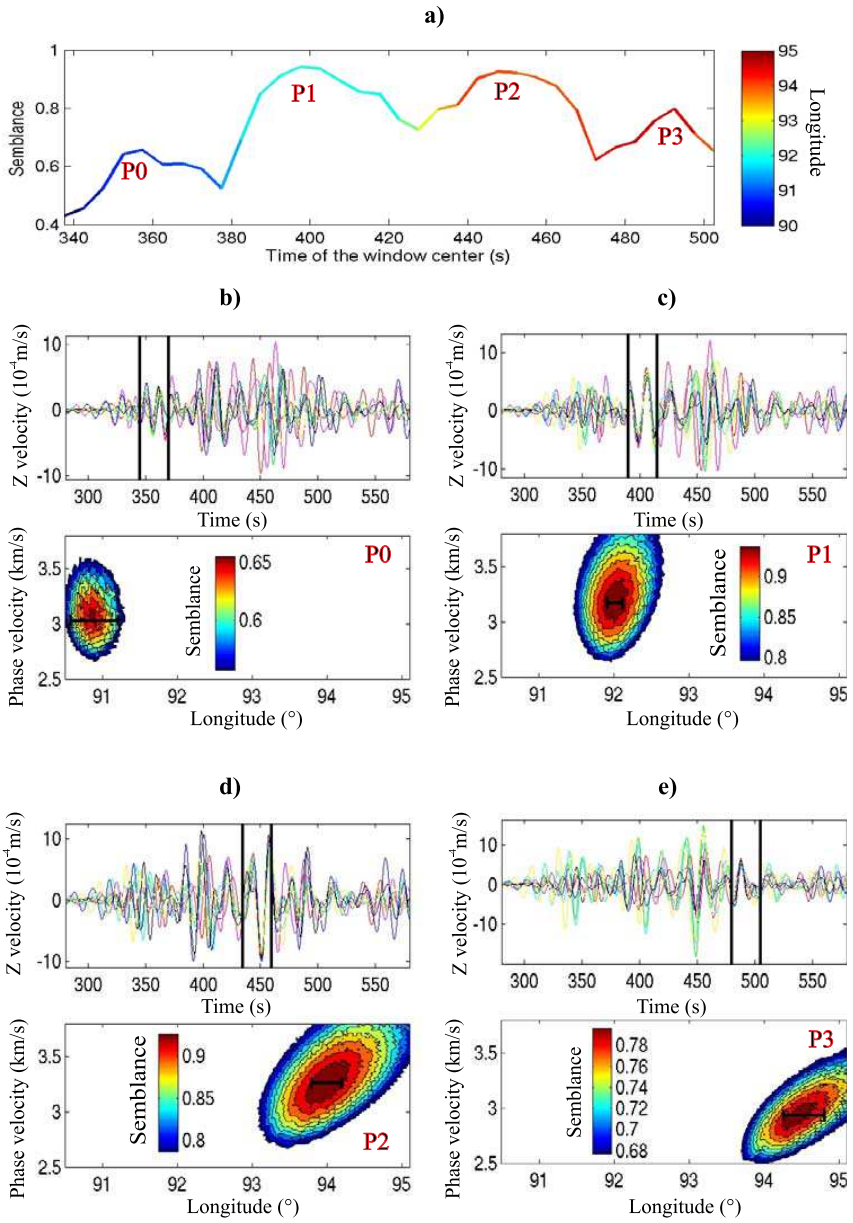

Figure 3. Array analysis of the Kokoxili earthquake Rayleigh waves. (a) Time-semblance diagram of the array analysis. Evolution of semblance over progressive time windows presents four local maxima, relative to the radiating points P0, P1, P2 and P3. Colors are associated with the optimal longitudes defined by the array analysis for each window. (b–e) Detailed analyses related to P0, P1, P2, and P3. See Figure 2a for more details on this location procedure. Note that seismograms in Figures 3b–3e may look different because of the applied normalization in each window. P0 is found close to the earthquake epicenter, P1 is located at 92.02°E (±0.1), P2 is located at 93.96°E (±0.2), and P3 is close to the earthquake termination (94.5°E) defined by other studies [*Lasserre et al.*, 2005; *Xu et al.*, 2006]. Error bars on longitude (thick horizontal lines) have been defined using a statistical analysis on noise-contaminated signals.

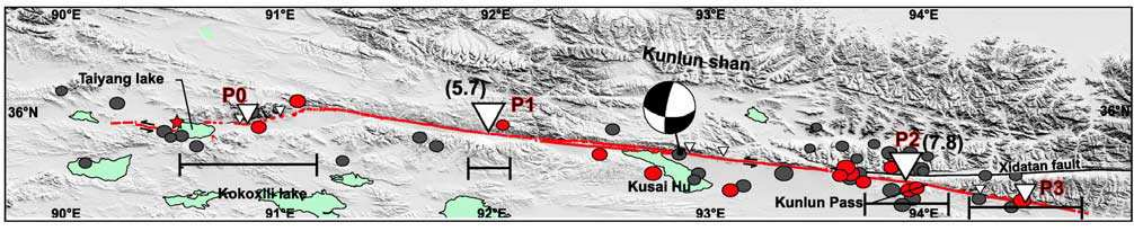

Figure 4. Location map of points imaged by array analysis (triangles, scaled to our level of confidence in the determination). Error bars relative to P0, P1, P2, and P3 are presented below the location of each point. Fault azimuth variations at P1 and P2 are represented as well as the Harvard CMT focal mechanism. Note that a pure vertical left-lateral strike-slip mechanism has been shown to better fit simultaneously surface and body waves [*Robinson et al.*, 2006]. Circles are the 1-year aftershocks of the NEIC catalog, and red circles are the aftershocks used for array calibration (Figure 2).

[17] The global results of the analysis for P1 (two aftershocks) and P2 (five aftershocks) are recorded in Table 2. The measurement is shown to be little dependent on the chosen aftershock. The onset time differences are associated with small errors in aftershock location and origin times, and in the exact location of *Pi*. We use the standard deviation of *T*2 (*T*1 has only two measurements, which is not enough to reliably determine standard deviation) as an estimate of this error source. Adding this standard deviation (0.95 s) to the uncertainty of the measure itself (0.7 s), the temporal analysis shows that P1 and P2 were activated at 44 s and 70 s, respectively (±1.65 s) after the earthquake origin time. The dispersion curves cannot be precisely picked for P0, P3 and some other points identified along the fault (Figure 4). Onset times associated with these radiating points are defined using an average group velocity of 2.94 km/s deduced from aftershocks. Gathering the spatial and temporal information, Figure 7 shows the time-distance evolution of the Kokoxili earthquake.

[18] Rupture velocity along the initial 130 km (before P1) is estimated between 2.7 and 3.3 km/s, which is close but lower than Rayleigh velocity. Behavior of the Kokoxili earthquake changes abruptly when rupture reaches P1. The distance between P1 and P2 is 175 km (±27 km) and the differential rupture time is 26 s (±3.3 s) which implies a rupture velocity between 5.1 and 8.9 km/s over this long segment of the Kunlun fault. Taking into account that, theoretically, the rupture velocity cannot exceed the *P* wave velocity in the shallow crust (6.5 km/s), the range of acceptable velocities is reduced to the interval 5.1–6.5 km/s. This directly shows that rupture velocity may not only be supershear but also very close to the *P* wave velocity. This behavior, indicated by source inversion methods [*Robinson et al.*, 2006; *Bouchon and Vallée*, 2003] (Figure 7) and

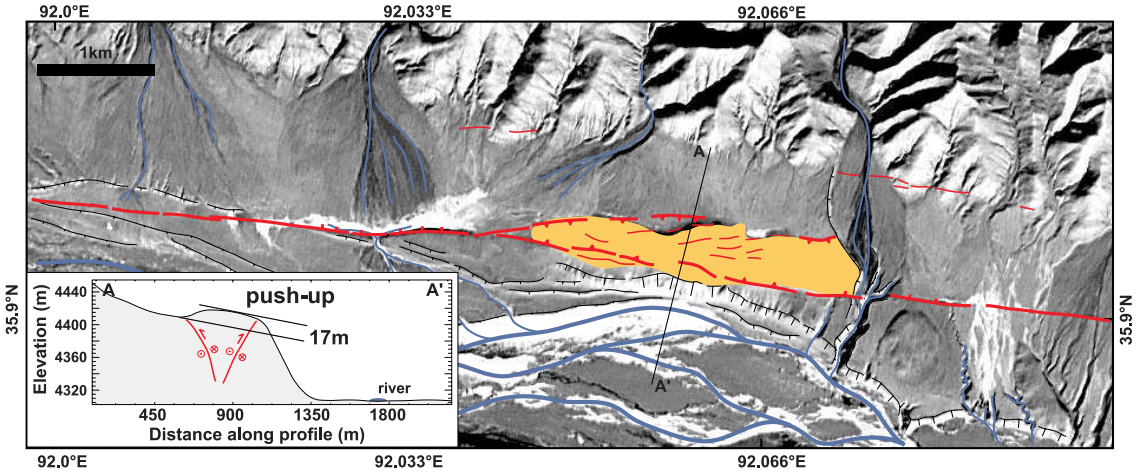

Figure 5. Push-up located along the Kokoxili rupture in P1, associated with the 5.7° change in rupture azimuth. Surface rupture associated to the 2001 earthquake, mapped in red, shows both strike-slip motion and thrust on the flanks of the push-up. Rivers are in blue. A-A′ topography cross section from SRTM digital elevation model shows elevation of the push-up and position of the main faults according to their surface expression. The total size of the push-up (2 km long, 500 m wide, 17 m high) indicates that the compressive jog has been active at least for a couple of earthquake cycles.

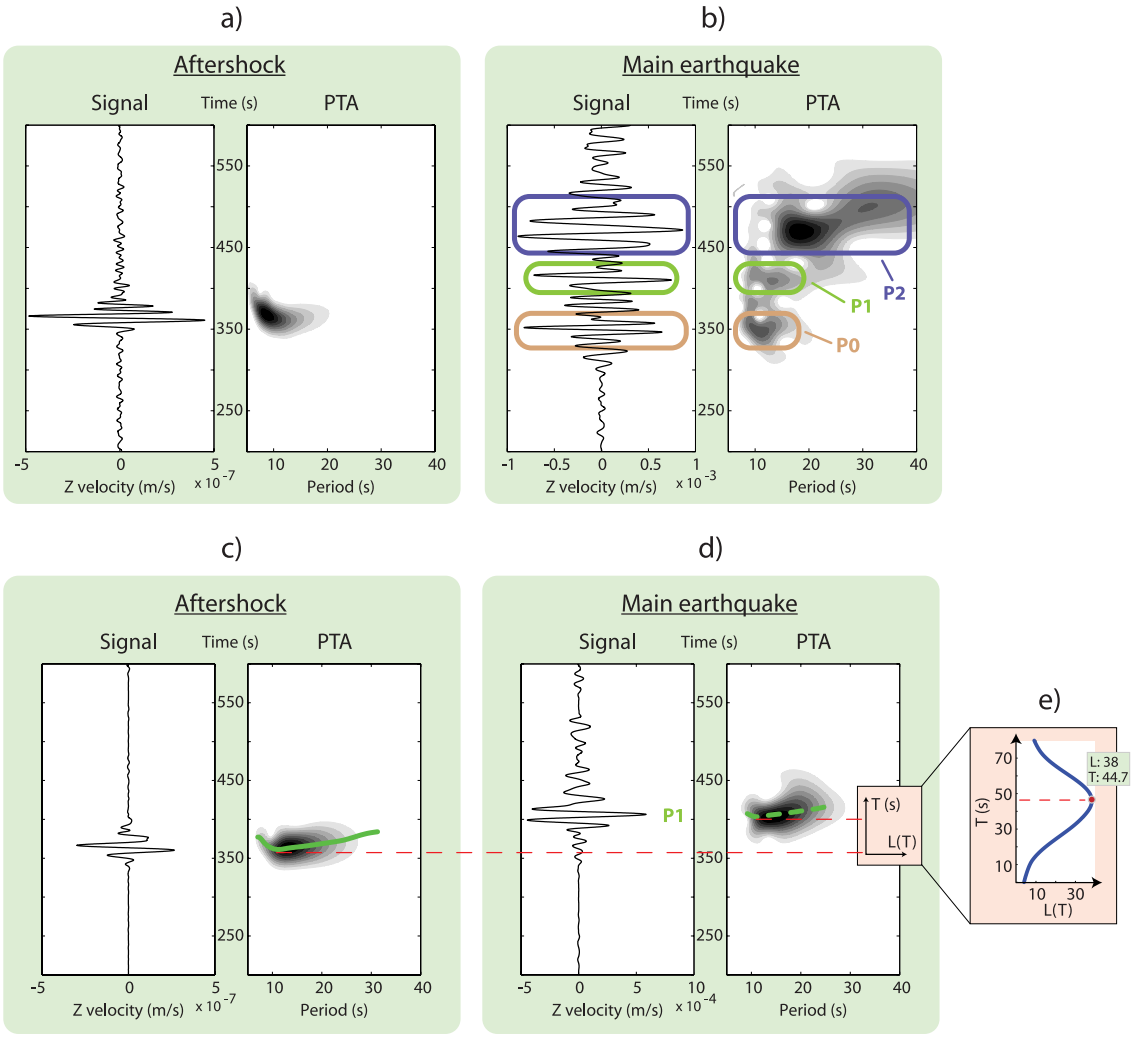

Figure 6. Determination of onset times by dispersion curve analysis. (a) Unfiltered signal and period-time analysis (PTA) of the ground velocities recorded at BUNG during the 21 November 2001 aftershock. (b) Unfiltered signal and PTA of the ground velocities recorded at BUNG during the main shock. PTA shows three energy bursts related to P0, P1, and P2. P3 cannot be clearly distinguished because it is shadowed by the coda of P2. (c) Weighted semblance stack filtered in 10–25 s period band and PTA of the 21 November 2001 aftershock signals. The dispersion curve (in green) is measured from the PTA. (d) Weighted semblance stack filtered in 10–25 s period band and PTA of the main shock signals. This stack is done using the P1 position and therefore efficiently isolates energy coming from this part of the fault. Figure 6d is easier to use than Figure 6b because energy associated with P1 is much better defined. (e) Evolution of $L(T)$, defined in equation (6). This function quantitatively estimates how the dispersion curve of the aftershock should be shifted in time (dashed green line in Figure 6d) to adequately simulate the dispersion curve of the main shock and gives therefore a measure of T1 (here 44.7 s).

predicted by theoretical studies [*Andrews*, 1976; *Day*, 1982; *Festa and Vilotte*, 2006], is here observed during the Kokoxili earthquake.

3.3. Acceleration and Deceleration Phases

[19] Existence of strong coherent arrivals clearly identified by the array analysis indicates that the origin of seismic radiation during this earthquake is highly localized. Several factors can be responsible for local energetic radiation: fault mechanism variations, large slip asperities, or rupture velocity changes [*Madariaga*, 1977; *Campillo*, 1983; *Sato*, 1994]. It can be argued that normal or inverse faulting components contaminating the dominant strike-slip mechanism could

Table 2. Calculation of the Onset Times T1 and T2 With Respect to Different Aftershocks, Using the Method Illustrated in Figure 6

Aftershock Date, Time (UT)	Onset Time (s)	
	T1	*T2*
P1		
21/11	44.7	
30/11, 0500	43.4	
P2		
16/11		70.7
18/11, 2145		69.2
18/11, 2200		68.7
19/11		71.3
22/11		70

locally generate stronger Rayleigh waves, responsible for radiation localization.

[20] To check which one of these hypotheses is realistic, we first apply the array analysis to transverse components (Figure 8). Seismograms have been projected along an average transverse direction, where Love surface waves are dominant. As transverse components are noisier for aftershock signals, we do not calibrate the array as we did for Rayleigh waves, but consider that the azimuthal correction remains the same. We have estimated the errors relative to the location emissions by the same statistical analysis conducted for Rayleigh waves. All array detections over the progressive time windows are recorded in Table S2 in the auxiliary material. Figure 8a, analogous to Figure 3a, reveals a similar pattern as the one revealed by Rayleigh waves: the positions L0, L1 and L3, relative to local maxima, match the position of P0, P1 and P2. L0 is better defined than P0 and confirms that this phase is emitted very close to the earthquake epicenter. The similarity between Love and Rayleigh wave observations shows that the strong energies emitted at P1 and P2 are not related to fault mechanism changes generating strong Rayleigh waves, but likely originate from a modification in the source process. The timing analysis of $Li(i = 0, 3)$ cannot be made precisely as we did for Rayleigh waves. As a matter of fact, the exact transverse direction rotates as the source moves, leading to a contamination of Love waves by Rayleigh waves. However, estimates of the rupture velocity based on an average group velocity and the times of the window center, also imply a supershear behavior in the segment 92°E–94°E.

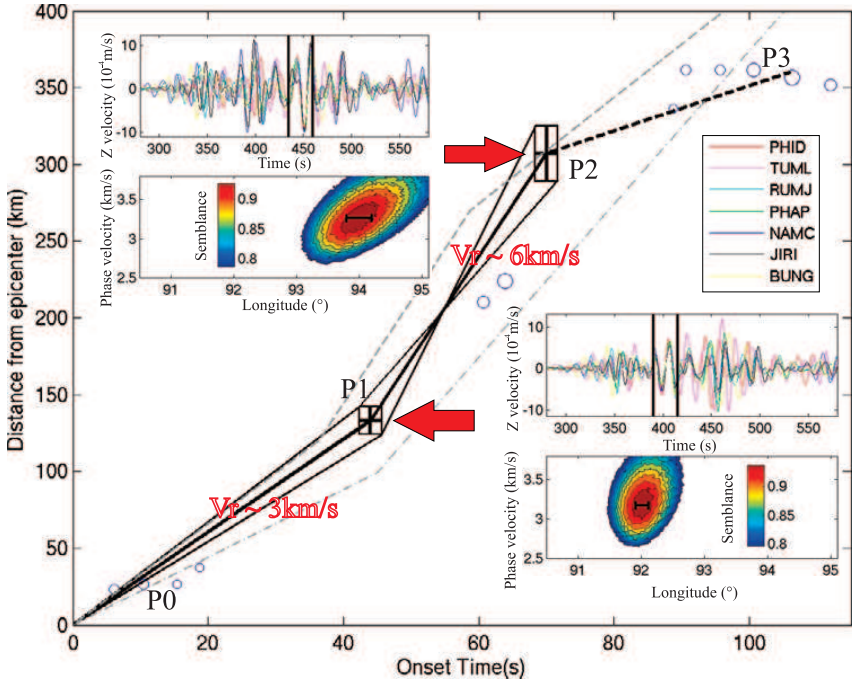

Figure 7. Time-distance evolution of the Kokoxili earthquake. Top left and bottom right insets show the location procedure for the two most coherent time windows corresponding to P1 and P2. Spatial and temporal uncertainties for P1 and P2 are represented by crosses in the time-distance diagram. Blue circles, with size proportional to semblance, show other points for which semblance is larger than 0.65. Since dispersion curves cannot be precisely picked for these points, the onset time is defined by using an average phase velocity of 2.94 km/s deduced from aftershocks. This diagram illustrates the three main phases of the Kokoxili earthquake: sub-Rayleigh rupture before P1, supershear rupture between P1 and P2, before returning to classical sub-Rayleigh rupture after P2. As a comparison, rupture velocity behaviors proposed by *Bouchon and Vallée* [2003] (dashed dotted line) and *Robinson et al.* [2006] (dashed line) are added.

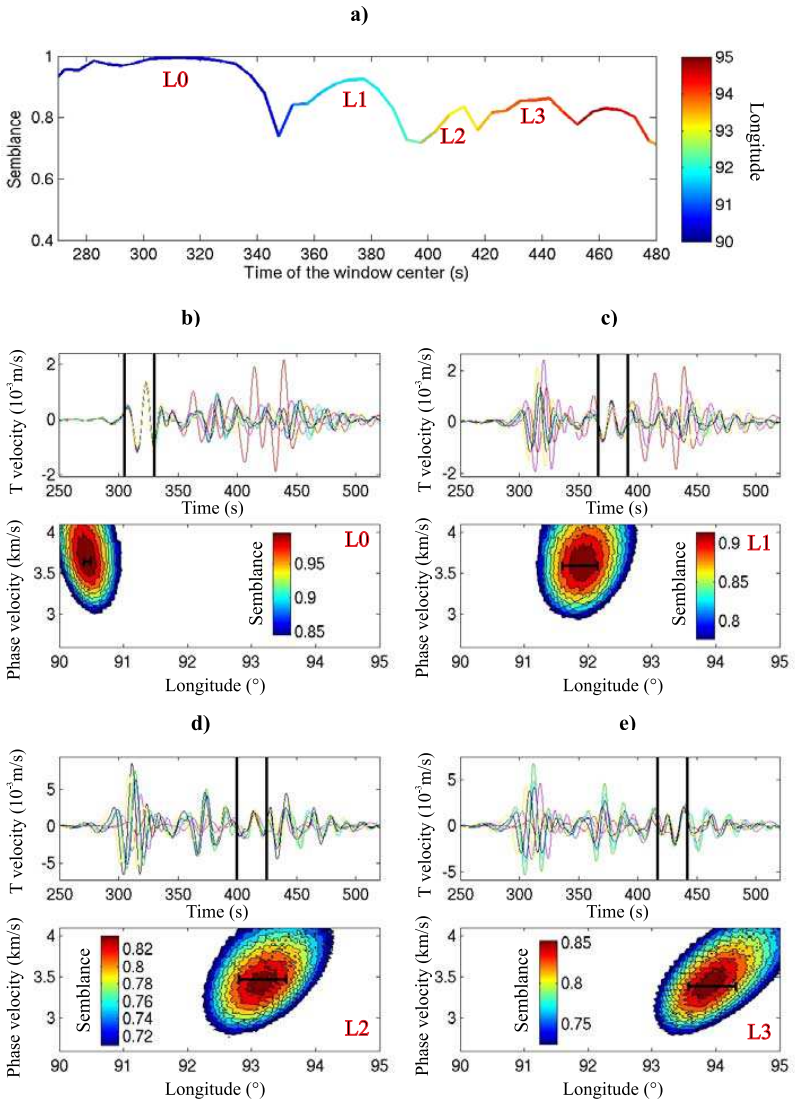

Figure 8. Array analysis of transverse components. Horizontal components have been projected along the azimuth 300°, which is an approximate transverse direction (because of array extension and rupture length). Love waves are therefore dominant on this component. (a) Analogous to Figure 3a. (b–e) Detailed analyses of four local maxima, relative to locations L0, L1, L2, and L3. See Figures 2a and 3 for more details on the procedure. Similar results as for vertical Rayleigh waves are found (Figure 3): L1 and L3 show energy bursts close to 92°E and 94°E, respectively, corresponding to P1 and P2. L0 images energy close to the epicenter, consistent with P0. L2 is related to a smaller energy burst, located at 93°E, that has not been well identified by Rayleigh waves.

[21] The hypothesis of the asperity generated radiation is also unlikely because locations of strongly radiating parts on fault are poorly correlated with maximum slip. The largest surface breaks (Figure 9b), as well as the largest slip imaged by interferometric synthetic aperture radar (INSAR) [*Lasserre et al.*, 2005], occurred in the segment between 92.6°E and 93.5°E. Therefore, rupture velocity changes imaged by the array are very likely themselves the cause of strong seismic radiation. To validate this assumption, we simulated seismic waveforms using a one-dimensional propagation medium deduced from the after-shock seismograms (Figure 10). Synthetic seismograms have been computed [*Bouchon*, 1981] using a pure left-lateral strike-slip mechanism following the Kunlun fault geometry. The kinematic model only considers the rupture velocity changes derived from array analysis (Figure 9c).

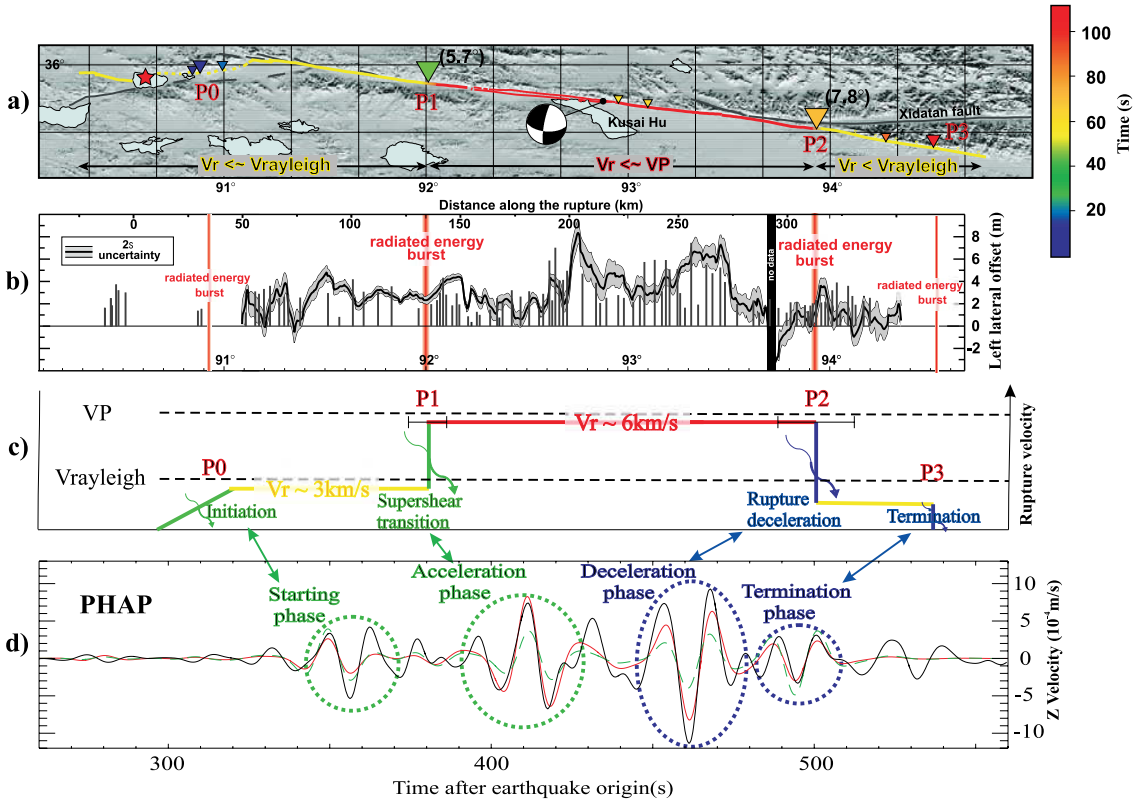

Figure 9. Rupture properties and seismic radiation of the Kokoxili earthquake. (a) Location map of points imaged by array analysis (triangles, scaled to our level of confidence in the determination). Colors are associated with onset times. Inferred rupture velocity regimes and azimuth variations at P1 and P2 are represented. (b) Comparison of energetic radiation locations with surface slip distribution deduced from optical correlation [*Klinger et al.*, 2006] (average values are shown with a black line and the shadowed area indicates the uncertainties) and field observation [*Xu et al.*, 2006] (shown with vertical bars). Little radiated energy is associated with the largest slip segment between 92.6°E and 93.5°E. Slip distributions inferred from other data, for example, INSAR analysis [*Lasserre et al.*, 2005], are very similar and do not show large slip in the high-frequency radiation areas. (c) Rupture velocity scheme of the Kokoxili earthquake deduced from array analysis. Location uncertainties for P1 and P2 are indicated. (d) This kinematic behavior is employed to simulate seismograms at PHAP, using a crustal structure deduced from aftershock waveform fitting (Figure 10). Two simple slip distributions are considered, relative to model 1 and model 2 defined in the text. Synthetics for model 1(dashed green) and 2 (red) are in good agreement with the data (black) complexity in the 0.04–0.1 Hz frequency band, showing that seismic radiation is directly related to acceleration and deceleration phases. Model 2 better explains the data amplitudes, suggesting that supershear rupture is associated with a larger slip.

We have considered two slip functions: the first one is a uniform slip model (model 1), whereas the second one assumes that slip is twice larger in the supershear region (model 2), which schematically models the detailed surface displacement (Figure 9b). Compared to the uniform model, model 2 only modulates the amplitude of the seismic radiation, but does not change the shape of the radiation complexity. The resulting synthetic seismograms related to model 1 (dashed green curve) and to model 2 (red curve) are presented in Figure 9d. Both models well explain the radiation complexity, showing that the wavefield is well described in terms of acceleration and deceleration phases. This last observation also indicates that the rupture was continuously supershear between P1 and P2, and that the observed radiation at P2 is not due to a triggered event ahead of the wavefront. As a matter of fact, such a process would generate an acceleration phase at P2, with an opposite polarity, and would not explain the seismograms. Model 2 better reproduces the seismogram amplitudes, suggesting that the supershear regime is associated with a larger slip.

[22] This analysis shows that rupture accelerations and decelerations have a first-order effect on the high-frequency seismic radiation, which is consistent with theoretical results

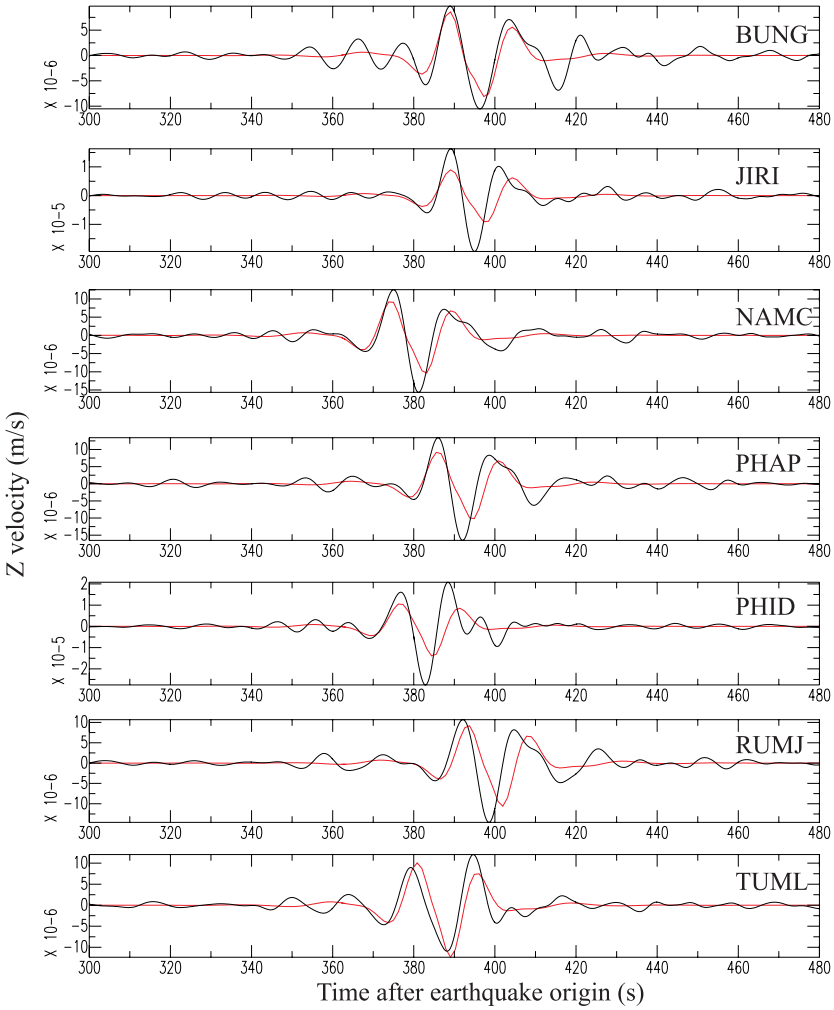

2001/11/18, 22h aftershock
strike, dip, rake = 280°,40°,112°
depth = 3.5km
Mw = 5.5
Half space structure (Vp,Vs,density,Qp,Qs) = (5.45km/s, 3.15km/s, 2700kg/m3, 600, 300)

Figure 10. Waveform modeling of the 18 November 2001 (2200 UT) aftershock. Using a focal mechanism consistent with Harvard CMT, associated with a simple velocity structure (presented at the bottom), Rayleigh surface waves of this aftershock are shown to be well modeled. Synthetics (red) and data (black) are band-pass-filtered between 0.04 and 0.1 Hz. The velocity structure is used to model the main shock waveforms in Figure 9d.

[*Madariaga*, 1977; *Campillo*, 1983; *Sato*, 1994]. The location of acceleration and deceleration phases governs the radiation complexity and slip variations only modulate the seismogram amplitudes. These observations have interesting consequences for the seismic source understanding. In terms of source analysis, the usual hypothesis that strong high-frequency radiation is associated with strong slip variations has to be reconsidered. In terms of seismic risk, it implies that the most damaged zones should be close to the rupture front irregularities rather than to the large slip areas.

4. Discussion and Conclusions

[23] The presented observations of the Kokoxili earthquake should help to fill a gap between theoretical and observational rupture seismology. We have directly put in light the relations between rupture propagation, fault com-

plexity, and high-frequency seismic radiation. We show that the earthquake initiation is associated with a first high-frequency seismic radiation (P0). Between P0 and P1, the rupture propagates with a classical subshear rupture velocity (~3 km/s). When the rupture arrives at P1, 130 km after its initiation, it brutally accelerates and approaches the *P* wave velocity (~6 km/s). This extreme rupture velocity, which has been inferred by indirect inversion techniques, is here directly observed by the array analysis. The abrupt regime change at P1 generates strong high-frequency radiation as predicted by theoretical and numerical studies [*Madariaga*, 1977; *Campillo*, 1983; *Sato*, 1994]. Once the supershear regime is established, between P1 and P2, little high-frequency radiation is emitted, as expected for a steady propagation. 175 km after P1, the rupture decelerates at P2, which is the origin of another high-frequency phase. This emission location is well correlated with the highest density of aftershocks, suggesting that the end of the supershear regime is a zone of complex stress reorganization. Finally, the rupture dies 50 km farther at P3, generating a last high-frequency radiation.

[24] The rupture velocity regimes are interestingly correlated with fault geometry. Beginning a few kilometers after P1, between 92.2°E and 92.9°E, the rupture is partitioned between the main strike-slip fault and an auxiliary normal fault [*King et al.*, 2005]. This could be understood because mode III rupture (here dip slip) cannot theoretically propagate at supershear speeds. Development of an auxiliary sub-Rayleigh fault would allow the accommodation of this slip component away from the strike-slip supershear segment. P1 and P2 themselves, the transition points where the rupture accelerates and decelerates, are not ordinary points of the Kunlun fault. P1 is a complex transition zone between two well localized fault segments with different azimuths (Figure 5). When the earthquake reaches this geometrical complexity, the rupture transfers from the main localized fault to a myriad of small faults before resuming on the next localized segment. Such a variation in the rupture propagation is likely to generate acceleration and deceleration phases, consistent with the collocation of P1. We can infer that when rupture arrives at P1, with a well established sub-Rayleigh velocity, a small modification of the fault properties may drive the rupture to the supershear regime. Moreover, the azimuth change at P1 (5.7° toward the extensional side of the fault) modifies the stress on the fault, and it has been experimentally and theoretically shown [*Rousseau and Rosakis*, 2003; *Bhat et al.*, 2004] that the rupture is generally promoted in this case. We propose that the conjoint effects of well established rupture, of a geometrical complexity, and of a favorable modification of the stress have driven the rupture to the supershear regime. At P2, the opposite effect occurs. The rupture encounters the strongest azimuth change of the fault (7.8°), which orients the subsequent rupture toward the compressional side. Moreover, the rupture propagates after P2 on an auxiliary fault with a larger inverse component, which impedes the supershear propagation.

[25] Our study not only shows that the acceleration and deceleration phases related to P1 and P2 exist, but also that they are the dominant signals of the seismograms. We demonstrate that the waveforms are very well explained by a simple rupture velocity model, where rupture velocity jumps to 6 km/s at P1, before decreasing at P2, and stopping at P3. Slip variations only have a second-order influence, modulating the radiation amplitude but not its shape. This finding has important implications in terms of earthquake source process inversion, classically conducted since the works of *Olson and Apsel* [1982] and *Hartzell and Heaton* [1983]. This last approach deduces from the seismic radiation the slip, rupture velocity and risetime on the fault. Contrary to our array analysis, where we can extract rupture velocity independently from the slip, these two parameters are retrieved conjointly in source inversion methods. A certain level of coupling between slip and rupture velocity has lead most studies to preferentially invert for slip, constraining or fixing the values of the rupture velocity. This assumption is generally argued by the fact that a number of earthquakes tends to have rupture velocity of the order of 80% of the shear velocity [e.g., *Heaton*, 1990]. Our results imply that this choice should be reconsidered, because rupture velocity may exhibit significant variations that result in strong radiation, at least when short periods (i.e., shorter than the source duration) are analyzed.

[26] Finally, the influence of the rupture velocity on the seismic radiation has important consequences for seismic scenarios of strong ground motion. These scenarios generally consider that the complexity of the high-frequency seismic radiation is closely related to the complexity of the static slip on the fault. This is, for example, the main idea of the initial k^2 model [*Herrero and Bernard*, 1994; *Bernard et al.*, 1996]. Our observation of the Kokoxili earthquake implies that the role of the rupture velocity should be enhanced, as proposed by *Hisada* [2000, 2001]. The radiation complexity would be linked to the complex variations of the rupture velocity, generating acceleration and deceleration phases, while the slip would only modulate this radiation. We have shown here that the array analysis of the Kokoxili earthquake provides information at a broad scale, from the mechanics of the earthquake rupture to the origins of strong ground motion generation. It should help a better understanding and modeling of the complex interaction between fault geometry, rupture properties and seismic radiation.

[27] **Acknowledgments.** We are grateful to Anne Sheehan, HIMNT experiment, and IRIS for easy access to the data. This work has benefited from very constructive reviews provided by Paul Spudich and an anonymous reviewer. We thank Pascal Bernard, Michel Bouchon, Cécile Lasserre, Jean Virieux, Pascal Favreau, Stéphane Gaffet, and Shamita Das for fruitful discussions. Comments by Matthew Yedlin, Jean-Mathieu Nocquet, and Christopher Wibberley have improved the initial manuscript.

References

Aagaard, B. T., and T. H. Heaton (2004), Near-source ground motions from simulations of substained intersonic and supersonic fault ruptures, *Bull. Seismol. Soc. Am.*, *94*, 2064–2078.

Andrews, D. J. (1976), Rupture velocity of plane strain shear cracks, *J. Geophys. Res.*, *81*, 5679–5687.

Antolik, M., R. E. Abercrombie, and G. Ekström (2004), The 14 November 2001 Kokoxili (Kunlunshan), Tibet, earthquake: Rupture transfer through a large extensional step-over, *Bull. Seismol. Soc. Am.*, *94*, 1173–1194.

Archuleta, R. J. (1984), A faulting model for the 1979 Imperial Valley earthquake, *J. Geophys. Res.*, *89*, 4559–4585.

Beresnev, I. A. (2003), Uncertainties in finite-fault slip inversions: To what extent to believe? (A critical review), *Bull. Seismol. Soc. Am.*, *93*, 2445–2458.

Bernard, P., and D. Baumont (2005), Shear Mach wave characterization for kinematic fault rupture models with constant supershear rupture velocity, *Geophys. J. Int.*, *162*, 431–447, doi:10.1111/j.1365-246X.2005.02611.x.

Bernard, P., A. Herrero, and C. Berge (1996), Modeling directivity of heterogeneous earthquake ruptures, *Bull. Seismol. Soc. Am.*, *86*, 1149–1160.

Bhat, H. S., R. Dmowska, J. R. Rice, and N. Kame (2004), Dynamic slip transfer from the Denali to Totschunda faults, Alaska: Testing theory for fault branching, *Bull. Seismol. Soc. Am.*, *94*, S202–S213.

Bizzarri, A., and P. Spudich (2008), Effects of supershear rupture speed on the high-frequency content of S waves investigated using spontaneous dynamic rupture models and isochrone theory, *J. Geophys. Res.*, *113*, B05304, doi:10.1029/2007JB005146.

Bouchon, M. (1981), A simple method to calculate Green's functions for an elastic layered medium, *Bull. Seismol. Soc. Am.*, *71*, 959–971.

Bouchon, M., and M. Vallée (2003), Observation of long supershear rupture during the magnitude 8.1 Kunlunshan earthquake, *Science*, *301*, 824–826, doi:10.1126/science.1086832.

Bouchon, M., N. Toksoz, H. Karabulut, M. P. Bouin, M. Dietrich, M. Aktar, and M. Edie (2000), Seismic imaging of the 1999 Izmit (Turkey) rupture inferred from the near-fault recordings, *Geophys. Res. Lett.*, *27*, 3013–3016.

Bouchon, M., M. P. Bouin, H. Karabulut, M. N. Toksoz, M. Dietrich, and A. J. Rosakis (2001), How fast is rupture during an earthquake? New insights from the 1999 Turkey earthquakes, *Geophys. Res. Lett.*, *28*, 2723–2726.

Campillo, M. (1983), Numerical evaluation of the near-field high-frequency radiation from quasidynamic circular faults, *Bull. Seismol. Soc. Am.*, *73*, 723–734.

Das, S. (2007), The need to study speed, *Science*, *317*, 889–890, doi:10.1126/science.1142143.

Day, S. M. (1982), Three-dimensional simulation of spontaneous rupture: the effect of nonuniform prestress, *Bull. Seismol. Soc. Am.*, *72*, 1881–1902.

Dunham, E. M. (2007), Conditions governing the occurrence of supershear ruptures under slip-weakening friction, *J. Geophys. Res.*, *112*, B07302, doi:10.1029/2006JB004717.

Dunham, E. M., and R. J. Archuleta (2004), Evidence for a supershear transient during the 2002 Denali fault earthquake, *Bull. Seismol. Soc. Am.*, *94*, S256–S268.

Ellsworth, W. L., M. Celebi, J. R. Evans, E. G. Jensen, M. C. Metz, D. J. Nyman, J. W. Roddick, P. Spudich, and C. D. Stephens (2004), Near-field ground motions of the *M* 7.9 November 3, 2002, Denali fault, Alaska, earthquake recorded at pump station 10, *Earthquake Spectra*, *20*, 597–615.

Engdahl, E. R., R. van der Hilst, and R. Buland (1998), Global teleseismic earthquake relocation with improved travel times and procedures for depth determination, *Bull. Seismol. Soc. Am.*, *88*, 722–743.

Festa, G., and J.-P. Vilotte (2006), Influence of the rupture initiation on the intersonic transition: Crack-like versus pulse-like modes, *Geophys. Res. Lett.*, *33*, L15320, doi:10.1029/2006GL026378.

Fletcher, J. B., P. Heaton, and L. M. Baker (2006), Rupture propagation of the 2004 Parkfield, California, earthquake from observations at the UPSAR, *Bull. Seismol. Soc. Am.*, *96*, S129–S142.

Hartzell, S. H., and T. H. Heaton (1983), Inversion of strong ground motion and teleseismic waveform data for the fault rupture history of the 1979 Imperial Valley, California earthquake, *Bull. Seismol. Soc. Am.*, *73*, 1553–1583.

Heaton, T. H. (1990), Evidence for and implications of self-healing pulses of slip in earthquake rupture, *Phys. Earth Planet. Inter.*, *64*, 1–20.

Herrero, A., and P. Bernard (1994), A kinematic self-similar rupture process for earthquakes, *Bull. Seismol. Soc. Am.*, *84*, 1216–1228.

Hisada, Y. (2000), A theoretical omega-square model considering the spatial variation in slip and rupture velocity, *Bull. Seismol. Soc. Am.*, *90*, 387–400.

Hisada, Y. (2001), A theoretical omega-square model considering spatial variation in slip and rupture velocity; part 2, Case for a two-dimensional source model, *Bull. Seismol. Soc. Am.*, *91*, 651–666.

Ishii, M., P. M. Shearer, H. Houston, and J. E. Vidale (2005), Rupture extent, duration, and speed of the 2004 Sumatra-Andaman earthquake imaged by the Hi-Net array, *Nature*, *435*, 933–936, doi:10.1038/nature03675.

Kennett, B. L. N. (1987), Observational and theoretical constraints on crustal and upper mantle heterogeneity, *Phys. Earth Planet. Inter.*, *47*, 319–332.

King, G. C. (1986), Speculations on the geometry of the initiation and termination processes of earthquake rupture and its relation to morphology and geological structures, *Pure Appl. Geophys.*, *124*, 567–585.

King, G. C., and J. Nabelek (1985), The role of fault bends in faults in the initiation and termination of earthquake rupture, *Science*, *283*, 984–987.

King, G., Y. Klinger, D. Bowman, and P. Tapponnier (2005), Slip partitioned surface breaks for the 2001 Kokoxili earthquake, China (M_w 7.8), *Bull. Seismol. Soc. Am.*, *95*, 731–738.

Klinger, Y., X. Xu, P. Tapponnier, J. Van der Woerd, C. Lasserre, and G. King (2005), High-resolution satellite imagery mapping of the surface rupture and slip distribution of the $M_w \sim 7.8$, November 14, 2001 Kokoxili earthquake (Kunlun fault, northern Tibet, China), *Bull. Seismol. Soc. Am.*, *95*, 1970–1987.

Klinger, Y., R. Michel, and G. King (2006), Evidence for a barrier model from M_w7.8 Kokoxili (Tibet) earthquake slip-distribution, *Earth Planet. Sci. Lett.*, *242*, 354–364.

Krüger, F., and M. Ohrnberger (2005), Tracking the rupture of the $M_w = 9.3$ Sumatra earthquake over 1,150 km at teleseismic distance, *Nature*, *435*, 937–939, doi:10.1038/nature03696.

Lasserre, C., G. Peltzer, F. Crampé, Y. Klinger, J. Van der Woerd, and P. Tapponnier (2005), Coseismic deformation of the 2001 $M_w = 7.8$ Kokoxili earthquake in Tibet, measured by synthetic aperture radar interferometry, *J. Geophys. Res.*, *110*, B12408, doi:10.1029/2004JB003500.

Levshin, A. L., T. B. Yanovskaya, A. V. Lander, B. G. Bukchin, M. P. Barmin, L. I. Ratnikova, and E. N. Its (1989), Recording, identification, and measurement of surface wave parameters, in *Seismic Surface Waves in a Laterally Inhomogeneous Earth*, edited by V. I. Keilis-Borok, pp. 131–182, Kluwer Publ., Dordrecht, Netherlands.

Madariaga, R. (1977), High-frequency radiation from crack (stress drop) models of earthquake faulting, *Geophys. J. R. Astron. Soc.*, *51*, 625–651.

Monsalve, G., A. Sheehan, V. Schulte-Pelkum, S. Rajaure, M. R. Pandey, and F. Wu (2006), Seismicity and one-dimenstional velocity structure of the Himalayan collision zone: Earthquakes in the crust and upper mantle, *J. Geophys. Res.*, *111*, B10301, doi:10.1029/2005JB004062.

Neidell, N., and M. T. Taner (1971), Semblance and other coherency measures for multichannel data, *Geophysics*, *36*, 482–497.

Olson, A. H., and R. J. Apsel (1982), Finite faults and inverse-theory with applications to the 1979 Imperial Valley earthquake, *Bull. Seismol. Soc. Am.*, *72*, 1969–2001.

Ozacar, A. A., and S. L. Beck (2004), The 2002 Denali fault and 2001 Kunlun fault earthquakes: Complex Rupture Processes of Two Large Strike-Slip Events, *Bull. Seism. Soc. Am.*, *94*, S278–S292.

Robinson, D. P., C. Brough, and S. Das (2006), The M_w 7.8, 2001 Kunlunshan earthquake: Extreme rupture speed variability and effect of fault geometry, *J. Geophys. Res.*, *111*, B08303, doi:10.1029/2005JB004137.

Rosakis, A. J., O. Samudrala, and D. Coker (1999), Cracks faster than shear wave speed, *Science*, *284*, 1337–1340.

Rousseau, C., and A. J. Rosakis (2003), On the influence of fault bends on the growth of sub-Rayleigh and intersonic dynamic shear ruptures, *J. Geophys. Res.*, *108*(B9), 2411, doi:10.1029/2002JB002310.

Sato, T. (1994), Seismic radiation from circular cracks growing at variable rupture velocity, *Bull. Seism. Soc. Am.*, *84*, 1199–1215.

Schulte-Pelkum, V., G. Monsalve, A. Sheehan, M. R. Pandey, S. Sapkota, R. Bilham, and F. Wu (2005), Imaging the Indian subcontinent beneath the Himalaya, *Nature*, *435*, 1222–1225, 30 June 2005—doi:10.1038/nature03678.

Shapiro, N. M., M. Campillo, A. Paul, S. K. Singh, D. Jongmans, and F. J. Sanchez-Sesma (1997), Surface wave propagation across the Mexican Volcanic Belt and the origin of the long-period sesimic wave amplification in the valley of Mexico, *Geophys. J. Int.*, *128*, 151–166.

Spudich, P., and E. Cranswick (1984), Direct observation of rupture propagation during the 1979 Imperial Valley earthquake using a short baseline accelerometer array, *Bull. Seismol. Soc. Am.*, *74*, 2083–2114.

Tocheport, A., L. Rivera, and J. Van der Woerd (2006), A study of the 14 November 2001 Kokoxili earthquake: History and geometry of the rupture from teleseismic data and field observations, *Bull. Seismol. Soc. Am.*, *96*, 1729–1741.

Van der Woerd, J., P. Tapponnier, F. J. Ryerson, A. S. Meriaux, B. Meyer, Y. Gaudemer, R. C. Finkel, M. W. Caffee, G. G. Zhao, and Z. Q. Xu (2002), Uniform postglacial slip-rate along the central 600 km of the Kunlun fault (Tibet), from Al-26, Be-10, and C-14 dating of riser offsets, and climatic origin of the regional morphology, *Geophys. J. Int.*, *148*, 356–388.

Xu, X., G. Yu, Y. Klinger, P. Tapponnier, and J. Van Der Woerd (2006), Reevaluation of surface rupture parameters and faulting segmentation of the 2001 Kunlunshan earthquake (M_w7.8), northern Tibetan Plateau, China, *J. Geophys. Res.*, *111*, B05316, doi:10.1029/2004JB003488.

Y. Klinger, M. Landès, and N. M. Shapiro, Institut de Physique du Globe de Paris, 4 place Jussieu, F-75252 Paris CEDEX 05, France. (klinger@ipgp.jussieu.fr; landes@ipgp.jussieu.fr; nshapiro@ipgp.jussieu.fr)

M. Vallée, Géosciences Azur, 250 avenue Albert Einstein, F-06560 Valbonne, France. (vallee@geoazur.unice.fr)

EDITORS' CHOICE

EDITED BY GILBERT CHIN AND JAKE YESTON

PHYSICS

Snapshot Magnetometry

In cold-atom chips, atoms are guided above tracks of wires that supply the magnetic field to keep them aloft. In applications ranging from quantum information processing to metrology, any deviation in the magnetic field from point to point over the chip could influence the delicate state of the atoms. Terraciano *et al.* introduce a technique that takes a snapshot image of the magnetic field landscape. Using a cloud of cold rubidium atoms, whose energy levels are sensitive to magnetic field, they let the cloud fall toward the chip and probe the atoms' state with a laser beam tuned to one of the magnetic transitions. The ability to take a two-dimensional snapshot image of magnetic field variations of 30 mG/cm above the atom chip over 5 mm with 250-μm resolution should prove useful in calibrating these chips for their envisioned applications. — ISO

Opt. Express **16**, 13062 (2008).

BIOCHEMISTRY

Translation Translocations

Ribosomes translate mRNA into protein with the help of GTPases: the elongation factors (EFs). In prokaryotes, as each mRNA codon is presented in the A site of the ribosome, EF-Tu loads a complementary, amino acid–bearing tRNA into the A site. After peptide bond formation, EF-G translocates the ribosome along the mRNA strand by three nucleotides, moving the tRNA (now carrying the nascent polypeptide chain) into the neighboring P site and bringing the next codon into the A site. The GTPase EF4/LepA was recently found to promote backward translocation of the ribosome along the mRNA strand, moving the tRNA from the P site back into the A site. This function may allow the ribosome to recover from forward translocations of the wrong number of nucleotides. Connell *et al.* have visualized EF4 in complex with a ribosome and associated tRNAs using single-particle cryo–electron microscopy (EM). Fitting the crystal structure of EF4 into the cryo-EM reconstruction revealed that its C-terminal domain forms multiple contacts with a tRNA in the A site, suggesting that EF4 promotes back-translocation by stabilizing the A-site tRNA position over the P-site tRNA position. — NM*

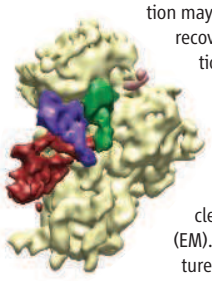

EF4 (red) grabs the A-site tRNA (purple).

Nat. Struct. Mol. Biol. **15**, 10.1038/nsmb.1469 (2008).

*Nilah Monnier is a summer intern in *Science*'s editorial department.

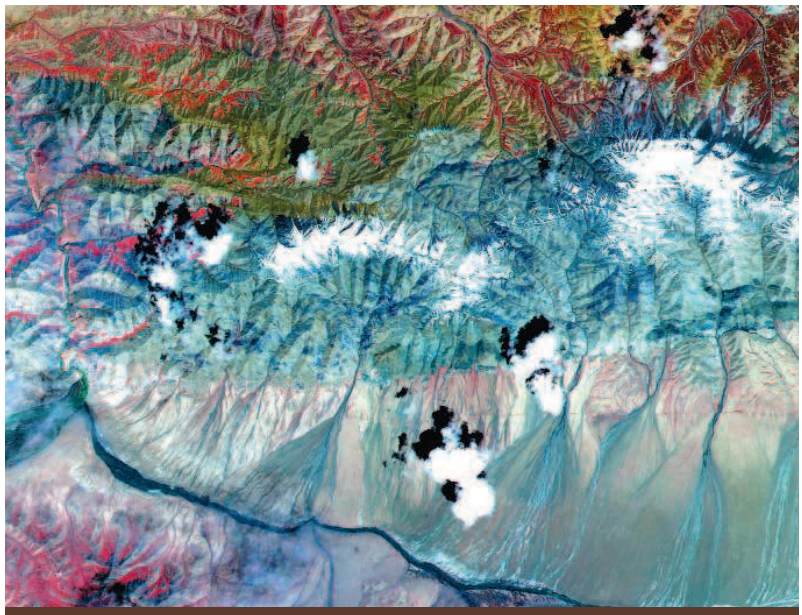

GEOPHYSICS

Sensing Supershear

Recent observations, supported by experiments, have indicated that some earthquake ruptures transiently exceed the local speed of sound along the fault zone. This "supershear" can explain enhanced shaking from these quakes; thus, supershear ruptures are critical in assessing seismic risks. Many of the details of how ruptures accelerate to above the sound speed and then decelerate, in some cases repeatedly, as a rupture progresses are unclear, as most supershear ruptures have been inferred by data inversions. Vallée *et al.* were able to observe these dynamics more directly in the 2001 Kokoxili earthquake (M = 7.8)—which ruptured 400 km along the Kunlun fault in northern Tibet—thanks to an array of seismometers in Nepal that were nearly parallel to the rupture. Their data show that the earthquake, which began in the west, accelerated to above the shear wave velocity after ripping 175 km eastward, at a bend in the fault. Rupture speeds nearly reached the compressional (p) wave velocity before decelerating at another bend. Much of the high-frequency seismic energy from the quake was radiated during these transitions. — BH

J. Geophys. Res. **113**, B07305 (2008).

CLIMATE SCIENCE

1000 Years of Hurricanes

The natural variability of hurricane activity is poorly known, not least because the historic record for hurricanes extends back only about 130 years. As a result, there has been controversy over whether hurricane activity will change—or is already changing—as a result of global warming. Sediments may hold clues to hurricane activity over longer time scales, but few studies have yielded sedimentary records of hurricane activity at annual resolution. Besonen *et al.* have now obtained an annually resolved lake sediment record from Lower Mystic Lake in Boston, Massachusetts, that covers the past 1000 years. The record contains anomalous features—unusually thick layers in which coarse sediments and terrestrial, organic detritus are overlain by progressively finer sediments—that are indicative of strong flooding. Comparison with the historic record shows that 10 out of 11 of these features

CREDITS (TOP TO BOTTOM): NASA/GSFC/METI/ERSDAC/JAROS, AND U.S./JAPAN ASTER SCIENCE TEAM; CONNELL *ET AL.*, *NAT. STRUCT. MOL. BIOL.* **15**, 10.1038/NSMB.1469 (2008)

Published by AAAS

II.2.3 Les ondes de Mach générées par les séismes supershear

Un certain paradoxe était apparu lors de l'observation des premiers séismes supershear. Les méthodes d'identification de ces vitesses de rupture rapides avaient en effet utilisé des approches variées (inversion, propriétés du champ proche généré, imagerie en réseau...), mais n'avaient pas mis en lumière les ondes de Mach régionales. Or ces ondes doivent se propager loin de la faille et avec une forte amplitude, ce qui devrait les rendre facilement détectables.

L'article suivant (*Vallée and Dunham*, 2012) présente la première observation de ces ondes lors du séisme de Kokoxili. La méthode proposée profite de la présence d'un petit séisme, voisin de l'épicentre du choc principal. Nous montrons que l'excellente corrélation entre les formes d'onde du choc principal et du petit séisme – dans certains azimuts uniquement - est une preuve de l'existence des ondes de Mach. Leur pouvoir amplificateur est aussi clairement mis en évidence.

GEOPHYSICAL RESEARCH LETTERS, VOL. 39, L05311, doi:10.1029/2011GL050725, 2012

Observation of far-field Mach waves generated by the 2001 Kokoxili supershear earthquake

M. Vallée[1] and Eric M. Dunham[2]

Received 21 December 2011; revised 13 February 2012; accepted 13 February 2012; published 14 March 2012.

[1] Regional surface wave observations offer a powerful tool for determining source properties of large earthquakes, especially rupture velocity. Supershear ruptures, being faster than surface wave phase velocities, create far-field surface wave Mach cones along which waves from all sections of the fault arrive simultaneously and, over a sufficiently narrow frequency band, in phase. We present the first observation of far-field Mach waves from the major Kokoxili earthquake (Tibet, 2001/11/14, M_w 7.9) and confirm that ground motion amplitudes are indeed enhanced on the Mach cone. Theory predicts that on the Mach cone, bandpassed surface wave seismograms from a large supershear rupture will be identical to those from much smaller events with similar focal mechanisms, with an amplitude ratio equal to the ratio of the seismic moments of the two events. Cross-correlation of 15–25 s Love waves from the Kokoxili event with those from a much smaller (M_w 5) foreshock indicates a high degree of similarity (correlation coefficients ranging from 0.8 to 0.95) in waveforms recorded at stations near the far-field Mach cone. This similarity vanishes away from the Mach cone. These observations provide further evidence for supershear propagation of the Kokoxili rupture, and demonstrate how this simple waveform correlation procedure can be used to identify supershear ruptures. **Citation:** Vallée, M., and E. M. Dunham (2012), Observation of far-field Mach waves generated by the 2001 Kokoxili supershear earthquake, *Geophys. Res. Lett.*, *39*, L05311, doi:10.1029/2011GL050725.

1. Introduction

[2] The speed at which an earthquake rupture propagates influences the amplitude and character of the radiated wavefield. Rupture velocities less than the shear wave speed β are typically inferred by source inversions and seismic imaging studies. In fact, β is the limiting velocity in certain geometries, including along-strike propagation of megathrust ruptures in subduction zones. However, under mode II loading conditions, in which slip occurs parallel to the rupture propagation direction, rupture velocities in excess of β become possible [*Burridge*, 1973; *Andrews*, 1976; *Xia et al.*, 2004]. Seismic studies suggest supershear rupture velocities in several major strike-slip earthquakes (Izmit, Turkey, 1999; Kokoxili, Tibet, 2001; Denali, Alaska, 2002) [*Bouchon et al.*, 2001; *Bouchon and Vallée*, 2003; *Ellsworth et al.*, 2004; *Dunham and Archuleta*, 2004; *Aagaard and Heaton*, 2004; *Robinson et al.*, 2006; *Vallée et al.*, 2008; *Walker and Shearer*, 2009].

[3] The most distinctive features of supershear ruptures are Mach fronts. These sharp wavefronts occur whenever the source propagates faster than the speed of the waves it radiates. Supershear ruptures thus produce shear wave Mach fronts [*Freund*, 1979; *Ben-Menahem and Singh*, 1987], as well as surface wave Mach fronts for ruptures in a half-space [*Dunham and Bhat*, 2008]. These Mach fronts are predicted to transport extremely large particle velocities and stress perturbations out to distances comparable to the fault width [*Bernard and Baumont*, 2005; *Dunham and Bhat*, 2008], though this effect has not been substantiated observationally, possibly due to lack of Mach front coherence [*Bizzarri et al.*, 2010; *Andrews*, 2010].

[4] Thus far, almost all theoretical and numerical studies have focused on the wavefield in the near-source region (i.e., distances within a few source dimensions). In this work we explore properties of Mach waves in the far-field limit. Our focus is on surface waves, which carry the largest ground motion amplitudes outside the near-source region. In particular, we characterize how waves radiated by different sections of the fault interfere with each other, and how this leads to extreme amplification of surface wave motions at stations located along the far-field Mach cone. This directivity pattern is quite different from that of subshear ruptures, which features maximum amplification in the forward direction.

[5] We next prove that at stations along the far-field Mach cone, narrowband seismograms from a large supershear earthquake will be identical to those from a small earthquake of similar focal mechanism (except for an overall amplitude difference equal to the ratio of seismic moments). We test our theoretical predictions using regional Love wave records from the Kokoxili earthquake, and confirm that maximum directivity effects indeed occur at stations located along the far-field Mach cone.

2. Far-Field Surface Waves From Supershear Ruptures

[6] In this section we discuss the relationship between far-field surface waves from a large supershear earthquake and a small earthquake located in the vicinity of the large one. Both earthquakes have identical focal mechanisms corresponding to horizontal slip on vertically dipping faults.

[7] First consider the small earthquake with seismic moment m_0. At sufficiently low frequencies, seismic wavelengths are larger than the source dimension and the earthquake can be described with the point source moment density $m_0\delta(\mathbf{x})H(t)$, where $\delta(\cdot)$ and $H(\cdot)$ are the delta function and

[1]Geoazur, University of Nice Sophia-Antipolis, IRD, OCA, Valbonne, France.
[2]Department of Geophysics and Institute for Computational and Applied Mathematics, Stanford University, Stanford, California, USA.

0094-8276/12/2011GL050725

unit step function, respectively. Within the approximation of a layered medium (i.e., neglecting lateral heterogeneity in material properties), the far-field displacement spectrum corresponding to fundamental mode surface waves can be written in the form [*Aki and Richards*, 2002]

$$\hat{u}_i(r_0, \phi, \omega) = m_0 \hat{F}_i(r_0, \phi, \omega) e^{ikr_0}, \quad (1)$$

where $r_0 = |\mathbf{x}|$ and ϕ are the distance and azimuthal angle between the source (at the origin) and the station, and ω is the natural frequency. The excitation function $\hat{F}_i(r_0, \phi, \omega)$ and wavenumber $k = k(\omega)$ are specific to the fundamental surface wave eigenmode, with the former also depending on the focal mechanism of the earthquake.

[8] Now consider a much larger earthquake, in the vicinity of the small one, involving unilateral rupture propagation at constant rupture velocity v_r. The seismic moment M_0 is released over width W and length L ($0 \le x \le L$). At frequencies less than $\sim \beta/W$, seismic wavelengths are larger than W and the source can be described in terms of the depth-averaged slip $\Delta u(x)$. The far-field surface wave displacement spectrum, in the far-field limit [*Aki and Richards*, 2002], is

$$\hat{U}_i(r_0, \phi, \omega) = \mu W \hat{F}_i(r_0, \phi, \omega) e^{ikr_0} \int_0^L \Delta u(x) e^{i\omega x/v_r - ikx\cos\phi} dx, \quad (2)$$

where μ is the shear modulus. We have introduced the phase factors $e^{i\omega x/v_r}$ and $e^{-ikx\cos\phi}$ to account for variations in surface wave arrival times due to both the rupture time and source-receiver distance, respectively, for points along the length of the fault.

[9] Using (1) to eliminate the excitation function, we rewrite (2) as

$$\hat{U}_i(r_0, \phi, \omega) = \hat{u}_i(r_0, \phi, \omega) \frac{\mu W}{m_0} \int_0^L \Delta u(x) e^{2ikX(\phi,\omega)/L} dx, \quad (3)$$

where

$$X(\phi, \omega) \equiv \frac{\omega L}{2v_r} \left[1 - \frac{v_r \cos\phi}{c(\omega)}\right] \quad (4)$$

captures the directivity effect involving the ratio of the rupture velocity v_r to the surface wave phase velocity $c(\omega) \equiv \omega/k(\omega)$.

[10] When $v_r < c(\omega)$, then receivers at any azimuth ϕ record wave arrivals in the chronological order in which they were emitted by the rupture; i.e., the first arrivals are from the hypocenter and the last are from the end of the fault. Maximum directivity effects occur at stations in the forward direction ($\phi \approx 0$). In contrast, for $v_r > c(\omega)$ there exist two distinct regions bounded by $\phi = \pm\phi_M(\omega)$, where

$$\phi_M(\omega) \equiv \arccos(c(\omega)/v_r) \quad (5)$$

is half the opening angle of the far-field Mach cone. Within the Mach cone (i.e., $|\phi| < \phi_M(\omega)$), the first arriving waves come from the last section of the fault to rupture, and waves from the hypocenter arrive last. On the Mach cone itself, waves from all sections of the fault arrive simultaneously and interfere constructively. The resulting amplification of ground motion exceeds that caused by even the fastest subshear ruptures.

[11] The Mach angle $\phi_M(\omega)$ is the value of ϕ for which $X(\phi, \omega) = 0$. Thus from (3) we see that on the Mach cone (and only on it), the displacement spectrum of the large earthquake is identical to that of the small earthquake:

$$\hat{U}_i(r_0, \phi_M(\omega), \omega) = (M_0/m_0)\hat{u}_i(r_0, \phi_M(\omega), \omega), \quad (6)$$

a result that holds even for spatially variable slip in the large event since $M_0 \equiv \mu W \int_0^L \Delta u(x) dx$. While a similar result holds for all ϕ at frequencies less than $\sim \beta/L$ (because $|X(\phi, \omega)| \ll 1$), we emphasize that (6) applies at frequencies less than $\sim \beta/W$. For large strike-slip earthquakes, this includes periods greater than about 5 s (considering W equal to 15 km and a shear wave speed of 3 km/s), rather than just those greater than ~100 s.

[12] Since surface wave phase velocities $c(\omega)$ are slightly less than the shear wave speed β, then the surface wave Mach cone will exist for supershear earthquakes (for which $v_r > \beta$). Since the Mach angle (5) depends on frequency, observational confirmation of our theory is facilitated by working with a limited frequency band centered on $\omega = \omega_0$ over which the average surface wave phase velocity is $\bar{c} \approx c(\omega_0)$. The corresponding Mach angle is $\bar{\phi}_M \approx \phi_M(\omega_0)$. For bandpassed signals recorded at stations along the Mach cone, we can inverse Fourier transform (6) to obtain the remarkable result

$$U_i(r_0, \bar{\phi}_M, t) \approx (M_0/m_0) u_i(r_0, \bar{\phi}_M, t). \quad (7)$$

At these stations, the bandpassed seismogram from the large event is predicted to match that of the small event, up to an overall normalization factor that is the ratio of the moments of the two events.

[13] To summarize, in the case of a long unilateral rupture ($L \gg W$) observed in the far field ($r_0 \gg L$), three key observations provide evidence for Mach waves and thus proof that an earthquake is supershear: (1) Bandpassed waveforms from the large and small events are proportional at stations in particular azimuthal directions (which define the far-field Mach cone). (2) On the Mach cone, the amplitude ratio of these waveforms (or their spectral amplitude) is equal to the moment ratio. (3) In all other directions, the waveforms of the large earthquake are more complex than those of the small one. The amplitude ratio also decreases because signals from the large event are spread in time and waves from different parts of the fault are subject to more destructive interference. This is substantially different than the directivity pattern for subshear ruptures, for which directivity is maximized in the forward direction ($\phi = 0$) and decreases monotonically as $|\phi|$ is increased to 180°.

3. Observation of Mach Waves From the Kokoxili Earthquake

[14] The left-lateral strike-slip Kokoxili earthquake (Tibet, 2001/11/14, M_w 7.9) is probably the earthquake for which the indications of supershear propagation are most numerous [*Bouchon and Vallée*, 2003; *Robinson et al.*, 2006; *Vallée et al.*, 2008; *Walker and Shearer*, 2009]. It ruptured a 350–400-km-long segment of the Kunlun fault. The fault geometry (Figure 1) has been accurately determined by field investigation and satellite imaging [*Klinger et al.*, 2005; *Lasserre et al.*, 2005; *Xu et al.*, 2006].

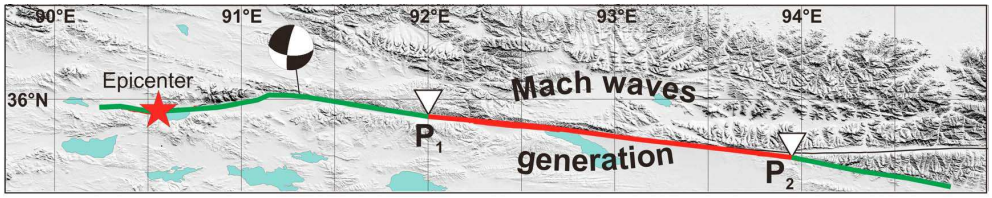

Figure 1. Fault rupture in the 2001 Kokoxili earthquake, with subshear rupture velocities on green segments and supershear velocities on red segments. The 170-km-long supershear segment between points P_1 and P_2 is the source region for the Mach waves. The epicenter (star) and focal mechanism are also shown.

[15] The rupture propagated unilaterally from west to east over about 100 s. After 130 km of subshear propagation, the rupture jumped into the supershear regime [*Vallée et al.*, 2008; *Walker and Shearer*, 2009; *Robinson et al.*, 2006]. The average rupture velocity over the following 170-km-long segment (bounded by points P_1 and P_2 in Figure 1) has been determined to be between 5 and 6.5 km/s, a value clearly higher the 3.5 km/s crustal shear wave velocity. The rupture velocity in the last part of the earthquake is less well known, but appears to be subshear.

[16] The Kokoxili earthquake, as well as a similar but much smaller foreshock (2000/11/26, M_w 5) located nearby, were recorded by several regional broadband seismometers belonging to the Federation of Digital Seismometers Network (FDSN; Figure 2). Because of the strike-slip character of the two earthquakes, the dominant waves are dispersive Love waves. We focus on 15–25 s Love waves to limit the effects of dispersion (see previous section). The average phase velocity $\bar{c}$ in this period range can be estimated from the recent regional group velocity maps derived from earthquakes [*Chen et al.*, 2010] or seismic noise [*Li et al.*, 2011]. This estimation can be made using the average value of 3.5 km/s for the phase velocity of the 25 s Love waves in the Kunlun fault area (GDM52 model of *Ekström* [2011]), and the relation between group and phase velocities. Also taking into account the variability of group velocity in the *Li et al.* [2011] model around the Kunlun fault, $\bar{c} = 3.3 \pm 0.2$ km/s. Acceptable values of $\bar{c}$, along with the possible values of rupture velocity v_r in the supershear regime, enable us to predict the geometry of the far-field Love wave Mach cone (Figure 2).

[17] Three stations (ULN, HIA, and KMI) are on the far-field Mach cone. In Figure 3 we show that at these stations, waveforms from the main shock are very similar to those of the small foreshock, as theoretically predicted. After aligning in time the Love wave arrivals, the normalized cross-correlation coefficient for the entire Love wave train exceeds 0.8 at these three stations, and even reaches 0.95 at station ULN. Moreover, when taking into account the amplifying factor applied in Figure 3, we observe that the amplitude ratio on the Mach cone is approximately 13,000–16,000. The predicted moment ratio between the events is 22,000, which is larger than the observed ratio. This discrepancy can be explained by the fact that the first segment of the Kokoxili event ruptured at a subshear speed. Generalizing the theory presented in the previous section to a compound rupture containing segments with different rupture speeds is straightforward, and for this specific earthquake we find that 20 s Love waves from the first (subshear) segment interfere destructively at stations along the Mach cone and contribute little to the overall waveform. Thus, only the supershear segment needs to be considered, and it likely released 60–80% of the overall moment [*Lasserre et al.*, 2005; *Robinson et al.*, 2006]. This reduces the expected moment ratio to values close to those observed.

[18] We also find that the cross-correlation values and the amplitude ratios are quite small for stations away from the Mach cone (either inside or outside it). As expected, both of these values reach a minimum when the stations are the furthest from the Mach cone (here for stations ENH and XAN, which are in the forward direction). Taken together,

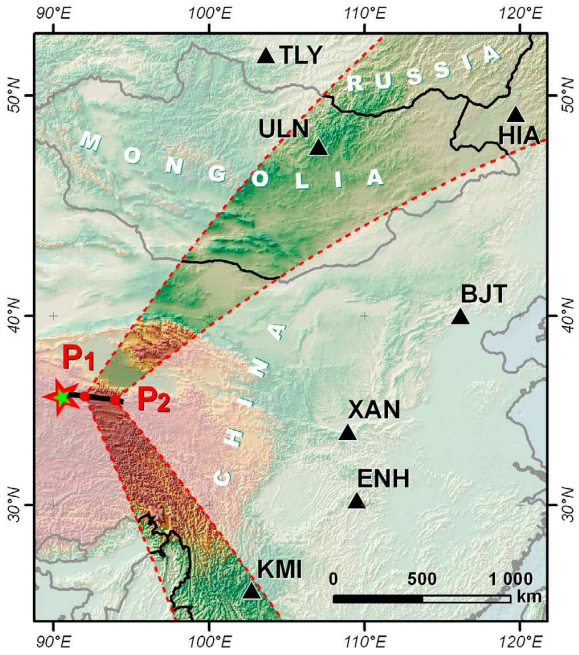

Figure 2. Geometry of the far-field Mach cone. The Kokoxili earthquake epicenter is shown by the red star and the ruptured fault by the black line. The small earthquake is represented only by its epicenter (green star) because it has a negligible extent. The supershear segment is bounded by the points P_1 and P_2. The Mach cone location, represented by the shaded area inside the red dashed lines, takes into account uncertainties in Love wave phase velocity and rupture velocity. The location and name of the broadband seismometers are indicated on the map.

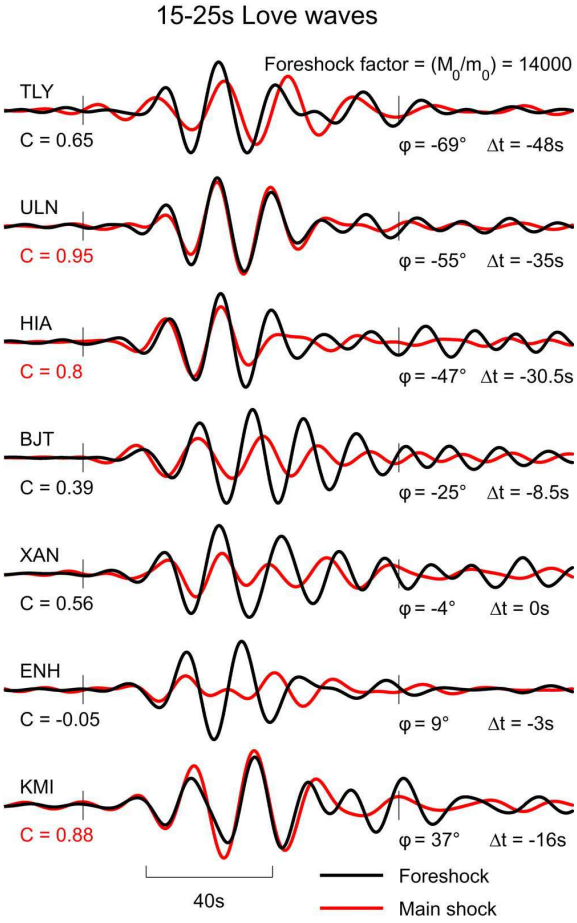

Figure 3. Love wave velocity seismograms from the Kokoxili earthquake (red) and a small foreshock (black), in the 15–25 s period range. ϕ, C, and Δt are respectively the station azimuth relative to the rupture direction, the zero-lag normalized cross-correlation calculated between the two ticks, and the time shift applied in order to align the records. Negative time shifts imply that the original main shock records are delayed, which is due to the initial subshear segment of the Kokoxili earthquake. Foreshock signals are scaled by an amplifying factor, equal to the inferred ratio of seismic moments of the supershear segment and the foreshock. Note the close similarity in amplitude and phase at stations on the Mach cone.

these results provide direct evidence of far-field Mach waves and thus supershear rupture speeds over a large section of the Kunlun fault.

4. Discussion

[19] We have developed a simple observational procedure using regional surface waves that discriminates between subshear and supershear rupture speeds for long strike-slip earthquakes. Because the model assumes seismic wavelengths greater than the fault width (≈10–15 km), the method is valid for periods greater than about 5 s and resolves supershear propagation over sections of the fault that are several times longer than the fault width. For these intermediate and long periods, our approach directly enlightens how the seismic radiation is greatly enhanced on the Mach cone. Moreover, our procedure has additional advantages: it is free from nonuniqueness issues associated with kinematic finite fault inversions and also provides a direct estimate of the moment released during supershear propagation, which helps constrain the length of the supershear segment.

[20] **Acknowledgments.** We thank IRIS for public and easy access to the data, P. Bernard, A. Ferreira, J.M. Nocquet and M. Bouchon for helpful comments, J. Trévisan and Y. Klinger for their help in designing some figures of this article. The review of the paper by Brad Aagaard has been very valuable.

[21] The Editor thanks Shamita M. Das and Brad Aagaard for their assistance in evaluating this paper.

References

Aagaard, B. T., and T. H. Heaton (2004), Near-source ground motions from simulations of sustained intersonic and supersonic fault ruptures, *Bull. Seismol. Soc. Am.*, *94*(6), 2064–2078.

Aki, K., and P. Richards (2002), *Quantitative Seismology*, Univ. Sci., Sausalito, Calif.

Andrews, D. J. (1976), Rupture velocity of plane strain shear cracks, *J. Geophys. Res.*, *81*(32), 5679–5687, doi:10.1029/JB081i032p05679.

Andrews, D. J. (2010), Ground motion hazard from supershear rupture, *Tectonophysics*, *493*, 216–221, doi:10.1016/j.tecto.2010.02.003.

Ben-Menahem, A., and S. J. Singh (1987), Supershear accelerations and Mach-waves from a rupturing front: Part 1. Theoretical model and implications, *J. Phys. Earth*, *35*, 347–365.

Bernard, P., and D. Baumont (2005), Shear Mach wave characterization for kinematic fault rupture models with constant supershear rupture velocity, *Geophys. J. Int.*, *162*(2), 431–447, doi:10.1111/j.1365-246X.2005.02611.x.

Bizzarri, A., E. M. Dunham, and P. Spudich (2010), Coherence of Mach fronts during heterogeneous supershear earthquake rupture propagation: Simulations and comparison with observations, *J. Geophys. Res.*, *115*, B08301, doi:10.1029/2009JB006819.

Bouchon, M., and M. Vallée (2003), Observation of long supershear rupture during the magnitude 8.1 Kunlunshan earthquake, *Science*, *301*(5634), 824–826, doi:10.1126/science.1086832.

Bouchon, M., M. Bouin, H. Karabulut, M. N. Toksöz, M. Dietrich, and A. J. Rosakis (2001), How fast is rupture during an earthquake? New insights from the 1999 Turkey Earthquakes, *Geophys. Res. Lett.*, *28*(14), 2723–2726, doi:10.1029/2001GL013112.

Burridge, R. (1973), Admissible speeds for plane-strain shear cracks with friction but lacking cohesion, *Geophys. J. R. Astron. Soc.*, *35*(4), 439–455, doi:10.1111/j.1365-246X.1973.tb00608.x.

Chen, Y., J. Badal, and J. Hu (2010), Love and Rayleigh wave tomography of Qinghai-Tibet plateau and its surrounding areas, *Pure Appl. Geophys.*, *167*(10), 1171–1203, doi:10.1007/s00024-009-0040-1.

Dunham, E. M., and R. J. Archuleta (2004), Evidence for a supershear transient during the 2002 Denali Fault earthquake, *Bull. Seismol. Soc. Am.*, *94*(6B), S256–S268, doi:10.1785/0120040616.

Dunham, E. M., and H. S. Bhat (2008), Attenuation of radiated ground motion and stresses from three-dimensional supershear ruptures, *J. Geophys. Res.*, *113*, B08319, doi:10.1029/2007JB005182.

Ekström, G. (2011), A global model of Love and Rayleigh surface wave dispersion and anisotropy, 25–250 s, *Geophys. J. Int.*, *187*(3), 1668–1686, doi:10.1111/j.1365-246X.2011.05225.x.

Ellsworth, W. L., et al. (2004), Near-field ground motion of the 2002 Denali Fault, Alaska, earthquake recorded at Pump Station 10, *Earthquake Spectra*, *20*(3), 597–615, doi:10.1193/1.1778172.

Freund, L. B. (1979), The mechanics of dynamic shear crack propagation, *J. Geophys. Res.*, *84*(B5), 2199–2209, doi:10.1029/JB084iB05p02199.

Klinger, Y., X. Xu, P. Tapponnier, J. Van der Woerd, C. Lasserre, and G. King (2005), High-resolution satellite imagery mapping of the surface rupture and slip distribution of the $M_w \sim 7.8$, November 14, 2001 Kokoxili earthquake (Kunlun fault, northern Tibet, China), *Bull. Seismol. Soc. Am.*, *95*(5), 1970–1987, doi:10.1785/0120040233.

Lasserre, C., G. Peltzer, F. Crampé, Y. Klinger, J. Van der Woerd, and P. Tapponnier (2005), Coseismic deformation of the 2001 $M_w = 7.8$ Kokoxili earthquake in Tibet, measured by synthetic aperture radar interferometry, *J. Geophys. Res.*, *110*, B12408, doi:10.1029/2004JB003500.

Li, H., S. Li, X. D. Song, M. Gong, X. Li, and J. Jia (2011), Crustal and uppermost mantle velocity structure beneath northwestern China from

seismic ambient noise tomography, *Geophys. J. Int.*, *188*, 131–143, doi:10.1111/j.1365-246X.2011.05205.x.

Robinson, D. P., C. Brough, and S. Das (2006), The Mw 7.8, 2001 Kunlunshan earthquake: Extreme rupture speed variability and effect of fault geometry, *J. Geophys. Res.*, *111*, B08303, doi:10.1029/2005JB004137.

Vallée, M., M. Landès, N. M. Shapiro, and Y. Klinger (2008), The 14 November 2001 Kokoxili (Tibet) earthquake: High-frequency seismic radiation originating from the transitions between sub-Rayleigh and supershear rupture velocity regimes, *J. Geophys. Res.*, *113*, B07305, doi:10.1029/2007JB005520.

Walker, K. T., and P. M. Shearer (2009), Illuminating the near-sonic rupture velocities of the intracontinental Kokoxili M_w 7.8 and Denali fault M_w 7.9 strike-slip earthquakes with global P wave back projection imaging, *J. Geophys. Res.*, *114*, B02304, doi:10.1029/2008JB005738.

Xia, K., A. J. Rosakis, and H. Kanamori (2004), Laboratory earthquakes: The sub-Rayleigh-to-supershear transition, *Science*, *303*(5665), 1859–1861, doi:10.1126/science.1094022.

Xu, X., G. Yu, Y. Klinger, P. Tapponnier, and J. Van Der Woerd (2006), Reevaluation of surface rupture parameters and faulting segmentation of the 2001 Kunlunshan earthquake (M_w 7.8), northern Tibetan Plateau, China, *J. Geophys. Res.*, *111*, B05316, doi:10.1029/2004JB003488.

E. M. Dunham, Department of Geophysics, Stanford University, 397 Panama Mall, Stanford, CA 94305, USA.

M. Vallée, Geoazur, University of Nice Sophia-Antipolis, IRD, OCA, 250 rue Albert Einstein, F-06560 Valbonne CEDEX, France. (vallee@geoazur.unice.fr)

II.3 Les récents apports de la sismo-géodésie

II.3.1 Accroissement de la capacité d'observation des séismes

La sismo-géodésie consiste à analyser les séries temporelles haute-fréquence (de l'ordre de 1Hz ou plus) enregistrées par un point GPS, pour en tirer l'évolution temporelle de son déplacement ou de sa vitesse. En cela, après traitement, les données sont très similaires à celles qui seraient enregistrées par un capteur sismique de bande extrêmement large. Cette absence de réponse instrumentale est un avantage théorique très grand des « sismogrammes » déduits des mesures GPS. En pratique, la bande est aussi limitée car l'analyse de longues séries temporelles montre des fluctuations, probablement liées aux effets du multi-trajet et de la variation de la troposphère durant la journée. Néanmoins, les fréquences de plusieurs milliHertz sont bien résolues dans ces sismogrammes GPS, qui constituent donc des données de très bonne qualité. La principale limitation est l'amplitude nécessaire du mouvement du sol, afin qu'elle puisse être extraite des incertitudes GPS : les ondes doivent générer un mouvement du sol de plusieurs millimètres, ce qui limite l'utilisation de cette technique aux séismes majeurs ou très proches.

Lors de ces séismes importants, les sismogrammes GPS accroissent donc notre capacité d'observation, d'autant plus qu'ils ne souffrent pas d'une éventuelle saturation lors de mouvements très forts. Nous avons commencé ces dernières années, en collaboration avec nos collègues géodésiens (Jean-Mathieu Nocquet, Mami Ueno), à appliquer des méthodes d'analyse sismologiques à ces nouveaux sismogrammes. Le but d'une telle analyse est double : en plus de chercher à mieux imager les processus de rupture, elle valide la qualité des données GPS et indique leurs éventuelles limitations. Cela peut permettre à nos collègues d'adopter les meilleures stratégies possibles pour le traitement GPS.

Afin d'illustrer l'accord qualitatif entre les sismogrammes GPS et les signaux accélérométriques, je présente dans la figure II.1 les mouvements du sol enregistrés lors du séisme de Tohoku (Japon, 2011/03/11, $M_w = 9$), à une distance d'environ 400km de la source.

De manière plus quantitative, nous avons aussi commencé à intégrer des données GPS haute-fréquence dans des analyses en réseau de la source sismique (voir section II.2.2). Cette approche permet une forte validation des données GPS, car elle nécessite une forte précision des signaux, à la fois sur le temps et la forme d'ondes. Nous avons utilisé les signaux GPS d'un petit réseau situé sur la faille du Kunlun, à proximité de la terminaison Est du séisme de Kokoxili de 2001 (Projet ANR « Lacunes », porté par Y. Klinger et P. Tapponnier). Ce réseau a enregistré la déformation transitoire du sol liée au séisme de Wenchuan du 12 mai 2008 ($M_w = 7.9$), situé à environ 1000km de distance. La géométrie d'observation est reportée dans la figure II.2. Le traitement des données haute-fréquence afin d'obtenir les sismogrammes GPS a été effectué par Mami Ueno et Jean-Mathieu Nocquet.

Nous montrons dans la figure II.3 que ce réseau identifie bien la direction

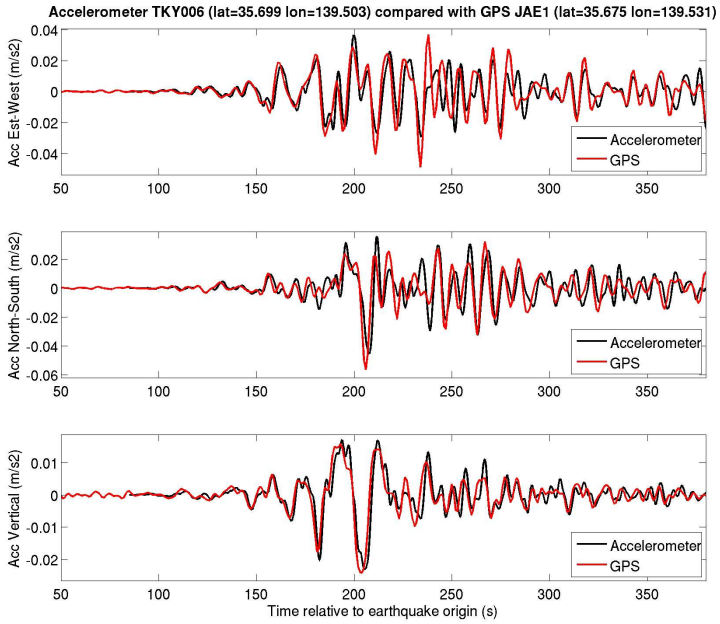

FIG. II.1 – Comparaison entre les signaux haute-fréquence GPS et les signaux accélérométriques enregistrés dans la région de Tokyo, lors du séisme de Tohoku. La station GPS JAE1 (Thomas Dautermann, DLR, supersites) est située à 4km de la station accélérométrique TKY006 du réseau Knet. Le signal GPS a été traité par J.-M. Nocquet pour obtenir le mouvement du sol. La figure présente la comparaison entre ce signal GPS – dérivé deux fois – et le signal accélérométrique, dans la gamme de fréquence [0.005Hz - 0.125Hz]. Une partie des faibles différences (à haute-fréquence) peut être imputée aux différences de localisation entre les stations.

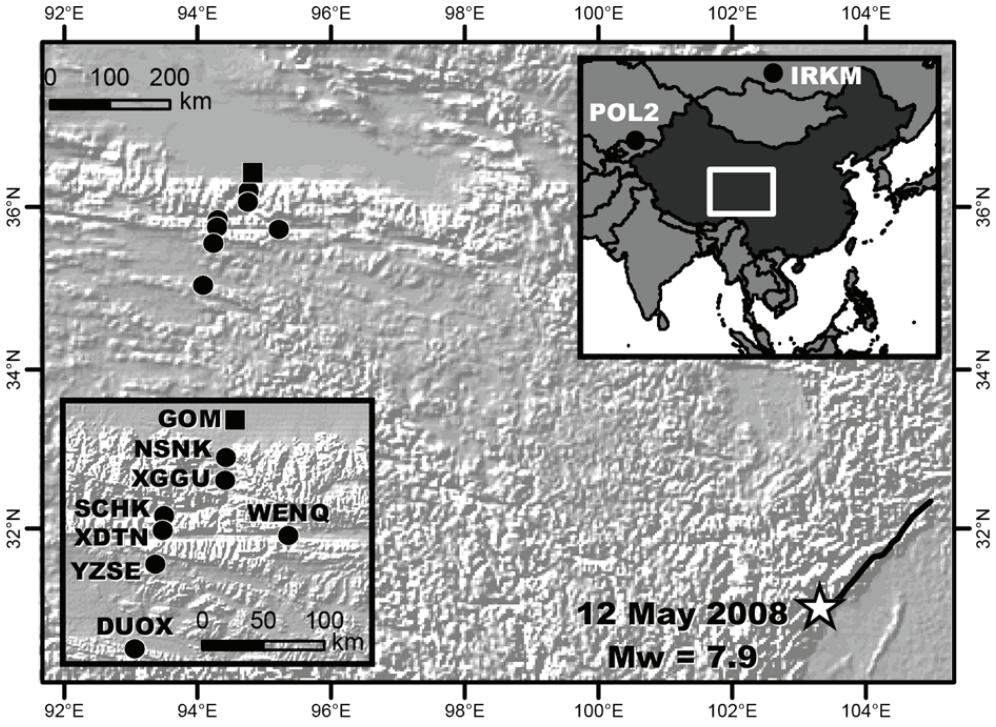

FIG. II.2 – Localisation des sites GPS haute-fréquence (cercles noirs), de l'hypocentre, et de la trace de rupture du séisme de Wenchuan.

générale de la source, située dans un back-azimut d'environ 120°. La direction d'arrivée des ondes est cohérente dans la fenêtre temporelle des ondes de volume et dans celle des ondes de surface. De plus, les caractéristiques typiques de vitesse de propagation des ondes de volume (P_n à cette distance régionale) et des ondes de surface sont bien identifiées. Cette analyse de réseau, effectuée ici dans la gamme de fréquence (0.02Hz-0.05Hz), a pu être menée alors que l'amplitude pic-a-pic des ondes de volume est de l'ordre de 2mm.

En travaillant à plus haute fréquence (0.07-0.12Hz), il est possible de détecter la progression de la rupture du séisme de Wenchuan, de manière similaire à l'étude du séisme du Kokoxili (section II.2.2). Les résultats, présentés dans la figure II.4, mettent bien en évidence la durée du séisme (90-100s) et sa propagation vers le Nord-Est sur une longueur d'environ 250km. Par rapport au séisme de Kokoxili, la rupture est plus difficile à suivre dans le détail, car des ondes de surface semblent être émises depuis une région voisine de l'hypocentre, pendant plus de 40s. Ensuite, il est difficile de détecter la rupture jusqu'à une nouvelle zone de radiation importante à plus de 200km de l'hypocentre.

Ce type d'étude montre le potentiel des données GPS pour accroître notre capacité d'observation des séismes majeurs : en les assimilant simplement à des sismogrammes, il est possible de leur appliquer des techniques sismologiques d'imagerie de la rupture. Des développements en cours sur la précision des traitements GPS à basse et haute fréquence pourraient encore faciliter ce type d'étude dans le futur.

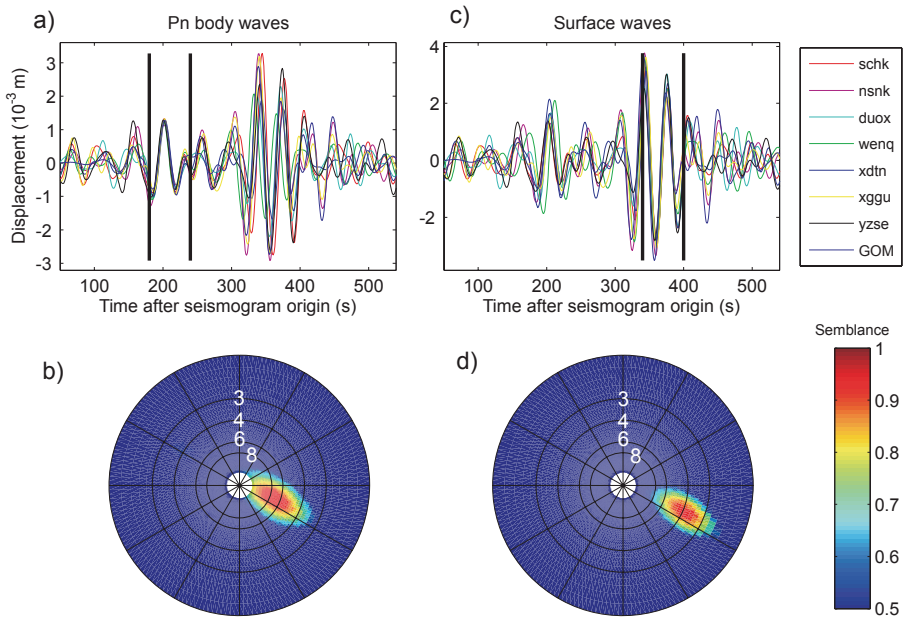

FIG. II.3 – Etude des caractéristiques globales de l'onde P_n (a-b) et des ondes de surface (c-d) au travers du réseau GPS. L'analyse est faite sur les déplacements radiaux, filtrés passe-bande entre 0.02 et 0.04Hz. Le back-azimut θ et la vitesse apparente au travers du réseau V_ϕ sont recherchés. a) et c) montrent la cohérence des signaux à chaque site, après correction du décalage en temps correspondant aux valeurs optimales de θ et V_ϕ. Les barres verticales montrent la fenêtre de 60s considérées dans l'analyse. b) et d) : valeurs de semblance (qualité de la cohérence), en fonction de θ et V_ϕ, présentés dans un diagramme polaire. θ et V_ϕ sont respectivement représentés selon l'angle et le rayon. Les iso-valeurs de V_ϕ correspondant aux vitesses de 8, 6, 4, et 3 $km.s^{-1}$ sont indiqués par les cercles noirs.

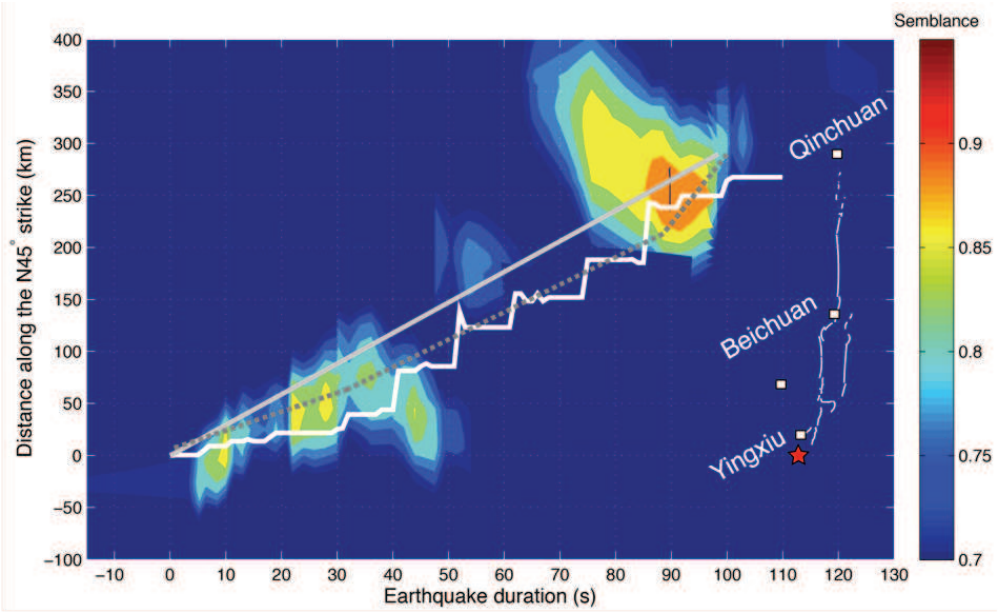

FIG. II.4 – Analyse en réseau montrant l'évolution de la semblance en fonction du temps et de la distance à l'épicentre. Les courbes blanches, grises et grises–pointillées indiquent la relation temps de rupture—distance proposées respectivement par *Xu et al.* (2009a), *Zhang and Ge* (2010) et *Huang et al.* (2012). Les lignes blanches fines montrent la trace de la rupture en surface de *Xu et al.* (2009b) ainsi que la position des villes principales le long de la faille.

II.3.2 L'observation des mouvements forts

Les données GPS haute-fréquence enregistrées à proche distance des séismes majeurs présentent plusieurs avantages par rapport aux données sismiques : tout d'abord, elles ne saturent pas quand le mouvement est très fort. En cela elles s'apparentent à des accéléromètres calibrés pour enregistrer des accélérations très importantes. Par rapport à ces derniers, elles présentent l'avantage d'un contenu basse-fréquence plus fiable, qui permet en particulier d'avoir accès - en plus de la phase transitoire - au déplacement statique final. La double intégration des accéléromètres, qui permettrait théoriquement aussi de retrouver ce mouvement final, est en effet un processus instable, peut-être à cause de perturbations venant du champ de rotation créé par les séismes (*Trifunac and Todorovska*, 2001 ; *Graizer*, 2005).

Lors du séisme de Maule (27 février 2010, $M_w = 8.8$), un ensemble de stations GPS haute-fréquence à distance régionale a pu être utilisé (voir Figure 1 de l'article suivant). Ces données étaient particulièrement précieuses car peu de données accélérométriques ont enregistré ce séisme majeur. Ces données ont été ajoutées aux données sismiques plus classiques (ondes de volume télésismiques, ondes de surface via la méthode de fonction de Green empirique) et aux données géodésiques (INSAR, GPS statique), pour bien contraindre le processus de rupture.

La suite de cette section reproduit l'article de *Delouis et al.* (2010), qui décrit l'approche utilisée et le processus de rupture déduit des données. Cet article met bien en évidence l'extension de la rupture (500km), sa durée (110s) et son aspect bilatéral (qui contraste avec la propagation vers le Sud des séismes connus de la marge Pérou-Chili : Sud-Chili 1960, Antofagasta 1995, Sud-Pérou 2001, Tocopilla 2007...). La profondeur maximale du glissement (50km) est en très bon accord avec les cartes de couplage calculées avant le séisme (*Ruegg et al.*, 2009). Cela illustre comment le potentiel sismique peut être précisément évalué par l'analyse des déformations intersismiques.

GEOPHYSICAL RESEARCH LETTERS, VOL. 37, L17305, doi:10.1029/2010GL043899, 2010

Slip distribution of the February 27, 2010 Mw = 8.8 Maule Earthquake, central Chile, from static and high-rate GPS, InSAR, and broadband teleseismic data

Bertrand Delouis,[1] Jean-Mathieu Nocquet,[1] and Martin Vallée[1]

Received 6 May 2010; revised 16 July 2010; accepted 4 August 2010; published 10 September 2010.

[1] The shallow depth underthrust earthquake of February 27, 2010 (Mw 8.8) ruptured the subduction plate interface in central Chile between 34°S and 38°S. We retrieve the spatial and temporal distribution of slip during this mega-earthquake through a joint inversion of teleseismic records, InSAR and High Rate GPS (HRGPS) data. Additionally, our model is shown to agree with broadband surface waves. Rupture initiated at about 32 km depth and propagated bilaterally resulting in two main slip zones located SSW and NNE of the hypocenter. Nucleation did not take place within or at the edge of one of these main asperities, but in between. During the first 30s, slip propagated predominantly southwards. Later on, the rupture evolved more slowly and more symmetrically. Eventually, the northern asperity became predominant with maximum slip reaching about 20 m. Most of the seismic moment was released within 110s, a relatively short time, explained by the bilateral propagation. The overall average rupture velocity is 2.6 km/s but propagation occurred initially faster towards the south (3.2 km/s). Large slip did not reach the trench, a result consistent with the moderate size of the tsunami. Down-dip, rupture stopped at about 50 km depth, in agreement with the lower limit of the locked zone inferred by Ruegg et al. (2009) from pre-seismic GPS data. **Citation:** Delouis, B., J.-M. Nocquet, and M. Vallée (2010), Slip distribution of the February 27, 2010 Mw = 8.8 Maule Earthquake, central Chile, from static and high-rate GPS, InSAR, and broadband teleseismic data, *Geophys. Res. Lett.*, *37*, L17305, doi:10.1029/2010GL043899.

1. Introduction

[2] Central Chile, in the vicinity of the cities of Concepción and Constitución, was struck by a major earthquake on February 27, 2010. The capital of Santiago de Chile was also strongly shaken by this event. Rapid source determinations from USGS (http://earthquake.usgs.gov/earthquakes/eqinthenews/2010/us2010tfan/#scitech), GCMT (http://www.globalcmt.org/), recently developed SCARDEC method (http://geoazur.oca.eu/spip.php?article675) all established the underthrust mechanism and moment magnitude (Mw) of 8.8. With a shallow depth (< 50 km) and a nodal plane dipping with a low angle to the East, it could be quickly categorized as an interplate subduction earthquake, at the interface between the subducting Nazca and overriding South-American plates. This was also immediately confirmed by the tsunami generated. Moreover, the subduction segment located between 35°S and 37°S had been shown to be strongly coupled [*Ruegg et al.*, 2009; *Madariaga et al.*, 2010] with a large slip deficit accumulated since the 1835 earthquake.

[3] Rapid slip during large earthquakes triggers seismic waves in the near, intermediate, and far fields that are detected on the Earth surface and that can be used to infer the characteristics of the rupture history. Geodetic data, by quantifying the static displacement on the Earth's surface resulting from the combination of the intermediate and near field terms, enable us to recover the spatial distribution of slip, but are insensitive to the time evolution of slip during the rupture. Seismological data are sensitive to both the spatial and temporal properties of the rupture, but trade-off between parameters describing the spatial and temporal distribution of slip can hardly be avoided without static constraints. Therefore, the most precise descriptions of the rupture history can be provided by joint inversions of seismological and geodetic data.

[4] In this study, we present a joint inversion of the Mw = 8.8, February 27, 2010 Chile earthquake rupture using static and 1Hz kinematic GPS, teleseismic, and InSAR data. High Rate GPS (HRGPS) records offer the advantage to directly record the position time evolution (instead of velocity or acceleration), and never saturate even in case of large and rapid motion, making this data particularly useful at short or regional distances. Such a comprehensive set of data enables us to reliably determine the main characteristics of the slip distribution of the mainshock, with only very minor contamination from possible post-seismic deformation.

2. Data

2.1. Static GPS Data

[5] We use the GAMIT/GLOBK software package v10.35 [*Herring et al.*, 2009] to process two sub-networks of 40 continuous GPS (CGPS) stations over South America provided by the International GNSS Service (IGS) [*Dow et al.*, 2009] and the Red Argentina de Monitoreo Satelital Continuo (RAMSAC, http://www.ign.gob.ar/ramsac). We first derive daily time series by combining the two sub-networks into a single position solution expressed with respect to the International Reference Frame 2005 (ITRF2005) [*Altamimi et al.*, 2007]. We carefully checked that the 18 sites used to define the frame were not impacted by the co-seismic displacement. Co-seismic displacements were estimated using an average of 7 days before the earthquake and the day following the earthquake to avoid any contamination of

[1]Geoazur, Observatoire de la Côte d'Azur, Université de Nice – Sophia Antipolis, CNRS, IRD, Valbonne, France.

0094-8276/10/2010GL043899

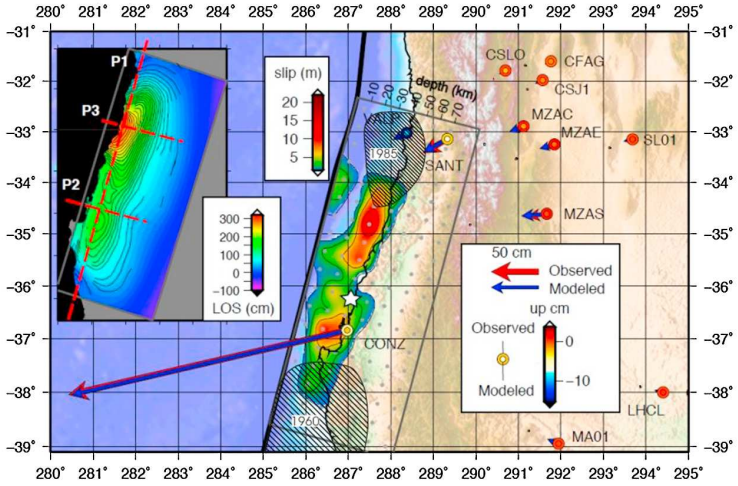

Figure 1. Location of the rupture model (gray rectangle) and slip distribution projected onto the Earth surface. Gray dots indicate the center of subfaults or points sources used to discretize the fault model. Heavy black line: trench; Red and blue arrows: observed and computed horizontal displacement from GPS, respectively. Bicolor circles: observed (outer ring) and computed (inner part) vertical displacement for GPS static data, respectively. Insert: unwrapped InSAR data (raw data © JAXA and METI, interferogram processed by NIED, see text for more details). Red dashed lines correspond to the three profiles shown in Figure 2a. The location of the cities of Concepción, Santiago, and Valparaiso is indicated by GPS stations CONZ, SANT, and VALP respectively. Hatched surfaces correspond to the rupture surfaces of the 1960 south Chile - Valdivia and 1985 central Chile – Valparaiso earthquakes. The 1960 rupture area is from *Plafker and Savage* [1970] and *Ruegg et al.* [2009], and the 1985 rupture zone is redrawn to combine the slip distribution obtained by *Mendoza et al.* [1994] and the aftershock area from *Barrientos* [1995].

the co-seismic displacement estimates by rapid post-seismic motion. The co-seismic displacement is determined with a precision better than one cm on the horizontal components and 2 cm on the vertical component. Figure 1 shows the GPS stations and their horizontal and vertical co-seismic displacements used in the inversion (auxiliary material Table S1).[1]

2.2. High Rate GPS Data

[6] For a subset of the CGPS sites, we processed 1 Hz data for a time window of one hour including the time of the earthquake using a two steps approach. First, single differences are formed to derive the Doppler shift (the rate of phase difference between two epochs of measurements) and we invert for the position change with respect to the first epoch of measurements. The obtained time series are used to determine the arrival time of the first seismic waves. We use this information to select a subset of reference sites in the far field (>800 km) that can be considered as fixed during the first 400 s following the earthquake. For each site in the near field, we used the track software [*Herring et al.*, 2009] which uses double-difference carrier phase to solve for the phase ambiguities and the 3D position at each epoch. We keep the same selection of satellite during the full time window to improve stability of the solution. We carefully check phase residuals for each satellite and remove GPS satellites PRN 17 & 4 because of their large systematic residuals. We chose RIO2 (longitude E292.25°, latitude −53.7855°) as the reference site providing the best stability of the result.

[7] We applied a sideral filtering [*Choi et al.*, 2004] using the time series from the day before the earthquake. Sideral filtering significantly reduces the long period drift (>100s). The static displacement obtained from the kinematic processing agree within 2 cm with the one derived from the GAMIT/GLOBK static processing, indicating very little rapid post-seismic deformation occurring hours after the earthquake. Depending on the quality of the displacement time series obtained, HRGPS records were high-pass filtered with a cut frequency varying between 0.005 and 0.02 Hz, and low-pass filtered at 0.03 Hz. As a result, the inversion is performed at low frequency, in a range appropriate to recover the main characteristics of the rupture process for such a mega-earthquake (Mw 8.8).

2.3. InSAR Data

[8] We use a Synthetic Aperture Radar (SAR) interferogram covering the essential part of the rupture zone of the February 27, 2010 earthquake. It was produced by NIED [*Ozawa*, 2010] from ALOS/PALSAR ScanSAR raw data of METI and JAXA (Ministry of Economy, Trade and Industry of Japan, and Japan Aerospace Exploration Agency). The InSAR image was released at http://supersites.unavco.org/chile.php. It corresponds to the descending path 422 of ALOS, with master 2008/04/10 and slave 2010/03/01. In the inversion, we incorporated 1172 points distributed along the fringes reproduced in Figure 1. Unwrapping of the InSAR data was performed using the static displacement at GPS station CONZ as a calibration point and inverting for a line of sight (LOS) offset.

[1] Auxiliary materials are available in the HTML. doi:10.1029/2010GL043899.

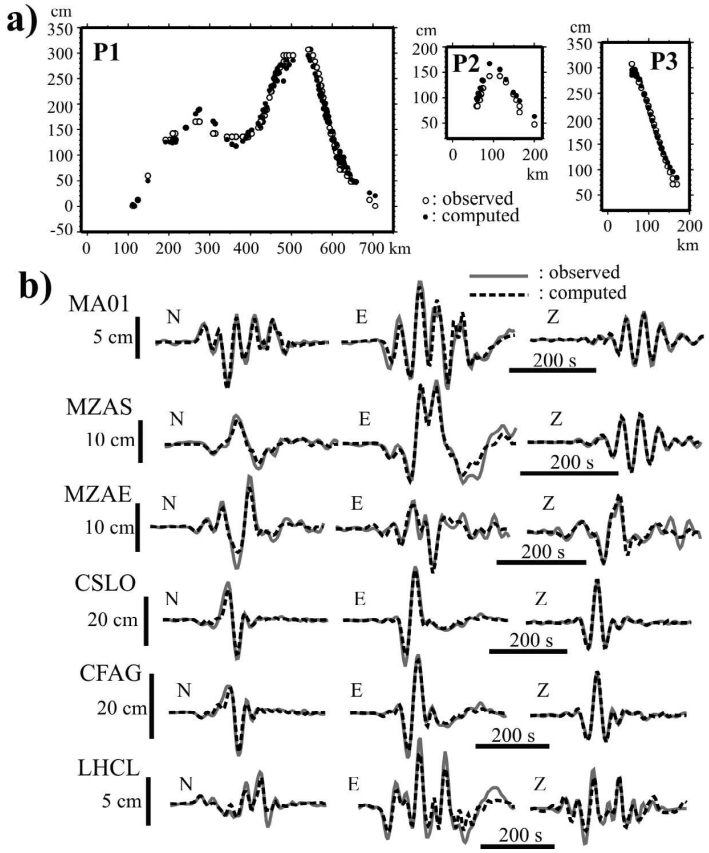

Figure 2. (a) Three profiles (P1, P2, P3) across the SAR interferogram to illustrate data fitting. LOS: Line Of Sight displacement (positive means increasing of the satellite-to-ground distance). Horizontal axes: distance with respect to an arbitrary origin. (b) Modeling of the HRGPS records. Station locations are shown in Figure 1.

2.4. Teleseismic Broadband Data

[9] Teleseismic waveforms of the FDSN (Federation of Digital Seismograph Networks) were retrieved from the IRIS data center (http://www.iris.edu/wilber) for 24 broadband stations located at distances comprised between 45° and 78° and sampling the range of available azimuths. Processing of the teleseismic records includes deconvolution from the instrument response, integration to obtain displacement, windowing around the P (vertical) and SH (horizontal transverse) wave trains, equalization to a common magnification and epicentral distance, bandpass filtering between 0.01 and 0.8 Hz for the P waves and 0.01 to 0.4 Hz for the S waves.

3. Inversion Procedure

[10] We first determined the focal mechanism of the February 27, 2010 earthquake by modeling the teleseismic waveforms. We performed a series of joint inversions and found that (strike, dip, rake) = (15, 18, 110) provides the best fit to the seismological and geodetic datasets. Our estimate is almost identical to the GCMT and USGS-CMT solutions, (strike, dip, rake) = (18, 18, 112) and (14, 19, 104) respectively.

[11] Our kinematic modeling follows the approach described by *Delouis et al.* [2002]. The model consists of a single fault segment, 720 km long and 280 km wide, subdivided into 126 subfaults measuring 40 km along strike and dip, evenly distributed on the fault plane. The model area is purposely taken larger than the expected rupture surface in order to discriminate clearly the areas which slipped from those which did not. The strike and dip angles of the fault are kept fixed: (strike, dip) = (15°, 18°). Rupture initiation, i.e. the model hypocenter, is located at 36.208°S, 72.963°W, provided by the DGF (Departamento de Geofisica, Universidad de Chile, http://www.dgf.uchile.cl) and at a depth of 32 km. Although DGF's epicenter is located 40 km to the SSW of the estimate from NEIC/USGS epicenter, this location was found to provide the optimal fit to the combined datasets, compared to NEIC/USGS epicenter and intermediate locations.

[12] To model the waveforms, the continuous rupture is approximated by a summation of point sources, one at the center of each subfault. To model the static displacements, subfaults are represented by dislocation surfaces. For each point source, a local source time function is defined, corresponding to the rate of seismic moment locally released. It is represented by three mutually overlapping

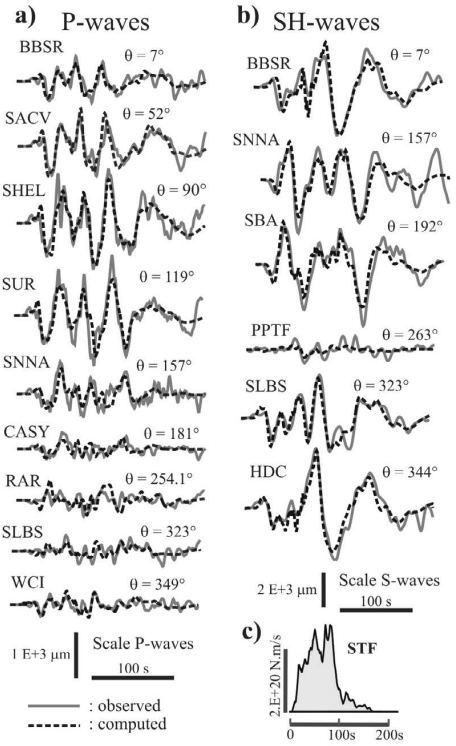

Figure 3. Modeling of the teleseismic records, for the (a) P-waves and (b) SH-waves. Amplitudes have been normalized to a common epicentral distance. Only a subset of data is displayed, the complete set of records is shown in the auxiliary material. (c) The overall source time function (STF). In Figures 2a and 2b θ is the azimuth of the station.

isosceles triangular functions of duration equal to 12s, allowing the local source time function to last for a maximum of 24s. For each of the 126 subfaults (points sources), the parameters to be inverted for are the slip onset time, the rake angle, and the amplitudes of the three triangular functions. Rupture onset times are bounded according to a minimum and a maximum rupture velocity of 1.8 and 3.5 km/s. The rake angle can vary between 100° and 120°.

[13] A non-linear inversion is performed using a simulated annealing optimization algorithm. Convergence criterion is based on the simultaneous minimization of the root mean square (rms) data misfit and of the total seismic moment. The rms misfit error is the average of the normalized rms errors of the individual data sets (teleseismic, InSAR, static GPS, and HRGPS), equally weighted. Minimization of the total seismic moment is required to reduce spurious slip in the fault model. We also verified that the main features of the slip model described below are stable when the relative weights of the individual datasets are modified by as much as 50%.

[14] Synthetic seismograms at local to regional distances (HRGPS data) are computed using the discrete wave number method of *Bouchon* [1981] designed for one-dimensional velocity models. Synthetic seismograms at teleseismic stations were generated using ray-theory approximation and the approach by *Nabelek* [1984]. We used the CRUST2.0 global crustal velocity model from Laske, Masters, and Reif (http://igppweb.ucsd.edu/~gabi/rem.html) in the epicentral area. Static displacements (for static GPS and InSAR) are computed using the dislocation formulation of *Savage* [1980] at the surface of a semi-infinite elastic half space.

4. Inversion Results and Resolution

[15] The slip map resulting from the joint inversion is projected onto the Earth surface in Figure 1. It displays two main slip zones, or asperities, located one SSW and the other NNE from the epicenter, therefore demonstrating the bilateral character of rupture propagation. Slip within the hypocentral area is relatively moderate (4 to 8m) while it reaches 13m and 21m at the SSW and NNE asperities respectively. Total rupture length is about 500 km along strike. In the up-dip direction, large slip stops 20–40 km from the trench (except between lat. −34.4° and −33.5°), a feature which certainly limited the size of the induced tsunami. In the down-dip direction, slip stops rather uniformly between 45 and 50 km depth (Figure 1).

[16] Observed versus values predicted by our joint inversion are shown in Figure 1 for the static GPS, in Figure 2 for the InSAR (a) and HRGPS (b), and in Figure 3 for the teleseismic records. The InSAR data, with a clear closure of the fringes in the north and in the south provide strong constraints on the rupture terminations (Figure 1) and display two well marked maxima corresponding to the two major slip zones (see profile P1 in Figure 2a). The HRGPS time series are modeled in the same way as would be strong motion records (Figure 2b). Figure 3 shows waveform modeling of the teleseismic P and SH waves for a subset of stations spanning different azimuths, the complete set of stations being shown in the auxiliary material. The mainshock source time function (STF, Figure 3c) indicates that most of the seismic moment was released during the first 110s. The slip weighted average rupture velocity is 2.6 km/s but on average, propagation was slightly faster towards the south (2.7 km/s) than towards the North (2.5 km/s). The difference is mainly due to the initial part of rupture propagation, which is faster towards the south (3.2 km/s) in the first 30s.

[17] To explore the stability of the solution with the discretization of the fault model, we carried out two additional joint inversions, one with the mesh of subfaults shifted 20 km towards the East, and one with a finer grid spacing, 20 km instead of 40 km. The corresponding slip maps are presented in the auxiliary material. These tests show that the results presented in this paper are stable with respect to reasonable variations of the mesh of subfaults.

[18] Figure 4a introduces a snapshot view of the rupture time evolution, displaying the cumulative slip pattern with six time steps. During the first 45s of rupture, slip developed essentially towards the south. At the same time the along-dip extent of the rupture was almost achieved. Thereafter (see t = 60s), the pattern became more symmetrical. From 75s on, the northern slip zone becomes predominant. Finally, the overall slip pattern is moderately asymmetrical, with 60% of the seismic moment released in the NNE and 40% in the SSW. The total seismic moment is 1.8E + 22 N. m (Mw = 8.8). The slip model is provided in ASCII format in the auxiliary material.

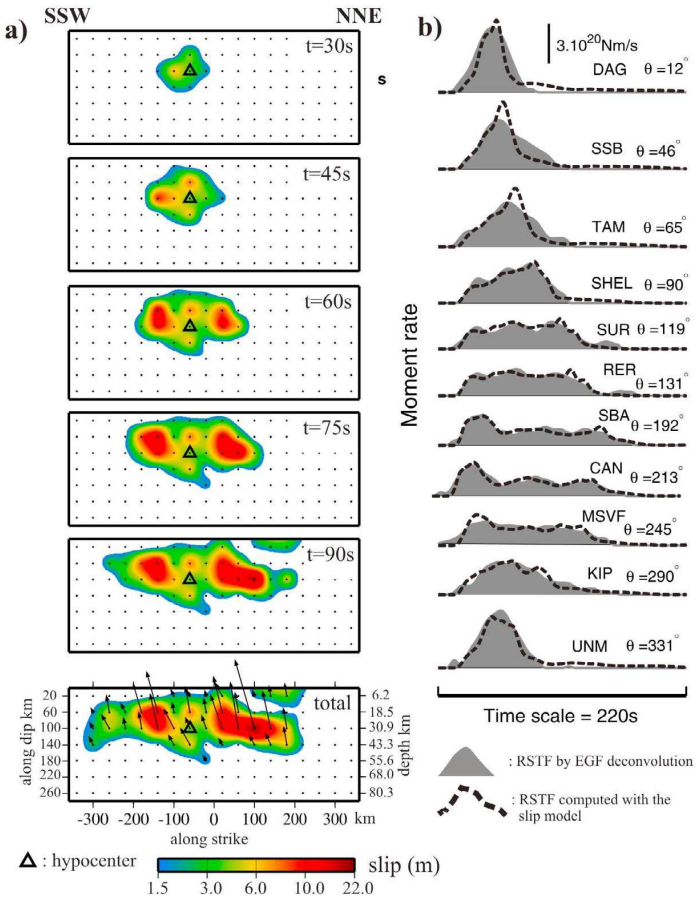

Figure 4. (a) Snapshots of the slip distribution resulting from the joint inversion. Cumulative slip shown in six time steps. The last map (bottom, indicated "total") displays the final slip distribution. Black arrows are the slip vectors. (b) Comparison between observed and computed RSTFs. Observed RSTFs (filled curves) are obtained by stabilized deconvolution of the 2010/03/05 aftershock (Mw = 6.6) transverse signals from the main shock transverse signals, in the Love-wave time window. Computed RSTFs (dashed curves) are computed from our rupture process model. A 10s smoothing is applied to both observed and computed RSTFs. The name and azimuth of the selected FDSN stations, as well as the amplitude scale, are shown. θ is the azimuth of the station.

[19] We further validate our kinematic source model through a comparison with broadband surface waves recorded at teleseismic stations. To do so, we adopt an Empirical Green Function (EGF) approach, using as EGFs two Mw = 6.6 aftershocks (2010/03/05 and 2010/03/16). Theoretically, the Relative Source Time Functions (RSTFs) can be obtained by a direct deconvolution of the EGF signal from the main shock signal [*Hartzell*, 1978]. However, the inherent instability of the deconvolution operator may pollute the results. To retrieve more reliable RSTFs, we apply the stabilized deconvolution technique of *Vallée* [2004], in which four physical constraints on the RSTFs (causality, positivity, limited duration, and equal area) are integrated in the deconvolution process. We verified that the RSTFs are little sensitive on the selected aftershock. Figure 4b shows the Love-waves RSTFs, recorded at 11 stations of the FDSN (filled curves), together with the RSTFs derived from our spatio-temporal model, considering a Love-waves phase velocity equal to 4.5 km/s [*Schwartz*, 1999]. Because variations of the RSTFs as a function of station azimuth are directly related to the rupture process characteristics, the high similarity between observed and computed RSTFs is a strong indicator of the realness of our proposed source model. It confirms two of the main earthquake propagation characteristics: (1) the dominant moment release North of epicenter, as shown by the more compact RSTFs in this direction (stations DAG, SSB, and UNM), and (2) the minor but early southward rupture propagation, as evidenced by the impulsive RSTF initiation at stations SBA and CAN.

[20] Synthetic tests were carried out in order to assess how the resolution of the slip distribution may vary on the fault model and what is the contribution of the different datasets. In addition, we assess the relative power of resolution of the separate and joint inversions. The synthetic model and the inversions are shown in the auxiliary material. The main results from those tests are: i) among the individual datasets,

the InSAR data provides the best constraint on the slip location. This is to be expected given the good coverage of the InSAR data points in the coastal area; ii) the best retrieval of the synthetic asperities is obtained with the joint inversion. This is usually the case, each individual dataset contributing to the overall resolution in the joint inversion; iii) slip in the upper part of the model, i.e. nearest to the trench, is less well resolved. This is related to the lack of measuring points offshore between the coast and the trench.

5. Discussion and Conclusion

[21] Our analysis of the 2010 Chile earthquake is performed at relatively low frequency, our aim being to recover the main and robust characteristics of the slip distribution of this mega earthquake. Further studies using additional data and higher frequencies will certainly provide finer details of the rupture process. However, our joint inversion clearly evidences a bilateral propagation of rupture, extending about 250 km on both sides of the epicenter, the overall slip pattern being moderately asymmetrical, with 20% more seismic moment released in the NNE than in the SSW. Remarkably, the depth of 50 km found for the down-dip end of the rupture agrees with estimates for the down-dip end of the locked zone derived from GPS surface measurements [*Ruegg et al.*, 2009]. It is also identical to that found for large interplate earthquakes in northern Chile [*Delouis et al.*, 1997; *Pritchard and Simons*, 2006; *Delouis et al.*, 2009], suggesting a transition from seismic to aseismic behavior at that depth for a large segment of the south American subduction. Near the trench, despite a lower resolution on the slip distribution, our model clearly shows that large slip did not occur in the uppermost part of the plate interface, a result consistent with the relatively moderate size of the tsunami triggered by such a large earthquake. The rupture timing is constrained by the teleseismic body waves and by the HRGPS records. Both data show that, during the first 30s, the rupture propagated southwards with a velocity faster than the average velocity (2.6 km/s). About 60s after rupture initiation, the slip distribution displays an almost symmetrical pattern on both sides of the hypocenter. After 75s, slip becomes predominant in the North. This time evolution is confirmed independently by the relative source time functions at teleseismic stations obtained from surface waves. The effective duration of rupture is about 110s, a relatively short duration for a Mw 8.8 earthquake, but well explained by the bilateral propagation, causing two areas to release a large amount of moment partially simultaneously. Slip in the epicentral area is relatively small with respect to the major slip zones on both sides. Clearly, the initiation of the 2010 Chile mainshock did not take place within a main asperity.

[22] The northern and southern termination of the rupture are well constrained, especially with the help of the InSAR data. Towards the south, large slip ends at 37.2°S and from there, rapidly decreases near 38°S. This corresponds within the uncertainty to the northern limit of the 1960 M > 9.5 south Chile - Valdivia earthquake [*Plafker and Savage*, 1970; *Cifuentes*, 1989, Figure 1]. To the North, large slip stops at 34.5°S and from there, slip decreases to reach 0 at 34.2°S. This corresponds to the southern limit of the 1985 central Chile- Vaparaiso earthquake [*Comte et al.*, 1986; *Mendoza et al.*, 1994; *Barrientos*, 1995, Figure 1]. The 2010 earthquake ruptured the seismic gap studied by *Campos et al.* [2002], but it extended further to the north.

[23] We retrieved the main properties of the 2010 central Chile earthquake rupture from the joint inversion of geodetic and seismological data. Among these data, High Rate GPS time series were used as if they were strong-motion records in the frequency domain below 1 Hz, providing ground displacement seismograms free of integration biases. Equipping potential rupture zones with High Rate GPS stations may provide a wealth of high quality data to constrain future earthquake source inversions.

[24] **Acknowledgments.** We are grateful to individuals and institutions operating CGPS stations in Chile and Argentine and contributing to the IGS (JPL, BKG, SHOA, G2, CERI). We deeply thank the Instituto Geográfico Nacional (IGN) from Argentine for making their data publicly available through the RAMSAC CGPS network (http://www.ign.gob.ar/ramsac). We thank the IRIS data center for providing easy access to worldwide broadband waveforms. We are grateful to the NIED Institute of Japan and Geo (http://supersites.unavco.org/main.php) for making the InSAR data publicly available.

References

Altamimi, Z., X. Collilieux, J. Legrand, B. Garayt, and C. Boucher (2007), ITRF2005: A new release of the International Terrestrial Reference Frame based on time series of station positions and Earth Orientation Parameters, *J. Geophys. Res.*, *112*, B09401, doi:10.1029/2007JB004949.

Barrientos, S. (1995), Dual seismogenic behaviour: The 1985 central Chile earthquake, *Geophys. Res. Lett.*, *22*, 3541–3544, doi:10.1029/95GL03316.

Bouchon, M. (1981), A simple method to calculate Green's functions for elastic layered Media, *Bull. Seismol. Soc. Am.*, *71*, 959–971.

Campos, J., D. Hatzfeld, R. Madariaga, G. Lopez, E. Kausel, A. Zollo, S. Barrientos, and H. Lyon-Caen (2002), The 1835 seismic gap in south central Chile, *Phys. Earth Planet. Inter.*, *132*, 177–195, doi:10.1016/S0031-9201(02)00051-1.

Choi, K., A. Bilich, K. M. Larson, and P. Axelrad (2004), Modified sidereal filtering: Implications for high-rate GPS positioning, *Geophys. Res. Lett.*, *31*, L22608, doi:10.1029/2004GL021621.

Cifuentes, I. L. (1989), The 1960 Chilean earthquakes, *J. Geophys. Res.*, *94*, 665–680, doi:10.1029/JB094iB01p00665.

Comte, D., A. Eisenberg, E. Lorca, M. Pardo, L. Ponce, R. Saragoni, S. K. Sing, and G. Suárez (1986), The central Chile earthquake of 3 March 1985: A repeat of previous great earthquakes in the region?, *Science*, *233*, 449–453, doi:10.1126/science.233.4762.449.

Delouis, B., et al. (1997), The Mw = 8:0 Antofagasta (northern Chile) earthquake of 30 July, 1995: A precursor to the end of the large 1877 gap, *Bull. Seismol. Soc. Am.*, *87*, 427–445.

Delouis, B., D. Giardini, P. Lundgren, and J. Salichon (2002), Joint inversion of InSAR, GPS, teleseismic and strong motion data for the spatial and temporal distribution of earthquake slip: Application to the 1999 Izmit mainshock, *Bull. Seismol. Soc. Am.*, *92*, 278–299, doi:10.1785/0120000806.

Delouis, B., M. Pardo, D. Legrand, and T. Monfret (2009), The Mw 7.7 Tocopilla earthquake of 14 November 2007 at the southern edge of the northern Chile seismic Gap: Rupture in the deep part of the coupled plate interface, *Bull. Seismol. Soc. Am.*, *99*, 87–94, doi:10.1785/0120080192.

Dow, J. M., R. E. Neilan, and C. Rizos (2009), The International GNSS Service in a changing landscape of Global Navigation Satellite Systems, *J. Geod.*, *83*, 191–198, doi:10.1007/s00190-008-0300-3.

Hartzell, S. (1978), Earthquake aftershocks as Green's functions, *Geophys. Res. Lett.*, *5*, 1–4, doi:10.1029/GL005i001p00001.

Herring, T. A., R. W. King, and S. C. McClusky (2009), *Documentation of the MIT GPS Analysis Software: GAMIT v 10.35*, Mass. Inst. of Technol., Cambridge.

Madariaga, R., C. Vigny, M. Métois, and J. Campos (2010), Central Chile finally breaks, *Science*, *328*, 181–182, doi:10.1126/science.1189197.

Mendoza, C., S. Hartzell, and T. Monfret (1994), Wide-band analysis of the 3 March 1985 central Chile earthquake: Overall source process and rupture history, *Bull. Seismol. Soc. Am.*, *84*, 269–283.

Nabelek, J. (1984), Determination of earthquake fault parameters from inversion of body waves, Ph.D. thesis, 361 pp., Mass. Inst. of Technol., Cambridge.

Ozawa, T. (2010), Utilization of ALOS-2 for crustal deformation detection of earthquake and volcano, paper presented at ALOS-2 symposium, Jpn. Aerosp. Explor. Agency, Tokyo, 26 March.

Plafker, G., and J. C. Savage (1970), Mechanism of the Chilean earthquake of May 21 and 22, 1960, *Geol. Soc. Am. Bull.*, *81*, 1001–1030, doi:10.1130/001607606(1970)81[1001:MOTCEO]2.0.CO;2.

Pritchard, M. E., and M. Simons (2006), An aseismic slip pulse in northern Chile and along-strike variations in seismogenic behavior, *J. Geophys. Res.*, *111*, B08405, doi:10.1029/2006JB004258.

Ruegg, J. C., A. Rudloff, C. Vigny, R. Madariaga, J. B. de Chabalier, J. Campos, E. Kausel, S. Barrientos, and D. Dimitrov (2009), Interseismic strain accumulation measured by GPS in the seismic gap between Constitución and Concepción in Chile, *Phys. Earth Planet. Inter.*, *175*, 78–85, doi:10.1016/j.pepi.2008.02.015.

Savage, J. C. (1980), Dislocations in seismology, in *Dislocations in Solids*, edited by F. R. N. Navarro, pp. 252–339, North-Holland, New York.

Schwartz, S. Y. (1999), Noncharacteristic behavior and complex recurrence of large subduction zone earthquakes, *J. Geophys. Res.*, *104*, 23,111–23,125, doi:10.1029/1999JB900226.

Vallée, M. (2004), Stabilizing the empirical Green function analysis: Development of the projected Landweber method, *Bull. Seismol. Soc. Am.*, *94*, 394–409, doi:10.1785/0120030017.

B. Delouis, J.-M. Nocquet, and M. Vallée, Geoazur, Observatoire de la Côte d'Azur, Université de Nice – Sophia Antipolis, CNRS, IRD, 250 rue A. Einstein, F-06560 Valbonne, France.

II.4 Perspectives : Intérêt des séismes particuliers

L'analyse détaillée de certains séismes permet de mettre en lumière des comportements méconnus de la rupture sismique. Cela a été le cas lors de nos analyses sur le séisme de Kokoxili (Tibet, 14/11/2001) : nous avons montré que la vitesse de rupture pouvait atteindre des valeurs extrêmes (proche de la vitesse de l'onde P). De telles observations stimulent les modélisations analogiques (*Rousseau et al.*, 2009 ; *Schubnel et al.*, 2011) et numériques (*Templeton et al.*, 2009 ; *Bizzarri et al.*, 2010 ; *Cruz-Atienza and Olsen*, 2010 ; *Kaneko and Lapusta*, 2010) de la rupture sismique en vue de mieux comprendre son fonctionnement.

Dans le futur, où de nouveaux séismes importants seront encore mieux enregistrés qu'aujourd'hui, j'ai donc l'intention de mettre en pratique les différentes approches décrites (fonction de Green empirique, analyse en réseau, champ proche) sur des données sismiques ou géodésiques haute-fréquence. Un des objectifs est d'observer les caractéristiques du front de rupture avec plus de détail. En effet, si les régimes principaux de la vitesse de rupture (subRayleigh ou supershear) sont décrits et observés, ce n'est pas le cas des phases de transition d'un régime à l'autre. Ces lieux d'accélération ou de décélération de la rupture devraient témoigner de caractéristiques mécaniques ou géométriques particulières, et ils ont théoriquement un rôle important dans les radiations générées (*Madariaga*, 1977 ; *Campillo*, 1983). De manière plus large, l'observation précise doit permettre de déceler si le concept de front de rupture unique est toujours bien adapté au mécanisme des séismes. Certaines suggestions récentes font en effet état de ruptures « composées » (*Lay et al.*, 2010 ; *Robinson et al.*, 2006), dans lesquelles le développement d'une rupture initiale donne naissance à une nouvelle nucléation en un autre point de la faille.

Un autre atout des données très proches est de permettre de mieux appréhender le comportement temporel local de la rupture (que l'on assimile souvent au « temps de montée »). Cette caractéristique est fortement reliée aux propriétés de friction de la faille (*Heaton*, 1990 ; *Cochard and Madariaga*, 1994 ; *Cruz-Atienza and Olsen*, 2010). Ces dernières sont mal connues, entre autres car la mise à l'échelle sismologique des expériences en laboratoire n'est pas un problème facile (*Marone*, 1998). L'utilisation de données très proches devrait aider à cette détermination, car l'effet d'intégration sur la faille des vitesses de glissement locales est réduit. Il n'est néanmoins pas absent et le degré de corrélation spatiale de cette vitesse de glissement conserve ainsi un rôle important dans la radiation sismique (*Ruiz et al.*, 2007), perturbant la résolution purement locale de la vitesse de glissement.

Ces quelques exemples sont l'illustration d'un objectif plus général : détecter des détails observationnels de la cinématique des séismes, qui puissent servir de « points d'entrée » à une meilleure modélisation et compréhension de la dynamique des séismes. Les pistes d'observation pourront être souvent anticipées, en suivant entre autres les quelques idées précédentes. Mais je crois aussi que les nouveaux éléments utiles à notre compréhension de la rupture viendront de surprises que nous apporteront certaines données très proches des séismes. En

cela, il me semblera important d'analyser ces nouvelles données avec une vision consciente mais détachée des modèles de rupture traditionnels.

Chapitre III

Replacer la rupture dans le cycle sismique : Sismogénèse dans une zone de subduction active, Les Andes du Nord

III.1 Introduction : Objectifs généraux du projet « ADN »

Le séisme de Sumatra-Andaman du 26 décembre 2004, puis ceux du Chili (27 février 2010) et du Japon (11 mars 2011) ont rappelé l'enjeu de la compréhension des mécanismes conduisant au déclenchement des grands séismes de subduction. Dans ce contexte, l'Equateur nous est apparu une cible d'interêt : la marge de subduction a été très active, comme en témoignent le séisme de magnitude 8.8 en 1906 et les trois autres séismes de très forte magnitude ($M_w \sim 8$) du XXème siècle (1942, 1958, 1979 ; voir *Kanamori and McNally*, 1982, *Beck and Ruff*, 1984, ainsi que la Figure III.1). Par ailleurs, la zone côtière était dépourvue d'observations proches, précises et permanentes.

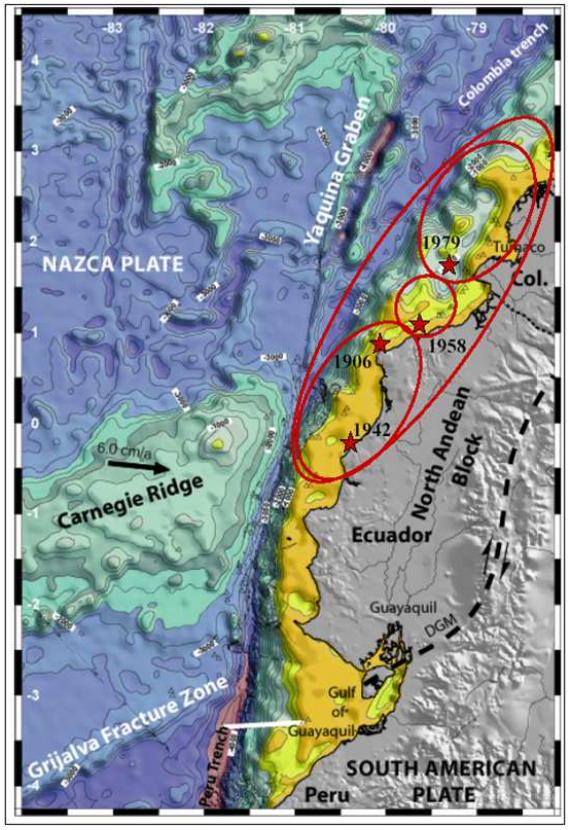

FIG. III.1 – Carte de situation de la marge Equatorienne. La plaque océanique Nazca subducte sous la Plaque Amérique du Sud, avec une vitesse de 5.5—6cm/an et une direction approximativement Est-Ouest (*Trenkamp et al.*, 2002 ; *Kendrick et al.*, 2003). Les hypocentres et zones de rupture des 4 grands séismes du XXème siècle sont représentés. Noter que seule celle du séisme de 1979 est déterminée avec une bonne précision. L'ellipse la plus grande est celle du séisme de 1906. D'après *Collot et al.* (2002) et *Vaca et al.* (2010).

Autre élément marquant, la sismicité interplaque de forte magnitude paraît s'être produite uniquement au Nord de la latitude -1^o. Le sud du pays, ainsi que l'ensemble du Nord du Pérou (Figure III.2) ne semble pas avoir connu de séismes de magnitude supérieure à 7.7. Une étude spécifique sur le Nord du Pérou (*Dorbath*, 1990) n'a pas révélé de séisme majeur depuis l'arrivée des colons espagnols.

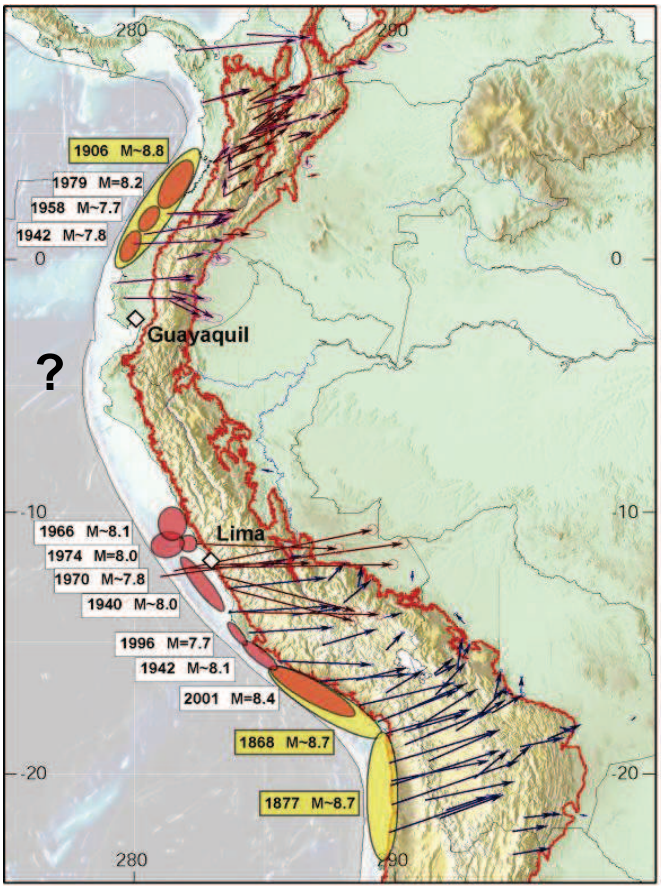

FIG. III.2 – Séismes de subduction majeurs le long de la marge des Andes du Nord. Sont représentés tous les événements de magnitude supérieure à 7.7 depuis 150 ans. L'absence de très forte sismicité est claire sur un segment d'environ 1000km depuis le Nord de Lima (Pérou) jusqu'au centre de l'Equateur. Figure de Mohamed Chlieh.

Sans plus d'informations, un tel « gap » de sismicité peut conduire à deux interprétations opposées. Il peut s'agir d'une zone où l'interface de subduction accumule peu de contraintes, auquel cas le risque de séisme interplaque majeur est intrinsèquement réduit. C'est la configuration par exemple de la zone de subduction des Mariannes ou de Ryukyu (*Ando et al.*, 2009). Le risque sismique dans une telle configuration n'est cependant pas absent, en particulier car des

séismes proches de la fosse peuvent générer d'importants tsunamis (exemple du séisme du Pérou du 21/02/1996, $M_w = 7.5$; *Ihmlé et al.*,, 1998). L'autre hypothèse est au contraire que la zone soit couplée mais que le seuil de résistance de l'interface soit suffisamment fort pour avoir empêché l'occurrence d'un séisme majeur pendant plus de 500 ans. Dans ce cas, le risque de catastrophes (de l'ampleur des séismes de Sumatra (2004) ou du Japon (2011)) est réel.

L'instrumentation géophysique permet d'apporter des éléments de réponse à cette indétermination majeure. En effet, dans un modèle simple du cycle sismique (Figure III.3), les vitesses géodésiques intersismiques enregistrées par GPS sont reliées à l'accumulation de contraintes sur l'interface de subduction. Le potentiel sismique peut donc être évalué à partir de la quantité de déformation et de la date des derniers séismes majeurs.

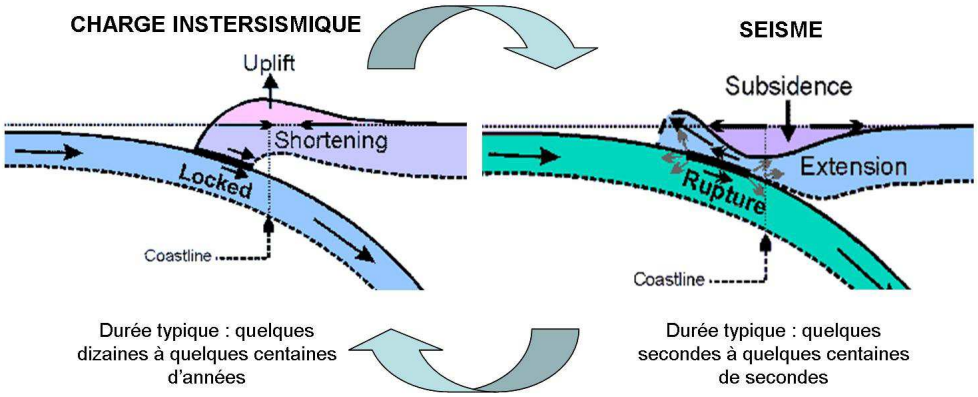

FIG. III.3 – Modèle simple de cycle sismique, reprenant les idées déjà proposées par *Reid* (1910). Le chargement intersismique d'une partie de l'interface de subduction (à gauche) se traduit par une déformation de la surface Terrestre. Cette énergie de déformation est relâchée durant un séisme majeur (à droite). Les mouvements GPS enregistrés durant la phase intersismique permettent donc d'estimer le potentiel sismique d'une zone de subduction.

En couplant ce type de recepteurs GPS avec des stations sismologiques, nous pouvons suivre les mécanismes de déformation sur des échelles de temps et d'amplitude variées (Figure III.4).

Un tel dispositif permet d'observer le cycle sismique, et de mettre en lumière les limites du modèle de rebond élastique présenté dans la figure III.3. En effet, de nombreux éléments sont négligés par ce modèle, comme les mouvements postsismiques ou la complexité intrinsèque à chaque nouveau séisme. Plus fondamentalement, ce modèle simple ne prévoit pas de phénomènes de déformation de durée intermédiaire, entre l'échelle de temps tectonique et celle de la rupture sismique. Or, dans les quinze dernières années, des phénomènes

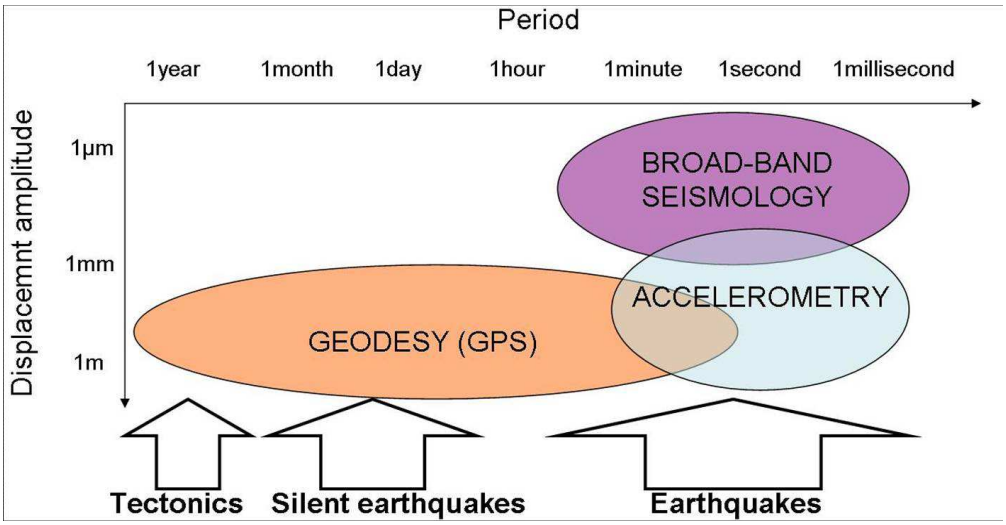

FIG. III.4 – Intérêt d'une station sismo-géodésique comportant un GPS, un capteur accélérométrique et un capteur large-bande. Le GPS permet de détecter les mouvements sur une large gamme de fréquences (du continu jusqu'à environ 1Hz), tant que leur amplitude est suffisante (au moins quelques millimètres). Les mouvements de haute fréquence, même d'amplitude faible, sont enregistrés par le sismomètre large-bande ou l'accéléromètre.

de relâchement lents de la contrainte (sur des durées typiques de mois ou de semaines) ont été observés dans plusieurs zones de subduction. Après avoir d'abord été détectés au Japon (*Hirose et al.*, 1999) et aux Cascades (*Dragert et al.*, 2001), ils sont maintenant documentés dans de nombreuses autres régions (voir *Schwartz et al.*, (2007), et la section III.4). Ces deux objectifs, à la fois de mieux documenter le potentiel sismique de la marge et de détecter les nouveaux signaux participant au cycle sismique, sont au cœur du projet « ADN ». Ce projet - qui a été financé par l'ANR sur la période 2007-2011 - s'est effectué en collaboration étroite avec l'Institut de Géophysique de Quito (IG-EPN) et avec le fort soutien de l'IRD. Ce chapitre ne décrit pas tous les aspects du projet ADN, dont les domaines vont de la tectonique au risque sismique, et dont le cadre géographique inclut la marge Nord-Péruvienne. Je me concentre principalement sur des études dans lesquelles j'ai été directement impliqué, réalisées à partir du réseau sismo-géodésique déployé sur la côte Centre-Nord Equateur.

Les aspects instrumentaux du projet sont détaillés dans la section III.2. La section III.3 documente les mécanismes de la sismicité modérée à forte, en les replaçant dans le contexte de la déformation observée par GPS. La section III.4 est consacrée à l'étude d'un séisme lent, et de sa sismicité associée, que nous avons détectés durant l'été 2010.

III.2 Instrumentation

Les stations sismo-géodésiques utilisées incluent chacune un capteur large-bande (CMG3ESP Compact, Guralp), un capteur accélérométrique (Episensor, Kinemetrics), une antenne et un récepteur GPS (NETRS, Trimble), ce dernier enregistrant à une fréquence d'échantillonnage de 5Hz. L'acquisition sismologique est faite par une station Kephren (Agecodagis) 6 voies. Un petit ordinateur communique avec la station Kephren et la station NETRS, afin de centraliser les données. Une vue de la station sismo-géodésique (hors capteurs) est proposée dans la Figure III.5. Le développement de cette station, en particulier les liens entre l'ordinateur et les stations d'acquisition, a été réalisé à Geoazur. Il a été rendu possible par l'interaction entre chercheurs (en particulier Jean-Mathieu Nocquet) et ingénieurs (Claude Pambrun, Maurin Vidal). Après une phase de test, un prototype de cette station a été installé près de Quito à l'automne 2007 (station QUEM, Figure III.6).

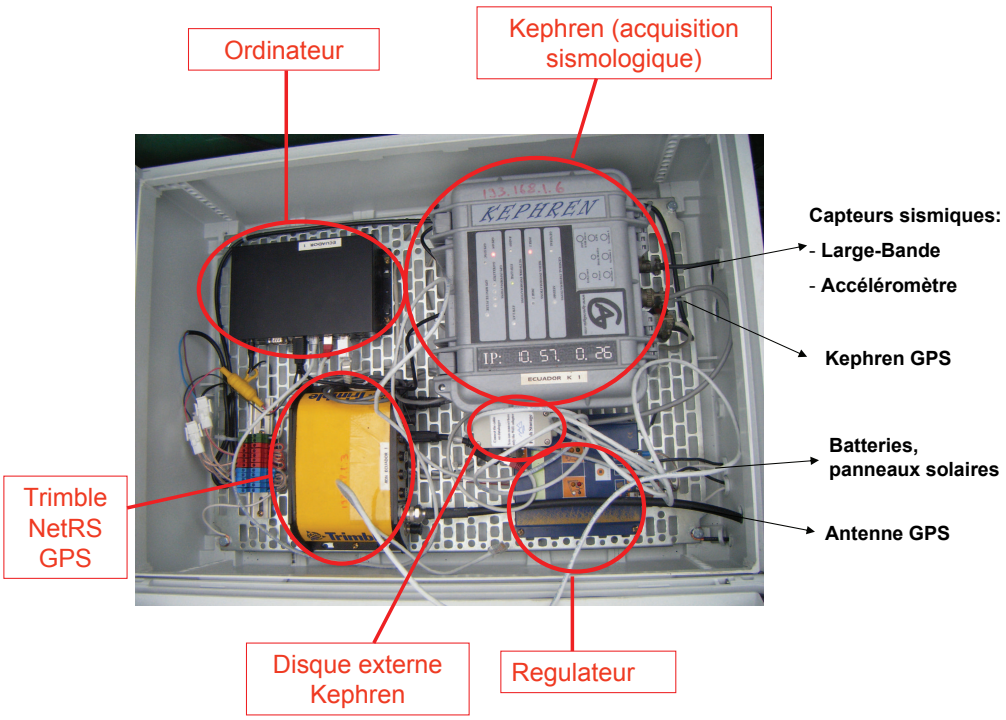

FIG. III.5 – Visualisation de l'intérieur de la caisse d'instrumentation de la station sismo-géodésique. L'ordinateur recueille les données enregistrées par la station sismologique et la station GPS, le tout étant alimenté par des panneaux solaires, au travers de batteries et d'un régulateur.

A partir de la fin de l'année 2008, nous avons déployé 9 de ces stations sur la côte Centre-Nord Equateur, en nous concentrant sur la zone des séismes ma-

jeurs passés (Figure III.1). La sélection des sites requérait une bonne ouverture du ciel pour le GPS, ainsi qu'une réponse sismique la moins bruitée possible. La localisation de chacune des stations est présentée dans la Figure III.6, et des configurations de stations sur le terrain sont illustrées dans la Figure III.7. La Figure III.7 montre également la redondance attendue de l'information sismique, lorsqu'un séisme est suffisamment fort pour être enregistré par l'accéléromètre, sans pour autant saturer le capteur large-bande.

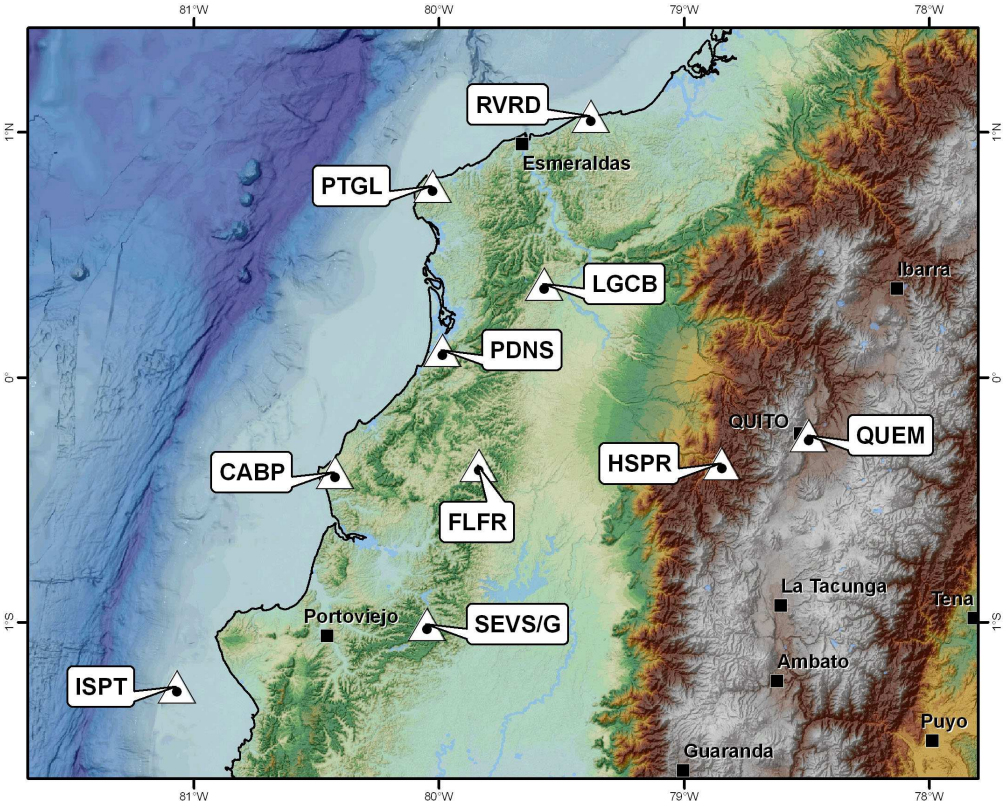

FIG. III.6 – Localisation des 9 stations sismo-géodésiques. Mi-2009, le prototype initial installé près de Quito (QUEM) a été déplacé à Severino (SEVS).

Dans la Figure III.8, nous présentons les caractéristiques de bruit sismique enregistrées aux stations, par rapport aux courbes de référence permettant d'évaluer la qualité des sites. Dans la gamme de fréquence [0.03Hz-0.2Hz], la réponse est très bonne. A fréquence plus basse, le bruit s'éloigne de la courbe optimale ; cela est sans doute dû à l'effet conjoint des capteurs utilisés (CMG3ESP compact) et de l'installation assez légère que nous avons réalisée (capteur enfoui à 1m-1m50, reposant sur une couche de béton). A fréquence plus élevée, les courbes de bruit diffèrent selon la proximité à l'océan.

Mise à part la station de l'Ile de la Plata (ISPT), ces stations ne sont pas encore télémétrées. Cet aspect est en cours de développement à l'IG-EPN. Des

tournées régulières (3 à 4 fois par an) sont donc effectuées pour vérifier l'état de fonctionnement, corriger certaines avaries, et récupérer les données. L'ensemble de ce travail d'installation puis de tournées n'aurait pu se faire sans l'aide des collègues Equatoriens de l'IG-EPN. Il aurait aussi été très difficile sans le soutien de l'IRD, qui a permis à plusieurs d'entre nous de partir en missions longue-durée ou en expatriation.

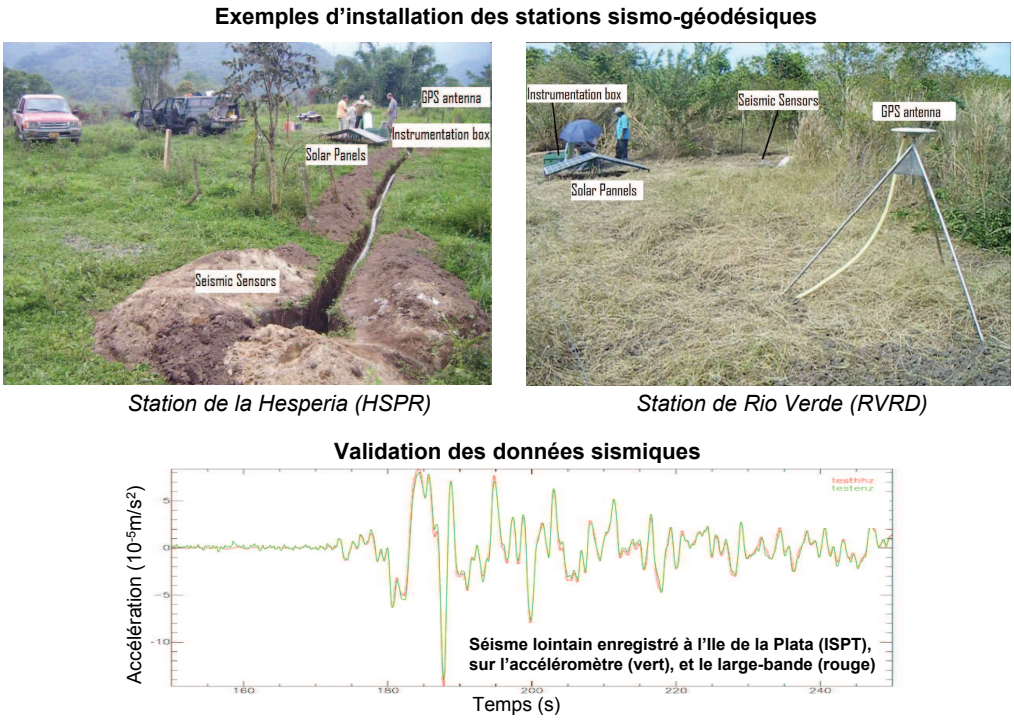

FIG. III.7 – Stations installées et exemple de données recueillies. En haut à gauche, vue de l'installation de la station HSPR. En haut à droite, vue de la station RVRD à la fin de l'installation. En bas, un séisme lointain enregistré à la station ISPT, montrant le bon fonctionnement des capteurs large-bande et accélérométrique.

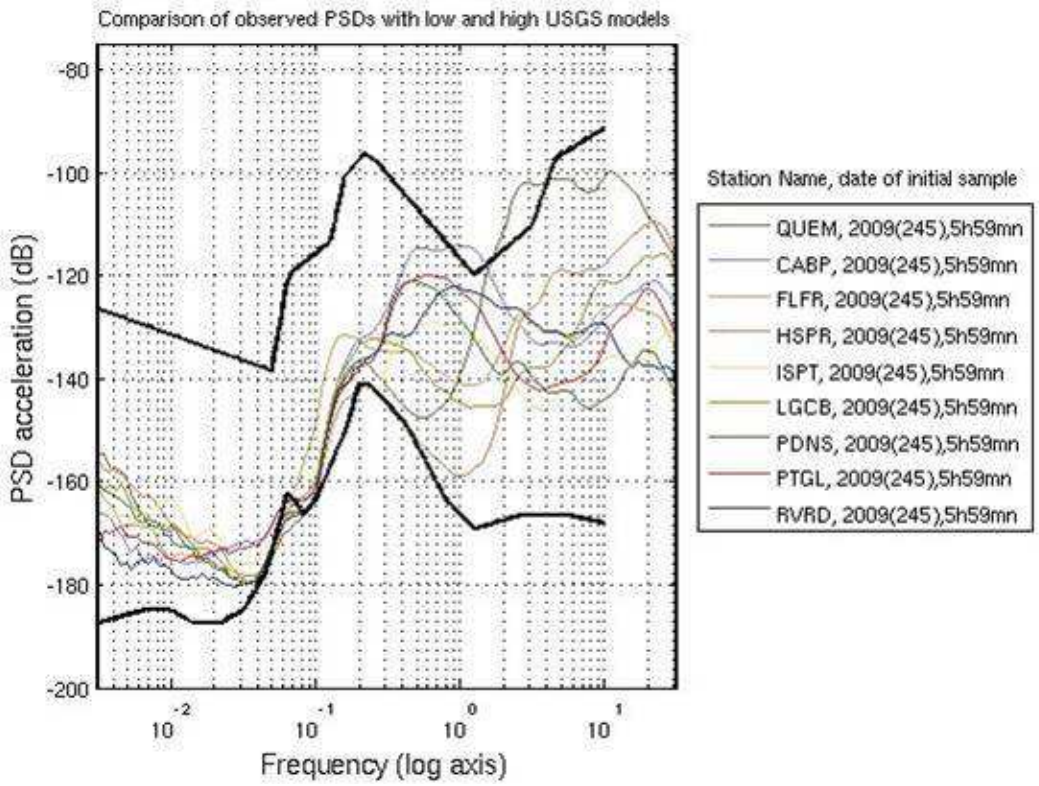

FIG. III.8 – Caractéristiques de bruit sismique des stations ADN, à partir de 2 heures communes de signal. Le bruit sismique est représenté de la manière classique, en densité de puissance spectrale (PSD). Les courbes obtenues à chaque station sont à comparer avec les deux courbes en gras fournies par l'USGS (*Peterson*, 1993): la courbe inférieure indique un site optimal, correspondant au bruit obtenu pour les meilleures stations du réseau mondial. La courbe supérieure correspond à des sites, également choisis par le réseau mondial, mais non optimaux en termes de bruit. Ces sites peuvent correspondre par exemple à des îles océaniques. Il apparaît que les stations ADN sont bien situées entre ces deux courbes, et tangentent la courbe optimale dans la gamme [0.03Hz-0.2Hz]. A plus haute fréquence, les stations de la côte (RVRD, PTGL, PDNS, CABP, ISPT) sont les plus bruitées et s'approchent de la courbe supérieure.

III.3 Caractéristiques de la sismicité modérée à forte

III.3.1 Sismicité passée de la marge Centre-Nord Equateur

Avant d'analyser les séismes récents grâce au réseau ADN, je présente l'activité sismique des dernières dizaines d'années dans la région. Les mécanismes des séismes majeurs (M>5–5.5) sont connus depuis 1976 grâce au catalogue Global CMT (`www.globalcmt.org`). La figure III.9 montre la localisation épicentrale et les mécanismes focaux des séismes de profondeur inférieure à 50km.

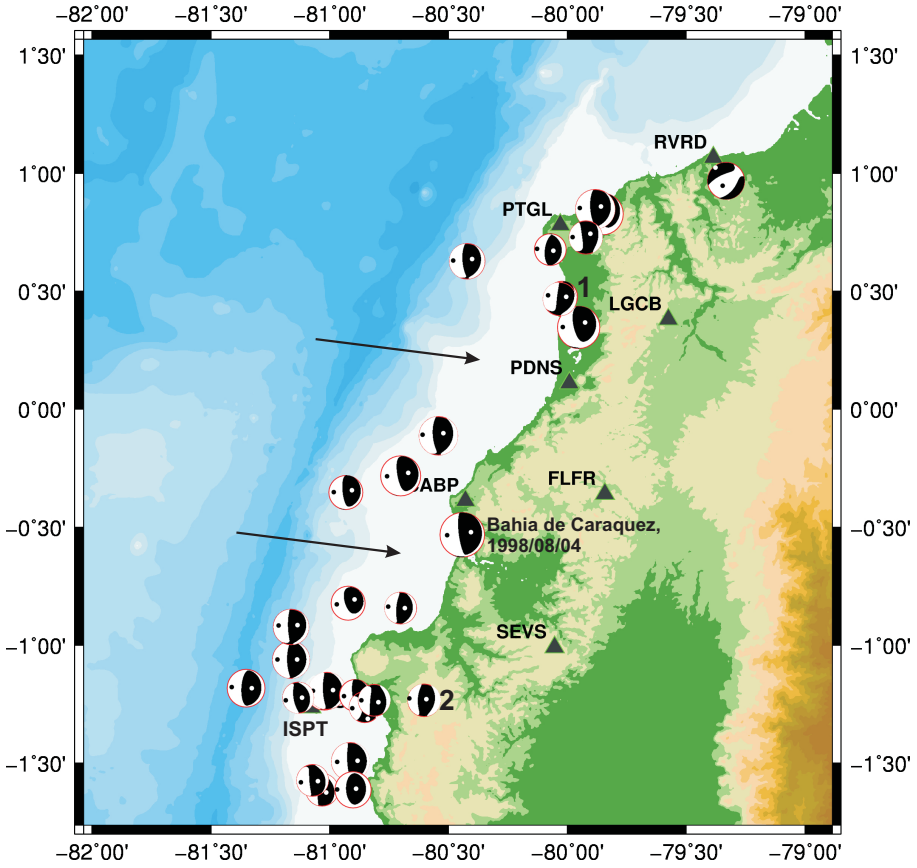

FIG. III.9 – Localisations épicentrales et mécanismes focaux sur la période 1976-2012, d'après le catalogue Global CMT. Les axes P et T des mécanismes sont indiqués, respectivement par les points noirs et blancs. La taille des sphères focales est représentative de la magnitude, qui varie entre 5. et 7.1. Le plus gros de ces séismes, celui de Bahia de Caraquez (4 aout 1998), est indiqué sur la carte. Sont également indiqués - par les chiffres « 1 » et « 2 » - les 2 séismes récents pour lesquels nous pouvons également avoir une détermination grâce au réseau ADN. Enfin, les deux flèches indiquent les zones de gap apparent de sismicité.

Les mécanismes traduisent logiquement l'activité de la zone interplaque de la subduction ; seuls 2 séismes sur les 29 de ce catalogue s'éloignent significativement d'un mouvement compatible avec l'entrée en subduction de la plaque Nazca. 9 de ces séismes ont une magnitude supérieure à 6, et un seul dépasse la magnitude 7, celui de Bahia de Caraquez du 4 août 1998 ($M_w = 7.1$, voir Figure III.9).

Les localisations épicentrales de ces séismes principaux ne sont pas réparties de manière homogène sur l'interface de subduction. Certaines zones, comme celle à l'aplomb de la station de Pedernales (PDNS), n'ont pas connu de séismes interplaques importants dans les 35 dernières années (voir flèches dans la Figure III.9). Nous pouvons explorer davantage cette observation par l'utilisation du catalogue EHB (*Engdahl et al.*, 1998), qui fournit des localisations sur la période 1960-2007, en incluant des magnitudes plus faibles (le seuil est autour de 4 pour les séismes récents). La carte correspondante est présentée dans la Figure III.10. Le gap de sismicité au large de PDNS, ainsi que l'autre gap de plus faible extension entre CABP et ISPT, persistent dans ce catalogue. Nous discuterons davantage de cet aspect après y avoir inclus les mécanismes des séismes récents (section III.3.3).

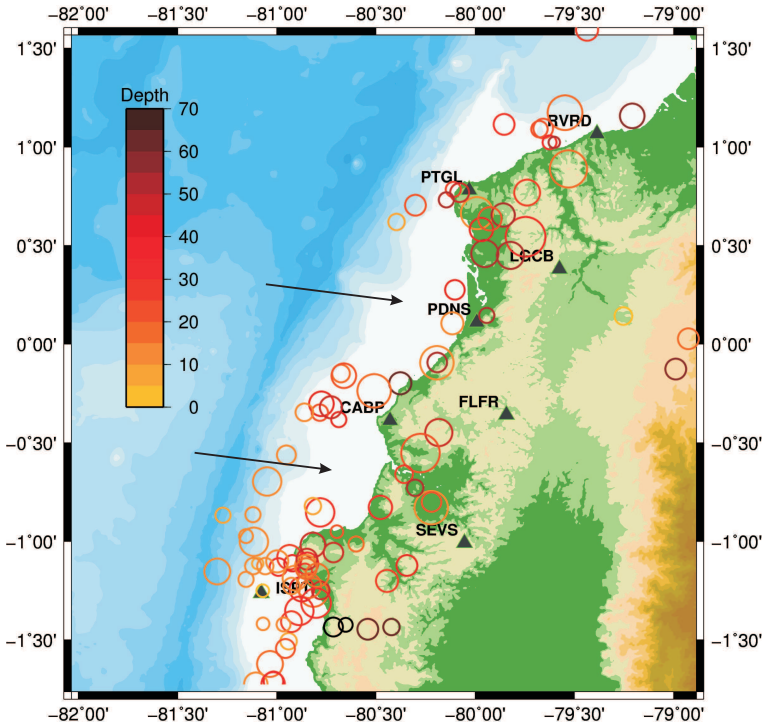

FIG. III.10 – Localisations hypocentrales sur la période 1960-2007, d'après le catalogue EHB. La profondeur est représentée par l'échelle de couleur, et la taille des cercles correspond à la magnitude M_b. Les plus petits séismes ont une magnitude M_b égale à 3.7-3.8. Les deux flèches sont les mêmes que sur la Figure III.9, et indiquent donc la persistance des zones de gap apparent de sismicité.

Un autre aspect intéressant de la sismicité de cette marge est sa répartition spatio-temporelle. Dans la Figure III.11, sont également représentés les épicentres des séismes du catalogue EHB, mais avec une échelle de couleur dépendant de leur année d'occurrence.

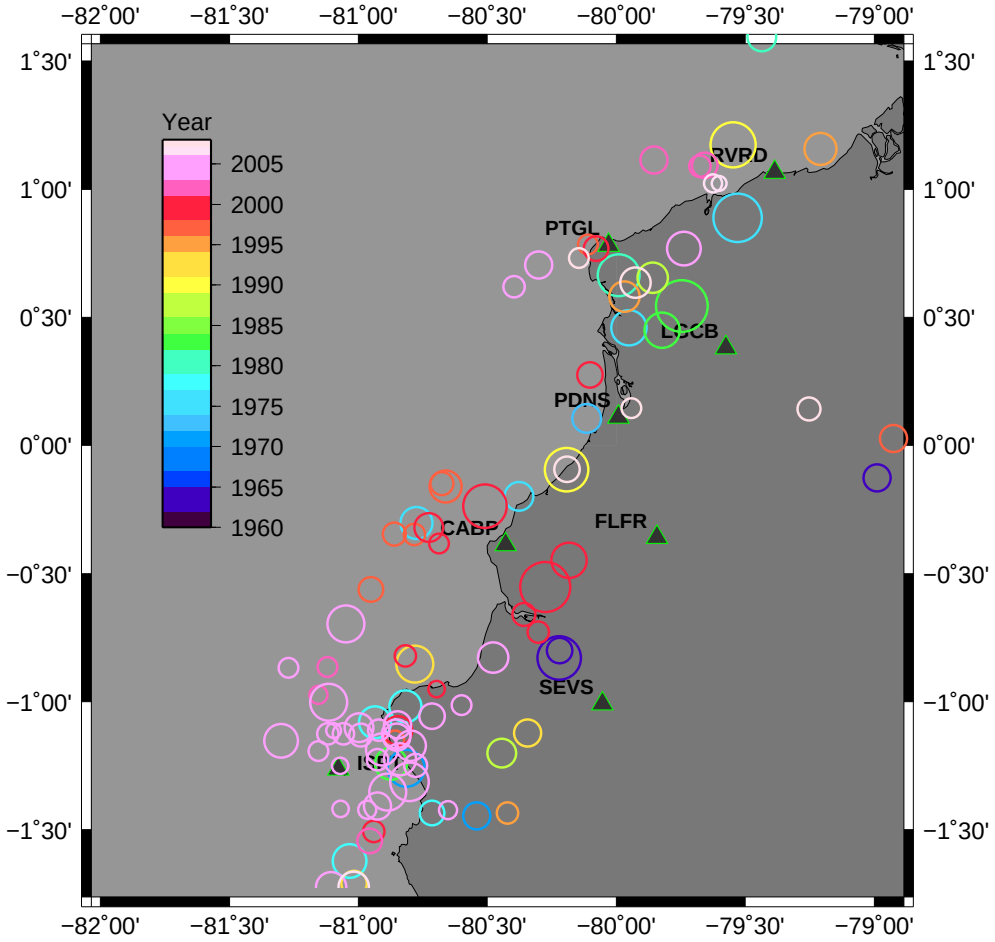

FIG. III.11 – Localisations épicentrales et dates d'occurrence sur la période 1960-2007, d'après le catalogue EHB. La date d'occurrence est représentée par l'échelle de couleur, et la taille des cercles correspond à la magnitude M_b. Les plus petits séismes ont une magnitude M_b égale à 3.7-3.8. Noter la forte activité en 2005 autour de l'Ile de la Plata (ISPT), contrastant avec une activité plus diffuse dans le temps dans la partie Nord.

La partie Nord de la zone d'étude ne présente pas de caractéristiques évidentes, la sismicité semblant temporellement bien répartie. En revanche, la partie Sud, et tout particulièrement la zone de l'Ile de la Plata (station ISPT), présente une grande densité de séismes se produisant en un court laps de temps. Ce caractère de « crise sismique » (appelé également « essaim » ou « swarm ») a été très marqué durant l'année 2005 : un nombre important de séismes s'est

produit, sans être relié à l'occurrence d'un seul séisme majeur. Les séismes principaux de cette séquence sont en effet 4 séismes de magnitude comprise entre 6.0 et 6.2. Cet essaim de séismes a logiquement été détecté par l'étude globale de *Holtkamp and Brudzinski* (2011) et par une étude similaire centrée sur l'Amérique du Sud (*Holtkamp et al.*, 2011). Ces auteurs ont évalué la durée de cette crise sismique à un peu plus d'un mois, en détectant 43 séismes à partir du catalogue PDE de l'USGS. En incluant des données locales, cette crise peut être encore mieux documentée (*Vaca et al.*, 2010) : environ 400 séismes ont pu être localisés durant ce mois d'activité, malgré une distribution de stations peu favorable. Dans la même région, *Vaca* (2007) indique deux essaims passés de taille plus modeste en 1998 et 2002. Les analyses télésimismiques (*Holtkamp and Brudzinski*, 2011) révèlent aussi une autre crise sismique en 1977, qui a été à la fois moins active (11 événements) et moins longue (20 jours). Ces derniers auteurs attribuent ces essaims sismiques à la présence de glissements lents. Nous reviendrons sur cette question dans la section III.4.

III.3.2 Déformations actuelles observées le long de la marge

Le réseau ADN, accompagné de plusieurs autres stations permanentes d'Equateur et de nombreux points de campagne GPS, permet d'estimer les déformations actives. La Figure III.12 présente les vitesses annuelles de ces points GPS, relatives à l'Amazonie considérée stable. L'image générale est bien en accord avec notre connaissance de la géodynamique de l'Equateur, avec deux régions où la déformation se localise : la chaîne Andine - où le mouvement vers le Nord-Est du bloc Nord-Andin (*Pennington*, 1981 ; *Kellog and Bonini*, 1982) est visible - et la subduction. En vue de bien modéliser les variations de couplage interplaque le long de la subduction, il est important de retirer précisément l'effet du bloc Nord-Andin, ce qui est un travail actuel de nos collègues géodésiens. Néanmoins, au premier ordre, nous pouvons raisonner sur l'observation des profils de vitesse Est-Ouest à différentes latitudes. Il apparaît clairement que des points situés à la même distance de la fosse ont une vitesse plus faible quand on se déplace du Nord vers le Sud de l'Equateur. Au niveau de l'Ile de la Plata (ISPT), le couplage est déjà fortement réduit, comme en témoigne la vitesse du point SEVG : ce point est à la même distance de la fosse que certains points du Nord (par exemple LGCB), mais l'effet de la subduction y est fortement atténué.

Ces déformations sont donc en accord avec les séismes majeurs du XXème siècle (voir section III.1), qui n'ont affecté que la partie Nord de l'Equateur. De manière schématique, les déformations géodésiques nous confirment le potentiel sismique du Nord-Equateur, nous informent que le Sud n'accumule pas de contraintes permettant la genèse d'un séisme majeur et que la zone de transition entre ces deux régimes se situe au voisinage de l'Ile de la Plata.

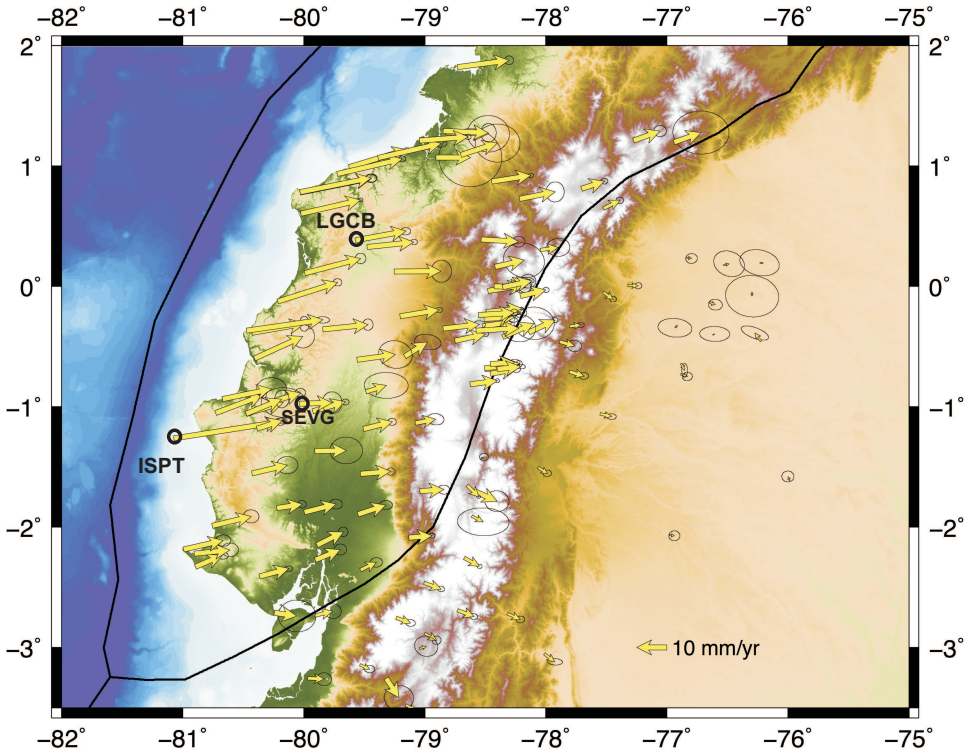

FIG. III.12 – Vitesses géodésiques observées, par rapport à l'Amérique du Sud stable (Amazonie). Cette carte combine les vitesses des stations permanentes GPS (réseau IG-EPN et ADN) avec celles des points de campagne remesurés dans la période 1994-2011 (réseau IGM). Carte de Jean-Mathieu Nocquet.

III.3.3 Mécanismes de la sismicité modérée récente

Les données large-bande et accélérométriques du réseau ADN sont utilisées pour déterminer les mécanismes de la sismicité modérée (magnitude supérieure à 4). Pour ce faire, nous faisons usage de la méthode des nombres d'onde discrets (*Bouchon*, 1981), qui nous permet de modéliser le champ d'onde complet dans un milieu à couches. Nous avons mis en place une méthode d'optimisation, dans laquelle le mécanisme (strike, dip, rake), la magnitude M_w et la profondeur sont les 5 caractéristiques principales recherchées. Nous permettons également une variabilité de la position épicentrale, du temps origine et du modèle de vitesse : ce modèle comporte deux couches surmontant un « manteau » considéré comme un demi-espace infini. Les caractéristiques des deux premières couches (épaisseurs et vitesses d'onde P), ainsi que la vitesse d'onde P dans le manteau, sont recherchées pour chaque séisme analysé. Le problème inverse comporte ainsi 13 paramètres [variation de la structure (5 paramètres), profondeur, strike, dip, rake,M_w, variation de la position épicentrale (2 paramètres), variation du temps origine].

La détermination du meilleur jeu de paramètres se fait par l'optimisation de l'accord entre données et synthétiques ; nous utilisons les formes d'ondes complètes, filtrées dans une bande de fréquences. A distance proche ou régionale, nous choisissons typiquement des fréquences de coupure passe-haut de 0.02-0.04Hz et passe-bas de 0.05-0.07Hz. Ces bandes de fréquence peuvent difficilement être plus élevées quand on utilise des stations situées à 100km ou plus de l'événement sismique. En effet, la simplicité et l'unicité du modèle de vitesse ne permettent pas d'expliquer les formes d'onde à plus haute fréquence. Pour cette raison, les séismes de magnitude inférieure à 3.5-4, qui n'ont pas un bon rapport signal sur bruit dans la gamme considérée, ne peuvent pas être analysés par cette approche.

L'avantage de cette méthode est de rendre l'analyse des mécanismes robuste, même dans un cas où la structure terrestre est compliquée et/ou mal connue. Cette technique s'affranchit également en partie de localisations hypocentrales imprécises, fréquentes lorsque le séisme se produit au large de la côte. La structure de vitesses retrouvée par cette méthode doit être vue comme une structure « équivalente », qui ne représente pas forcément la réalité Terrestre. Néanmoins, dans les différents contextes où nous avons appliqué cette méthode (Côte de l'Equateur, Andes, Haïti (*Mercier de Lepinay et al.*, 2011)), nous retrouvons des épaisseurs de croûte compatibles avec les informations externes.

Je présente ici l'analyse des séismes de la côte dont la magnitude préliminaire (magnitude de durée ou magnitude M_b) est plus grande que 4.3. La période d'analyse s'étend de l'été 2009 à fin 2011. Les mécanismes, profondeurs et magnitudes des 11 séismes étudiés sont présentés dans la Figure III.13. Les accords aux données observées, pour deux séismes de magnitude différente, sont présentés dans les Figures III.14 et III.15. Les deux séismes de magnitude supérieure à 5 de l'échantillon ont également été analysés par Global CMT (Figure III.9). L'accord entre les deux solutions est bon.

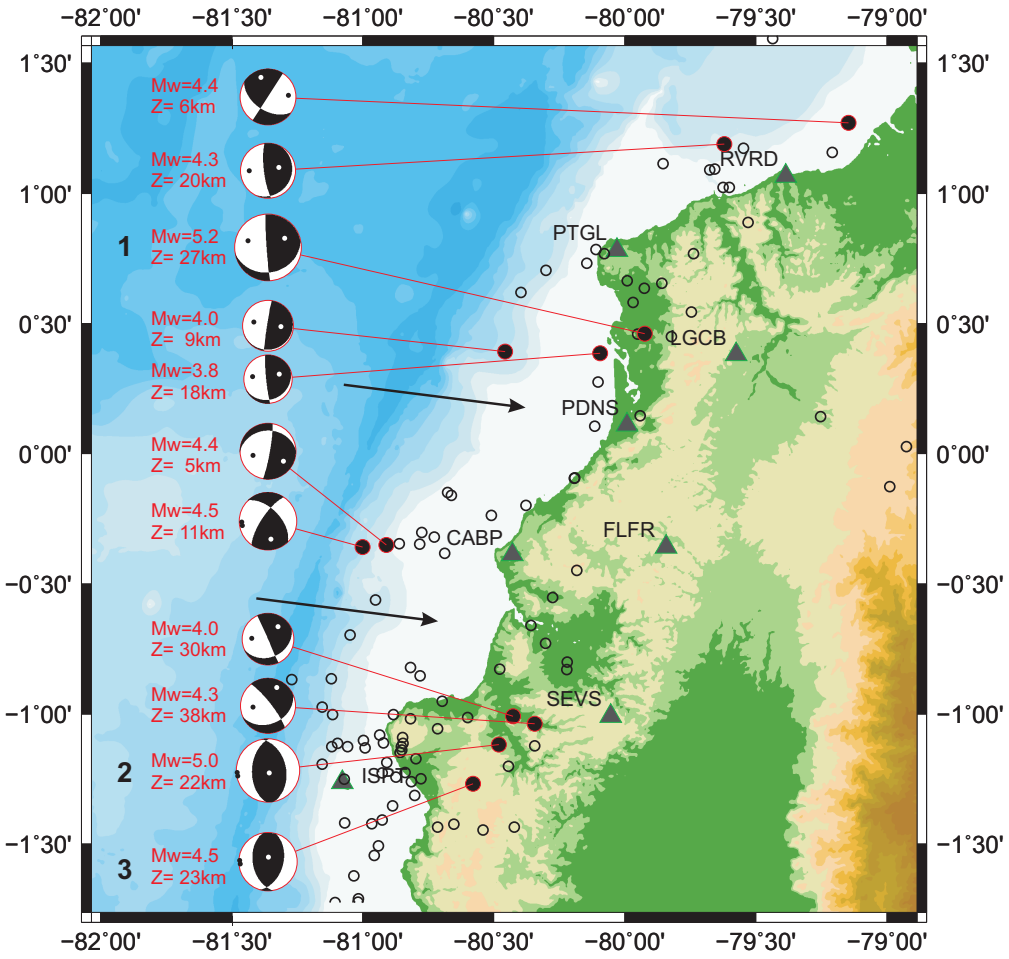

FIG. III.13 – Mécanismes, profondeurs, et magnitudes des séismes de la côte dans la période 2009-2011. Les axes P et T de compression et tension maximales sont ajoutés au mécanisme. La sismicité du catalogue EHB est indiquée par les petits cercles. Les deux flèches sont les mêmes que sur la Figure III.9, indiquant les zones de gap apparent de sismicité dans le catalogue EHB. Les séismes numérotés « 1 » et « 2 » sont les deux séismes les plus forts, dont le mécanisme a été également calculé par Global CMT (voir Figure III.9). Pour les séismes numérotés « 1 » et « 3 », les accords entre données et synthétiques sont respectivement présentés dans les Figures III.14 et III.15.

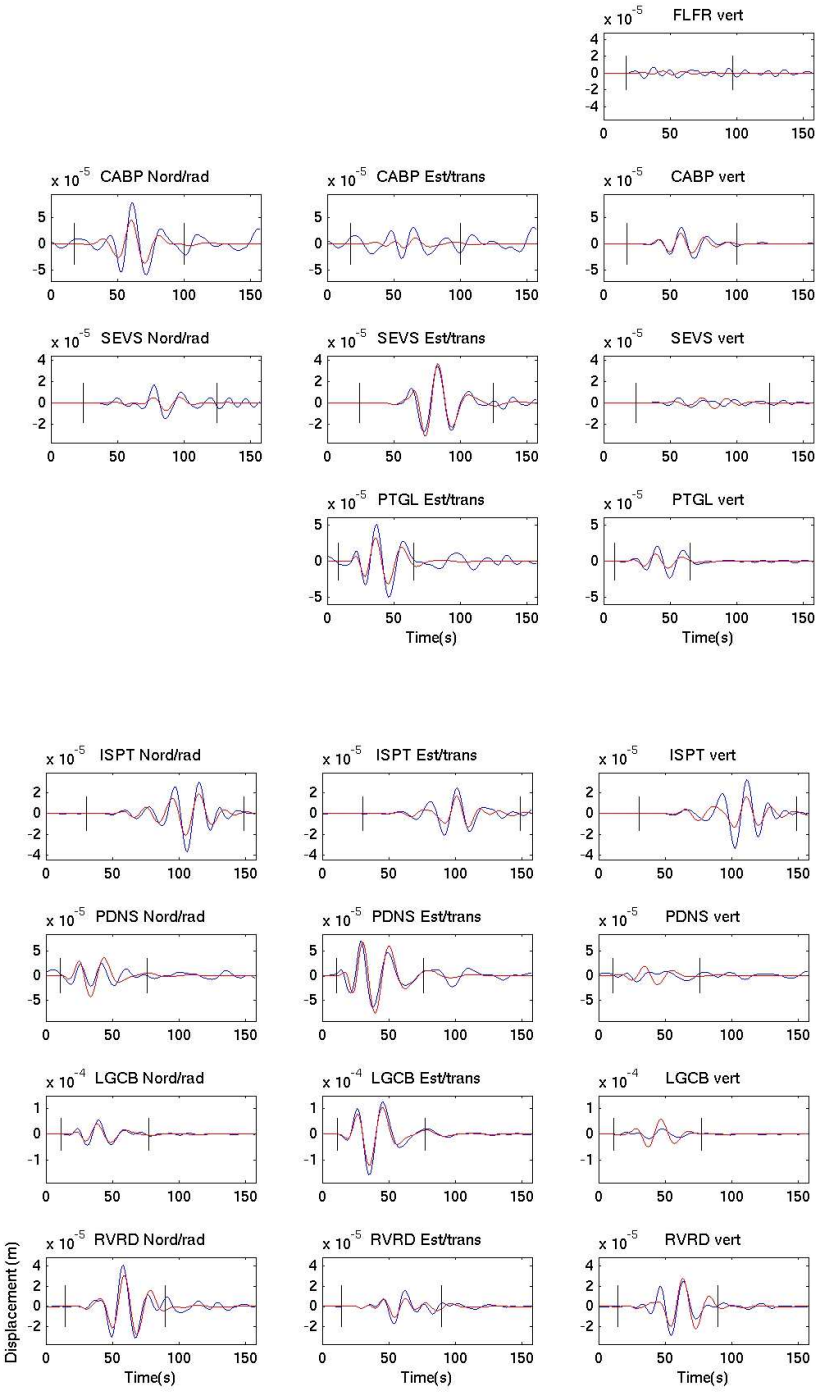

FIG. III.14 – Accord entre données (en bleu) et synthétiques (en rouge) pour le séisme du 25/11/2010 ($M_w = 5.2$), noté « 1 » dans la Figure III.13. Données et synthétiques, sur les 3 composantes (Nord, Est, verticale), sont filtrés dans la bande de fréquence [0.03Hz–0.06Hz]. La fenêtre temporelle utilisée pour chaque station est indiquée par les barres verticales. La référence de l'échelle temporelle est le temps origine du séisme.

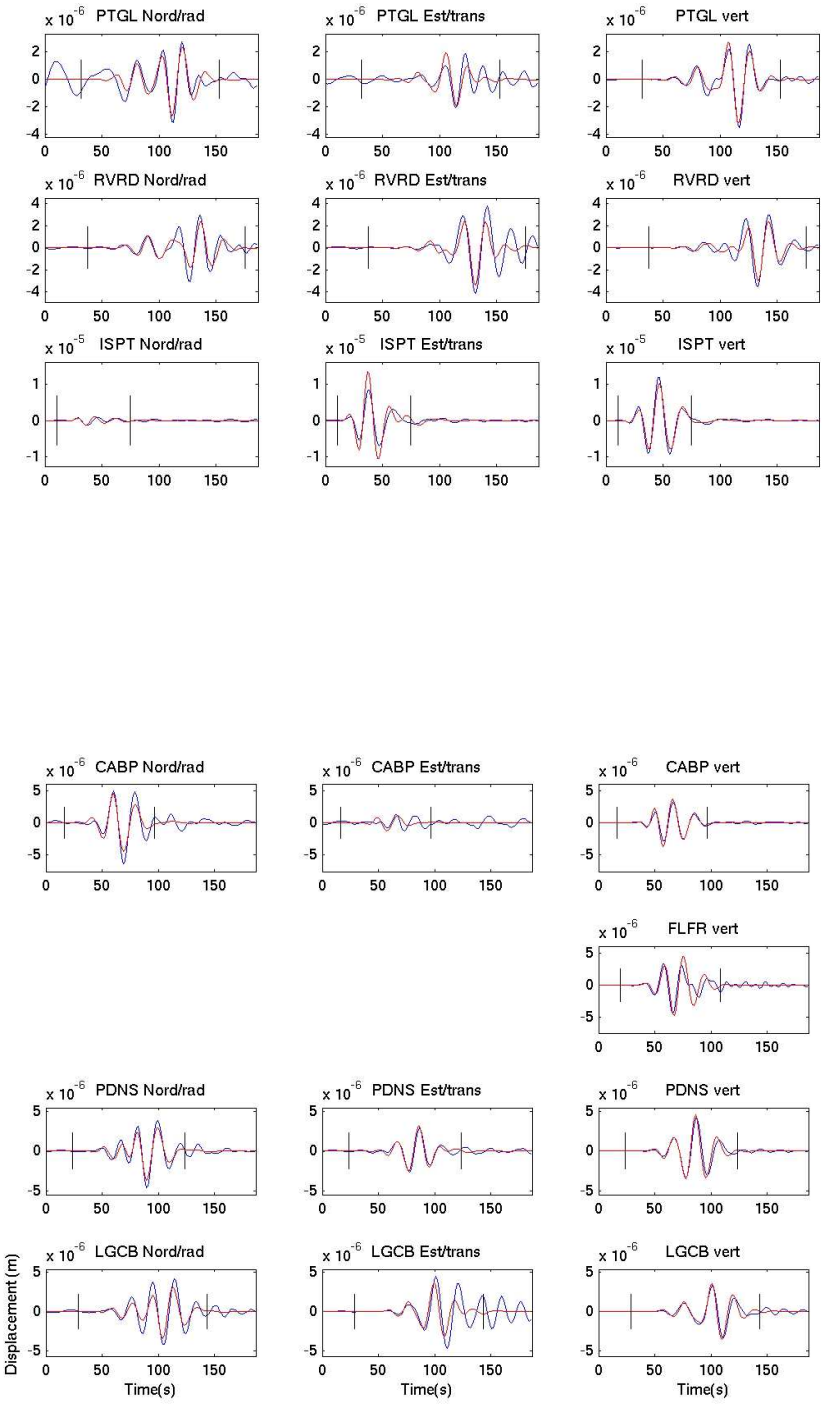

FIG. III.15 – Accord entre données (en bleu) et synthétiques (en rouge) pour le séisme du 16/09/2009 ($M_w = 4.5$), noté « 3 » dans la Figure III.13. Données et synthétiques, sur les 3 composantes (Nord, Est, verticale), sont filtrés dans la bande de fréquence [0.03Hz–0.06Hz]. La fenêtre temporelle utilisée pour chaque station est indiquée par les barres verticales. La référence de l'échelle temporelle est le temps origine du séisme.

Les mécanismes obtenus présentent plus de variabilité que ceux de la sismicité vue par Global CMT depuis 35 ans (Figure III.9). 5 séismes traduisent en effet un mécanisme différent d'un glissement inverse sur l'interface. Néanmoins, tous les séismes ont leur axe maximal compressif « P » avec un azimut Est-Ouest et un pendage faible, ce qui est une indication de leur compatibilité avec les contraintes régionales. La même remarque a été faite par *Béthoux et al.* (2011) à partir de la microsismicité observée aux latitudes $[-1.5^o \ -1^o]$, lors de la campagne SISTEUR de 2000. Ces mécanismes différents peuvent traduire des réajustements de contraintes locaux et mineurs, ce qui expliquerait pourquoi ils sont essentiellement visibles dans la sismicité faible à modérée.

Les localisations présentent de fortes similarités avec la sismicité passée. Dans la Figure III.13, sont également présentés les épicentres du catalogue EHB. Nous pouvons observer qu'à une exception près, les zones de « gap » et de forte activité déjà observés persistent : la zone à l'aplomb de Pedernales (PDNS) n'est pas activée ainsi que celle juste au Sud de Cabo Pasado (CABP). Au contraire, la région à la latitude de l'Ile de la Plata est la plus active.

Cette situation présente des similarités – à une échelle réduite - avec la côte Est de Honshu (Japon), où s'est produit le séisme du 11 mars 2011 ($M_w = 9$). Des séismes modérés à forts se produisent assez régulièrement à l'aplomb de la côte, comme celui de Bahia de Caraquez du 4 août 1998. Au large, la subduction présente des zones très peu actives, alors que les déformations mesurées par GPS montrent que des contraintes s'accumulent. Ces zones, non déchargées par des séismes réguliers, deviennent ainsi des foyers potentiels de séismes majeurs. La région à l'aplomb de Pedernales regroupe ces caractéristiques, et peut être interprétée comme la zone de rupture du séisme de 1942 ($M_w \sim 8$, voir Figure III.1).

L'abondante sismicité dans la région de l'Ile de la Plata, souvent regroupée en essaims sismiques, semble témoigner d'autres mécanismes. Nous discutons dans la section suivante comment l'observation récente d'un séisme lent apporte un éclairage sur cette activité sismique.

III.4 Un séisme lent, générateur d'une abondante sismicité

A l'automne 2010, le suivi régulier des séries temporelles GPS effectué par nos collègues géodésiens a montré un comportement anormal à la station de l'Ile de la Plata (ISPT). Durant une semaine, entre le 26 août et le 2 septembre, le mouvement des composantes Est et verticales s'est brutalement renversé, témoignant de la présence d'un séisme lent. En observant la sismicité à la même station, dans cette même semaine, nous avons remarqué une augmentation brutale de l'activité.

Cette section, qui décrit et documente cette observation, est présentée sous la forme d'un article en préparation. Actuellement, les participants à cette étude sont : Martin Vallée, Jean-Mathieu Nocquet, Jean Battaglia, Monica Segovia, Yvonne Font, Marc Régnier, Patricia Mothes, Paul Jarrin, David Cisneros, Mohamed Chlieh, Sandro Vaca et Hugo Yepes. Je souligne en particulier les deux participations suivantes :

- celle de J.-M. Nocquet pour la détection du séisme lent, l'analyse du couplage sismique dans la zone, et la modélisation du glissement lent
- celle de J. Battaglia pour la description de la sismicité en termes de familles

L'étude présentée ici est volontairement assez descriptive ; certaines pistes de discussion seront abordées dans la section III.5.

Intense interface seismicity triggered by a shallow slow-slip event in the Central-Ecuador subduction zone

Abstract

Interseismic geodetic observations along the Nazca-South America subduction zone in central Ecuador show weak coupling south of the rupture area of the Mw=8.8 1906 megathrust earthquake. In this context, we document a one week long slow-slip event (SSE) which occurred in August 2010, with an equivalent moment magnitude of 6.0-6.3. Inversion of interseismic coupling and co-SSE displacement reveals that the SSE occurred at shallow depth (~10 km) within the downdip limit of a local (50 x 50 km) shallow (3-12 km) locked asperity. The presence of a broad-band seismometer and a continuous geodetic station located at the La Plata island, 10km above the SSE, has enabled a careful analysis of the relations between slow and rapid processes of stress release on the subduction interface. During the slow slip sequence, the seismic data reveal a brutal increase of the local seismicity, with more than 650 earthquakes detected, among which 50 have a moment magnitude between 1.8 and 4.1. The moment released through earthquakes account at most for 0.5% of the total moment release estimated from GPS displacement. Most of the larger earthquakes are located along the subduction interface and have a focal mechanism consistent with the relative plate motion. While the earthquake sizes show a classical distribution (Gutenberg-Richter law with a b-value close to 1), the space-time occurrence presents a specific pattern. First, the larger earthquakes appear to occur randomly during the slow slip sequence, which is a further evidence that the seismicity is driven by the stress fluctuations related to aseismic slip. Moreover, the seismicity is partitioned between individual events and families of repeating earthquakes. This indicates that the SSE stress increments induced by episode of aseismic slip may lead to brutal seismic release or to progressive rupture within locked patches of the subduction interface. This study further documents the links between shallow slow-slip and seismicity which have been recently observed in some other subduction zones, in particular in New Zealand. It also offers an *a posteriori* interpretation of the seismogenesis in the Central-Ecuador subduction zone, where intense seismic swarms have been observed (1977, 2005). These swarms have been likely triggered by large magnitude slow-slip events.

III.4.1 Introduction

Slow slip events (SSE) have been documented in numerous locations of the circumPacific subduction zone (Cascades, Japan, Mexico, Costa Rica... see *Schwartz et al.*, 2007 for a review). These SSEs, which can last from days to months, occur along the subduction interface with a mechanism releasing some of the stress accumulated by plate convergence. They were first observed at depths of 30-50km, close to the downdip limit of strongly coupled subduction interfaces (Southwest Japan, *Hirose et al.*, 1999; Cascades, *Dragert et al.*, 2001), and were interpreted as the expression of the frictional transitional zone of a coupled subduction interface. Above this zone and up to shallow depths, the interface accumulates strong slip deficit, which is mostly released during large earthquakes. Below it, the plates are freely slipping. More recently, The SSEs were also observed at shallower depths, at least in three subduction zones (Boso Peninsula, Japan, *Ozawa et al.*, 2003, *Sagiya*, 2004; Hikurangi, New Zealand, *Douglas et al.*, 2005, *McCaffrey et al.,* 2008, *Wallace and*

Beavan, 2010; Nicoya, Costa Rica, *Outerbridge et al.*, 2010). Nonetheless, in the two latter cases (Hikurangi, northern New Zealand and Costa Rica), the locus of the SSEs remains consistent with the view of a downdip frictional transition zone, because the locking depth is shallow is these two areas. The case of the Boso peninsula shows a more complex pattern, because the location of the 1996 SSE appears to be adjacent to a coupled zone (*Sagiya*, 2004).

Since the discovery of SSEs, this proximity between the slow slip processes and earthquake-prone areas has raised the question of their seismic triggering potential (e.g. *Dragert et al.*, 2001; *Mazzotti and Adams*, 2004). As a matter of fact, these SSEs modify the stress in the surrounding areas and should promote the seismic rupture on some fault segments (and inhibit it on other ones), in a similar way of a main shock generating aftershocks. The close relationships between SSEs and seismic processes have been evidenced, but generally not with classical seismicity: SSEs re often shown to be accompanied by a peculiar seismic activity, referred as non-volcanic tremors (NVT, *Rogers and Dragert*, 2003). These NVTs clearly differ from the usual seismicity because of their long duration and of the absence of clear wave arrivals. Triggering of large interplate earthquakes by slow slip events have not been observed, even if such a process has been proposed for the 2011 Tohoku (Japan) earthquake, based on indirect seismicity properties (*Kato et al.,* 2012). Concerning the lower magnitude seismicity, earthquakes rate has been shown to clearly increase during the SSEs in only two subduction areas, the Boso peninsula (*Ozawa et al.*, 2003; *Sagiya,* 2004), and the Hikurangi subduction zone (*Delahaye et. al.*, 2009). In the case of the Guerrero (Mexico) SSEs, *Liu et al.* (2007) have identified some changes of the seismicity pattern, but they were clearer at the beginning and end of the SSEs than during the process itself. Direct seismic triggering therefore appear to be mainly restricted to the shallow SSEs (*Delahaye et. al.*, 2009), even if a recent study (*Vidale et al.*, 2011) also points out the triggering of a few earthquakes during a 2010 SSE in the Cascades region. In the case of the Hikurangi subduction zone, *Delahaye et al.* (2009) have shown some properties of this associated seismicity, in particular that they are consistent with reverse faulting downdip of the SSE, on or close to the subduction interface.

In this study, we first describe some seismic and geodetic characteristics of the Central Ecuador subduction zone (see Figure III.16), and show that this area shares some characteristics with the Northern Hikurangi (New Zealand) subduction zone. The seismic coupling is globally low and restricted to the shallower part of the interface. In this context, a shallow SSE occurred during one week, in August 2010, with a location near the bottom of the coupled interface and likely including part of it. The geometry of observation is unusual and favourable, as we benefit from a GPS and a seismic station located directly above the SSE, which occurs at depths close to 10km. This station, located on the La Plata Island (Figure III.16), reveals a strong and abrupt change of the microseismicity during the SSE. We describe in this study how this seismicity is organized - in terms of location, time and mechanisms - and how it is intimately related to the slow slip itself. This study confirms and further documents the strong seismic triggering potential of SSEs, even if it is restricted in this particular case to small earthquakes. Moreover, the swarm nature of the seismic crisis, together with the frequent past occurrence of large swarms in this area, indicate that slow slip processes may play an important role in the stress release along this segment of the Nazca/south America subduction zone.

III.4.2 Seismicity and interseismic coupling along the Central Ecuador subduction zone

The central Ecuador margin (Figure III.16) is a peculiar region of the North-Andean subduction zone. While major earthquakes (magnitude 7.7 and more) have been observed North of the latitude ~0.5°S (in 1906, 1942, 1958, 1979, see *Kanamori and McNally*, 1982), they seem to be absent in Southern Ecuador, as well as in Northern Peru (*Dorbath*, 1990). Seismically, the region close to La Plata Island thus appears to be a transitional area, delimiting the termination of the major earthquakes activity. However, this simple observation is reversed if looking at the moderate to strong (up to magnitude 6.5) magnitudes (Figure III.16).

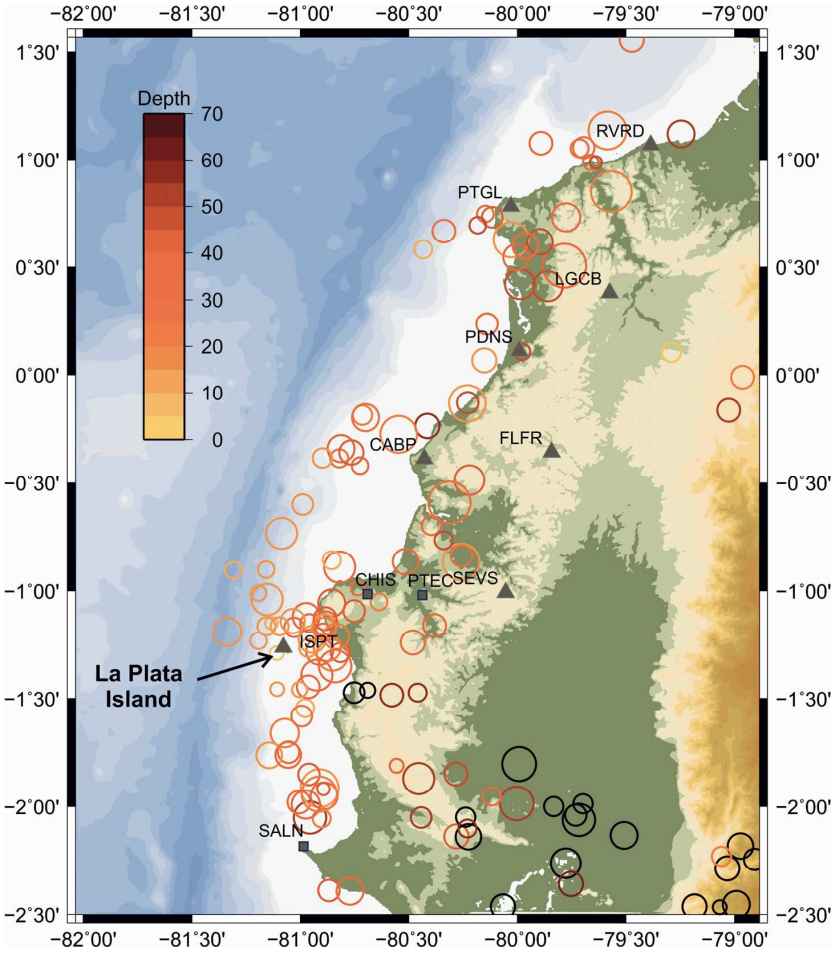

Figure III.16 : Seismicity of the Ecuadorian subduction zone. The circles are the earthquakes of the EHB catalog (REF) in the period 1960-2007. Depth is indicated by the color scale, and the symbol size is relative to Mb magnitudes, ranging from to 3.8 to 6.5. The stations of the ADN project are shown by the triangles and some of the permanent GPS stations of the Institute of Geophysics in Quito (IG-EPN), used later in the SSE analysis, are shown by the squares.

In this case, this region is very active, with frequent and recurrent activity: in January-February 2005, a large one-month-long swarm occurred there, with the four largest earthquakes having a magnitude between 6 and 6.2. In this swarm, 8 other earthquakes have a magnitude between 5 and 6, and in total 43 earthquakes were located by the NEIC with a magnitude threshold around 4. This sequence was a typical swarm, as evidenced by the absence of a unique main shock and by the fact that the largest earthquakes appear to occur randomly in time. This swarm has been documented by *Vaca et al.* (2010) using both local and distant seismic data, as well as by *Holtkamp and Brudzinski* (2011) and *Holtkamp et al.* (2011) at the global scale. These last two studies also point out a smaller swarm in the same region in 1977.

Since the end of 2008, the Ecuadorian coast is continuously monitored by an array of 9 stations including on each site a GPS station (recording at 5Hz), a broad-band seismometer, and an accelerometer ("ADN" project, Figure III.16). This French-Ecuadorian project has been built in collaboration with the Institute of Geophysics of Quito (IG-EPN, Ecuador). The new instrumentation, together with the stations of the IG-EPN seismic and GPS networks, allow us to monitor a broad range of processes acting in a subduction zone, from aseismic movements to large earthquakes. During the last three years, it has also helped to better image the interseismic coupling along the subduction interface. To determine its spatial distribution, we have used a combination of the continuous GPS stations progressively installed since 2008 and campaign data observed since 1994. The full description of the processing strategy will be described in a separate manuscript (*Nocquet et al.*, in preparation), but we discuss here the points relevant for the analysis of the SSE and the interseismic coupling determination.

When expressed in a stable South America reference frame (see Figure III.12), velocities in southern Ecuador show the contribution of crustal tectonics and inter-seismic elastic deformation induced by the inter-seismic locking along part of the subduction interface. In order to separate the two contributions, we take advantage of low coupling observed in southern Ecuador (around latitude 2°S) where GPS sites behave rigidly at the millimetre per year level. In particular, no shortening in the East-West detection is detected in the data and the velocities are consistent with the ones observed in southern Colombia (IGS site BOGT). Such a motion represents the motion of the North Andean Block (*Pennington*, 1981, *Trenkamp et al.*, 2002, *White et al.*, 2003). It is equivalent to a constant translation motion of 9.5 mm/yr in a N75-80° direction for southern Ecuador. Residual velocities with respect to the North Andean Block, presented in Figure III.17, are then modelled in terms of elastic locking along the subduction interface.

We use the back slip approach first proposed by *Savage* (1983) to invert for the coupling along the subduction interface. Back slip approach has been shown to be a good approximation, even in the case of non-planar geometry (*Kanda and Simmons*, 2010). The modelled fault surface follows the geometry proposed by *Font et al.* (submitted) which includes results from marine surveys in the area of La Plata Island (*Graindorge et al.*, 2004) and a relocation of earthquake hypocenters in a 3-D velocity model. The use of a complex geometry rather than a simplified planar fault model is justified by the fact that very shallow dipping subduction interface (~5°) is observed close to the trench (*Graindorge et al.*, 2004), with increasing dip further inland, that changes the distance of the GPS sites relative to the subduction interface. It also enables to account for the 25° change of strike of the trench from South to North in the investigated domain. Our fault surface is discretized in 467 subfaults of 11.1 x 11.2 km, covering about 250 km along strike of the trench and ending at 60 km depth.

Our model uses a rake fixed to the Nazca/North Andean Block relative motion (Figure III.17) and a homogeneous semi-infinite elastic half-space. Our inversion scheme follows the approach recently described in *Radiguet et al.* (2011), following *Tarantola* (2005), where we minimize the cost function S(m) defined as :

$$S(m) = \frac{1}{2}\left[(Gm-d)^t C_d^{-1}(Gm-d) + (m-m_0)^t C_m^{-1}(m-m_0)\right],$$

where m is the unknown parameter model including the amount of back-slip for each subfault, m_0 an a priori model for back-slip distribution taken here as 0, d is the vector of observation including the GPS velocity components, G is the transfer matrix including the contribution of each individual subfault back-slip contribution to d. C_d and C_m are the variance-covariance matrices associated with the data and the model respectively. C_d is taken as a diagonal matrix including the standard deviation coming out from the geodetic analysis. C_m is taken in the form of :

$$C_m(i,j) = \left(\sigma_m \frac{L}{L_0}\right)^2 \exp\left(-\frac{d(i,j)}{L}\right)$$

where $d(i,j)$ is the distance between two subfaults i and j, L the critical distance for correlation for slip, and L_0 a scaling factor fixed at 10 km. We show the results obtained for L=50km, which is found to be a good value between the roughness of the model and the misfit to the observed GPS velocities.

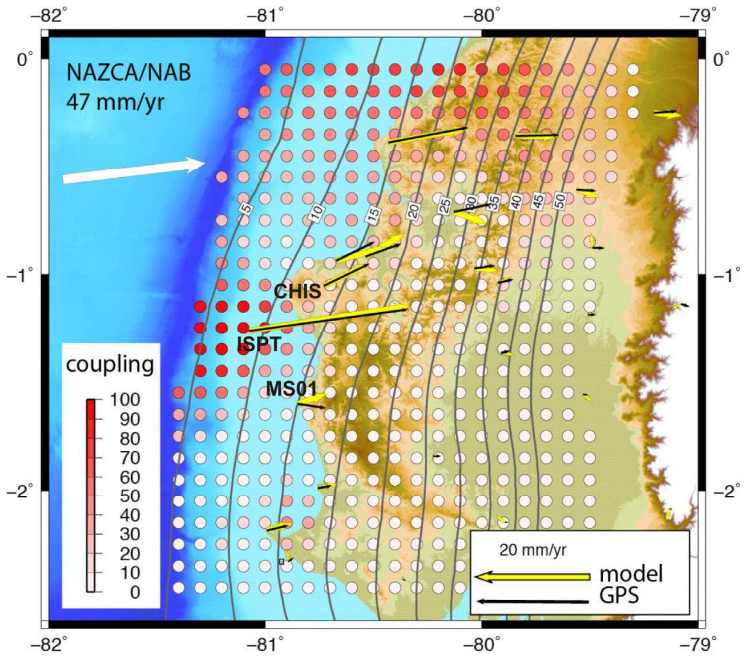

Figure III.17 : Interseismic coupling along the Central Ecuador subduction zone. Observed GPS velocities (in black) are shown with respect to the North Andean block. The three stations discussed in the text (ISPT, CHIS, MS01) are indicated on the map. The modelled velocities (in yellow) correspond to the optimal spatial distribution of coupling along the subduction interface, which is shown by the colour scale from white to red.

In general terms, low coupling is expected south of the area with velocity of the order of 4 mm/yr or less at about 70 km from the trench. On the contrary, velocities of the order of 20 mm/yr are found at latitude 0.25°S, indicating a high level of locking in the northernmost part of the area. Indeed, our inversion shows high coupling down to depths of 40-45 km in the northern part of the studied area, corresponding to the southern part of the rupture area of the 1906 Mw=8.8 and the 1942 Mw=7.8 earthquakes. Low to null coupling is found in the southern part of the domain. Between the two, the inversion reveals the existence of a local (50 x 50 km) highly coupled area. High coupling is required to explain the magnitude of the velocity (28.5±0.5 mm/yr) at station ISPT. The downdip extension (~15 km) is well constrained by the sharply decreasing velocities magnitudes from ISPT to CHIS (8.8±0.5 mm/yr) and MS01 (5.4±1.5 mm/yr), both located at 70 km from the trench. Along strike extension of the high coupling area is constrained by the increasing northwards component of velocity at station CHIS and its surrounding. Station MS01 rules out any significant coupling at depth ~15km at latitude 1.5°S, but cannot exclude any significant coupling close to the trench.

III.4.3 Slow slip observation and modelling

Figure III.18 shows the East component time evolution of the continuous GPS sites expressed in the North Andean Block reference frame. In this reference frame, the trends of increasing East displacement through time directly witness the elastic effect of coupling along the subduction interface. Time series have been corrected for the common mode network motion (*Wdowinsky et al.,* 1997). They typically have weekly repeatability of the order of 1-2 mm enabling to have a precise monitoring of short term transient.

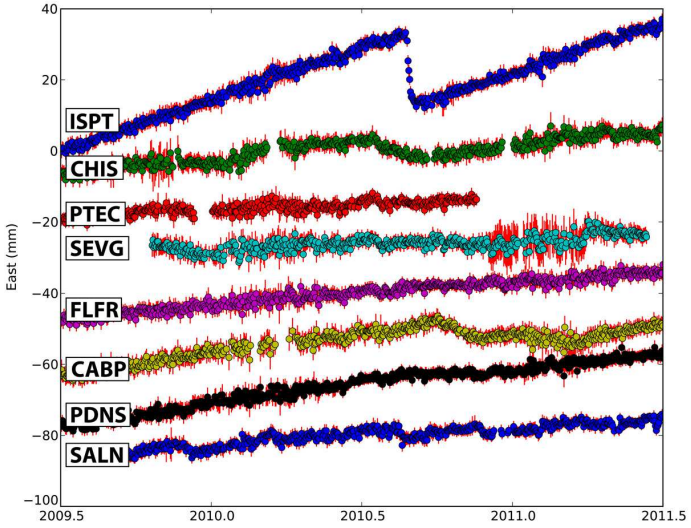

Figure III.18: Continuous GPS Time series (East component) for the 2009.5-2011.5 period. Relative positions are shown every day, with respect to the North Andean Block. Note the brutal reversal of the interseismic deformation at ISPT, during 6 days in the summer 2010.

At station ISPT, the time series clearly show a ~2 cm progressive westwards displacement detected from the 26th of August 2010, decelerating from the 30th of August 2010 for a few days, before recovering a constant rate interseismic displacement. Mainly

because of the lower precision of the GPS vertical component, no clear progressive motion is seen on the vertical component (Figure III.19). Nonetheless, we average the position 5 days before and after the SSE and find a total displacement of -19.6±1.1, -2.0±1.0, 11.25±3.3 mm on the East, North and Up component respectively (uncertainties are 1-σ confidence interval). During the same period of time, no significant displacement is found neither at the closest station to ISPT, CHIS, nor at PTEC (see location of the stations in Figure III.16 and their three-component displacements in Figure III.19). An independent slow slip signal is visible at station CABP, about one month after the main displacement at ISPT. There are some indications of an increased seismic activity, offshore CABP, during this period. However, the detailed analysis is made difficult by the larger distance between stations and trench, in the CABP area. We thus focus our attention on the main SSE signal, detected at the end of August 2010 at station ISPT.

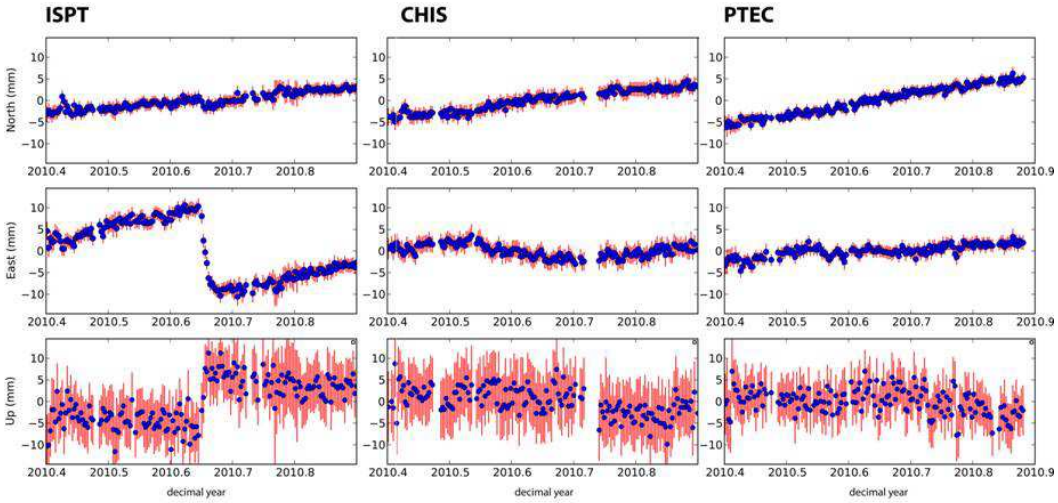

Figure III.19: Time series for the 3 continuous GPS sites used in the parameters search of the SSE characteristics, spanning 3 months around the SSE. The SSE is clear on the East and vertical components of ISPT, but its signal is very small on the North component of ISPT, as well as on all the components of CHIS and PTEC.

With only one site having significant displacement during the SSE, any proper inversion of the slip distribution is excluded. Nonetheless, we can examine the constraints provided by the data at stations ISPT, CHIS, and PTEC in order to evaluate the range of models able to explain them. In order to reduce the number of parameters to be searched, we use an a priori model of the slip distribution in the form:

$$s(\lambda,\phi) = s_{\max} \exp(-((\lambda-\lambda_0)^2 + (\phi-\phi_0)^2)/(R_t D)^2),$$

where s is the slip along the subduction interface at longitude λ and latitude φ. (λ_0,φ_0) is the location of maximum slip, R_t the radius of the Earth, and D the characteristic radius of significant slip. The rake is fixed at 90°. We then examine the constraints provided by the total displacement observed at ISPT and the null displacements at the nearby sites CHIS and PTEC (taken at the precision of the GPS, here found to be 1.1 mm on the horizontal components at CHIS and PTEC and 3.9 mm on the vertical component, at the 1-σ confidence level).

The first constraint is that very small North component of displacement is found at ISPT. That means that, either motion was homogeneous over a large area surrounding the site ISPT or that the slip was at the first order symmetrical either side the ISPT site. The lack of displacement noticed at CHIS favours the latter hypothesis (this hypothesis will be further confirmed by the seismicity location, see corresponding section). φ_0 was therefore kept fixed to the latitude of ISPT during the grid search. We therefore investigate the range of possible models, by varying λ_0 from the trench (-81.4°E) to -80.5°E and D varying from 3 to 40 km. For each (λ_0 , D), s_{max} is a simple scaling factor that can be directly estimated using a least-squares inversion. Using this formulation, we investigate how the observations constrain the range of possible models (Figure III.20).

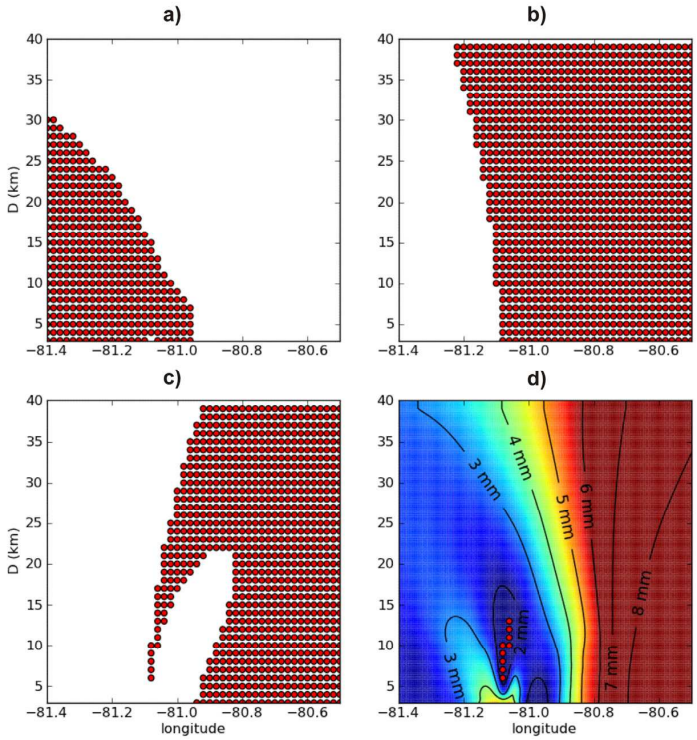

Figure III.20 : Exploration of the possible spatial characteristics of the SSE. All subfigures show the acceptable models by red dots, in the bi-dimensional parameter space (λ,D). a), b) , and c) show how some specific features of the observed displacements forbids some parts of the parameter space (see main text for more details). d) includes all the information to show the possible location and size of the slow slip patch. wrms values (in mm) are shown by the contours and the colour scale.

The absence of any significant displacement detected at CHIS and PTEC excludes any significant amount of slip in the deeper part of the subduction interface. Figure III.20a shows the acceptable region of the parameter space which meets the criterion of 2 cm eastwards displacement at ISPT and a null displacement at CHIS and PTEC (at the 3-σ confidence level). The second constraint is the upwards displacement observed at ISPT. Analytic solutions for a 2-D thrust buried dislocation (e.g. *Freund and Barnett* (1976), *Rani and Singh* (1992), *Tomar and Dhiman* (2003), *Cohen* (1999)) indicate that, for a buried thrust fault, vertical surface displacements are predicted to be upwards on the updip side of the dislocation

and downwards on the downdip side, the transition between the two regimes occurring above the dislocation. Figure III.20b shows the region filling the criterion of upwards displacement at ISPT. Taken together, these two constraints limit the range of possible slip area from about -81.12°E to -80.96°E and a characteristic radius below 18 km. A final constraint is provided by the ratio between the Up and East displacements which is of the order of -1/2. Taking the uncertainties into account, this ratio is considered acceptable in the range [-0.77 -0.38]. Respecting such a ratio range indicates two possible ranges of slip location with respect to ISPT (Figure III.20c). One class of models corresponds to slip located in the very near vicinity of ISPT, in agreement with the previous constraints. The second class is obtained for slip located further east of ISPT, that can be discarded due to the absence of slip observed at station CHIS. Taking all these constraints into account, we find that the range of possible values is rather narrow : the longitude λ_0 of maximum slip is located between -80.08°E and -80.06°E and the characteristic slip radius D is in the range [6km 13km] (see Figure III.20d). For any solution belonging to these intervals, the *wrms* is below 2 mm, therefore in agreement with the GPS displacements uncertainties. The amount of maximum slip is not well resolved - ranging between 97mm and 407 mm -, because it is highly correlated to the patch radius. However, the moment is well resolved and always remains in the range of Mw=6.0-6.1. Figure III.21 shows the slip distribution for the two extreme models. (λ_0=81.06°E, D=13 km and λ_0=81.08°E, D=6 km).

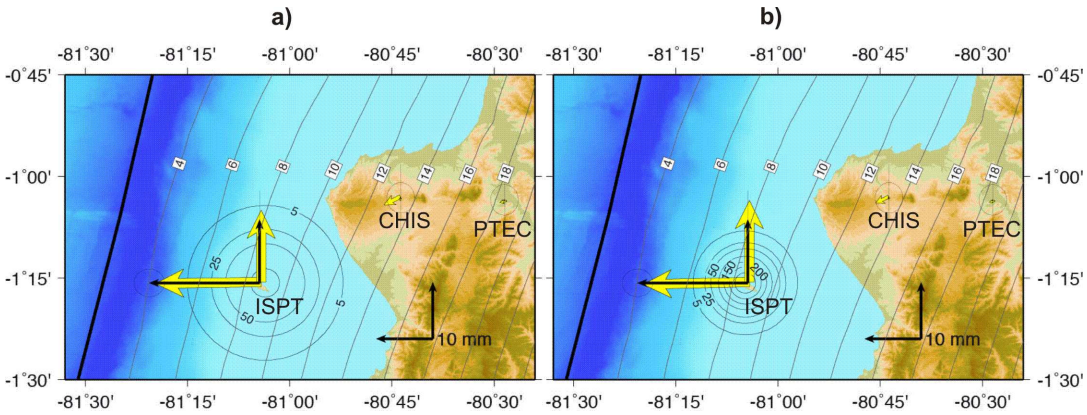

Figure III.21 : Map view of the two extreme possible slip models. (a) Model corresponding to a characteristic radius of 13km. In this case, the maximum slip is about 10cm. (b) Model corresponding to a characteristic radius of 6km. In this case, the maximum slip is about 40cm. In both cases, we show the agreement between observed (black) and modelled (yellow) displacements, on the horizontal and vertical components. The isovalues of slow slip (in mm) and the depth contours of the subduction interface are indicated.

Our parameter search shows that the main area of slip is located close to the downdip limit of the high coupled area during the interseismic phase (Figure III.17). It suggests that some of the slip overlapped with the highly coupled area, but the range of acceptable radius found in the grid search prevents any further quantification. However, our parameter grid search rules out any slip distribution occurring from the trench to the downdip limit of the locked zone, or even any slip distribution centered west of ISPT. In terms of moment release, our search does not account for along strike extension of the slip. We might therefore underestimate the moment release, as an aspect ratio of 3 would increase the magnitude by 0.3. Taking this into account, the equivalent magnitude released during the SSE is found in the range 6-6.3.

III.4.4 Properties of the associated seismicity

III.4.4.1 Evidence of intense triggered seismic activity

Visual screening of data recorded at station ISPT shows a rate of transient events higher than usual during the period of occurrence of the SSE. To quantify this increase of activity, we applied to the continuous data a LTA/STA detection algorithm using a LTA of 60s and a STA of 1s. The counting of events detected using this technique is presented in Figure III.22. Despite a relatively high background number of detections related mainly to the proximity of the station the oceanic coast, the curve clearly points to an increase in the number of seismic transient activity during the SSE. We also note that the period of strongest seismic activity (26/08-29/08) correlates very well with the strongest aseismic displacement recorded by the GPS station. During these four days, several distinct peaks in the number of events are visible, suggesting variations of seismic activity during the SSE itself. Most of the events are not detected at other stations of the ADN array, located about 120km away (CABP and SEVS, see Figure III.16), which indicates that the seismicity is dominated by local and low-magnitude earthquakes.

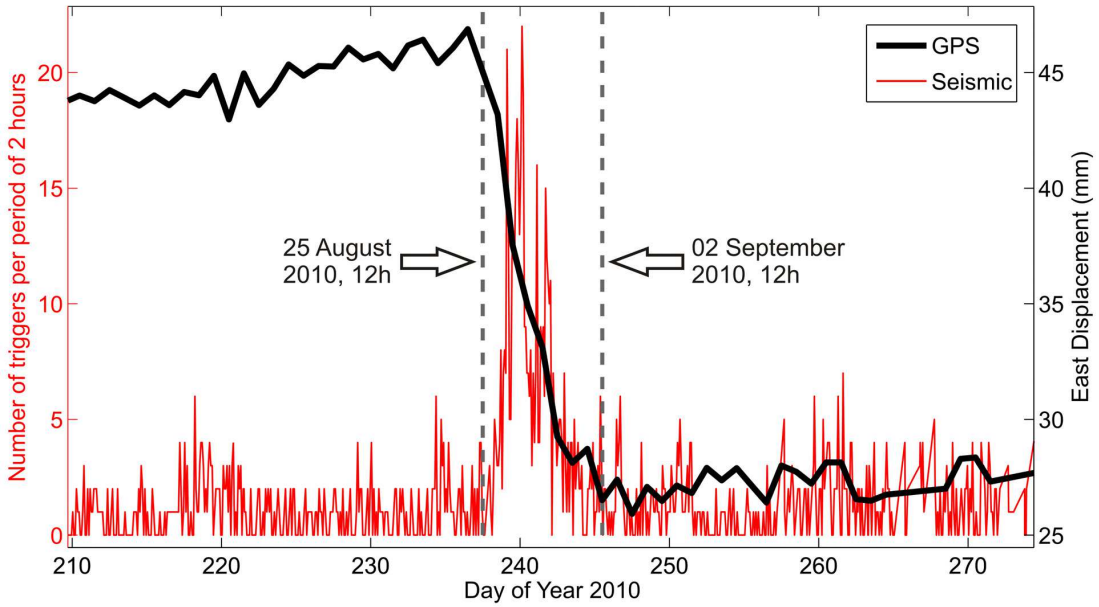

Figure III.22: Conjoint observation of the geodetic displacement and of the seismicity rate at La Plata Island (ISPT station). (Red) Number of seismic events detected per 2 hours for an LTA/STA ratio higher than 6.0. (Black) East displacement recorded by the GPS station.

The local character of the seismicity is confirmed by the visual shape of the waveforms. Most events show clear P and S arrivals, with a time difference of the order of 1.5-3s. The impulsive arrivals of the waves do not differ from those of local earthquakes regularly recorded along the Ecuadorian coast. While this "classical" seismicity increase is very clear during the SSE, the tremor-like activity does not seem to have been triggered by the SSE. Both visual screening of the seven-day long sequence and analysis of the energy variations in successive time windows (*Payero et al.*, 2008) do not indicate peculiar features. Even if some minor tremor activity might be discovered by refined analyses (*Kim et al.*, 2011), it clearly appears that the seismicity is the main seismic process associated to this SSE.

In the following paragraphs, we therefore concentrate on the properties of this triggered seismicity. Two approaches are considered. We first use the three components of the broad-band station to locate and characterize the largest events of the seismic sequence. This reduces the analysed activity to a total of about 50 events. On the other hand, we directly compare each event to the others, based on cross-correlation techniques. Such an approach do not provide the absolute source parameters, but has the double advantage (1) to give a robust estimate of the number of tectonic events (while LTA/STA ration may include technical artefacts) and most importantly (2) to enlighten how part of the seismicity is organized in terms of repeating events.

III.4.4.2 Location and source properties of the largest events

Because most events are only recorded by station ISPT, we cannot use standard phase picking techniques to locate them. However, the events exhibit clear P and S wave arrivals, with a small time difference between P and S waves and a large P wave amplitude on the vertical component (see Figure III.23). This indicates that a large number of earthquakes have an epicentre close to the La Plata Island. We can therefore estimate the earthquakes location using only the ISPT signals, with the following methodology. We first determine the back-azimuth of the earthquake by rotating the horizontal components and finding the orientation which minimizes the waveform energy along one of the rotated components. Using this information, we repeat the previous operation with the radial and vertical components to retrieve the incidence angle of the P wave (see illustration and more information about this procedure in Supplementary Figure III.A.1). Finally, the differential time between P and S waves allows us to locate the earthquake along the P-ray.

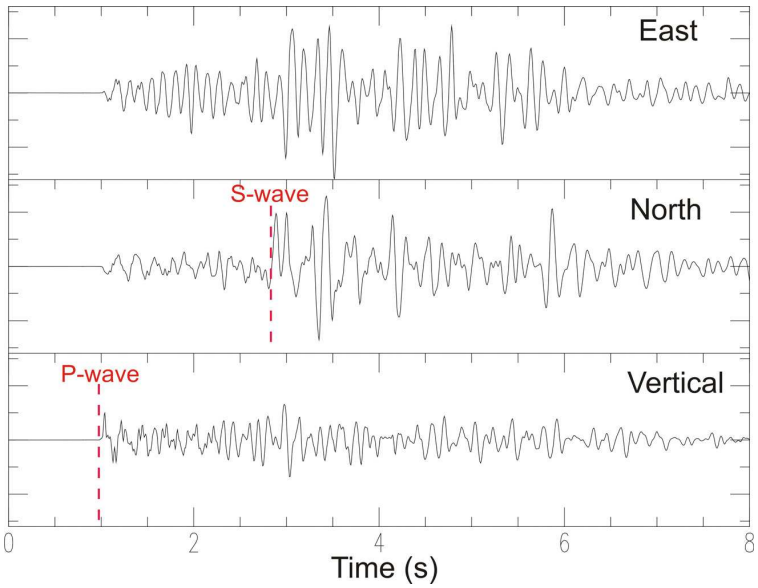

Figure III.23: Typical local earthquake waveforms (in velocity) recorded at ISPT station (origin time of the event : 2010/08/27, 08h57m15s). The three components are shown at the same scale.

The variations of the crustal wave velocities add some complexity to this simple approach. In this study, we neglect the effects of the lateral variations and only consider the dominant effects of wave velocities increasing with depth. In this one-dimensional model, the back-azimuth determination is not affected. The incidence angle determination is made more difficult, because the radial component includes both the direct P wave and P-S waves refracted below the station. If using unfiltered signals over a duration including some P-S waves, the determination of the incidence angle is biased by these different wave types arriving on the vertical and radial components. If using very short time windows close the first P wave arrival, the determination is less stable and only reflects the incidence angle in the very shallow part of the crust. To obtain a more robust value, we band-pass the signal between 1Hz and 4Hz, and use the first 0.4s following the P wave arrival. Such a filtering reduces the potential number of analysable earthquakes, because of the low signal-to-noise ratio for small events waveforms low-passed at 4Hz. Based on amplitude criteria, we finally select 49 earthquakes for which the determination of back-azimuth and incidence angles can be reliably made.

East of ISPT			**West of ISPT**		
Depth (km)	P velocity (km/s)	S velocity (km/s)	Depth (km)	P velocity (km/s)	S velocity (km/s)
0-2	4.3	2.48	0-5	4.3	2.48
2-	6	3.46	5-	6	3.46

Table III.1 : One-dimensional models used to locate the triggered seismicity.

The location of the hypocenter along the P-ray is more directly dependent on the wave velocity structure. To estimate its realistic variation close the La Plata Island, we use the study of *Graindorge et al.* (2004), who have derived an East-West crustal model by inversion of wide-angle seismic data. This profile is located only 15km South of La Plata Island, and is therefore well adapted to the present study. The depth of interplate seismicity, observed during a seismic experiment (SISTEUR, *Béthoux et al.*, 2011), was shown to be consistent with the *Graindorge et al.* (2004) model. It reveals that, below the La Plata Island, solid crustal rocks ("Pinon" formation, with P wave velocities of the order of 6-6.5km/s) are already present at 2-5km depth. This is a favourable configuration for the location technique, as the ray geometry of the P wave should remain simple between the subduction interface and superficial depths. Based on the *Graindorge et al.* (2004) model, we derive two average layered models (presented in Table III.1) to take into account that the top of the Pinon formation is deeper West of ISPT. Depending on the back-azimuth, we select the corresponding model to locate the hypocenter along the P-ray using the differential S-P time.

In Figure III.24, we present the determined hypocentral locations, both in map and projected on an West-East vertical plane. The depth locations for earthquakes located below ISPT (8-10km) are in good agreement with the depth of the subduction interface determined by *Graindorge et al.* (2004). These depths are little affected if using different realistic velocity values for the first layer, because the ray is almost vertical. Depths for earthquakes East of ISPT are more sensitive to the first layer parameters, as faster velocities inside this first layer lead to steeper rays which result in deeper hypocenters. However, all models result in an increasing depth for earthquakes located more and more inland, in agreement with events occurring on or close to the subduction interface. Using the model presented in Table III.1, the best average dip East of ISPT is found equal to 10°, the same value as in the *Graindorge et al.* (2004) model. In Figure III.24b), we add to the depth location the polarities read on the vertical component of the ISPT station. As expected for thrust earthquakes occurring on an

almost flat interface, most polarities are positive East of ISPT and negative West of ISPT. These elements are consistent with a typical activation of the subduction interface, releasing part of the compressive stress accumulated during the interseismic period.

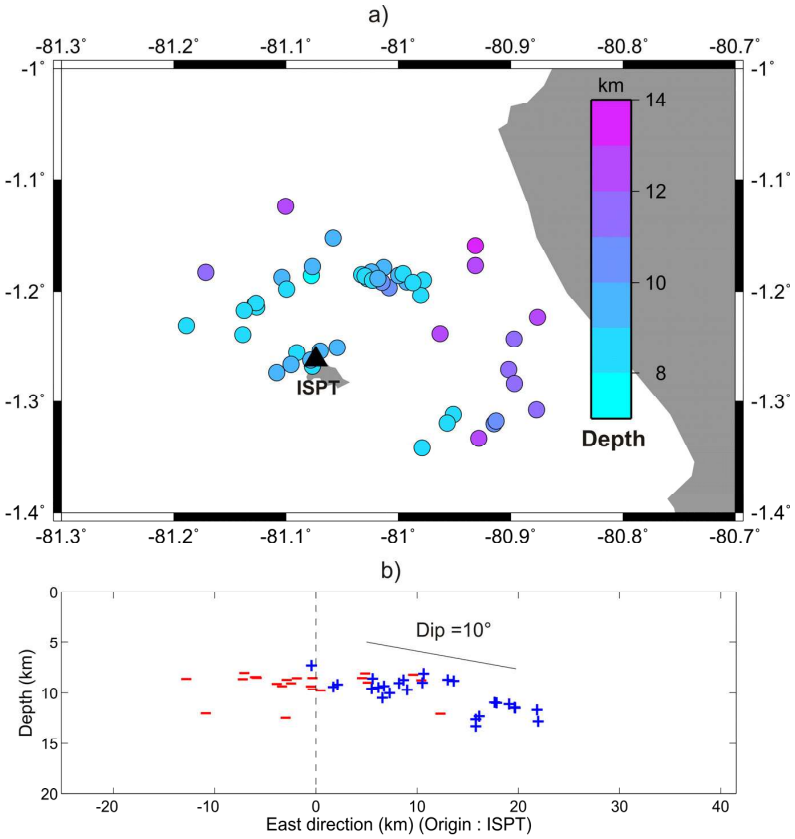

Figure III.24 : Hypocentral location of the largest events : a) Map location with color scaled to depth. b) Projection on the West-East vertical plane. The optimal linear fit of the events East of ISPT defines a 10° dip, presented on the figure. Polarities read on the vertical component of the ISPT broadband station are added on this cross-section.

The magnitude distribution can be estimated by modelling the waveforms of the earthquakes. We invert the waveforms - filtered in the [1Hz 2.5Hz] range – to retrieve the mechanism and moment magnitude, using a window starting at the P wave arrival and ending 1s after the S wave. To do so, we have developed an inversion scheme based on the wavefield modelling by the discrete wavenumber method (*Bouchon*, 1981). The mechanism determination may be ambiguous, but the magnitude is expected to be meaningful. Figure III.25a shows the location map of the triggered seismicity, with circle sizes scaled to the moment magnitude. When analysing the classical magnitude scaling laws (Figure III.25b and III.25c), we note that the Gutenberg-Richter law is well respected with a classical b-value close to 1. On the other hand, Figure III.25c) shows that the triggered seismicity does not follow a mainshock-aftershock behaviour (Omori law): large and small magnitude events appear to occur randomly, with the largest shocks (Mw=3.8 and 4.1) occurring on August 29th, several days after the beginning of the sequence. This observation is a further evidence that the seismicity is driven by an external cause - the SSE -, and not by internal stress interaction.

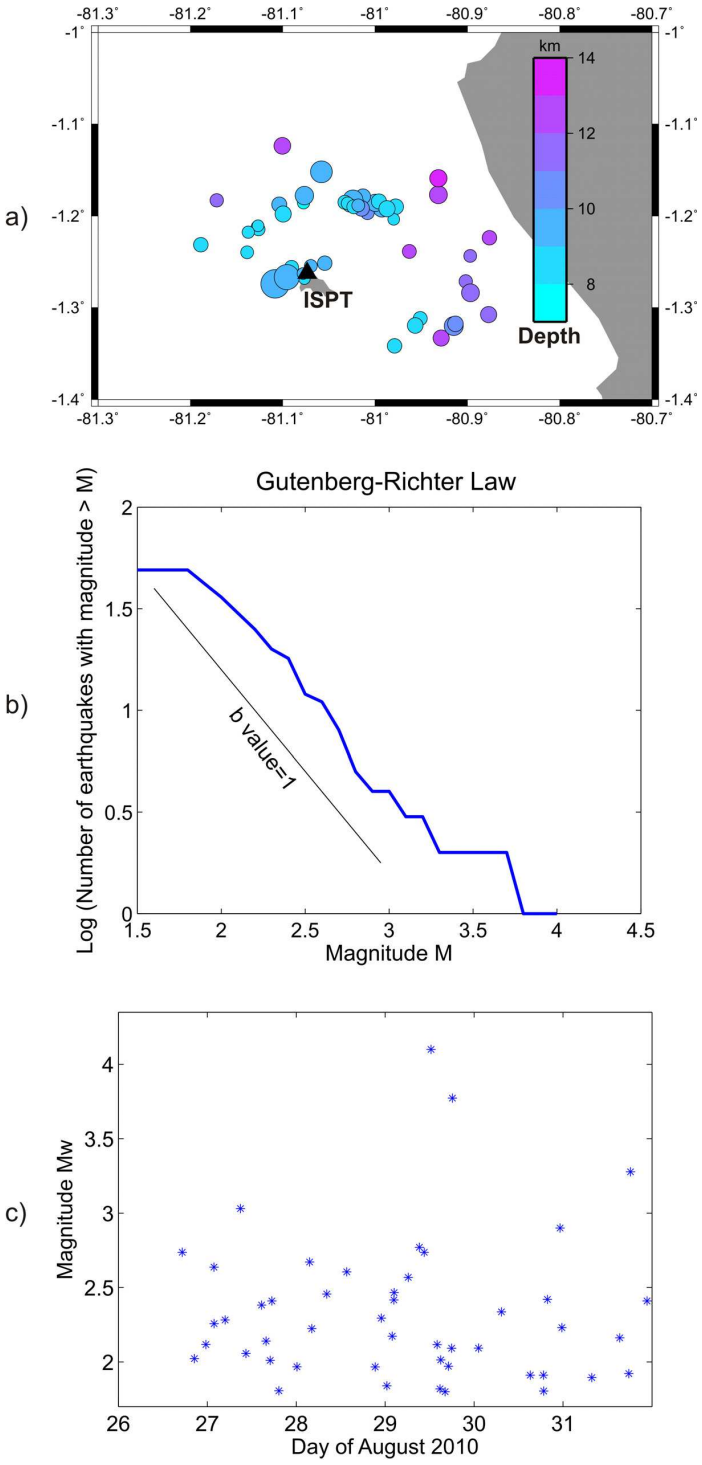

Figure III.25 : Magnitude distribution of the triggered seismicity. a) Map location, with color scaled to depth and size to moment magnitude (Mw). The smallest circles are events of Mw=1.8 and the largest one is a Mw=4.1 earthquake. b) Gutenberg-Richter law with the classical b-value slope (equal to 1) presented on the left part of the figure. c) Distribution of magnitude as a function of occurrence time.

As the focal mechanism may be unreliably retrieved by the analysis of only one seismic station, we adopt a different strategy to further check that the seismicity is consistent with a thrusting mechanism along the interface: we impose such a thrust mechanism in the inversion process, and evaluate if the waveforms can be adequately modelled. We present in Figure III.26 an example of waveforms modelling (same earthquake as in Figure III.23), illustrating that P and S waves are satisfactorily modelled, on the three components, by a typical subduction mechanism. For the earthquakes with Mw>2.5, we found that 9 earthquakes over 12 have both their polarities and their waveforms in agreement with inverse slip on the subduction interface.

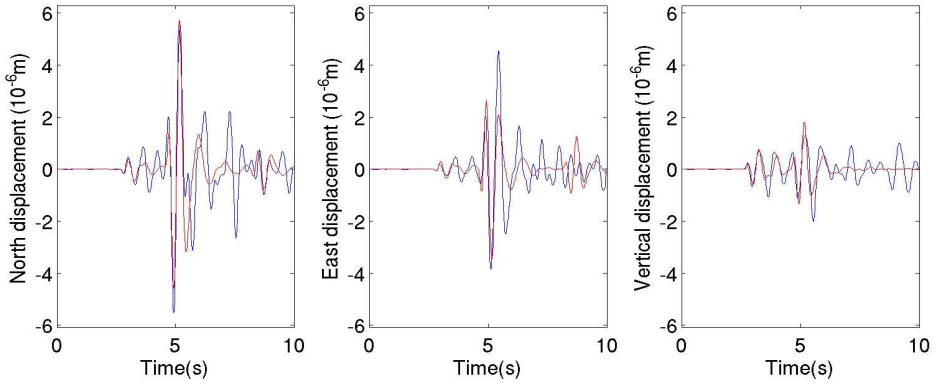

Figure III.26 : Comparison between displacements recorded at ISPT station (blue) and synthetics (red), for the 2010/08/27, 08h57m15s, event (see raw data in Figure III.23). Both signals are band-pass filtered between 1Hz and 2.5 Hz. This earthquake has been located at (Latitude, longitude, depth) = (-1.19°, -81.02°, 9.5km) by the location procedure. The source parameters corresponding to synthetics are (strike,dip,rake)= (13°,9°,80°) and Mw=3. The good agreement between data and synthetics shows that this earthquake is consistent with a thrust mechanism along the subduction interface.

As shown in Figure III.25, the largest events of the sequence are two earthquakes of moment magnitude equal to 3.8 and 4.1. We estimate the cumulated moment released by the smaller earthquakes by integrating the Gutenberg Richter law (see *Andrews and Schwerer,* 2000), and obtain a equivalent moment magnitude of 3.7. As a whole, the seismicity released a seismic moment equivalent to a Mw=4.2 earthquake, much smaller than the moment magnitude of the SSE (Mw larger than 6). Together with the location, timing and mechanism analysis, this observation is fully consistent with a slip on the subduction interface mostly accommodated by the SSE, which has triggered seismic slip on small and local locked patches of the interface. To better characterize the behaviour of these locked patches, we now specifically analyse how the whole triggered seismicity (and not only the largest earthquakes) is organized in terms of repeating events.

III.4.4.3 Organization of the seismicity

We now select all transients with a LTA/STA higher than 4.0 between 28/7/2010 and 6/10/2010 and in addition those with a LTA/STA between 3.0 and 4.0 between 25/8/2010 and 2/9/2010. The choice of such low detection threshold targets the analysis of small amplitude events but will also include numerous noise transients that will be disregarded later in the processing. For the 8971 triggers, we extracted for the vertical component of ISPT windows

with a 2048-sample (16.4 s) length starting 500 samples (4 s) before the triggering times. All waveforms have been compared to each other using cross-correlation after filtering between 3 and 17 Hz. We consider that an event belongs to a family if it has a correlation higher than 0.80 with at least one of the other events. The classification indicates the presence of 34 families of similar tectonic earthquakes (Figure III.27) including more than 5 events and grouping a total of 270 earthquakes. Thirty of these families only include events which occurred during the SSE. Additionally, 406 earthquakes are grouped in smaller families of less than 5 events. This procedure allows to determine the main clusters of activity during the SSE and during the few months around. The similarity of waveforms guaranties that events belonging to a same family have both similar hypocentral locations and source processes.

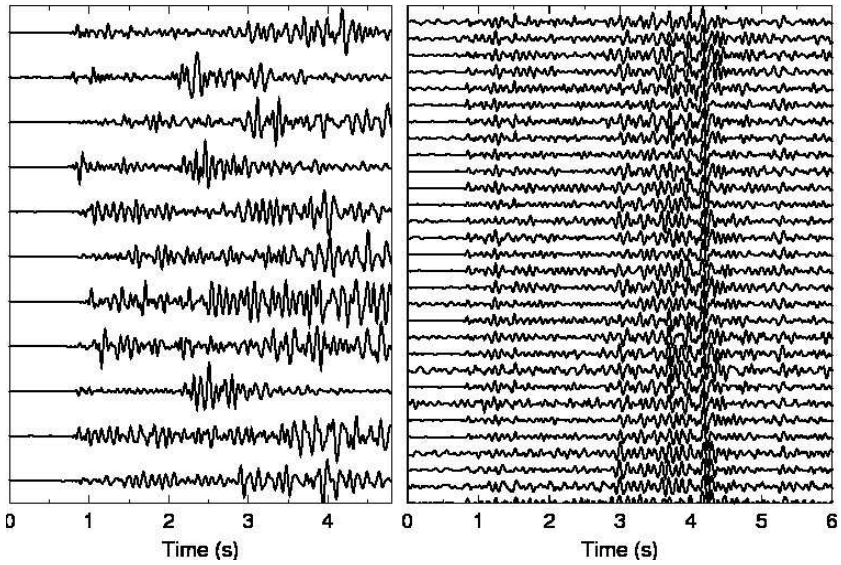

Figure III.27: Left plot shows examples of reference stacks used to scan the data. Right plot shows examples of similar waveforms detected for the largest family active during the SSE.

To recover precisely the time history of the 34 largest families over a duration longer than that of the LTA/STA detection, as well as to identify events possibly missed in the detection or in the classification, we scanned the data using a matched-filter technique. We generated for each family a synthetic waveform of 600 samples (4.8 s) obtained by stacking all similar events (Figure III.27). These waveforms, calculated for the vertical component of ISPT, include for most of them both P and S phases indicating hypocentral distances between 10 and 20 km. The stacks have been used to scan the data by sliding the reference waveforms along the continuous data in search of similar signal windows. The scanning has been performed after band-pass filtering both the reference traces and the continuous data between 3 and 17 Hz. We analyzed the entire period from 2009/07/08 to 2010/10/06. To detect a maximum number of events similar to the reference stacks, we consider as similar each time window with a cross-correlation higher than 0.7. The procedure allows to significantly increase the number of events involved in each family as for the chosen correlation threshold 573 events are involved in the 34 main clusters. For 30 of the families, temporal distributions are similar to those shown in Figure III.28(top), with most of the events occurring only during the SSE. On the contrary, the 4 remaining clusters are active indifferently of the occurrence of the SSE. This result shows that specific seismogenic structures are activated only during the SSE.

Comparing with the 49 earthquakes located in section III.4.4.2, we directly find that 11 of these larger earthquakes belong to one of the 30 main families. Two pairs of located earthquakes belong to the same family, which informs us on the internal quality of the location procedure: we find that the locations differ by about 1km for earthquakes belonging to the same family. Using again the matched-filter technique, we further check if some of these larger earthquakes are really orphan or if the family-behaviour is the rule for this triggered seismicity (Figure III.29). We find that 23 earthquakes cannot be associated with more than one event. The 6 largest earthquakes (with Mw larger or equal than 2.8) belong to this group where events occur as singlets or doublets. The other earthquakes present a repeating character, which can be moderate (10 earthquakes can be integrated in families of less than 10 events), or very active : 4 earthquakes belong to families of more than 20 events (pink to red colours in Figure III.29), the largest one grouping 65 events (see also Figure III.28). These observations show that the SSE triggers different types of seismicity. Part of it can be understood as immediate stress release on locked patches of the interface, resulting in orphan events. The largest earthquakes belong to this category, and illustrate the triggering potential of SSE for large interplate earthquakes. The events grouped into families indicate that the stress release on some areas of the interface is more complex, with the conjugate effect of SSE stress loading and earthquake interaction. We present in Figure III.30 the temporal activation of the 4 main families. As for the whole sequence, the magnitude occurrence inside each family as a function of time does not follow a simple law. This observation suggests that the time-dependent stress induced by the SSE is a dominant factor and that a small seismogenic area is progressively ruptured by this regular stress increase. However, earthquake interaction also plays a role in the seismicity rate inside a family. This is clear for family 1, where higher seismic activity is present just after the largest earthquake of this family (Figure III.30).

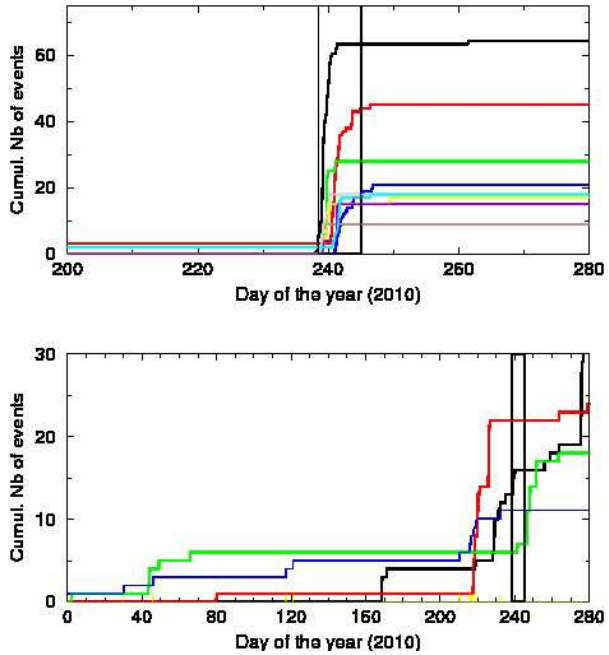

Figure III.28: Upper plot shows, for the 10 largest families active during the SSE, the cumulated number of events detected since 2009/07/08. Lower plot shows similar cumulated numbers for families active during months around the SSE.

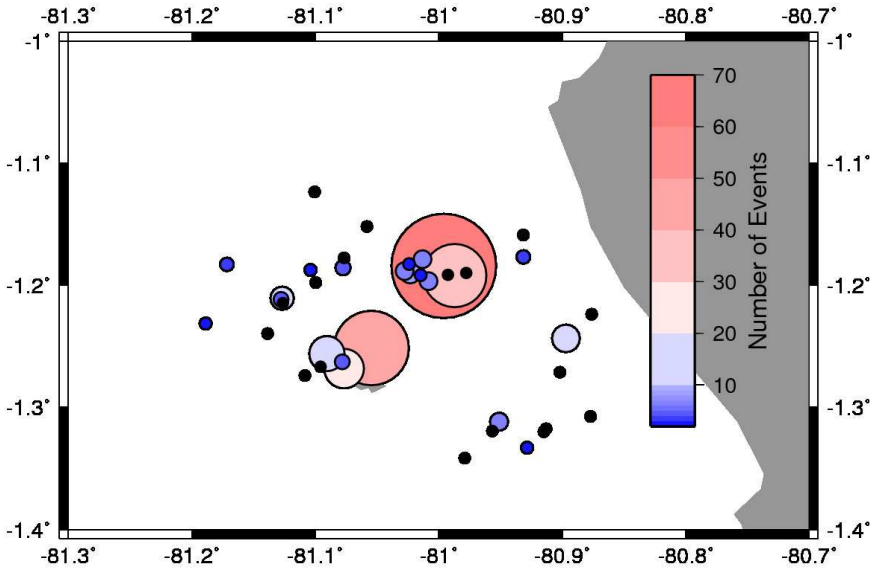

Figure III.29: Family character of the located seismicity. The circle sizes and colors are scaled to the number of events present in the family (see colorscale on the right). Black dots show individual events, small and dark blue circles show doublets, and the larger circles show more numerous families.

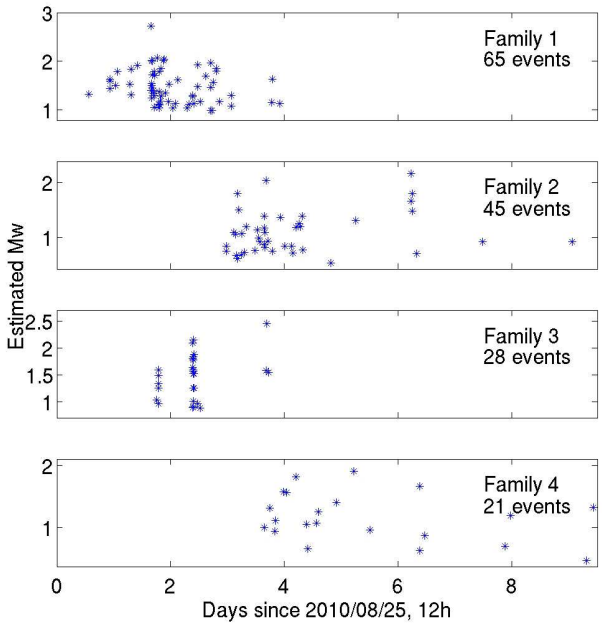

Figure III.30: Temporal activation of the 4 main seismicity families. The moment magnitude (Mw, vertical scale) has been derived using the amplitude ratio between each event and the larger event of the family, for which we have an independent estimate of the magnitude (see section III.4.4.2)

III.4.5 Spatial relations between slow slip and seismicity

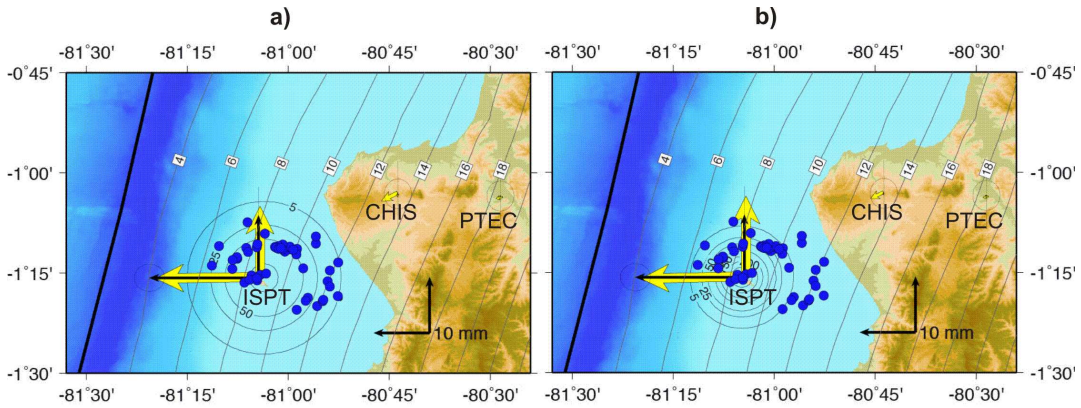

Figure III.31: Map view of the slow slip models (see Figure III.21) and of the associated seismicity (blue circles). In the case a), which corresponds to the upper bound of the slow slip dimensions, all the seismicity is located inside the slow slip area. In the case b), which corresponds to the lower bound of the slow slip area, only the easternmost events are located outside the slow slip area.

Figure III.31 presents the spatial distribution of the slow slip and of its associated seismicity. It reveals that most of the seismicity occurred inside or very close to the zone affected by the slow slip. This is consistent with a mostly aseismic subduction interface, but over which small and localized patches break seismically. The size of the breaking patches have to be small to account for the large deformation ratio between seismic and aseismic processes. Considering an upper bound of the moment magnitude of the seismicity (Mw=4.3) and a lower bound for the SSE (Mw=6), the moment ratio is larger than 350. Simple calculations show that the SSE stress drop is comparable to the one of a classical earthquake, in the range 2-25 bars (see following section III.5 for more details). We can therefore apply simple scaling relations to the SSE and seismicity. Using the relation $M_0 \sim A^{3/2}$ (M_0 and A are seismic moment and rupture area, respectively), we find that the aseismic surface is at least 50 times larger than the seismic one.

This observation indicates that the spatial extension of the seismic crisis is a good first-order evaluation of the size and location of the SSE. This was not the case for seismicity associated to other SSEs (Hikurangi, New Zealand, *Delahaye et al.*, 2009; Boso, Japan, *Sagiya*, 2004; Guerrero, Mexico, *Liu et al.,* 2007), where the earthquakes were adjacent to the slow slip area. We propose that these latter cases are more related to stress transfer outside the SSE. Here, on the contrary, the seismicity and slow slip observed during the 2010 La Plata sequence are more intimately related. They indicate that mixed phenomena - seismic and aseismic - may coexist on a subduction interface.

In the same region, such phenomena are likely to have occurred in the past. An obvious candidate is the strong 2005 seismic swarm. If referring to its larger spatial extension, to its longer duration (1 month instead of one week), and to the larger cumulated seismic moment (Mw ~6.5, compared to Mw~4.2), we strongly suggest that this seismicity originated from a larger scale SSE.

Supplementary material :

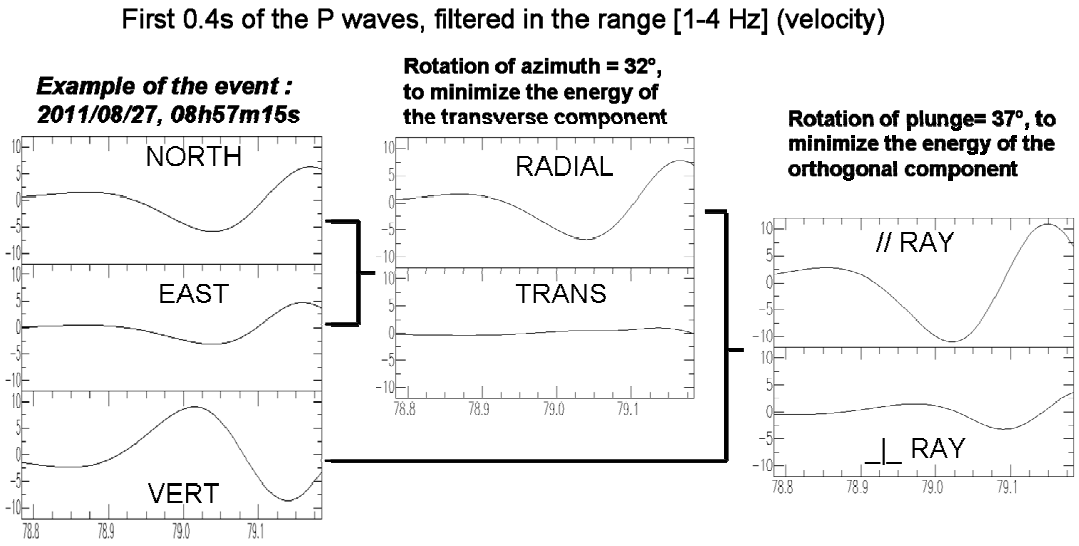

Supplementary Figure III.A.1 : Procedure used to determine the earthquakes location. (Left of the figure) : The three components are band-passed (1-4Hz) and windowed (0.4s) after the P wave arrival. (Middle) Search for the rotation angle (R_α) of the horizontal components minimizing the average squared amplitude on the initial East component. The back-azimuth of the earthquake is equal to R_α when the initial North component is anticorrelated with the vertical component. It is equal to (R_α +180°) in the case of positive correlation. The back-azimuth is here found equal to 32°. (Right of the figure) Same operation with the radial and vertical component to determine the optimal apparent incident angle of the ray, here found equal to 37°. Note that this angle is apparent because it is not the real incidence angle due to free surface effects (see Aki and Richards, 2002). Relative amplitude between the vertical and radial components imply that the measured angle is (2j), where j is the angle of the reflected S-wave corresponding to the real P-wave incidence i. Simple application of the Snell-Descartes law allows us to retrieve i from (2j). This relation between 2j and i is not dependent on the absolute value of the wave velocities, but only on the ratio between P-velocity and S-velocity, here taken equal to √3. Using this relation, i=33.4°. From the value of i, the ray geometry is predicted using the two-layer model of table III.1, and the hypocenter position along this ray is determined by the S-P time.

III.5 Perspectives : Mouvements asismiques et sismicité

L'observation détaillée dans la section précédente devrait motiver de nouvelles études sur les interactions entre mouvements lents et sismicité en zone de subduction. Ces relations avaient été quelque peu délaissées ces dernières années au profit des liens entre les trémors non-volcaniques et les mouvements lents.

Notre étude apporte, en premier lieu, une image claire du potentiel déclencheur des mouvements lents sur la sismicité. Dans les zones de subduction, ce lien de causalité a été vu dans d'autres régions du monde (Peninsule de Boso, Japon ; Hikurangi, Nouvelle Zélande ; Guerrero, Mexique), mais de manière plus floue dans les liens spatio-temporels unissant les deux phénomènes. Il a aussi été suggéré ces dernières années à partir de seules caractéristiques anormales de la sismicité (*Holtkamp and Brudzinski*, 2011 ; *Holtkamp et al.*, 2011 ; *Kato et al.*, 2012 ; *Bouchon et al.*, 2011). Nous appuyons ainsi fortement l'hypothèse qu'un comportement particulier de la sismicité, sous forme d'essaims ou d'événements répétés, peut avoir son origine dans un mouvement lent.

En Equateur, cette corrélation entre les deux phénomènes nous suggère fortement qu'un mouvement lent soit à l'origine de l'essaim sismique de 2005. Si l'on s'en réfère simplement à l'échelle de cet essaim (durée d'un mois et magnitude cumulée équivalant à $M_w \sim 6.5$), ce glissement lent fut probablement d'une forte amplitude. Il n'a pas été détecté par une analyse interférométrique *Holtkamp et al.*, 2011), mais comme l'expliquent ces auteurs, cela est principalement dû à la perte de cohérence des images satellitaires. L'occurrence de séismes lents répétés dans la région de l'Ile de la Plata expliquerait aussi pourquoi les séismes majeurs du XXème siècle ne sont pas propagés plus au Sud : rencontrant une zone où les contraintes sont régulièrement relâchées, ces séismes se seraient « éteints » car le mécanisme moteur de la rupture serait devenu trop faible. Il apparaît ainsi que ces essaims sismiques sont des témoins de processus de plus grande échelle, qui jouent eux-mêmes un rôle important dans le cycle sismique. Leur détection devrait donc être un objectif spécifique des réseaux sismiques ; cette dernière peut parfois être faite à l'échelle télésismique (*Holtkamp and Brudzinski*, 2011), mais des réseaux locaux sont nécessaires pour une analyse exhaustive.

En revenant sur le cas particulier de la séquence de 2010, il est intéressant de replacer cet épisode dans les lois d'échelle des phénomènes de déformation (*Ide et al.*, 2007 ; *Peng and Gomberg*, 2010 ; *Gao et al.*, 2012). La durée du glissement par rapport à sa magnitude (6-7 jours et $M_w = 6 - 6.3$) est en bon accord avec les autres glissements lents connus. En revanche, la chute de contrainte associée est typique des séismes classiques plutôt que des séismes lents de subduction. Si l'on applique la simple loi $\Delta\sigma = 7\ M_0/(16\ R^3)$, qui relie la chute de contrainte $\Delta\sigma$ au moment sismique M_0 pour une rupture circulaire de rayon R, la chute de contrainte est de l'ordre de 2–25 bars. C'est une valeur

nettement plus élevée que celle des séismes lents connus, qui est typiquement dans la gamme 0.001bars–0.1bars (*Gao et al.*, 2012). Cette observation appelle deux commentaires. D'une part, cela indique que les séismes lents peuvent partager certaines des caractéristiques de leurs homologues rapides, ce qui diffère des conclusions de l'étude de *Ide et al.* (2007). Ces auteurs proposent en effet deux comportements complètement distincts pour les déformations lentes ou rapides. En ce sens, notre observation va dans le sens de *Peng and Gomberg* (2010), qui proposent une plus grande diversité dans les lois d'échelles de déformation. D'autre part, nous pouvons envisager que la forte sismicité associée soit précisément due à cette chute de contrainte importante. Davantage d'observations de sismicité associées à des glissements lents sont nécessaires pour mieux évaluer cette hypothèse.

Le cas bien documenté de l'Ile de la Plata en août 2010, peut aussi servir d'exemple réel pour calibrer des modélisations numériques ou expérimentales. Nous montrons en effet que la sismicité se produit sur une grande partie de l'interface affectée par le glissement lent, mais qu'elle ne représente que quelques millièmes de la déformation globale (en termes de moment). Une hypothèse serait que certains points de l'interface glissent de manière fragile dans un premier temps ; une fois que le contact entre des petites aspérités de la faille est ainsi rompu, un glissement plus fort, asismique et lent, pourrait continuer à faire glisser ces points. Nous montrons également que cette sismicité n'est pas répartie de manière homogène. Certaines zones très localisées sont sujettes à une activité sismique intense, comme en témoignent les familles de séismes observées. Les séismes de ces familles, fortement similaires, ne sont pas non plus exactement semblables : ils pourraient ainsi correspondre à la rupture progressive, étalée dans le temps, d'une aspérité très localisée. Ces caractéristiques peuvent être comparées ou discutées par rapport à des expériences en laboratoire, comme celle de *Lengliné et al.* (2012). En retour, une image plus réaliste des caractéristiques frictionnelles de l'interface de subduction pourrait être fournie par ces expériences analogiques.

Nous avons également peu exploré les caractéristiques plus fines de la sismicité associée au séisme lent, et en particulier les propriétés des formes d'ondes générées. Au premier abord, la sismicité modérée semble présenter un caractère classique, avec des ondes de volume P et S clairement identifiables. Leur contenu spectral semble également comparable avec la sismicité régulièrement observée. Cependant, nous n'avons pas encore réellement quantifié ces valeurs, entre autres par rapport à la loi ω^{-2}. Par ailleurs, nous n'avons pas spécifiquement recherché des signaux sismiques plus ténus, qui pourraient traduire des processus encore plus riches que la relation glissement lent – sismicité observée.

Enfin, nous souhaitons chercher à mieux documenter de nouveaux épisodes autour de l'Ile de la Plata. En effet, l'analyse de la séquence de 2010 a bénéficié de la situation idéale de la station ISPT, mais a été limitée par l'absence d'autres observations proches. Aujourd'hui, l'instrumentation est plus nombreuse dans cette région grâce au programme OSISEQ (`https://geoazur.oca.eu/spip.`

`php?article1186`) : 5 OBS ont été déployés en octobre 2011 à proximité de la fosse et 6 capteurs sismiques ont été installés sur la presqu'ile de Manta, en face de l'Ile de la Plata.

Bibliographie

Références citées dans le texte, hors articles publiés

Aki, K., Scaling law of seismic spectrum, *J. Geophys. Res.*, **72**, 1217–1231, 1967.

Aki, K., and P. Richards, Quantitative Seismology, Univ. Sci., Sausalito, Calif, 2002.

Aksoy M.E., M.A. Meghraoui, M. Vallée, and Z. Cakir, Rupture Characteristics of the 1912 Mürefte (Ganos) Earthquake Segment of the North Anatolian Fault (Western Turkey), *Geology*, **38**, 991–994, 2010.

Ammon, C.J., A.A. Velasco, and T. Lay, Rapid estimation of rupture directivity: application to the 1992 Landers (M_S = 7.4) and Cape Mendocino (M_S = 7.2), California earthquakes, *Geoph. Res. Lett.*, **20**, 97–100, 1993.

Ammon, C. J., H. Kanamori, T. Lay, and A. A. Velasco, The 17 July 2006 Java Tsunami Earthquake, *Geophys. Res. Lett.*, **33**, L24308, 2006.

Ammon, C.J., T. Lay, H. Kanamori, and M. Cleveland, A rupture model of the 2011 off the Pacific coast of Tohoku Earthquake. *Earth Planets Space*, **63**, 693–696, 2011.

Ando, M., M. Nakamura, T. Matsumoto, M. Furukawa, K. Tadokoro, and M. Furumoto, Is the Ryukyu subduction zone in Japan coupled or decoupled?—The necessity of seafloor crustal deformation observation, *Earth Planets Space*, **61**, 1031–1039, 2009.

Andrews, D.J., Rupture velocity of plane strain shear cracks, *J. Geophys.*

Res., **81**, 5679–5687, 1976.

Andrews, D.J., and E. Schwerer, Probability of rupture of multiple fault segments, *Bull. Seismol. Soc. Am.*, **90**,1498–1506, 2000.

Andrews, D.J., Ground motion hazard from supershear rupture, *Tectonophysics*, **493**, 216–221, 2010.

Bassin, C., G. Laske, and G. Masters, The Current Limits of Resolution for Surface Wave Tomography in North America, *EOS, Trans. Am. Geophys. Un.*, **81**, F897, 2000.

Beck, S. L., and L. J. Ruff, The rupture process of the great 1979 Colombia earthquake: evidence for the asperity model, *J. Geophys. Res.*, **89**, 9281–9291, 1984.

Bernard, P., and D. Baumont, Shear Mach wave characterization for kinematic fault rupture models with constant supershear rupture velocity, *Geophys. J. Int.*, **162**, 431–447, 2005.

Bertero, M., D. Bindi, P. Boccacci, M. Cattaneo, C. Eva, and V. Lanza, Application of the projected Landweber method to the estimation of the source time function in seismology, *Inverse Problems*, **13**, 465–486, 1997.

Béthoux N., M. Segovia M., V. Alvarez, J.Y. Collot, P. Charvis, A. Gailler, and T. Monfret, Seismological study of the central Ecuadorian margin: Evidence of upper plate deformation, *Journal of South American Earth Sciences*, **31**, 139–152, 2011.

Bilek, S.L., and T. Lay, Rigidity variations with depth along interplate megathrust faults in subduction zones, *Nature*, **400**, 443–446, 1999.

Bilek, S.L., T. Lay, and L.J. Ruff, Radiated seismic energy and earthquake source duration variations from teleseismic source time functions for shallow subduction zone thrust earthquakes, *J. Geophys. Res.*, **109**, B09308, 2004.

Bilek, S.L., Using earthquake rupture variations along the Sumatra-Andaman subduction system to examine fault zone variations, *Bull. Seismol. Soc. Am.*, **97**, S62–S70, 2007.

Bizzarri, A., E.M. Dunham, and P. Spudich, Coherence of Mach fronts during heterogeneous supershear earthquake rupture propagation:

Simulations and comparison with observations, *J. Geophys. Res.*, **115**, B08301, 2010.

Bos, A.G., G. Nolet, A. Rubin, H. Houston and J.E. Vidale, The duration of deep earthquakes determined by stacking of GSN seismograms, *J. Geophys. Res.*, **103**, 21059–21066, 1998.

Bouchon, M., A simple method to calculate Green's functions for elastic layered media, *Bull. Seism. Soc. Am.*, **71**, 959–971, 1981.

Bouchon, M., and M. Vallée, Observation of long supershear rupture during the Ms=8.1 Kunlunshan (Tibet) earthquake, *Science*, **301**, 824–826, 2003.

Bouchon, M., and H. Karabulut, The Aftershock Signature of Supershear Earthquakes, *Science*, **320**, 1323–1325, 2008.

Bouchon, M., H. Karabulut, M. Aktar, S. Özalaybey, J. Schmittbuhl, and M.P. Bouin, Extended Nucleation of the 1999 M-w 7.6 Izmit Earthquake, *Science*, **331**, 877–880, 2011.

Burridge, R. Admissible speeds for plane-strain shear cracks with friction but lacking cohesion, *Geophys J. Roy. Astr. Soc.* **35**, 439–455, 1973.

Campillo, M., Numerical evaluation of the near-field high-frequency radiation from quasidynamic circular faults, *Bull. Seismol. Soc. Am.*, **73**, 723–734, 1983.

Cerný, V., Thermodynamical approach to the traveling salesman problem: An efficient simulation algorithm, *Journal of Optimization Theory and Applications*, **45**, 41–51, 1985.

Chung, W.Y., and H. Kanamori, Variation of seismic source parameters and stress drops within a descending slab and its implications in plate mechanics, *Phys. Earth. Planet. Inter.*, **23**, 134–159, 1980.

Clayton, R.W., and Wiggins, R.A., Source shape estimation and deconvolution of teleseismic body waves, *Geophys. J. R. Astr. Soc.* **47**, 151–177, 1976.

Cochard, A., and R. Madariaga, Dynamic Faulting Under Rate-Dependent Friction, *Pure Appl. Geophys.*, **142**, 419–445, 1994.

Cohen, S.C., Numerical Models of Crustal Deformation in Seismic Zones, *Adv. Geophys.*, **41**, 133–231, 1999.

Collot J-Y, P. Charvis, and the Sisteur Scientific party, Exploring the Ecuador-Colombia active margin and inter-plate seismogenic zone, *American Geophysical Union, EOS*, **83**, 185–190, 2002.

Courboulex, F., S.K. Singh, J.F Pacheco, and C.J. Ammon, The 1995 Colima-Jalisco, Mexico, earthquake (Mw 8): a study of the rupture process, *Geoph. Res. Lett.*, **24**, 1019–1022, 1997.

Cruz-Atienza, V.M., and K.B. Olsen, Supershear Mach-waves expose the fault breakdown slip, *Tectonophysics*, **493**, 285—296, 2010.

Delahaye, E.J., J. Townend, M.E. Reyners, G. Rogers, Microseismicity but no tremor accompanying slow slip in the Hikurangi subduction zone, New Zealand. *Earth Planet. Sci. Lett.*, **277**, 21–28, 2009.

Delouis, B., D. Giardini, P. Lundgren, and J. Salichon, Joint inversion of InSAR, GPS, teleseismic and strong motion data for the spatial and temporal distribution of earthquake slip: Application to the 1999 Izmit Mainshock, *Bull. Seismol. Soc. Am.*, **92**, 278–299, 2002.

Delouis, B., M. Vallée, M. Meghraoui, E. Calais, S. Maouche, K. Lammali, A. Mahsas, P. Briole, F. Benhamouda, and K. Yelles, Slip distribution of the 2003 Boumerdes-Zemmouri earthquake, Algeria, from teleseismic, GPS, and coastal uplift data, *Geophys. Res. Lett.*, **31**, L18607, 2004.

Delouis, B., J.-M. Nocquet, and M. Vallée, Slip distribution of the February 27, 2010 Mw = 8.8 Maule Earthquake (Central Chile) from static and high-rate GPS, InSAR, and broadband teleseismic data, *Geophys. Res. Lett.*, **37**, L17305, 2010.

Dorbath, L., A. Cisternas, and C. Dorbath, Assessment of the size of large and great historical earthquakes in Peru, *Bull. Seismol. Soc. Am.*, **80**, 551–576, 1990.

Douglas, A., J. Beavan, L. Wallace and J. Townend, Slow slip on the northern Hikurangi subduction interface, New Zealand, *Geophys. Res. Lett.* **32**, L16305, 2005.

Dragert, H., K. Wang, and T. S. James, A silent slip event on the deeper Cascadia subduction interface, *Science*, **292**, 1525–1528, 2001.

Dunham, E. M., Conditions governing the occurrence of supershear ruptures under slip-weakening friction, *J. Geophys. Res.*, **112**, B07302, 2007.

Duputel, Z., L. Rivera, H. Kanamori, and G. Hayes, Wphase source inversion for moderate to large earthquakes (1990-2010), *Geophys. J. Int.*, **189**, 1125–1147, 2012.

Ekström, G., and E.R. Engdahl, Earthquake source parameters and stress distribution in the Adak Island region of the central Aleutian Islands, *J. Geophys. Res.*, **94**, 15,499–15,519, 1989.

Ellsworth, W.L., M. Celebi, J.R. Evans, E.G. Jensen, M.C. Metz, D.J. Nyman, J.W. Roddick, P. Spudich, and C.D. Stephens, Near-field ground motions of the M 7.9 November 3, 2002, Denali fault, Alaska, earthquake recorded at pump station 10, *Earthquake Spectra*, **20**, 597–615, 2004.

Engdahl, E.R., R. van der Hilst, and R. Buland, Global teleseismic earthquake relocation with improved travel times and procedures for depth determination, *Bull. Seism. Soc. Am.*, **88**, 722–743, 1998.

Freund L.B. and D.M. Barnett D M, A two dimensional analysis of surface deformation due to dip-slip faulting, *Bull. Seis. Soc. Am.*, **66**, 667–675, 1976.

Fukao, Y., and M. Kikuchi, Source retrieval for mantle earthquakes by iterative deconvolution of long-period P-waves, *Tectonophysics*, **144**, 249–269, 1987.

Fukuyama, E., and K. Irikura, Rupture process of the 1983 Japan Sea (Akita-Oki) earthquake using a waveform inversion method, *Bull. Seism. Soc. Am.*, **76**, 1623–1640, 1986.

Gao, H., D. A. Schmidt, and R. Weldon, Scaling relationships of source parameters for slow slip events, *Bull. Seis. Soc. Am.*, **102**, 352–360, 2012.

Graindorge, D., A. Calahorrano, P. Charvis, J.-Y. Collot, and N. Bethoux, Deep structures of the Ecuador convergent margin and the Carnegie Ridge, possible consequence on great earthquakes recurrence interval, *Geophys. Res. Lett.*, **31**, L04603, 2004.

Graizer, V.M., Effect of tilt on strong motion data processing, *Soil*

Dyn. Earthq. Eng., **25**, 197–204, 2005.

Hartzell, S.H., Earthquake aftershocks as Green's functions, *Geoph. Res. Lett.*, **5**, 1–4, 1978.

Hartzell, S.H., and T.H. Heaton, Inversion of strong ground motion and teleseismic waveform data for the fault rupture history of the 1979 Imperial Valley, California, earthquake, *Bull. Seism. Soc. Am.*, **73**, 1553–1583, 1983.

Heaton, T.H., Evidence for and implications of self-healing pulses of slip in earthquake rupture, *Phys. Earth Planet. Inter.*, **64**, 1–20, 1990.

Hirose, H., K. Hirahara, F. Kimata, N. Fujii, and S. Miyazaki, A slow thrust slip event following the two 1996 Hyuganada earthquakes beneath the Bungo Channel, southwest Japan, *Geophys. Res. Lett.*, **26**, 3237–3240, 1999.

Holtkamp, S.G., and M.R. Brudzinski, Earthquake swarms in circum-Pacific subduction zones, *Earth Planet. Sci. Lett.*, **305**, 215–225, 2011.

Holtkamp, S.G., M.E. Pritchard, and R.B. Lohman, Earthquake Swarms in South America, *Geophys. J. Int.*, **187**, 128–146, 2011.

Huang, B.-S., J. Chen, Q. Liu, Y.-G Chen, X.W. Xu, C.-Y. Wang, S.-J. Lee, and Z.-X. Yao, Estimation of rupture processes of the 2008 Wenchuan Earthquake from joint analyses of two regional seismic arrays, *Tectonophysics*, in press, doi: 10.1016/j.tecto.2011.12.026, 2012.

Ide, S., G.C. Beroza, D.R. Shelly, and T. Uchide, A scaling law for slow earthquakes, *Nature*, **447**, 76–79, 2007.

Ihmlé, P.F., J. Gomez, P. Heinrich, and S. Guibourg, The 1996 Peru tsunamigenic earthquake: Broadband source process, *Geophys. Res. Lett.*, **25**, 2691–2694, 1998.

Kanamori, H., and McNally, K.C., Variable rupture mode of the subduction zone along the Ecuador-Colombia coast, *Bull. Seismol. Soc. Am.*, **72**, 1241–1253, 1982.

Kanamori, H., W phase, *Geophys. Res. Lett.*, **20**, 1691–1694, 1993.

Kanamori, H., and L. Rivera, Source inversion of W phase: speeding up seismic tsunami warning, *Geophys. J. Int.*, **175**, 222–238, 2008.

Kanda, R.V.S., and M. Simons, An elastic plate model for interseismic deformation in subduction zones, *J. Geophys. Res.*, **115**, B03405, 2010.

Kaneko, Y., and N. Lapusta, Supershear transition due to a free surface in 3-D simulations of spontaneous dynamic rupture on vertical strike-slip faults, *Tectonophysics*, **493**, 272–284, 2010.

Kato, A., K. Obara, T. Igarashi, H. Tsuruoka, S. Nakagawa, and N. Hirata, Propagation of Slow Slip Leading Up to the 2011 M_w 9.0 Tohoku-Oki Earthquake, *Science*, **33**, 705–708, 2012.

Kellogg J. N., and W.E. Bonini, Subduction of the Caribbean Plate and Basement, Uplifts in the overiding South American Plate, *Tectonics*, **1**, 251–276, 1982.

Kendrick E., M. Bevis, R. Smalley Jr., B. Brooks, R.B. Vargas, E. Lauria, L.P. Souto Fortes, The Nazca-South America Euler vector and its rate of change, *Journal of South American Earth Sciences*, **16**, 125–131, 2003.

Kim M.J., S.Y. Schwartz and S. Bannister, Non-volcanic tremor associated with the March 2010 Gisborne slow slip event at the Hikurangi subduction margin, New Zealand, *Geophys. Res. Lett.*, **38**, L14301, 2011.

Kirkpatrick, S., C.D. Gelatt, and M.P. Vecchi, Optimization by Simulated Annealing, *Science*, **220**, 671–680, 1983.

Komatitsch, D., J. Ritsema, and J. Tromp, The spectral-element method, Beowulf computing, and global seismology, *Science*, **298**, 1737–1742, 2002.

Kurahashi, S., and K. Irikura, Source model for generating strong ground motions during the 2011 off the Pacific coast of Tohoku Earthquake, *Earth Planets Space*, **63**, 571–576, 2011.

Lay, T., C.J. Ammon, A.R. Hutko, and H. Kanamori, Effects of kinematic constraints on teleseismic finite-source rupture inversions: Great Peruvian earthquakes of 23 June 2001 and 15 August 2007, *Bull. Seism. Soc. Am.*, **100**, 969–994, 2010.

Lengliné, O., J.E. Elkhoury, G. Daniel, J. Schmittbuhl, R. Toussaint, J.-P. Ampuero and M. Bouchon, Interplay of seismic and aseismic

deformations during earthquake swarms: an experimental approach, *Earth Plan. Sci. Lett.*, **331—332**, 215–223, 2012.

Liu, Y., J.R. Rice, K.M. Larson, Seismicity variations associated with aseismic transients in Guerrero, Mexico, 1995—2006, *Earth Planet. Sci. Lett.*, **262**, 493–504, 2007.

Madariaga, R., High-frequency radiation from crack (stress drop) models of earthquake faulting, *Geophys. J. R. Astron. Soc.*, **51**, 625–651, 1977.

Madariaga, R., and K.B. Olsen, Criticality of rupture dynamics in 3-D, *Pure Appl. Geophys.*, **157**, 1981–2001, 2000.

Marone, C., Laboratory-derived friction laws and their application to seismic faulting, *Annu. Rev. Earth Planet. Sci.*, **26**, 643–696, 1998.

Mazzotti, S., and J. Adams, Variability of near-term probability for the next great earthquake on the Cascadia subduction zone, *Bull. Seismol. Soc. Am.*, **94**, 1954–1959, 2004.

McCaffrey, R., L.M. Wallace, and J. Beavan, Slow slip and frictional transition at low temperature at the Hikurangi subduction zone, *Nature Geoscience*, **1**, 316–320, 2008.

Menke, W., Imaging fault slip using teleseismic waveforms, analysis of a typical incomplete tomography experiment, *Geophys. J. R. Astr. Soc.*, **81**, 197–204, 1985.

Mercier de Lepinay, B., A. Deschamps, F. Klingelhoefer, Y. Mazabraud, B. Delouis, V. Clouard, Y. M. Hello, J. Crozon, B. Marcaillou, D. Graindorge, M. Vallée, J. Perrot, M.-P. Bouin, J.-M. Saurel, P. Charvis, and M. St-Louis, The 2010 Haiti earthquake: a complex fault pattern constrained by seismologic and tectonic observations, *Geophys. Res. Lett.*, **38**, L22305, 2011.

Mori, J., and A. Frankel, Source parameters for small events associated with the 1986 North Palm Springs, California, earthquake determined using empirical Green functions, *Bull. Seism. Soc. Am.*, **80**, 278–295, 1990.

Mueller, C.S., Source pulse enhancement by deconvolution of an empirical Green's function, *Geoph. Res. Lett.*, **12**, 33–36, 1985.

Olson, A.H., and R.J. Apsel, Finite fault and inverse theory with

applications to the 1979 Imperial Valley earthquake, *Bull. Seism. Soc. Am.*, **72**, 1969–2001, 1982.

Outerbridge, K.C., T.H. Dixon, S.Y. Schwartz, J.I. Walter, M. Protti, V. Gonzalez, J. Biggs, M. Thorwart, and W. Rabbel, A tremor and slip event on the Cocos-Caribbean subduction zone as measured by a global positioning system (GPS) and seismic network on the Nicoya Peninsula, Costa Rica, *J. Geophys. Res.*, **115**, B10408, 2010.

Ozawa, S., S. Miyazaki, Y. Hatanaka, T. Imakiire, M. Kaidzu, and M. Murakami, Characteristic silent earthquakes in the eastern part of the Boso peninsula, Central Japan, *Geophys. Res. Lett.*, **30**, 1283, 2003.

Payero, J., V. Kostoglodov, N. Shapiro, T. Mikumo, A. Iglesias, X. Pérez-Campos, and R. Clayton, Nonvolcanic tremor observed in the Mexican subduction zone, *Geophys. Res. Lett.*, **35**, L07305, 2008.

Peng, Z., and J. Gomberg, An integrated perspective of the continuum between earthquakes and slow-slip phenomena, *Nature Geoscience*, **3**, 599–607, 2010.

Pennington, W.D., Subduction of the Eastern Panama Basin and Seismotectonics of Northwestern South America, *J. Geophys. Res.*, **86**, 10,753–10,770, 1981.

Peterson, J., Observations and modelling of background seismic noise. *Open-file report 93-322, U. S. Geological Survey*, Albuquerque, New Mexico, 1993.

Radiguet, M., F. Cotton, M. Vergnolle, M. Campillo, B. Valette, V. Kostoglodov, and N. Cotte, Spatial and temporal evolution of a long term slow slip event: the 2006 Guerrero Slow Slip Event, *Geophys. J. Int.*, **184**, 816–828, 2011.

Rani, S., and S.J. Singh, Static deformation of a uniform half-space due to a long dip-slip fault, *Geophys. J. Int.*, **109**, 469–476, 1992.

Reid, H.F., The Mechanics of the Earthquake, The California Earthquake of April 18, 1906, *Report of the State Investigation Commission*, **2**, Carnegie Institution of Washington, Washington, D.C., 1910 (see especially pages 16-28).

Ritsema, J., H.J. van Heijst, and J.H. Woodhouse, Complex shear wave velocity structure imaged beneath Africa and Iceland, *Science*, **286**,

1925–1928, 1999.

Ritsema, J., A. Deuss, H.J. van Heijst and J.H. Woodhouse, S40RTS: a degree-40 shear velocity model for the mantle from new Rayleigh wave dispersion, teleseismic traveltimes, and normal-mode splitting function measurements, *Geophys. J. Int.*, **184**, 1223–1236, 2011.

Robinson, D.P., S. Das, A.B. Watts, Earthquake rupture stalled by a subducting fracture zone, *Science*, **312**, 1203–1205, 2006.

Rogers, G., and H. Dragert, Episodic tremor and slip on the Cascadia subduction zone: The chatter of silent slip, *Science*, **300**, 1942–1943, 2003.

Rousseau, C.-E., and A.J. Rosakis, Dynamic path selection along branched faults: Experiments involving sub-Rayleigh and supershear ruptures, *J. Geophys. Res.*, **114**, B08303, 2009.

Ruegg, J.C., A. Rudloff, C. Vigny, R. Madariaga, J.B. de Chabalier, J. Campos, E. Kausel, S. Barrientos, and D. Dimitrov, Interseismic strain accumulation measured by GPS in the seismic gap between Constitución and Concepción in Chile, *Phys. Earth Planet. Inter.*, **175**, 78–85, 2009.

Ruff, L.J., Dynamic Stress Drop of Recent Earthquakes: Variations within Subduction Zones, *Pure Appl. Geophys.*, **154**, 409–431, 1999.

Ruiz, J., D. Baumont, P. Bernard, and C. Berge-Thierry, New approach in the kinematic k?2 source model for generating physical slip velocity functions, *Geophys. J. Int.*, **171**, 739–754, 2007.

Sagiya, T., Interplate coupling in the Kanto district, central Japan, and the Boso Peninsula silent earthquake in May 1996, *Pure Appl. Geophys.*, **161**, 2601–2616, 2004.

Sambridge, M., Geophysical inversion with a neighbourhood algorithm. I. Searching a parameter space, *Geophys. J. Int.*, **138**, 479–494, 1999.

Savage, J.C., A dislocation model of strain accumulation and release at a subduction zone, *J. Geophys. Res.*, **88**, 4984–4996, 1983.

Schubnel, A., S. Nielsen, J. Taddeucci, S. Vinciguerra, and S. Rao, Photo-acoustic study of subshear and supershear ruptures in the laboratory, *Earth Planet. Sci. Lett.*, **308**, 424–432, 2011.

Schwartz S.Y., and J.M. Rokosky, Slow slip events and seismic tremor at circum-pacific subduction zones, *Reviews of Geophysics*, **45**, RG3004, 2007.

Singh, S.K., and F. Mortera, Source Time Functions of Large Mexican Subduction Earthquakes, Morphology of the Benioff Zone, Age of the Plate, and Their Tectonic Implications, *J. Geophys. Res.*, **96**, 21,487–21,502, 1991.

Tarantola, A., Inverse problem theory and methods for model parameter estimation, *Society for Industrial and Applied Mathematics (SIAM)*, Philadelphia, 2005.

Templeton, E.L., A. Baudet, H.S. Bhat, R. Dmowska, J.R. Rice, A.J. Rosakis, and C.-E. Rousseau, Finite element simulations of dynamic shear rupture experiments and dynamic path selection along kinked and branched faults, *J. Geophys. Res.*, **114**, B08304, 2009.

Tocheport, A., L. Rivera, and S. Chevrot, A systematic study of source time functions and moment tensors of intermediate and deep earthquakes, *J. Geophys. Res.*, **112**, B07311, 2007.

Tomar, S., and N.K. Dhiman, 2-D Deformation Analysis of a Half-space due to a Long Dip-slip Fault at Finite Depth, *Journal of Earth System Science*, **112**, 587–596, 2003.

Trenkamp, R., J.N. Kellogg, J.T. Freymueller, and P. Mora, Wide plate margin deformation, southern Central America and northwestern South America, CASA GPS observations, *Journal of South American Earth Sciences*, **15**, 157–171, 2002.

Trifunac, M.D., and M.I. Todorovska, A note on the usable dynamic range of accelerographs recording translation, *Soil Dyn. Earthq. Eng.*, **21**, 275–286, 2001.

Vaca, S., Sismotectonique de la région de Manta-Equateur, *Rapport de Master 2*, *Université de Nice Sophia Antipolis*, Nice-France, 2007.

Vaca, S., M. Regnier, N. Bethoux, V. Alvarez, B. Pontoise, Sismicidad de la región de Manta (Ecuador): enjambre sísmico de Manta-2005, *Geología y Geofísica Marina y Terrestre del Ecuador*, *Spec. Pub. INOCAR-IRD*, 151–166, 2010.

Vallée, M., Stabilizing the empirical Green function analysis : deve-

lopment of the projected Landweber method, *Bull. Seism. Soc. Am.*, **94**, 394–409, 2004.

Vallée, M., and M. Bouchon, Imaging coseismic rupture in far field by slip patches, *Geophys. J. Int.*, **156**, 615–630, 2004.

Vallée, M., and F. Di Luccio, Source analysis of the 2002 Molise, southern Italy, twin earthquakes (10/31 and 11/01), *Geophys. Res. Lett.*, **32**, L12309, 2005.

Vallée, M., Rupture properties of the giant Sumatra earthquake imaged by empirical Green function analysis, *Bull. Seismol. Soc. Am.*, **97**, S103–114, 2007.

Vallée, M., M. Landès, N.M. Shapiro, and Y. Klinger, The 2001/11/14 Kokoxili (Tibet) earthquake: high frequency seismic radiation originates from the transitions between subRayleigh and supershear rupture velocity regimes, *J. Geophys. Res.*, **113**, B07305, 2008.

Vallée, M., J. Charléty, A.M.G. Ferreira, B. Delouis, and J. Vergoz, SCARDEC : a new technique for the rapid determination of seismic moment magnitude, focal mechanism and source time functions for large earthquakes using body wave deconvolution, *Geophys. J. Int.*, **184**, 338–358, 2011.

Vallée M., and E.M. Dunham, Observation of far-field Mach waves generated by the 2001 Kokoxili supershear earthquake, *Geophys. Res. Lett.*, **39**, L05311, 2012.

Velasco, A.A., C.J. Ammon, and T. Lay, Empirical Green function deconvolution of broadband surface waves: rupture directivity of the 1992 Landers, California ($M_W = 7.3$), *Bull. Seism. Soc. Am.*, **84**, 735–750, 1994.

Vidale J.E., and H. Houston, The depth dependence of earthquake duration and implications for rupture mechanisms, *Nature*, **365**, 45–47, 1993.

Vidale, J.E., A.J. Hotovec, A. Ghosh, K.C. Creager, and J. Gomberg, Tiny intraplate earthquakes triggered by nearby episodic tremor and slip in Cascadia, *Geochem. Geophys. Geosyst.*, **12**, Q06005, 2011.

Wallace, L. M., and J. Beavan, Diverse slow slip behavior at the Hikurangi subduction margin, New Zealand, *J. Geophys. Res.*, **115**, B12402, 2010.

Wang, D., and J. Mori, The 2010 Qinghai, China, Earthquake: A Moderate Earthquake with Supershear Rupture, *Bull. Seismol. Soc. Am.*, **102**, 301–308, 2012.

Wdowinski, S., Y. Bock, J. Zhang, P. Fang, and J. Genrich, Southern California permanent GPS geodetic array: spatial filtering of daily positions for estimating coseismic and postseismic displacements induced by the 1992 Landers earthquake, *J. Geophys. Res.*, **102**, 18057–18070, 1997.

White S.M., R. Trenkamp, J. Kellogg, Recent crustal deformation and the earthquake cycle along the Ecuador-Colombia subduction zone, *Earth Planet. Sci. Lett.*, **216**, 231–242, 2003.

Xu, Y., K.D. Koper, O. Sufri, L. Zhu, and A.R. Hutko, Rupture imaging of the Mw7.9 12 may 2008 Wenchuan earthquake from back projection of teleseismic P waves, *Geochem. Geophys. Geosyst.*, **10**, Q04006, 2009a.

Xu, X., X. Wen, G. Yu, G. Chen, Y. Klinger, J. Hubbard, and J. Shaw, Coseismic reverse- and oblique-slip surface faulting generated by the 2008 Mw 7.9 Wenchuan earthquake, China, *Geology*, **37**, 515–518, 2009b.

Zhang, H., and Z. Ge, Tracking the rupture of the 2008 Wenchuan Earthquake by using the relative back-projection method, *Bull. Seismol. Soc. Am.*, **100**, 2551–2560, 2010.

Annexes

A.1 Curriculum Vitae

Martin VALLEE Né le 19/11/1976

GéoAzur
250, avenue Albert Einstein
F - 06560 Valbonne
(0033) 4 92 94 26 47
email : vallee@geoazur.unice.fr

- Sismologue -

Expérience professionnelle

Depuis Déc 2004 ---------- Chercheur à l'Institut de Recherche pour le Développement (IRD), affecté au laboratoire Géoazur (Nice, France). CR1 depuis décembre 2008. Dans la période 2008-2011, séjours de longue durée (durée cumulée supérieure à un an) à l'Institut de Géophysique à Quito (Equateur).

Jan 2004 - Nov 2004 -------- Postdoctorat (bourse européenne Marie Curie) à l'Osservatorio Vesuviano (INGV, Naples, Italie) : « *Analyse des séismes récents d'Italie du Sud* ».

Mar 2003 - Déc 2003 ------- Postdoctorat au Laboratoire de Détection Géophysique (CEA, Paris, France) : « *Etude de la source sismique et liens avec l'aléa associé* »

Juin 2001-Sep 2001 : ------- Visiteur à l'University of California Santa Cruz (UCSC, Etats-Unis) : *«Etude de la subduction d'Amérique Centrale : Costa-Rica et El Salvador* ».

Jun 1998-Sep 1998: --------- Stage à Elf Exploration Angola : « *Cartes isobathes régionales*».

Formation

Nov 1999 – Jan 2003 ------- Doctorat en sismologie au LGIT - Laboratoire de Géophysique Interne et Tectonophysique - à Grenoble, France. *« Etude cinématique de la rupture sismique en champ lointain: méthodes et résolution* »
Direction: Michel Bouchon
Soutenance le 6 Janvier 2003

Juin 1999: ---------- Diplôme d'ingénieur ENSPG, Ecole Nationale Supérieure de Physique de Grenoble, France.

1998-99 : ---------- DEA MMGE - Mécanique des Milieux Géophysiques et Environnement , Grenoble, France : « *Etude de la sismicité équatorienne : séismes et transferts de contraintes* »

Langues

Français : ---------- Langue maternelle
Anglais, Italien, Espagnol :- Courant

A.2 Publications

Publications dans des revues à comité de lecture internationale (rang A):

[1] Vallée, M., M. Bouchon, and S.Y. Schwartz, The 13 January 2001 El Salvador earthquake: a multi-data analysis, *J. Geophys. Res., **108***(B4), 2203, doi:10.1029/2002JB001922, 2003.

[2] Bouchon, M., and M. Vallée, Observation of long supershear rupture during the Ms=8.1 Kunlunshan (Tibet) earthquake, *Science, **301***, 824-826, 2003.

[3] Le Pichon, A., J. Guilbert, M. Vallée, J.X. Dessa, and U. Munkhuu, Infrasonic imaging of the Kunlun mountains during the great 2001 China earthquake, *Geophys. Res. Lett.*, ***30***(15), 1814, doi:10.1029/20003GL017581, 2003.

[4] Vallée, M., Stabilizing the empirical Green function analysis : development of the projected Landweber method, *Bull. Seism. Soc. Am., **94***, 394-409, 2004.

[5] Vallée, M., and M. Bouchon, Imaging coseismic rupture in far field by slip patches, *Geophys. J. Int.*, ***156***, 615-630, 2004.

[6] Delouis, B., M. Vallée, M. Meghraoui, E. Calais, S. Maouche, K. Lammali, A. Mahsas, P. Briole, F. Benhamouda, and K. Yelles, Slip distribution of the 2003 Boumerdes-Zemmouri earthquake, Algeria, from teleseismic, GPS, and coastal uplift data, *Geophys. Res. Lett.*, ***31***, L18607, doi:10.1029/2004GL020687, 2004.

[7] Vallée, M., and F. Di Luccio, Source analysis of the 2002 Molise, southern Italy, twin earthquakes (10/31 and 11/01), *Geophys. Res. Lett.*, **32**, L12309, doi:10.1029/2005GL022687, 2005.

[8] Vallée, M., Rupture properties of the giant Sumatra earthquake imaged by empirical Green function analysis, *Bull. Seismol. Soc. Am.*, 97, S103-114, doi: 10.1785/0120050616, 2007.

[9] Vallée, M., M. Landès, N.M. Shapiro, and Y. Klinger, The 2001/11/14 Kokoxili (Tibet) earthquake: high frequency seismic radiation originates from the transitions between subRayleigh and supershear rupture velocity regimes, *J. Geophys. Res.*, **113**, B07305, doi:10.1029/2007JB005520, 2008.
Science Editor's choice (**321**, 1272, 5 September 2008)

[10] Delouis B., J. Charlety, and M. Vallée, A method for rapid determination of moment magnitude M-w for moderate to large earthquakes from the near-field spectra of strong-motion records (MWSYNTH), *Bull. Seismol. Soc. Am.*, **99**, 1827-1840, 2009.

[11] Delouis, B., J.-M. Nocquet, and M. Vallée, Slip distribution of the February 27, 2010 Mw = 8.8 Maule Earthquake (Central Chile) from static and high-rate GPS, InSAR, and broadband teleseismic data, *Geophys. Res. Lett.*, **37**, L17305, doi:10.1029/2010GL043899, 2010.

[12] Aksoy M.E., M.A. Meghraoui, M. Vallée, and Z. Cakir, Rupture Characteristics of the 1912 Mürefte (Ganos) Earthquake Segment of the North Anatolian Fault (Western Turkey), *Geology*, **38**, 991-994, 2010.

[13] Bouchon M., H. Karabulut, M.P. Bouin, J. Schmittbuhl, M. Vallée, R. Archuleta, S. Das, F. Renard, and D. Marsan, Faulting characteristics of supershear earthquakes, *Tectonophysics*, **493**, 244-253, 2010.

[14] Vallée, M., J. Charléty, A.M.G. Ferreira, B. Delouis, and J. Vergoz, SCARDEC : a new technique for the rapid determination of seismic moment magnitude, focal mechanism and source time functions for large earthquakes using body wave deconvolution, *Geophys. J. Int.*, **184**, 338-358, 2011.

[15] Feuillet, N., F. Beauducel, E. Jacques, P. Tapponnier, B. Delouis, S. Bazin, M. Vallée, and G. King, The Mw = 6.3, November 21, 2004, Les Saintes earthquake (Guadeloupe). Tectonic setting, slip model and static stress changes, *J. Geophys. Res.*, **116**, B10301, 2011.

[16] Mercier de Lepinay, B., A. Deschamps, F. Klingelhoefer, Y. Mazabraud, B. Delouis, V. Clouard, Y. M. Hello, J. Crozon, B. Marcaillou, D. Graindorge, M. Vallée, J. Perrot, M.-P. Bouin, J.-M. Saurel, P. Charvis, and M. St-Louis, The 2010 Haiti earthquake: a complex fault pattern constrained by seismologic and tectonic observations, *Geophys. Res. Lett.*, **38**, L22305, 2011.

[17] Vallée, M., and E.M. Dunham, Observation of far-field Mach waves generated by the 2001 Kokoxili supershear earthquake, *Geophys. Res. Lett.*, **39**, L05311, 2012.

A.3 Pilotage et participation à des projets de recherche

Andes Du Nord

– Projet ADN (Variability of the subduction process and seismic potential along the northern Andes margin) financé par l'Agence Nationale de la Recherche de 2007 à 2011 (responsable : J.-M. Nocquet)
Responsable de la partie « sismologie », participation active à l'installation du réseau et à sa maintenance. Collaboration scientifique avec l'IG—EPN : 1 Mission sur place de 8 mois en 2009, 3 missions Longue-Durée de 2 mois en 2008, 2010 et 2011, et 3 autres missions plus courtes en 2007, 2010 et 2011. Mise en place de procédures d'analyse de qualité des sites (bruit), de détermination rapide de la magnitude de moment et du mécanisme au foyer.

– Laboratoire Mixte International (LMI Séismes et Volcans dans les Andes du Nord), financé par l'IRD, initié en 2012 (responsables : J.-M. Nocquet, J.-L. Le Pennec, Hugo Yepes)
Ce LMI poursuit et agrandit les contours du projet ADN, en associant les laboratoires Geoazur, Magmas et Volcans, et ISTerre à l'Institut de Géophysique à Quito. Implication dans le thème « Cycle et rupture sismique ».

– Projet Equasis (Aléa et risque sismique en Equateur), financé par le CNRS (PICS), initié en 2012 (responsable : F. Courboulex)
Projet lié au projet ADN, davantage orienté vers les conséquences d'un futur séisme. Implication dans la modélisation de la source sismique.

Analyse des séismes majeurs

– Contrat CNRS-CEA de collaboration sur les techniques d'analyse rapide des séismes majeurs. Financé par le CEA sur la période Novembre 2007-Novembre 2010 (responsable « CNRS », M. Vallée ; responsable CEA, J. Guilbert)
Projet de soutien personnel aux développements des méthodes d'analyse rapides. Ce contrat m'a aidé au développement de la méthode SCARDEC au travers d'un financement partiel du postdoctorat de Jean Charléty, et de l'achat d'une machine de calcul puissante (48 cœurs).

– Partenariat Hubert Curien Alliance (PHC France–Royaume Uni, Caractéristiques sismologiques des séismes majeurs de subduction). Financé en 2010 et 2011 par le ministère des Affaires étrangères et européennes (res-

ponsable en France, M. Vallée ; responsable au Royaume Uni, A. Ferreira)
Projet bilatéral avec Ana Ferreira à l'University of East Anglia, sur la complémentarité des analyses par ondes de volume et ondes de surface. Ce projet a permis plusieurs visites dans nos laboratoires respectifs, et entre autres aidé à la validation de la méthode SCARDEC.

– Projet SAFER (Seismic eArly warning For EuRope), financé par l'European Union Sixth Framework Program sur la période 2006-2009 (responsable "CNRS" : B. Delouis)
Travail sur les techniques d'analyses rapides de la source sismique. Notre contribution concernait les approches permettant de déterminer le mécanisme, la magnitude et une première estimation de l'étendue de rupture.

– Projet NERA (Network of European Research Infrastructures for Earthquake Risk Assessment and Mitigation), financé par la Communauté Européenne sur la période 2010-2014 (Responsable francais du Workpackage concerné : B. Delouis)
Contribution : Workpackage sur les techniques d'analyse et de partage efficace des données sismiques. Ce projet nous a déjà permis des échanges avec la sismologie opérationnelle, qui ont aidé au passage en temps quasi-réel de la méthode SCARDEC.

– Projet RAP-Antilles, financé par le GIS RAP en 2007 (responsable : F. Courboulex)
Contribution : travail sur la crise des Saintes de 2004 en utilisant les données accélérométriques du réseau RAP : détermination des paramètres de la source du choc principal et de certaines répliques.

– Projet TO_EOS (Le séisme de Tohoku-Oki de la Terre, aux océans et à l'espace : un cas d'étude critique pour l'anticipation des séismes et tsunamis), financé par l'ANR Flash « Great Tohoku Earthquake » sur la période 2011-2013 (responsable : Anthony Sladen)
Contribution : Analyse des propriétés de source (fonctions source) de la sismicité passée, du choc principal et des répliques.

– Projet QSHA (Quantitative Seismic Hazard Assesment), financé par l'ANR de 2004 à 2007 (Co-responsables : J. Virieux et P-Y Bard).
Contribution : Travail sur la modélisation des formes d'ondes d'un séisme dans la région niçoise.

A.4 Encadrement de travaux de recherche

– **Postdoctorant :**

Jean **Charléty**, 2007–2009 (encadrement : 75% M. Vallée, 25% B. Delouis) : détermination rapide des caractéristiques de source, à partir de données proches et lointaines. Travail spécifique sur le développement de la méthode SCARDEC.

– **Doctorants :**

Damien **Pageot**, 2008–2012 (encadrant principal : S. Operto) : Utilisation du champ d'onde télésismique pour l'imagerie lithosphérique

Antonella **Orefice**, 2009–2012 (encadrant principal : A. Zollo, Université de Naples) : Analyse de la séquence sismique de l'Aquila (2009) par fonction de Green empirique. J'ai encadré cette partie de thèse durant son séjour doctoral de 6 mois à Géoazur en 2011.

– **Stages de Master 2 :**

Jean-Baptiste **Ammirati**, 2011 (encadrant : M. Vallée) : Etude de la variabilité des propriétés de la source sismique: Application aux séismes majeurs de subduction ($M_w \geq 7$) entre 1994 et 2011.

Victor **Alfonso-Naya**, 2010 (encadrants : F. Courboulex et M. Vallée) : Simulation d'un fort séisme andin à Quito, en utilisant l'approche par fonction de Green empirique.

– **Stages de Master 1 et L3 :**

Valentin **Loir**, 2011 (encadrants : N.Béthoux et M. Vallée) : Etude du bruit de fond enregistré par le réseau Andes du Nord : Essai de détection de trémors non volcaniques.

Emilie **Ribeiro**, 2008 (encadrants : F. Courboulex et M. Vallée) : Simulation d'un séisme dans la région niçoise

Emeline **Maufroy**, 2005 (encadrant : M. Vallée) : Localisation relative des séismes principaux de la séquence sismique des Iles Vanuatu en 2003-2004.

A.5 Enseignement

Depuis mon arrivée à Geoazur, j'ai donné plusieurs cours de sismologie, en général en deuxième cycle:

- Licence 3, Sciences de la Terre (Université de Nice) : « Alea sismique » (12h) en 2005/2006.

- Master Omega (Formation de Physique de l'Université de Nice) : « Introduction à la sismologie » (12h) en 2006/2007.

- Master Prefalc (Master en co-tutelle entre l'Université de Nice, l'Ecole Polytechnique Nationale de Quito (Equateur), et l'Université de Lima (Pérou)) : « Introduction à la sismologie »
  15h de cours donnés en 2008/2009 et 2009/2010 à Quito
  15h de cours donnés en 2008/2009 et 2009/2010 à Lima

- Master IMMEN (Imagerie de Milieux Naturels, Université de Nice) : « Imagerie des séismes » (14h), en 2009/2010 et 2011/2012.

A.6 Animation scientifique

- Membre du groupe de sismologie, représentant le laboratoire avec T. Monfret (2007—2009)
- Correspondant du portail national de données Fosfore (piloté par N. Shapiro), représentant Géoazur avec C. Maron (2007-2010)
- Membre du comité scientifique Geoscope depuis 2008
- Organisation des séminaires à Geoazur (2005–2008)
- Animateur du « Thème subduction » à Géoazur, avec E. Tric et N. Béthoux (2008—2009)